Doctoral Thesis

Charge Carrier Dynamics in Metal Oxide Semiconductors for Solar Water Splitting

Juan Carlos Expósito Gálvez

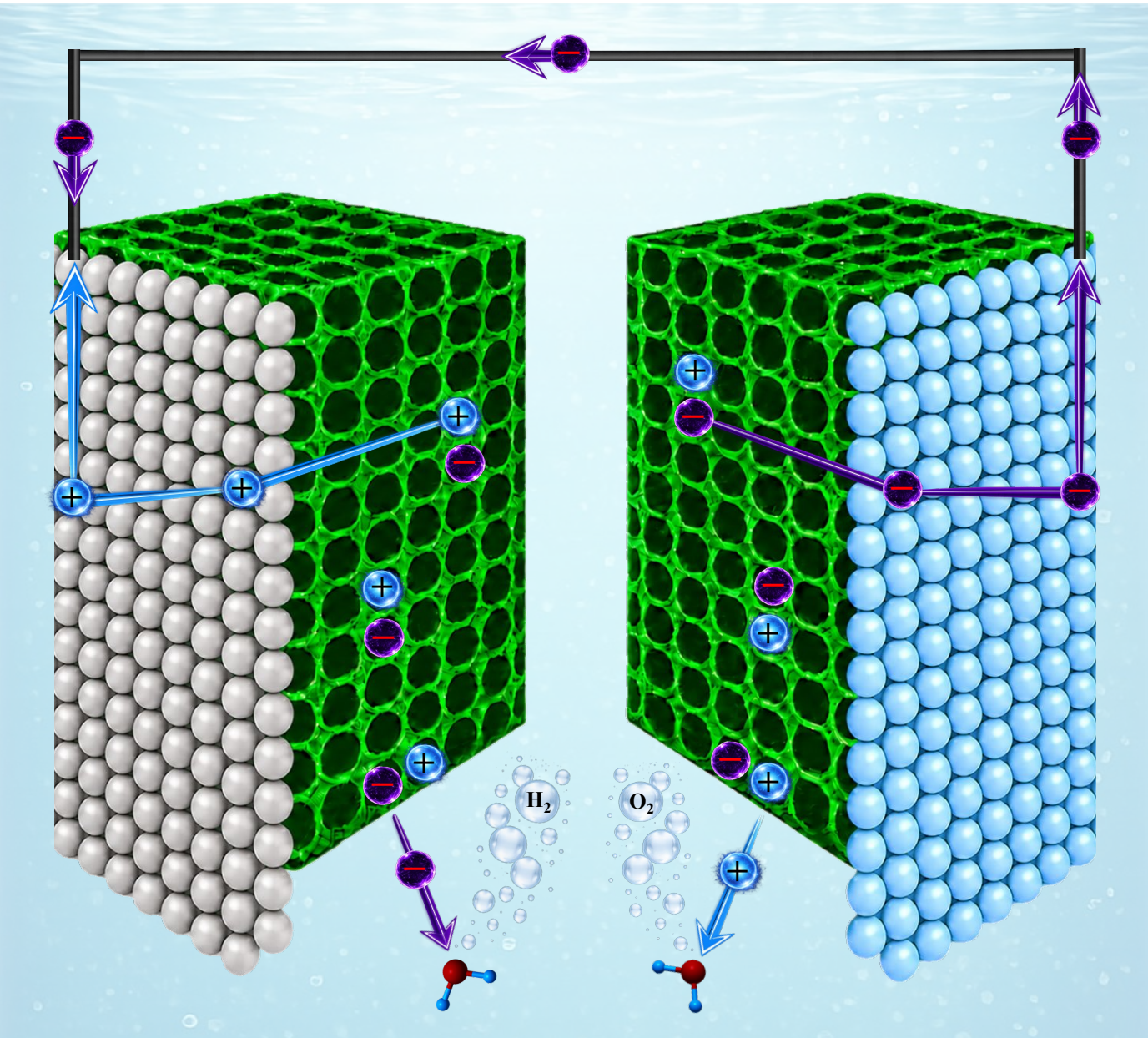

Universidad Pablo de Olavide
Seville, Spain 2026

UNIVERSIDAD PABLO DE OLAVIDE SEVILLA

Doctoral Thesis

Charge Carrier Dynamics in Metal Oxide Semiconductors for Solar Water Splitting

Author:

Juan Carlos Expósito Gálvez

Supervisor:

Prof. Gerko Oskam

Energy Conversion Nanomaterials & Devices group

Center for Nanoscience and Sustainable Technologies (CNATS)

Department of Physical, Chemical and Natural Systems

Seville, Spain 2026

A mis padres y a mi hermana

Agradecimientos

En primer lugar, quisiera agradecer profundamente a mi director de tesis, Gerko Oskam, por haberme dado esta oportunidad, por su tiempo, paciencia y dedicación durante estos años. Por haber sido guía indiscutible de este proceso, por ser tan humano, por tantas charlas "cortas" de 3 h, por todo el conocimiento y pensamiento crítico transmitidos, por darme libertad creativa y ayudarme a mejorar como científico y persona. También agradecer a Juan Antonio Anta por darme la oportunidad de formar parte de su grupo de investigación, por su confianza, y por contribuir en mi crecimiento profesional.

Quisiera agradecer a Roberto Gómez, así como a los miembros de su grupo, por acogerme en la Universidad de Alicante y por su apoyo durante mi estancia de investigación.

I would also like to thank Wey Yang Teoh, as well as the members of his research group at Universiti Malaya, for hosting me and for making my stay such a rewarding cultural and scientific experience.

Por otro lado, agradecer a los miembros pasados y presentes del grupo Energy Conversion Nanomaterials & Devices, así como a los vecinos de laboratorio, por vuestra ayuda, por haber compartido todos estos momentos, y por hacer el tiempo más ameno.

Gracias a mis familiares y amigos por acompañarme durante todo este tiempo y por estar siempre presentes.

A mis padres, Isabel y Juan Carlos, y a mi hermana María, por el apoyo incondicional brindado en todo momento, por vuestra educación y por creer en mí hasta el final. Sin vosotros esta tesis no hubiera sido posible; es tan vuestra como mía.

Abstract

The continuous increase in global energy demand, together with the environmental impact associated with fossil fuel consumption, has intensified the search for sustainable and carbon-neutral energy technologies. In this context, solar-driven hydrogen production has emerged as a promising strategy for storing renewable energy in the form of chemical fuel. Among the different approaches, photoelectrochemical (PEC) water splitting offers a direct pathway for converting solar energy into hydrogen using semiconductor materials. However, its practical implementation remains limited.

This thesis investigates the mechanisms governing charge carrier behaviour in semiconductor materials for PEC water splitting, with a particular focus on metal oxides. The central objective is to identify the key factors limiting performance, and to establish strategies to mitigate these limitations through tailored material and interface design.

A comprehensive experimental approach is employed, combining structural, morphological, and optical characterisation with advanced (photo)electrochemical techniques. In particular, electrochemical impedance spectroscopy (EIS) and intensity-modulated photocurrent spectroscopy (IMPS) are used to probe charge carrier dynamics under operating conditions. These small-signal techniques enable analysis of interfacial kinetics, allowing the deconvolution of competing processes within a unified kinetic framework.

Different material systems are investigated to address specific limiting factors. Photoelectrochemical properties of PCN-222, a metal-organic framework (MOF) composed of Zr_6 oxo-cluster and porphyrinic linkers, are tuned through metal modification (Ti and W) and with the incorporation of charge-selective interfaces (TiO_2 and NiO_x). These

strategies enable control over band alignment, leading to tuning of photocurrent directionality and improved charge separation, thereby highlighting the role of interfacial engineering in hybrid systems.

The influence of morphology is subsequently examined through a comparative study of WO_3 nanoparticles and nanoparticulate, porous nanofibres. The results indicate that, although light absorption remains largely unchanged, variations in particle size and surface area strongly influence charge carrier dynamics. While nanofibres exhibit improved performance in photocatalytic dye degradation, their performance decreases when they are integrated as photoelectrodes under applied potential. This behaviour is attributed to limitations in electron transport and enhanced recombination, highlighting the trade-offs associated with morphological control.

Finally, metal vanadate semiconductors and their alloys are analysed using frequency-resolved techniques to resolve charge carrier dynamics. In this study, the combined use of IMPS and EIS enables discrimination of the effects of copper substitution by alkaline earth cations (Ca and Mg). This substitution induces the formation of oxygen vacancies and alters interfacial charge transfer by introducing surface states that improve hole transfer dynamics. As a result, the interplay between charge transfer and recombination is modified, providing direct insight into the mechanisms governing the performance of these materials.

Overall, these results demonstrate that photoelectrochemical performance is governed not only by the intrinsic properties of the semiconductor, but also by the interplay between morphology, defects, and interfacial processes. The insights obtained provide useful guidelines for the development of more efficient photoelectrodes for solar fuel production.

Resumen

El continuo incremento de la demanda energética global, junto con el impacto ambiental asociado al consumo de combustibles fósiles, ha intensificado la búsqueda de tecnologías energéticas sostenibles y neutras en carbono. En este contexto, la producción de hidrógeno impulsada por energía solar ha emergido como una estrategia prometedora para el almacenamiento de energía renovable en forma de combustibles químicos. Entre los diferentes enfoques, la división fotoelectroquímica (PEC) del agua ofrece una vía directa para convertir la energía solar en hidrógeno utilizando materiales semiconductores. Sin embargo, su implementación práctica sigue estando limitada por ineficiencias fundamentales relacionadas con la dinámica de los portadores de carga.

Esta tesis investiga los mecanismos que gobiernan el comportamiento de los portadores de carga en materiales semiconductores para la división PEC del agua, con un enfoque particular en óxidos metálicos. El objetivo central es identificar los factores clave que limitan el rendimiento y establecer estrategias para mitigar estas limitaciones mediante el diseño optimizado de materiales e interfaces.

Para ello, se emplea un enfoque experimental integral que combina técnicas de caracterización estructural, morfológica y óptica con técnicas avanzadas de caracterización (foto)electroquímica. En particular, la espectroscopía de impedancia electroquímica (EIS) y la espectroscopía de fotocorriente modulada en intensidad (IMPS) se utilizan para estudiar la dinámica de los portadores de carga bajo condiciones de operación. Estas técnicas de pequeña perturbación permiten un análisis cualitativo de la cinética interfacial, facilitando la deconvolución de procesos competitivos dentro de un marco cinético unificado.

En esta tesis se investigan diferentes sistemas materiales para abordar factores limitantes específicos. Las propiedades fotoelectroquímicas de PCN-222, una red metal-orgánica (MOF) compuesta por oxo-clústeres de Zr_6 y ligandos porfirínicos, se ajustan mediante la modificación metálica (Ti y W) y la incorporación de interfaces selectivas de carga (TiO_2 y NiO_x). Estas estrategias permiten controlar la alineación de bandas, lo que conduce a la modulación de la direccionalidad de la fotocorriente y a una mejora en la separación de cargas, destacando el papel de la ingeniería interfacial en sistemas híbridos.

La influencia de la morfología se examina posteriormente mediante un estudio comparativo de nanopartículas y nanofibras de WO_3. Los resultados indican que, aunque la absorción de luz permanece prácticamente inalterada, las variaciones en el tamaño de partícula y el área superficial influyen de manera significativa en la dinámica de los portadores de carga. Mientras que las nanofibras muestran un mayor rendimiento en la degradación fotocatalítica de colorantes, su desempeño disminuye cuando se integran como fotoelectrodos bajo polarización aplicada. Este comportamiento se atribuye a limitaciones en el transporte electrónico y a un aumento de la recombinación, poniendo de manifiesto los compromisos asociados al control morfológico.

Finalmente, los semiconductores de vanadatos metálicos y sus aleaciones se analizan mediante técnicas resueltas en frecuencia para estudiar cualitativamente la dinámica de los portadores de carga. En este estudio, el uso combinado de IMPS y EIS permite discernir los efectos de la sustitución del cobre por cationes alcalinotérreos (Ca y Mg). Esta sustitución induce la formación de vacantes de oxígeno y modifica la transferencia de carga interfacial mediante la introducción de estados superficiales que mejoran la dinámica de transferencia de huecos. Como resultado, la interacción entre la transferencia de carga y la recombinación se ve modificada, proporcionando una visión directa de los mecanismos que gobiernan el rendimiento de estos materiales.

En conjunto, estos resultados demuestran que el rendimiento fotoelectroquímico está gobernado no solo por las propiedades intrínsecas del semiconductor, sino también por la interacción entre morfología, defectos y procesos interfaciales. Los conocimientos

obtenidos proporcionan directrices útiles para el desarrollo de fotoelectrodos más eficientes para la producción de combustibles solares.

Motivation and objectives

The development of efficient semiconductor photoelectrodes for solar water splitting requires a detailed understanding of the processes that determine their behaviour under illumination and electrochemical operation. The measured photoelectrochemical response results from several coupled phenomena, including light absorption, charge generation, carrier transport, recombination, and interfacial charge transfer. Therefore, improving photoelectrode performance requires not only evaluating the photocurrent produced by a given material, but also identifying the physical and kinetic processes that control it.

In this context, the general objective of this doctoral thesis is to study how material properties and electrode design influence the photoelectrochemical performance of semiconductor photoelectrodes for solar water splitting, with the aim of advancing the understanding of the charge carrier processes that determine their behaviour under operating conditions.

More specifically, this thesis pursues the following objectives:

i) To fabricate and evaluate semiconductor photoelectrodes for photoelectrochemical water-splitting applications.

ii) To study how structural, morphological, compositional, and interfacial modifications affect the photoelectrochemical performance of semiconductor photoelectrodes for solar water splitting.

iii) To combine steady-state photoelectrochemical measurements with small-perturbation techniques to investigate the charge carrier processes governing photocurrent generation and the overall response of semiconductor photoelectrodes.

iv) To gain deeper insight into the role of charge separation, transport, recombination, and interfacial charge transfer in determining the efficiency of semiconductor photoelectrodes.

v) To identify common performance-limiting factors across the studied systems and extract general principles that may contribute to the design of improved photoelectrodes for solar water splitting.

These objectives are addressed throughout the thesis by combining the fabrication and characterisation of selected semiconductor photoelectrodes with steady-state and small-perturbation photoelectrochemical measurements. After introducing the theoretical background and experimental methodology, the results chapters examine different material and electrode design strategies as model cases to evaluate their influence on photocurrent generation and charge carrier dynamics. Finally, the **general conclusions** bring together the main findings and discuss the common factors limiting the performance of the studied systems.

Contributions to the Scientific Community

The most relevant publications resulting from this thesis are:

1. **Comparing the performance of WO_3 nanoparticles and nanofibers: photocatalytic dye degradation versus photoelectrochemical water oxidation**. Juan Carlos Expósito-Gálvez, Ludek Hromadko, Marcela Sepúlveda, Francisco J. Peón-Díaz, Sayda Dinorah Coria-Quiñones, Omar Jiménez-Sandoval, Jan M. Macak*, and Gerko Oskam*. Electrochimica Acta, **2024**, 474. DOI:10.1016/j.electacta.2023.143545. (2024 JCR: Q1, 11/44, IF: 5.6).

2. **Charge dynamics as probed by small signal-modulated photocurrent and impedance spectroscopy of metal vanadate semiconductors and alloys**. Juan Carlos Expósito-Gálvez, Abhishek Rawat, Krishnan Rajeshwar*, and Gerko Oskam*. ACS Appl. Opt. Mater., **2025**, 3, 1684-1695. DOI:10.1021/acsaom.5c00154. (2024 JCR: Q2, 34/125, IF: 3.8).

3. **Tuning the photoelectrochemical properties of Ti/W-modified PCN-222 using charge-selective interfaces**. Juan Carlos Expósito-Gálvez, Florencia Vattier, José María Pedrosa, Carolina Carrillo-Carrión*, and Gerko Oskam*. ACS Appl. Mater. Interfaces, **2026**, 18 (6), 9877-9891. DOI:10.1021/acsami.5c22732. (2024 JCR: Q1, 83/461, IF: 8.2).

Other publications closely related to this thesis are:

1. **The effect of oxidative functionalization of carbon nanotubes on the morphological, optical, and photoelectrochemical properties of modified titanium dioxide photoanodes**. Francisco J. Peón-Díaz, Rodrigo Segura del Río*, Samuel Hevia, Fernanda Olivares, Juan Carlos Expósito-Gálvez, Renán Escalante, Karen Valadez-Villalobos, Antonio J. Riquelme, Gerko Oskam, and Ricardo Henríquez. J. Mater. Sci., **2023**, 58 (12), 5372-5388. DOI:10.1007/s10853-023-08351-4. (2023 JCR: Q2, 185/439, IF: 3.5).

2. **Exploring the charge carrier dynamics in carbon nanotubes-TiO_2 composites for water photooxidation**. Francisco J. Peón-Díaz, Juan Carlos Expósito-Gálvez, Rodrigo Segura del Río*, Ricardo Henríquez, Juan A. Anta*, and Gerko Oskam*. Catal. Today, **2024**, 438. DOI:10.1016/j.cattod.2024.114789. (2024 JCR: Q1, 16/75, IF: 5.3).

3. **Synthesis, characterization and photoelectrochemical performance of $Bi_2Fe_4O_9$ thin films**. Deimer R. Gómez-Mejía, Juan Carlos Expósito-Gálvez, Gerko Oskam, Daniel Olguín-Melo, and Omar Jiménez-Sandoval*. Mater. Today Chem, **2024**, 40, 102250. DOI:10.1016/j.mtchem.2024.102250. (2024 JCR: Q1, 46/239, IF: 6.7).

4. **Charge carrier dynamics of chemical vapor deposited carbon-doped titanium dioxide photoanodes**. Francisco J. Peón-Díaz*, Juan Carlos Expósito-Gálvez, Rodrigo Segura-del-Río*, Ricardo Henríquez, Sandra Fuentes Villalobos, Dani J. Rodríguez, and Gerko Oskam*. Ceram. Int., **2024**, 50 (24), 55134-55142. DOI:10.1016/j.ceramint.2024.10.359. (2024 JCR: Q1, 3/33, IF: 5.6).

5. **Silver copper oxide: a p-type transparent conductive oxide?** Abhishek Rawat, Juan Carlos Expósito-Gálvez, Mohammad Arham Shamim, Abhishek K. Adak, Chuzhong Zhang, Clement U. Nwokeji, Riddhi Ananth, Anushka Dasgupta, Enrique Ramirez, Sumit Kewalramani, Péter S. Tóth, Vinod K. Sangwan, Mark C. Hersam, Joseph H. Ngai, Gerko Oskam, Csaba Janáky, Michael J. Bedzyk, Tobin J. Marks, Efstathios I Meletis, and Krishnan Rajeshwar*. ACS Appl. Energy Mater. **2025**, 8 (21), 16179-16191. DOI:10.1021/acsaem.5c02655. (2024 JCR: Q2, 34/125, IF: 3.8).

A book chapter related to this thesis is:

1. **Photoelectrochemical characterization of metal oxide semiconductor for solar water splitting using intensity-modulated photocurrent spectroscopy**. Gerko Oskam, Sayda Dinorah Coria Quiñones, Juan Carlos Expósito-Gálvez, Omar Jiménez Sandoval, and Ingrid G. Rodríguez Gutiérrez. In Photoelectrochemical Engineering for Solar Harvesting, Elsevier, **2024**, pp 311-352. DOI:10.1016/B978-0-323-95494-5.00013-6.

Manuscripts submitted during this thesis and currently under review are:

1. **Energy-efficient rapid thermal processing for enhanced photoelectrochemical performance of WO_3 photoanodes**. Juan Carlos Expósito-Gálvez*, Maxime Contreras, Florencia Vattier, Roberto Gómez, and Gerko Oskam*. Under review in Catalysis Today. (2024 JCR: Q1, 16/76, IF: 5.3).

2. **Interfacial charge carrier dynamic of $Bi_2Fe_4O_9$ photoanodes: interplay between charge transfer and recombination**. Juan Carlos Expósito Gálvez*, Francisco J. Peón-Díaz, Deimer R. Gómez-Mejía, Omar Jiménez-Sandoval, and Gerko Oskam*. Under review in International Journal of Hydrogen Energy. (2024 JCR: Q1, 6/44, IF: 8.3).

* Corresponding author(s)

List of abbreviations

AM1.5G	Air mass 1.5 global
aq	Aqueous
ATR-FTIR	Attenuated total reflectance Fourier transform infrared
BSE	Backscattered electrons
CB	Conduction band
CCDC	Cambridge Crystallographic Data Centre
CE	Counter electrode
COD	Crystallography Open Database
CV	Cyclic voltammetry
DLS	Dynamic light scattering
DMF	N-N-dimethylformamide
DRS	Diffuse reflectance spectroscopy
EDX	Energy-dispersive X-ray spectroscopy
EIS	Electrochemical impedance spectroscopy
EL	Electrolyte
ETL	Electron transport layer
FE-SEM	Field-emission scanning electron microscopy
FTO	Fluorine-doped tin oxide
FWHM	Full width at half maximum
g	Gas
GAXRD	Grazing angle X-ray diffraction
HER	Hydrogen evolution reaction
HF	High frequency
HTL	Hole transport layer
IHP	Inner Helmholtz plane
IMPS	Intensity-modulated photocurrent spectroscopy

l	Liquid
LDA	Laser Doppler anemometry
LED	Light-diode emitting
LH	Low frequency
LMCT	Ligand-to-metal charge transfer
LSV	Linear sweep voltammetry
MB	Methylene blue
MOF	Metal-organic frameworks
MW	Microwave-assisted
NHE	Normal hydrogen electrode
NIR	Near infrared spectroscopy
OER	Oxygen evolution reaction
OHP	Outer Helmholtz plane
PCN-222	Porous Coordination Network-222
PDF	Powder diffraction file
PEC	Photoelectrochemical
PEIS	Photoelectrochemical impedance spectroscopy
POM	Polyoxometalate
PSM	Postsynthetic modification
PTA	Phosphotungstic acid
PV	Photovoltaic
PVD	Physical vapour deposition
PXRD	Powder X-ray diffraction
RCF	Relative centrifugal field
RE	Reference electrode
RHE	Reversible hydrogen electrode
ROS	Reactive oxygen species
SC	Semiconductor
sccm	Standard cubic centimetres per minute
SCR	Space charge region
SCS	Solution combustion synthesis
SE	Secondary electrons
SEM	Scanning electron microscopy
SOS	Spin-orbit splitting
SS	Surface states
UV	Ultraviolet

VB	Valence band
Vis	Visible
WE	Working electrode
XPS	X-ray photoelectron spectroscopy
XRD	X-ray diffraction

List of chemicals

Ag/AgCl	Silver/silver chloride
$BiVO_4$	Bismuth vanadate
$Ca_{0.1}Cu_{0.9}V_2O_6$	Calcium copper vanadate
$CaFe_2O_4$	Calcium ferrite
CO_2	Carbon dioxide
$CuBi_2O_4$	Copper bismuth oxide
$CuFeO_2$	Copper iron oxide
$CuNbO_4$	Copper niobium oxide
CuO	Cupric oxide
Cu_2O	Cuprous oxide
CuV_2O_6	Copper vanadate
$CuWO_4$	Copper tungstate
$[Fe(CN)_6]^{3-}$	Ferricyanide ion
$[Fe(CN)_6]^{4-}$	Ferrocyanide ion
H^+	Proton
H_2	Molecular hydrogen
H_2O	Water
$H_3PW_{12}O_{40}$	Phosphotungstic acid hydrate
KCl	Potassium chloride
$K_3Fe(CN)_6$	Potassium ferricyanide
$K_4Fe(CN)_6$	Potassium ferrocyanide
$LaTiO_2N$	Lanthanum titanium oxynitride
$Mg_{0.1}Cu_{0.9}V_2O_6$	Magnesium copper vanadate
NiO_x	Nickel oxide
O_2	Molecular oxygen
OH^-	Hydroxyl ion
$PW_{12}O_4^{3-}$	Phosphotungstate anion
TaON	Tantalum oxynitride

$TBAPF_6$	Tetrabutylammonium hexafluorophosphate
$TiCp_2Cl_2$	Bis(cyclopentadienyl)titanium(IV) dichloride
TiO_2	Titanium dioxide
WO_3	Tungsten trioxide
$ZnFe_2O_4$	Zinc ferrite
$[Zr_6(\mu_3\text{-}O)_4(\mu_3\text{-}OH)_4]$	Hexanuclear zirconium(IV) oxo-hydroxo cluster
$Zr_6O_4(OH)_4$	Hexanuclear zirconium oxo-hydroxo cluster (simplified form)
$\alpha\text{-}Fe_2O_3$	Hematite

List of physical constants

c	Speed of light	2.99792458×10^{8}	$\mathrm{m\ s^{-1}}$
e	Elementary charge	$-1.602176634 \times 10^{-19}$	C
h	Planck constant	$6.62607015 \times 10^{-34}$	J s
K	Scherrer constant	0.89	–
k_B	Boltzmann constant	1.380649×10^{-23}	$\mathrm{m^2\ kg\ s^{-2}\ K^{-1}}$

List of symbols

A	Absorptance	–
$A_{photodiode}$	Area of the photodiode	m^2
$A_{photoelectrode}$	Area of the photoelectrode	m^2
ABPE	Applied bias photon-to-current conversion efficiency	%
Abs	Absorbance	–
APCE	Absorbed photon-to-current conversion efficiency	%
B	Proportionality constant	$eV^{\gamma-1}$ $cm^{-\gamma}$
BE	Binding energy	eV
C	Capacitance	F cm^{-2}
C_{eff}	Effective capacitance	F cm^{-2}
C_H	Helmholtz capacitance	F cm^{-2}
CPE	Constant phase element	–
Csc	Semiconductor capacitance	F cm^{-2}
C_{ss}	Surface states pseudocapacitance	F cm^{-2}
C_T	Total capacitance	F cm^{-2}
d	Interplanar spacing	m
D_h	Hydrodynamic size	nm
D_t	Translational diffusion coefficient	m^2 s^{-1}
E	Potential	V
e^-	Electron	–
$E^\circ_{Ag/AgCl}$	Standard potential of the Ag/AgCl reference electrode	V
E_{CB}	Conduction band edge energy	eV
E_F	Fermi level	eV

E_F^{redox}	Fermi level of the redox couple in the electrolyte	eV
$E_{F,Q}$	Quasi-Fermi level	eV
E_F^n	Quasi-Fermi level for electrons	eV
E_F^p	Quasi-Fermi level for holes	eV
E_g	Bandgap energy	eV
E_{kin}	Measured kinetic energy	eV
E_{ox}	Oxidation energy of the redox couple in the electrolyte	eV
E°_{ox}	Oxidation potential of the redox couple in the electrolyte	V
EQE	External quantum efficiency	%
EQE_{DC}	DC external quantum efficiency	%
EQE_{max}	Maximum external quantum efficiency	%
E_{red}	Reduction energy of the redox couple in the electrolyte	eV
E°_{red}	Reduction potential of the redox couple in the electrolyte	V
E_{RHE}	Potential vs reversible hydrogen electrode	V
E_{VB}	Valence band edge energy	eV
f	Frequency	Hz
f_{max}	Frequency at the maximum of the loop of the 1st quadrant of the IMPS spectra	Hz
f_{min}	Frequency at the minimum of the loop of the 4th quadrant of the IMPS spectra	Hz
f_{min2}	Frequency at the minimum of the second loop of the 4th quadrant of the IMPS spectra	Hz
$F(R_\infty)$	Kubelka-Munk function	–
H	IMPS transfer function	–
h^+	Hole	–
I	Current	A
$\tilde{I}_{light}$	Modulated light intensity	$cm^{-2}\ s^{-1}$

$\tilde{I}$	Modulated current	A
$I(\lambda)$	Transmitted light intensity	W cm^{-2}
I_0	amplitude of the current	A
$I_0(\lambda)$	Incident light intensity for transmittance	W cm^{-2}
IPCE	Incident photon-to-current conversion efficiency	%
IQE	Internal quantum efficiency	%
IQE_{DC}	DC internal quantum efficiency	%
IQE_{max}	Maximum internal quantum efficiency	%
J	Current density	A cm^{-2}
j_0	Amplitude of the modulated light intensity	W cm^{-2}
J-E	Current density-potential	–
j_h	Hole current at the surface	A
j_{ph}	Amplitude of the modulated photocurrent	A
$\tilde{j}_{ph}$	Modulated photocurrent	A cm^{-2}
J-t	Current density-time	–
k_{rec}	Surface recombination constant	Hz
k_{tr}	Charge transfer constant	Hz
LHE	Light-harvesting efficiency	%
n	Concentration of electrons	cm^{-3}
Δn	Additional concentration of electrons induced by light	cm^{-3}
n_0	Equilibrium electron concentration in dark	cm^{-3}
N_{CB}	Effective density of states in the conduction band	cm^{-3}
n_{CPE}	Ideal capacitive behaviour	–
n_{surf}	Surface electron concentration	cm^{-3}
N_{VB}	Effective density of states in the valence band	cm^{-3}
m	Order of reflection	–
p	Concentration of holes	cm^{-3}

p_0	Equilibrium hole concentration in dark	cm^{-3}
Δp	Additional concentration of holes induced by light	cm^{-3}
PDI	Polydispersity index	–
P_{light}	Light power intensity	$W\ m^{-2}$
Q, CPE	Constant phase element	$\Omega^{-1}\ s^{n,CPE}$
R	Resistance	Ω
R^2	Coefficient of determination	–
R_{ct}	Charge transfer resistance	$\Omega\ cm^2$
R_p	Parallel resistance	$\Omega\ cm^2$
R_s	Series resistance	$\Omega\ cm^2$
$R_T(\lambda)$	Reflectance	%
R_{trap}	Trapping resistance	$\Omega\ cm^2$
$SS^{0/+}$	Surface states	–
$[SS^+]$	Surface-trapped hole population	cm^{-3}
SR	Spectral response	$A\ W^{-1}$
STH	Solar to hydrogen	%
t	Time	s
T	Temperature	K
$T(\lambda)$	Transmittance	–
V_H	Helmholtz potential drop	V
$\widetilde{V}$	Modulated voltage	V
x	Distance	Å
α	Absorption coefficient	cm^{-1}
β	Broadening at half maximum intensity	°
γ	Nature of the electronic transition	–
δ_p	Light penetration depth	μm
ζ	Zeta potential	mV
η	Viscosity	Pa s
η_{tr}	Relative charge transfer efficiency	%
θ	Bragg Angle	Rad
2θ	Scattered angle	°

λ	Wavelength	nm
ν	Frequency of light	Hz
τ	Crystallite size	nm
ϕ	Photon flux	$cm^{-2}\ s^{-1}$
Φ	Work function of the spectrometer	eV
φ	phase shift	rad
ω	Angular frequency	$rad\ s^{-1}$

Contents

Chapter 1

Introduction

Summary

This chapter presents the current energy challenge and discusses the potential role of photoelectrochemical (PEC) water splitting in addressing it. In this context, the main factors that limit the efficiency and stability of PEC systems are examined. Building on this, the strategies that have been developed to overcome these limitations are introduced, providing the basis for the work presented in the following chapters.

1.1 From energy demand to solar hydrogen production

Over the last decades, the continuous increase in global power demand has been driven by the population growth together with the improvement of living standards, resulting in the need for energy generation infrastructure with a power capacity exceeding 20 TW, with projections approaching 30 TW by 2050. Despite this trend, the global energy system still relies predominantly on fossil fuels, which account for the majority of the total energy supply, as shown in **Figure 1.1**. [1–3]

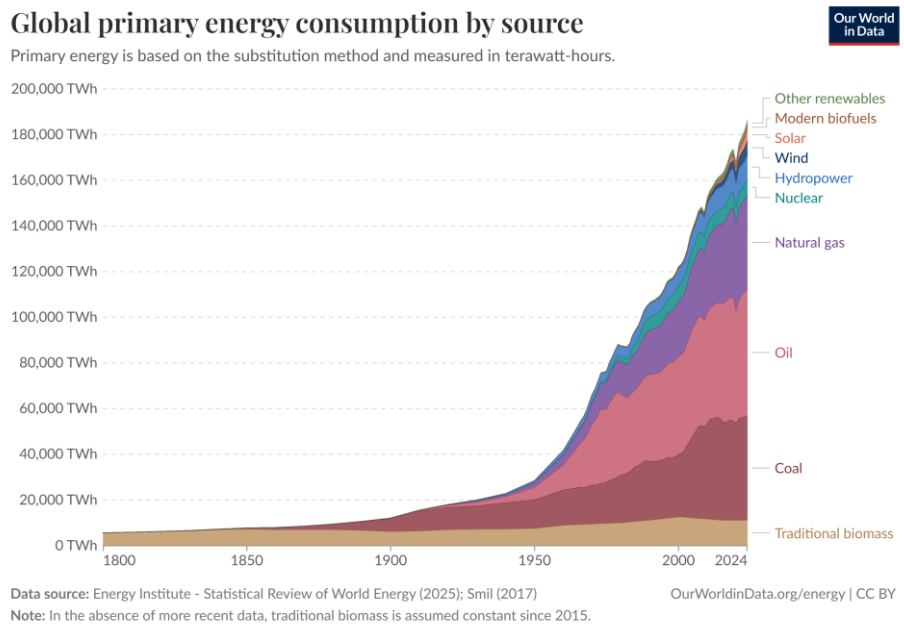

Figure 1.1. Global primary energy consumption by source.[2] Data reproduced under Creative Commons BY license (CC BY 4.0) (https://creativecommons.org/licenses/by/4.0/).

Their intensive use has led to severe environmental consequences, primarily associated with greenhouse gas emissions and climate change. The atmospheric concentration of CO_2 has increased from pre-industrial levels around 280 ppm to values above of 420 ppm, principally as a result of fossil fuel combustion, contributing to the greenhouse effect and the

notable increase in global temperatures. If this trend continues, CO_2 levels will surpass the 550 ppm this century, with the consequent higher risk of severe climate-related effects.[4–7]. In addition, the extraction of fossil resources is becoming progressively more difficult and less cost-effective, further motivating the transition towards sustainable energy technologies.[1,8]

Under these circumstances, the development of an alternative energy technology capable of satisfying future demand while minimising the environmental impact becomes crucial. Among the different green energy sources available, solar driven processes are considered the most promising, since the solar energy reaching the Earth's surface is on the order of 10^5 TW, that far exceeds the global power consumption.[9–11]

The most common approach is the direct solar energy conversion into electricity using photovoltaic (PV) solar cells, which has been widely developed in recent years, reaching high efficiencies.[12,13] However, due to the intermittent nature of the sun (day and night), solar energy conversion into chemical energy is interesting, particularly when long-term storage is required. Hydrogen has received special attention as a clean energy carrier because its combustion produces only water. Furthermore, it exhibits a higher energy density than conventional fossil fuels.[14,15]

Among the different approaches for hydrogen production, coupled photovoltaic-electrolysis system, photocatalytic and photoelectrochemical (PEC) water splitting have attracted particular attention. These methods are based on the use of semiconductor materials to absorb light and drive the water splitting reaction, but they differ in their configuration and operation.[16] In the electrolysis coupled to photovoltaic system, solar irradiation is absorbed by the PV cell, generating the voltage and photocurrent required to drive water electrolysis in a separate electrochemical cell. The PV cell is directly connected to the electrochemical system but remains physically isolated from the aqueous electrolyte to prevent degradation. This configuration offers important advantages, as it avoids the need for storage of electrical energy generated from sunlight such as batteries. However, it also presents several challenges, particularly related to system integration and

the high cost of electrolysers containing noble metal catalysts, such as Pt, Ir, and Ru.[17–19] In the photocatalytic method, the process takes place in a dispersed system, where semiconductor particles are suspended in an aqueous solution. Upon light absorption, electron-hole pairs are generated and drive the reduction and oxidation reactions directly at the particle surface. This approach is conceptually simple and does not require an external circuit, however, it often suffers from low efficiency due to high charge recombination and limited control over charge separation, as well as difficulties in the separation of the evolved hydrogen and oxygen gases.[20–22]

On the other hand, the photoelectrochemical method is carried out in an electrochemical cell, where the semiconductor is integrated as a photoelectrode. In this configuration, photogenerated charge carriers are spatially separated and transported through an external circuit, which generally enhances efficiency, allowing a greater degree of control over the reaction dynamics. In addition, this configuration enables the separate collection of hydrogen and oxygen at different electrodes through the use of a membrane. As a result, higher efficiencies can be achieved, although the system is typically more complex.[21,23,24]

1.2. Requirements for efficient PEC systems

In order to select a good photoelectrode candidate for water splitting, several requirements should be taken into consideration, as shown in **Figure 1.2**.[25,26] The spectral absorption of a semiconductor is determined by its bandgap (E_g). For water splitting, the band gap of a semiconductor must exceed the theoretical energy requirement (1.23 eV), plus thermodynamic losses (0.3–0.4 eV) and extra overpotentials to ensure fast reaction kinetics (0.4–0.6 eV). As a consequence, the bandgap should be higher than approximately 1.9 eV, which corresponds to an absorption edge of around 650 nm. On the other hand, it should not exceed about 3.1 eV (400 nm), as this marks the upper limit of the visible region of the solar spectrum.[27–29] **Figure 1.3** schematically compares the bandgap energies and band edge positions of different semiconductor materials relative to the redox potentials of water. The chemical stability

of photoactive semiconductors under operational conditions, such as under illumination, applied potential and immersed in an electrolyte, is a crucial factor. Generally, the photocorrosion stability of a semiconductor increases with its bandgap, leading to a trade-off between strong light absorption and long-term chemical stability.[30,31]

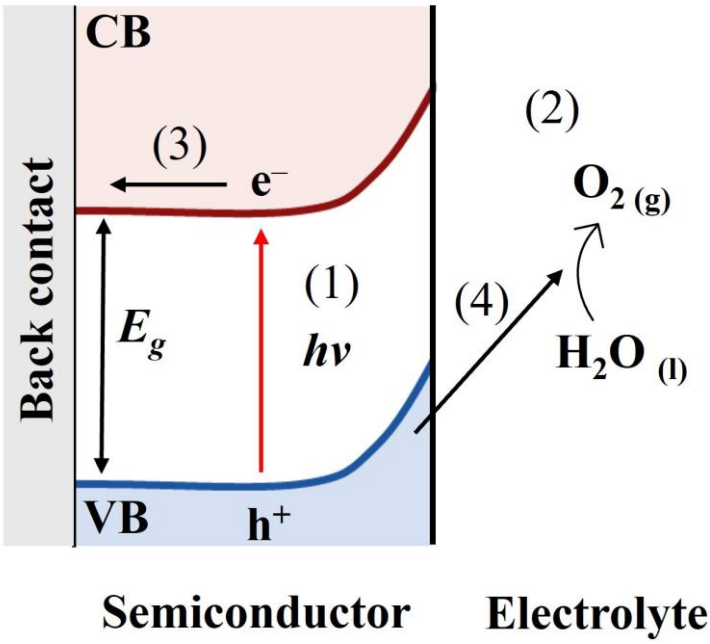

Figure 1.2. Schematic representation of the main requirements for an n-type semiconductor for photoelectrochemical water splitting: (1) photogeneration of electron-hole pair, (2) alignment of the band edges with the redox potentials of water, (3) charge transport, and (4) charge transfer.

Another important requirement is the proper alignment of the band edges with the redox potentials of water. Specifically, the conduction band (CB) must be located at a higher energy than the reduction potential, while the valence band (VB) should lie at lower energy than the oxidation potential. In addition, charge transport properties can vary significantly depending on the semiconductor. In TiO_2, electron mobility is relatively fast and does not represent a major limitation.[32–35] In

contrast, in hematite (α-Fe_2O_3), the much lower electron diffusion coefficient makes charge transport one of the main factors limiting performance.[36–40] A further requirement is that the interfacial transfer of electrons and holes, corresponding to the oxidation and reduction reactions, must be sufficiently fast to overcome electron-hole recombination.[41,42]

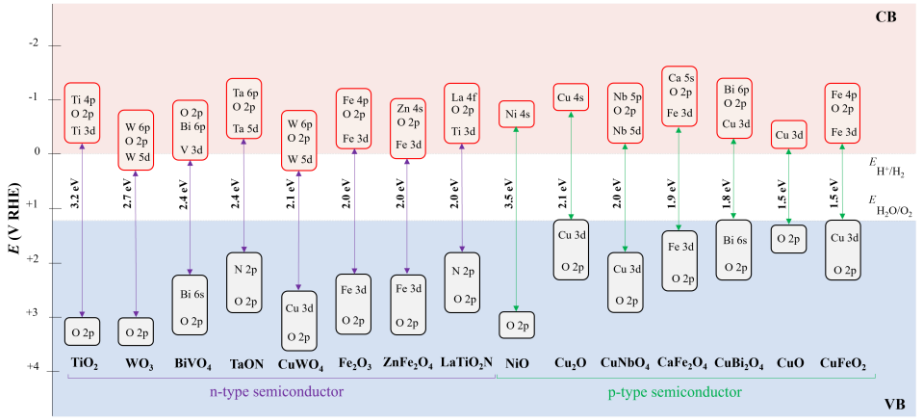

Figure 1.3. Schematic comparison of the bandgap energies and band edge positions of different semiconductor materials relative to the redox potential of water.[26]

In fact, a material that fulfils all of these requirements has not been yet identified. In practice, improving one property often comes at the expense of another, leading to unavoidable trade-offs. As a result, research is focused on developing materials that combine these properties as effectively as possible, while also being low-cost and composed of earth-abundant elements.[43,44]

1.3. Strategies for improving PEC systems

Different strategies to improve performance of PEC system are schematised in **Figure 1.4**. One of the most effective methods to enhance the performance of PEC systems is the control of the semiconductor morphology, especially via nanostructuring (**Figure 1.4a**). This approach is particularly crucial for materials with short charge carrier diffusion

lengths, where a substantial fraction of photogenerated carriers recombines before reaching the surface. By reducing the characteristic dimensions of the material to the nanoscale, the distance that charge carriers must travel is shortened, facilitating their collection at the back contact or the transfer to the electrolyte. Furthermore, nanostructuring significantly enhances the surface-to-volume ratio, thereby increasing the surface area and the number of active sites available for reactions.[45–47] For example, nanostructures like nanorods or nanowires have been widely utilized in materials with poor charge transport properties, such as hematite, resulting in significant enhancements in photocurrent.[48,49] However, this approach can also present certain disadvantages. The increased surface area may promote surface recombination by introducing surface states, while the greater exposure to the environment can compromise the chemical stability of the material under operating conditions.[50,51] Additionally, the need for well-defined nanostructures may induce reproducibility challenges.[26]

Another widely used technique to boost PEC efficiency is impurity doping (**Figure 1.4b**), which involves the incorporation of foreign atoms into the semiconductor lattice, tailoring its electronic properties. By introducing dopants with different valence states, the density of charge carriers can be increased, leading to enhanced electrical conductivity and more efficient charge transport. Moreover, doping can modify the optical properties by introducing new electronic states within the bandgap, which may extend light absorption into the visible region. However, excessive doping may lead to the introduction of recombination centres, thereby limiting the performance.[26,52–54] Similarly, defect engineering (**Figure 1.4c**) through the generation of vacancies is widely used to tune the properties of semiconductors. Vacancies are missing atoms in the crystal network, which can locally modify the electronic structure and influence charge distribution within the material. Such vacancies can act as adsorption centres for hydroxyl groups and also as shallow electron donors, which have been shown to enhance photoelectrochemical. However, their impact strongly depends on their concentration and distribution, as an excessive density of defects may promote charge recombination and ultimately reduce the efficiency of the system.[26,55–57]

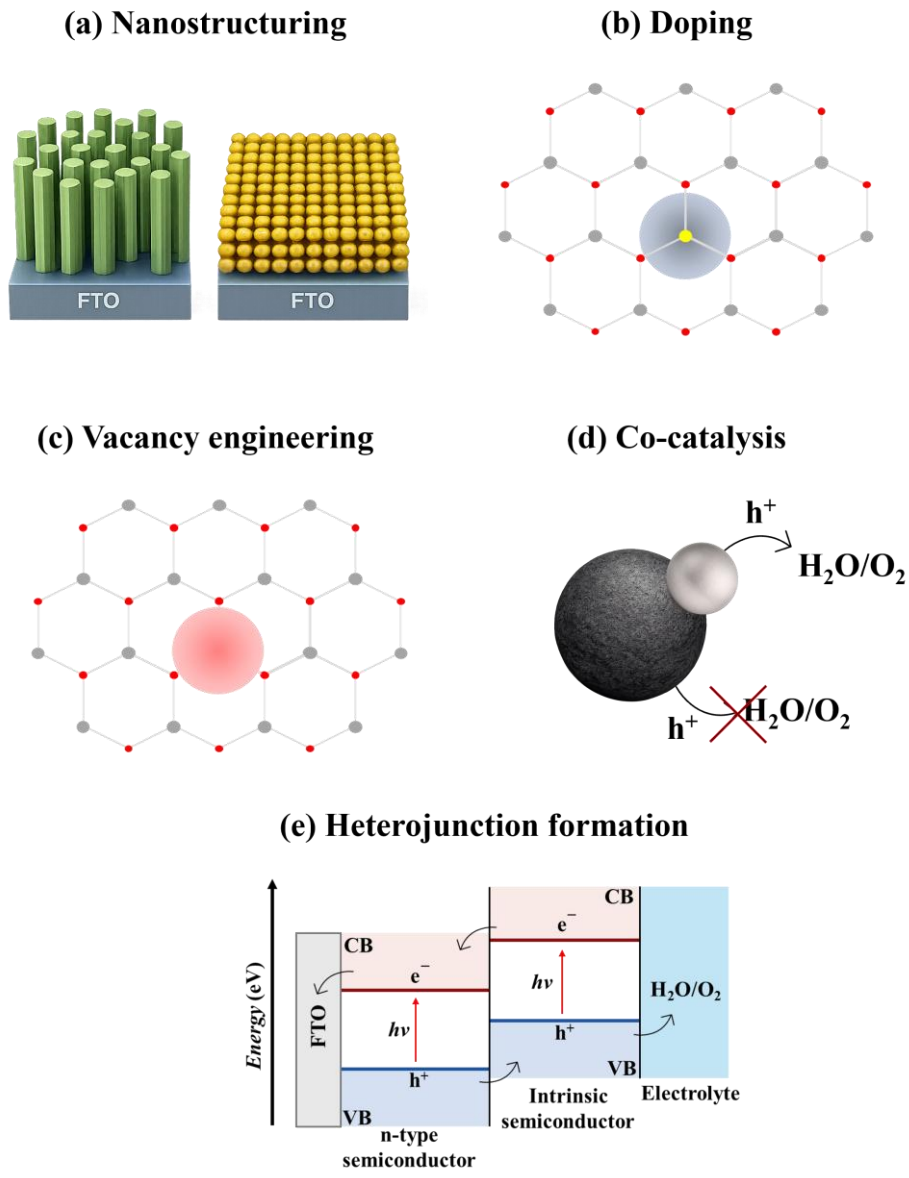

Figure 1.4. Schematic representation of different strategies to improve PEC performance: (a) nanostructuring, (b) doping, (c) vacancy engineering, (d) co-catalysis, and (e) heterojunction formation.

Co-catalysts (**Figure 1.4d**) are often incorporated onto the surface of semiconductor photoelectrodes to improve the interfacial charge transfer efficiency, as they provide catalytically active sites, facilitating surface

charge transfer, prevent charge accumulation at the interface and therefore minimizing surface recombination. In addition, co-catalysts can promote specific reaction pathways by stabilizing reaction intermediates. However, their effectiveness strongly depends on factors such as their composition, dispersion, and surface coverage, as an excess of co-catalyst can hinder light absorption or introduce additional recombination pathways.[58–62] Finally, the use of heterojunctions (**Figure 1.4e**) and selective layers, such as passivation, blocking, or transport layers represent an additional approach to improve interfacial properties and will be discussed in more detail in **Chapter 2**.

Despite the significant progress achieved through the strategies described above, the development of materials that simultaneously meet all the requirements for efficient PEC water splitting remains a major challenge. In this context, the exploration of new materials and surface modification approaches are essential to further improve device performance. This thesis is therefore focused on investigating the factors that limit the efficiency of PEC systems, with particular attention to charge transport and interfacial processes, as well as on the development of strategies to overcome these limitations.

Chapter 2

Theoretical background

Summary

This chapter introduces the fundamental concepts governing photoelectrochemical systems, including light absorption, charge generation and separation, and interfacial charge transfer processes. Particular attention is given to the role of semiconductor/electrolyte interfaces, surface states, and distribution of the electrochemical potential under operating conditions. A kinetic framework describing the competition between charge transfer and recombination is presented, together with the influence of heterojunctions and charge-selective layers on carrier dynamics. These concepts provide the basis for the interpretation of the experimental result discussed in the following chapters.

2.1. Photoelectrochemical water splitting principle

In the photoelectrochemical water splitting process, illumination of a semiconductor generates electron-hole pairs that are separated and directed towards different interfaces, where they drive the hydrogen (HER) and oxygen (OER) evolution reactions.

In alkaline electrolyte, the overall water splitting can be divided into two half-reactions

$$4H_2O_{(l)} + 4e^- \leftrightarrow 2H_{2\,(g)} + 4OH^-_{(aq)} \quad E^\circ_{red} = -0.828 \text{ V vs NHE} \quad (2.1)$$

$$4OH^-_{(aq)} + 4h^+ \leftrightarrow 2H_2O_{(l)} + O_{2\,(g)} \quad E^\circ_{ox} = +0.401 \text{ V vs NHE} \quad (2.2)$$

and in acidic electrolyte

$$4H^+_{(aq)} + 4e^- \leftrightarrow 2H_{2\,(g)} \quad E^\circ_{red} = +0.000 \text{ V vs NHE} \quad (2.3)$$

$$2H_2O_{(l)} + 4h^+ \leftrightarrow 4H^+_{(aq)} + O_{2\,(g)} \quad E^\circ_{ox} = +1.229 \text{ V vs NHE} \quad (2.4)$$

From a thermodynamic perspective, water splitting is a non-spontaneous process requiring a minimum potential difference of 1.23 V under standard conditions, which corresponds to a positive Gibbs free energy change of 237 kJ mol^{-1}. In practice, additional energy is needed to overcome kinetic barriers and recombination losses, resulting in higher operational potentials. [7,63–66]

As illustrated in **Figure 2.1**, the PEC configuration determines where photogenerated electrons and holes are consumed in the HER and OER. In photoanode-based cells (**Figure 2.1a**), photogenerated holes drive water oxidation at the semiconductor/electrolyte interface, while electrons are collected at the back contact and transported through the external circuit, driven by the potential difference across the cell (typically assisted by an external potential), to a metallic counter electrode, where hydrogen evolution occurs. In a photocathode-based cell (**Figure 2.1b**), photogenerated electrons reduce protons at the semiconductor/electrolyte interface, while the corresponding holes are neutralised with electrons supplied through the external circuit. The

complementary oxidation reaction takes place at the metallic counter electrode, driven by the potential difference across the cell.

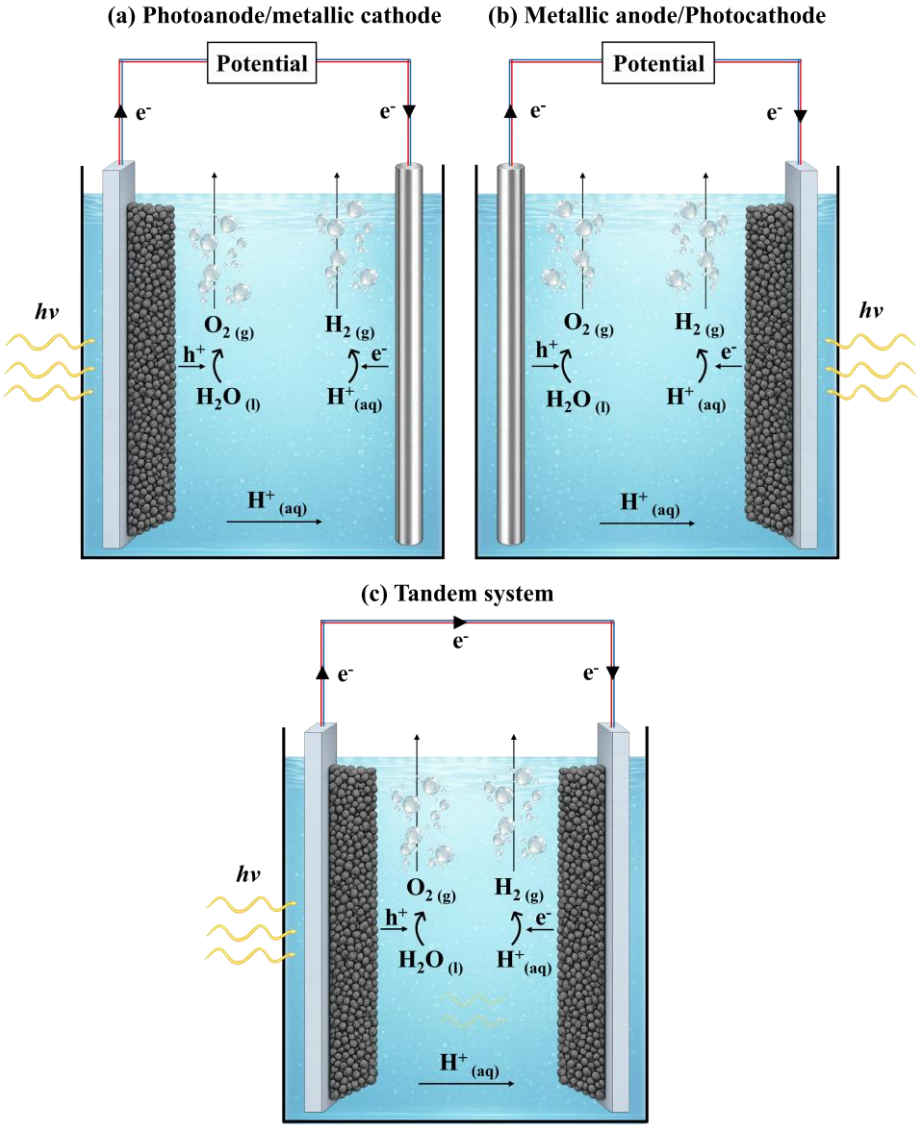

Figure 2.1. Photoelectrochemical water splitting configurations in acidic environment of a (a) photoanode/metallic cathode, (b) photocathode/metallic anode, and (c) tandem system (photoanode/photocathode).

On the other hand, in a tandem configuration (**Figure 2.1c**), a photoanode and a photocathode are combined so that electron-hole pair generation occurs in both electrodes, providing sufficient photovoltage to drive the overall reaction without the need for an external potential. In this case, electrons generated at the photoanode are transported to the photocathode, where they recombine with photogenerated holes, while holes at the photoanode drive water oxidation and electrons at the photocathode drive proton reduction.

2.2. Photoactive semiconductor materials

Solid materials can be broadly classified as conductors, semiconductors, or insulators, according to their electronic structure, as illustrated in **Figure 2.2**.

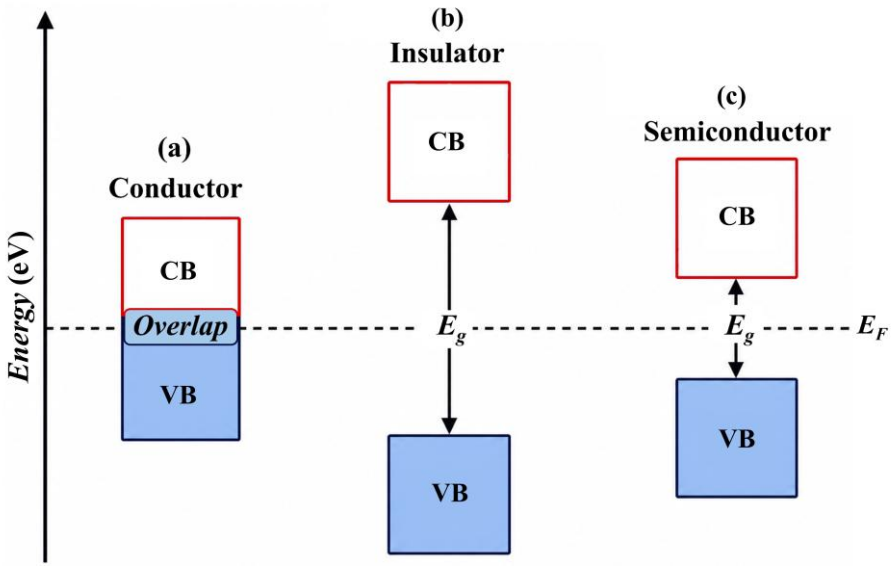

Figure 2.2. Schematic representation of the electronic structure of (a) conductors, (b) insulators, and (c) semiconductors.

The interaction between atomic orbitals gives rise to energy bands, namely the valence band which is typically occupied by valence electrons, and the conduction band, which is largely unoccupied. The

energy difference between these two bands is defined as the bandgap. In conductors (**Figure 2.2a**), the valence and conduction bands overlap or are partially filled, allowing electrons to move freely. In contrast, insulators (**Figure 2.2b**) exhibit a large bandgap that prevents the excitation of charge carriers under normal conditions. Semiconductors (**Figure 2.2c**) lie between these two extremes, possessing a moderate bandgap that enables the generation of mobile charge carriers upon optical excitation, making them particularly suitable for energy conversion applications.[64,67,68]

Optical absorption arises from the interaction between photons and the electronic transition from the valence band to the conduction band, as illustrated in **Figure 2.3**. These transitions occur when the photon energy is equal to or greater than the bandgap energy, which defines the absorption edge of the semiconductor.

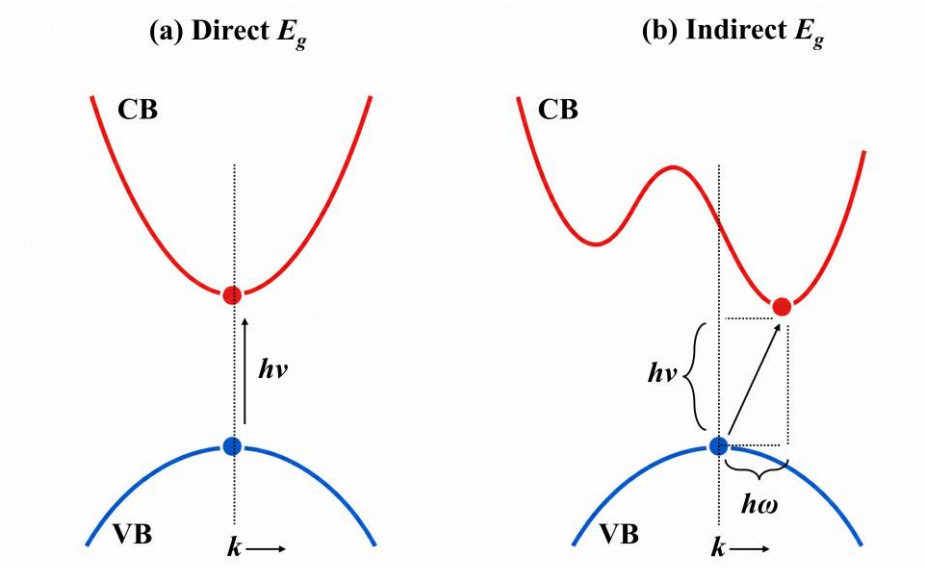

Figure 2.3. Schematic representation of (a) direct and (b) indirect bandgap semiconductors. *k* represents the crystal momentum.

The nature of the bandgap plays a crucial role in the absorption process. In direct bandgap semiconductors (**Figure 2.3a**), the maximum of the valence band and the minimum of the conduction band are located at the

same momentum, allowing electronic transition to occur without a change in the crystal momentum. This leads to large absorption coefficients, enabling efficient light absorption within relatively short penetration depths. In contrast, indirect bandgap semiconductors (**Figure 2.3b**) exhibit a mismatch in momentum between the valence band maximum and the conduction band minimum. In this case, optical transition requires simultaneous involvement of a phonon (i.e., vibration of the crystalline network, $h\omega$) to conserve momentum. As a result, these transitions are less probable, leading to lower absorption coefficients and requiring thicker materials to achieve significant light absorption.[64,69,70]

2.3. Charge carrier properties

The electrical behaviour of semiconductor materials is determined by how electronic states are distributed and occupied within the valence and conduction bands. These bands arise from the interaction of a large number of atomic orbitals, which transform discrete energy level into a quasi-continuous distribution of allowed energy states, commonly described by the density of states (DOS). The occupancy of these states defines the population of charge carriers present in the material and is described in terms of the Fermi level (E_F), which represents the energy at which the probability of finding an electron is 50% under equilibrium conditions. The distribution of electronic states and the position of the Fermi level in intrinsic and extrinsic doped semiconductors, are schematically illustrated in **Figure 2.4**.

In intrinsic semiconductors (**Figure 2.4a**), the valence band is essentially filled, while the conduction band remains largely unoccupied. Upon illumination, electrons can be excited across the bandgap from the valence band to the conduction band, generating electrons and holes as mobile charge carriers. This process results in equal concentrations of electrons and holes. The population of charge carriers can be modified through the introduction of dopants or the presence of intrinsic defects. This process alters the concentration and type of charge carriers within the material. Donor species such as oxygen vacancies introduce additional electrons, leading to n-type behaviour (**Figure 2.4b**), where

electrons are the majority carriers. Conversely, acceptor species such as metal vacancies generate holes, resulting in p-type behaviour (**Figure 2.4c**), where holes are the majority carriers. These modifications in carrier population are accompanied by shift in the Fermi level within the bandgap, which moves closer to the conduction band in n-type materials and towards the valence band in p-type materials, reflecting the corresponding change in the equilibrium distribution of occupied states.[64,71]

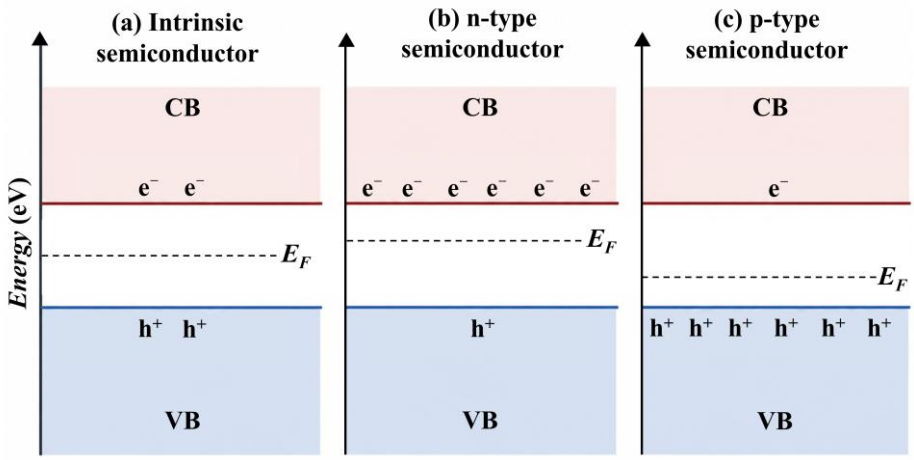

Figure 2.4. Schematic representation of (a) intrinsic, (b) n-type, and (c) p-type semiconductors.

The resulting changes in carrier population has a direct impact on the electrical conductivity of the material, which depends not only on the concentration of charge carriers but also on their mobility within the semiconductor. In this context, the energetic position of donor and acceptor states within the bandgap is particularly relevant. Shallow states, located close to the band edges, can be readily ionized and therefore contribute effectively to the free carrier population, enhancing conductivity. In contrast, deep states lie further within the bandgap and are less easily ionized, so they do not significantly increase the number of free carriers and often act as trapping or recombination centres.[64,71,72]

Under equilibrium conditions (i.e., no illumination and not current flow), and assuming non-degenerate behaviour, the concentrations of electrons

in the conduction band and holes in the valence band can be expressed as:

$$n = N_{CB} \exp\left(-\frac{E_{CB} - E_F}{k_B T}\right) \quad (2.5)$$

$$p = N_{VB} \exp\left(-\frac{E_F - E_{VB}}{k_B T}\right) \quad (2.6)$$

Where n and p denote the concentrations of electrons and holes, respectively, E_{CB} and E_{VB} correspond to the conduction and valence band edge energies, respectively, k_B is the Boltzmann constant, and T is the absolute temperature. The parameters N_{CB} and N_{VB} represent the effective densities of states in the conduction and valence bands, respectively, describing the number of available electronic states near the band edges.

In intrinsic semiconductors, the concentrations of electrons and hole are equal, and can be expressed as:

$$np = n_i^2 = N_{CB} N_{VB} \exp\left(-\frac{E_{CB} - E_{VB}}{k_B T}\right) \quad (2.7)$$

These expressions reveal the exponential dependence of carrier concentrations on the position of the Fermi level. Consequently, the shift in E_F induced by doping or intrinsic defects leads to a significant variation in the population of charge carriers. It should be noted that these relations are valid for non-degenerate semiconductor where the Fermi level lies within the bandgap and sufficiently far from the band edges.[7,64,73,74]

2.4. Semiconductor/electrolyte interface

When a semiconductor is brought into contact with an electrolyte, charge redistribution occurs at the interface until thermodynamic equilibrium is established, as illustrated in **Figure 2.5**. Prior to contact (**Figure 2.5a**), the Fermi level of the semiconductor and the electrochemical potential of the redox couple in the electrolyte (E_F^{redox}) are generally different. Upon contact (**Figure 2.5b**), this difference in energy levels leads to a redistribution of charge carriers at the interface, involving charge transfer

between the semiconductor and the electrolyte until the Fermi level is aligned across the system.

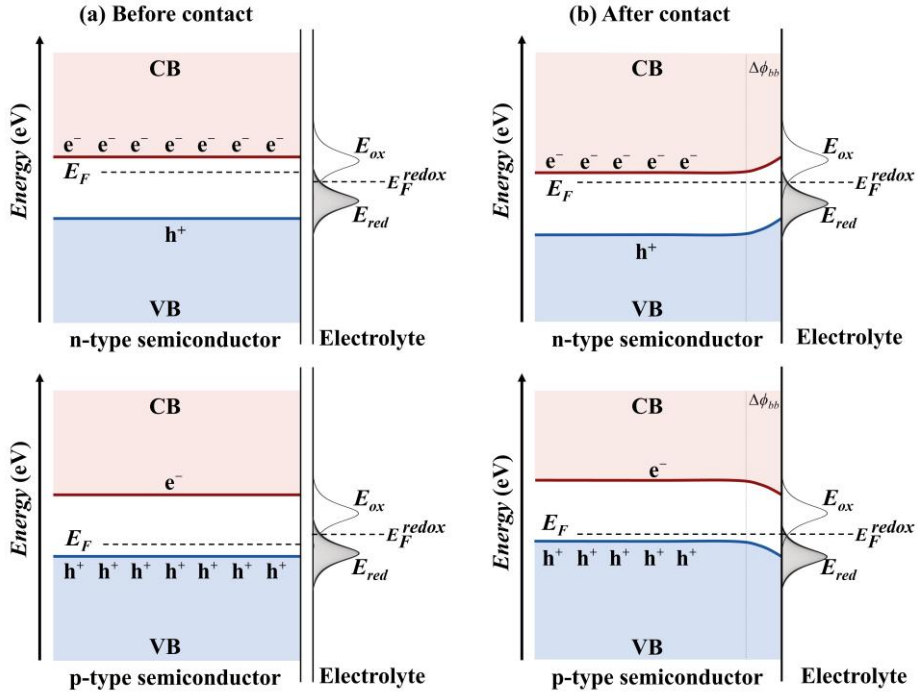

Figure 2.5. Schematic energy diagram of the semiconductor/electrolyte interface for n-type and p-type semiconductors (a) before and (b) after contact (i.e., at equilibrium). E_{ox} and E_{red} denote the oxidation and reduction energies of the redox couple in the electrolyte.

The redistribution of charge gives rise to a potential difference at the interface, which is distributed between the semiconductor and the electrolyte, as schematically illustrated in **Figure 2.6**. On the electrolyte side, this potential drop (V_H) occurs across the electrical double layer, commonly referred to as the Helmholtz layer. This interfacial region includes the inner Helmholtz plane (IHP), formed by specifically adsorbed ions such as H^+ and OH^- directly interacting with the semiconductor surface, and the outer Helmholtz plane (OHP), corresponding to the closest approach of solvated ions near the surface. The potential drop across this compact interfacial region gives rise to the Helmholtz capacitance (C_H), which is generally defined by the distance

between the electrode surface and the solvated ions located at the OHP. On the semiconductor side, the equilibration process leads to a spatial variation of the potential near the interface, which is reflected in the bending of the conduction and valence bands and gives rise to a capacitance (C_{sc}) associated with charge redistribution in the semiconductor. [7,64,65,75–78]

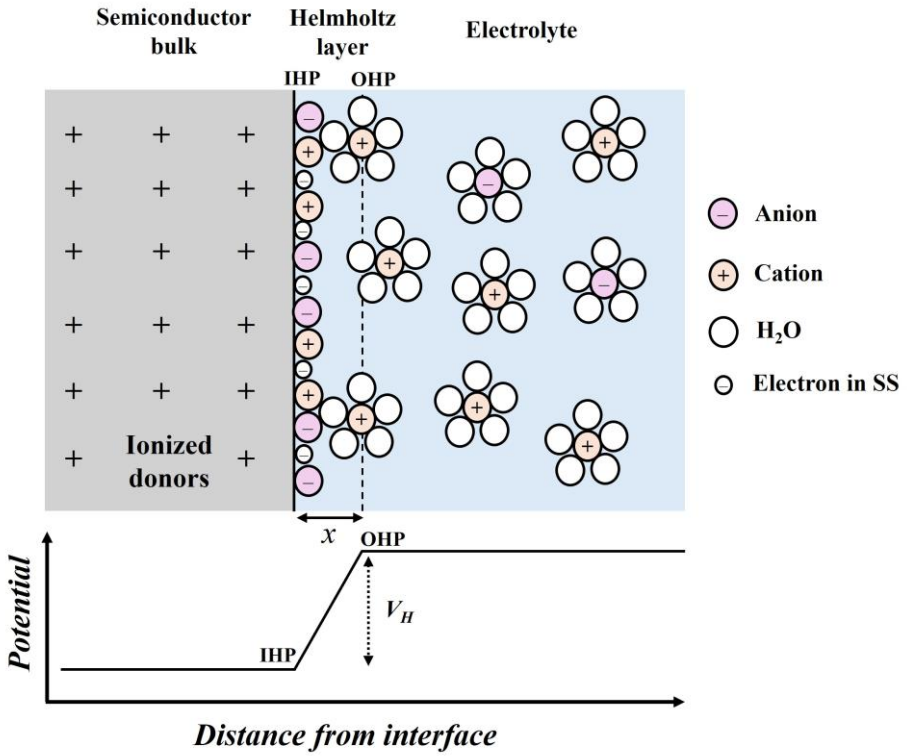

Figure 2.6. Schematic representation of the potential distribution at the semiconductor/electrolyte and the Helmholtz layer. The distance x is around 2−5 Å.

The nature of the semiconductor determines the type of charge transfer that occurs in order to reach the equilibrium. In n-type semiconductor, donor states introduce electronic states close to the conduction band, increasing the electron concentration and shifting the Fermi level towards the conduction band. Upon contact with an electrolyte, electrons may be transferred from the semiconductor to the electrolyte until a

common Fermi level is established across the interface. Consequently, the near-surface region becomes depleted of electrons, leading to a net positive charge. This charge is compensated by the accumulation of oppositely charged ions in the electrolyte, within the Helmholtz layer, giving rise to upward (i.e., towards higher energies) band bending ($\Delta\phi_{bb}$). In p-type semiconductors, acceptor states introduce electronic levels close to the valence band, increasing the hole concentration and shifting the Fermi level towards the valence band. Upon contact with an electrolyte, holes may be transferred from the semiconductor to the electrolyte until equilibrium is reached. This charge is similarly compensated by the accumulation of oppositely charged ions in the electrolyte, leading to downward (i.e., towards lower energies) band bending. As a result, a common Fermi level is established across the semiconductor/electrolyte interface, indicating that thermodynamic equilibrium has been reached.[79,80]

In conventional bulk semiconductors, the variation of the potential on the semiconductor side is often described in terms of space charge region (SCR), where mobile charge carriers are depleted and the potential varies over a characteristic length scale. This description is commonly used to account for the band bending at the interface. However, in nanostructured materials, this classical description is not always strictly applicable. The characteristic dimensions of the semiconductor nanoparticles can be comparable to or smaller than the depletion width, which limits the formation of a well-defined space charge region. As a result, the interfacial behaviour is more strongly influenced by surface and interface processes rather than by bulk charge separation.[81–84]

2.5. Photoelectrochemical systems under operating conditions

2.5.1. Illumination

Under operating conditions, such as under illumination and applied potential in a photoelectrochemical cell, the semiconductor/electrolyte interface is driven out of thermodynamic equilibrium, as illustrated in

Figure 2.7 for n-type semiconductors with photoanode behaviour. In the dark (**Figure 2.7a**), the system remains at equilibrium, and a single Fermi level describes the distribution of charge carriers across the semiconductor and the metallic counter electrode, aligned with the electrochemical potential of the electrolyte.

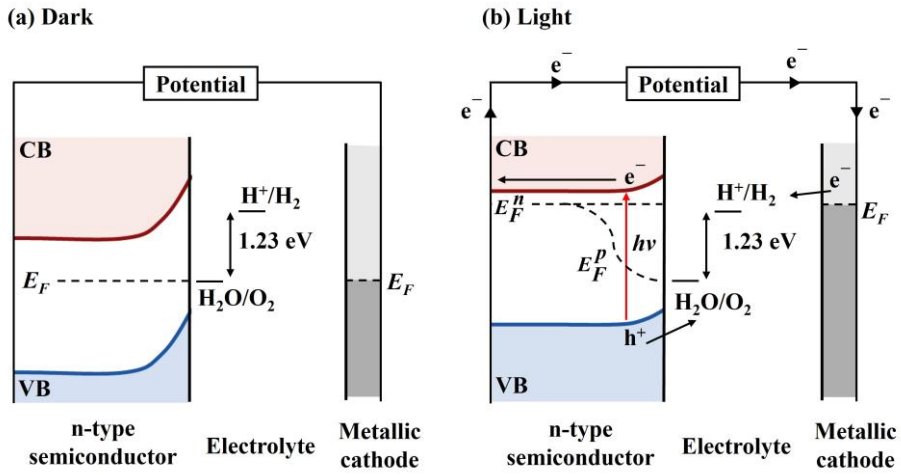

Figure 2.7. Schematic band diagram for n-type photoanodes in the (a) dark and under (b) illumination and applied potential.

Upon illumination (**Figure 2.7b**), photons with energy exceeding the bandgap generate electron-hole pairs in the semiconductor. As a result, the distribution of charge carriers can no longer be described by a single Fermi level. Instead, separate quasi-Fermi levels ($E_{F,Q}$) are introduced for electrons and holes, denoted as E_F^n and E_F^p, respectively. These quasi-Fermi levels describe the non-equilibrium carrier populations and are directly related to the local concentrations of electrons and holes in the semiconductor. In non-degenerate semiconductors, the **Eqs. 2.5** and **2.6** can be rewritten as:

$$n = n_0 + \Delta n = N_{CB} \exp\left(-\frac{E_{CB} - E_F^n}{k_B T}\right) \tag{2.8}$$

$$p = p_0 + \Delta p = N_{VB} \exp\left(-\frac{E_F^p - E_{VB}}{k_B T}\right) \tag{2.9}$$

Where n_0 and p_0 are the equilibrium electrons and holes concentration in dark, respectively, and Δn and Δp are the additional electrons and holes created by illumination, respectively.

In n-type semiconductors, the electron quasi-Fermi level typically remains nearly constant, since the total electron density does not change significantly under illumination, whereas the hole quasi-Fermi level exhibits a pronounced variation near the interface due to the presence of photogenerated minority carriers. This spatial variation of the quasi-Fermi levels reflects the establishment of a carrier gradient within the semiconductor, which drives the separation of photogenerated charges. As a result, photogenerated holes are driven towards the semiconductor surface, where they can participate in oxidation reactions, while electrons are transported through the semiconductor and collected via the external circuit towards the metallic counter electrode, where they can participate in reduction reactions. Under illumination, this charge separation and transport give rise to a photocurrent flowing through the external circuit. The sign of the photocurrent depends on the type of photoelectrode: it is positive for a photoanode, corresponding to electron flow towards the counter electrode, and negative for a photocathode, where electrons are supplied from the counter electrode.[7,42,64,65,85,86]

2.5.2. Applied potential

In addition to illumination, the application of an external potential further modifies the energy distribution within the system. The applied potential shifts the Fermi level of the semiconductor relative to the redox potential of the electrolyte, thereby altering the band bending at the interface. The extent of this effect depends on how the potential drop is distributed across the interface, which can be described in terms of the interfacial capacitances:

$$\frac{1}{C_T} = \frac{1}{C_H} + \frac{1}{C_{sc}} \tag{2.10}$$

Where C_T, C_H and C_{sc} correspond to the total, Helmholtz and semiconductor capacitances, respectively. When the semiconductor capacitance is smaller than the Helmholtz capacitance ($C_{sc} << C_H$), the

potential drops mainly across the semiconductor, leading to significant changes in band bending. In this case, the band edges at the surface remain effectively fixed with respect to the electrolyte, while the Fermi level shifts relative to them (band edge pinning). Under these conditions, in n-type semiconductors, a positive potential typically enhances band bending, promoting charge separation by driving holes towards the interface and electrons towards the bulk. This also reduces the concentration of electrons at the semiconductor surface, thereby limiting surface recombination and facilitating interfacial charge transfer. Conversely, a negative potential reduces band bending, increasing the electron concentration at the surface and promoting recombination of photogenerated carriers at the semiconductor/electrolyte interface. Analogous behaviour is observed in p-type semiconductors.

In contrast, when the Helmholtz capacitance is smaller ($C_H << C_{sc}$), the potential drops predominantly across the Helmholtz layer, and the band bending remains largely unchanged. In this regime, the applied potential does not significantly affect charge separation within the semiconductor. Instead, it shifts the electrochemical potential of the electrolyte relative to the semiconductor, resulting in a displacement of the band edges with respect to the redox levels (band edge unpinning). This modifies the overpotential for interfacial reactions, and consequently, the rate of charge transfer across the interface, which can either facilitate or hinder the transfer of photogenerated carriers.[7,65,72,75,87,88]

A similar shift of the energy levels can be induced by changes in the pH of the electrolyte. The positions of both the semiconductor band edges and the water redox potentials typically shift by approximately 59 mV per pH unit, as described by the Nernst equation. Since both the band edges and the water redox potentials shift by approximately the same value, their relative alignment remains nearly unchanged, when water is the only redox-active component in the system. Consequently, a variation in pH does not significantly modify the thermodynamic driving force for charge transfer for water oxidation or reduction, although it may still influence interfacial kinetics.[64]

2.5.3. Surface states

At the semiconductor/electrolyte interface, deviations from ideal behaviour can arise from several factors, among which surface states (SS) play a significant role. These states arise from structural defects, under-coordinated atoms, or chemical species absorbed at the semiconductor surface, introducing electronic levels within the bandgap.[64]

Surface states can significantly influence the interfacial behaviour by acting as charge trapping centres. Photogenerated electrons or holes can be captured by these states, which may subsequently recombine, introducing additional recombination dynamics that compete with charge transfer. In addition to recombination, surface states can also participate in interfacial charge transfer. Depending on their energetic position and occupancy, they can act as intermediate states between the semiconductor and the electrolyte, thereby influencing the mechanism and rate of charge transfer across the interface. Under illumination, their occupancy is determined by the quasi-Fermi levels, linking their activity to the local carrier populations at the interface.[89–94]

Surface states can also modify the interfacial energy alignment by altering the distribution of charge at the interface. Depending on their density and energetic distribution, they may alter the response of the interfacial potential to the applied potential. As a result, the distribution of the potential may deviate from that expected based on the semiconductor and Helmholtz capacitances, since the potential-dependent occupancy of surface states introduces an additional, pseudocapacitive contribution at the interface (C_{ss}).[86,95–97]

2.6. Kinetic model for charge transfer and recombination

The interfacial processes discussed in the previous sections can be described within a kinetic framework, described by Laurence M. Peter and co-workers, that accounts for the competition between interfacial charge transfer and surface recombination at the

semiconductor/electrolyte interface, as schematically represented in **Figure 2.8** for n-type photoanodes.[42,96,98–101]

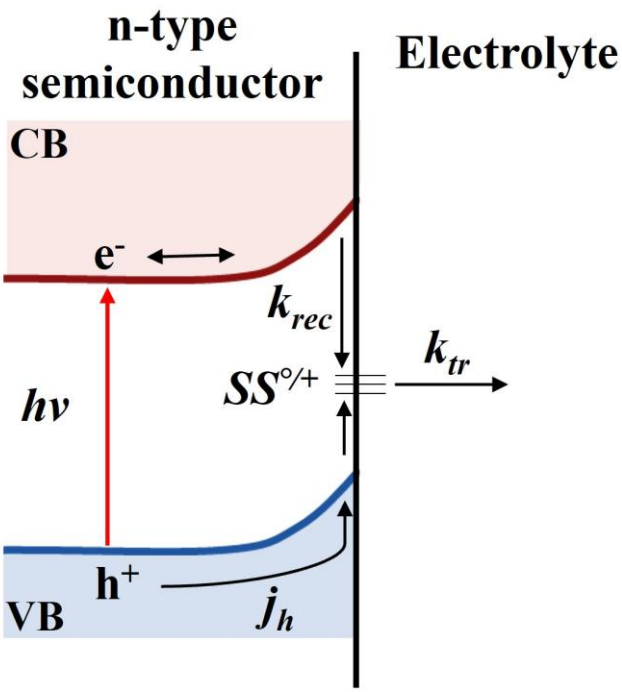

Figure 2.8. Schematic representation of the kinetic model for charge transfer and recombination at the semiconductor/electrolyte interface for an n-type photoanode. Upon light absorption, electron-hole pairs are generated, with electrons in the conduction band and holes in the valence band. Holes are driven to the surface, where they are captured by surface states and can either be transferred to the electrolyte or recombine with electrons.

Under illumination, photogenerated holes in the valence band are directed towards the semiconductor/electrolyte interface, giving rise to a hole current (j_h) at the surface. This current represents the flux of minority carriers available for interfacial processes and is determined by the generation and transport of carriers, which can be described thought the generation-collection Gärtner equation.[102] Although direct hole transfer from the valence band to the electrolyte is, in principle, possible, this pathway is generally less likely when surface states are present

within the bandgap. In such cases, photogenerated holes are first captured by surface states, which act as intermediate sites for interfacial charge transfer.

Within this model, the surface-trapped hole population, defined by $[SS^{+}]$, can follow two competing pathways: charge transfer from surface states to the electrolyte, described by the rate constant k_{tr}, and surface recombination with electron from the conduction band, described by the rate constant k_{rec}. Thus, the rate of interfacial charge transfer (j_{tr}) can be expressed as

$$j_{tr} = k_{tr} \left[SS^{+}\right] \tag{2.11}$$

Similarly, the surface recombination rate (j_{rec}) is expressed as

$$j_{rec} = k_{rec} \left[SS^{+}\right] \tag{2.12}$$

While k_{tr} is a first-order rate constant, k_{rec} is a pseudo-first-order constant that depends on the surface electron concentration (n_{surf}) as

$$k_{rec} = k'_{rec}\, n_{surf} \tag{2.13}$$

At this point, the surface electron concentration can be related to the bulk electron concentration (n_{bulk}) through the potential drop within the semiconductor. Under conditions where a well-defined variation of the internal potential exist, this relationship can be expressed as:

$$n_{surf} = n_{bulk} \exp\left(-\frac{e\,\Delta\phi_{bb}}{k_B T}\right) \tag{2.14}$$

Where e is the elementary charge. While n_{surf} can be approximated from the local potential using equilibrium-like relations, reflecting the quasi-equilibrium distribution of majority carrier in n-type semiconductors, $[SS^{+}]$ is not governed by such relations. Instead, it is determined by non-equilibrium conditions and by the balance between the flux of photogenerated holes reaching the surface and the competing interfacial transfer and recombination processes.

Therefore, k_{rec} can be interpreted as an effective pseudo-first-order recombination constant that depends not only on the intrinsic recombination kinetics of the surface states, but also on the surface electron concentration.

The relative magnitude of k_{tr} and k_{rec} governs the competition between interfacial charge transfer and recombination at the semiconductor/electrolyte interface. When k_{tr} dominates, photogenerated holes are efficiently transferred to the electrolyte, contributing to the photocurrent. In contrast, when k_{rec} becomes comparable to or larger than k_{tr}, surface recombination limits the fraction of carriers available for interfacial reactions.

Although this model is described here for n-type photoanodes, the same kinetic framework can be extended to p-type photocathodes by reversing the role of the charge carriers, with photoelectrons acting as the minority carriers participating in the interfacial charge transfer processes.

2.7. Heterojunctions and charge selective interfaces

When two semiconductors are brought into contact, a heterojunction is formed at their interface as a result of differences in their electronic structures, leading to band realignment and charge redistribution at equilibrium. Based on this alignment, heterojunctions are generally classified into three main types. In type I (straddling gap) heterojunctions, the band edges of one semiconductor are entirely enclosed within those of the other resulting in the accumulation of both electrons and holes in the same material. In type II (staggered gap) heterojunctions, the conduction and the valence bands are offset. In type III (broken gap) heterojunctions, the conduction band of one semiconductor lies below the valence band of the other, creating a discontinuity in the band structure.[103–106]

In this thesis, particular attention is given to type II heterojunctions, in which the offset between the conduction and valence bands of both

semiconductors promotes the spatial separation of photogenerated electrons and holes, as shown **Figure 2.9**.

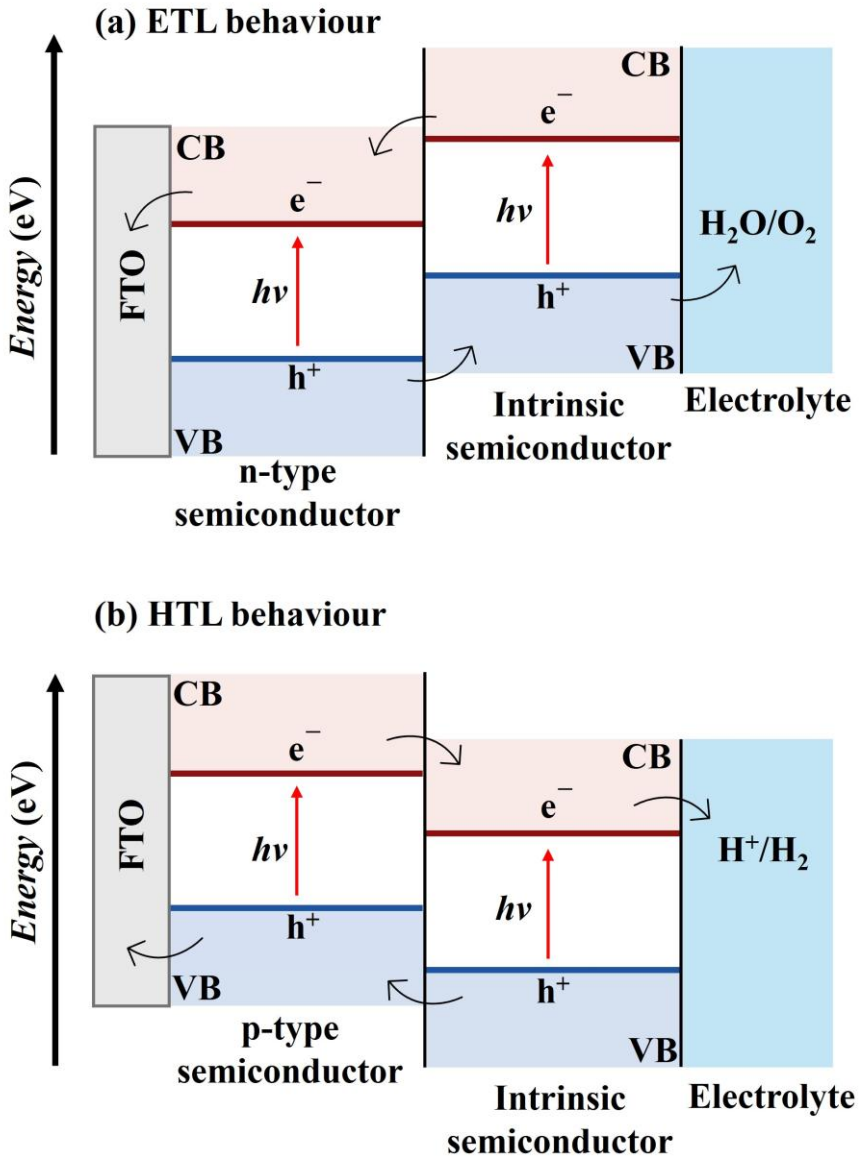

Figure 2.9. Schematic illustration of type II heterojunctions showing charge separation and selective charge transport: (a) electron transport layer (ETL) and (b) hole transport layer (HTL).

When both components of the heterojunction are photoactive, charge carriers are generated in each material, and their subsequent transfer across the interface is governed by the relative positions of their conduction and valence bands. In this context, charge selective interfaces enable preferential extraction of one type of carrier while limiting the transfer of the opposite one. This aspect is particularly relevant for intrinsically undoped materials, where no preferential direction for charge transfer is defined. In **Figure 2.9a**, the electron transport layer (ETL) collects photogenerated electrons from the adjacent component and transports them towards the external circuit, while photogenerated holes are transferred across the heterojunction and subsequently to the electrolyte, where they participate in oxidation reactions. In **Figure 2.9b**, the hole transport layer (HTL) performs the opposite function, collecting holes and transporting them to the external circuit, while electrons are transferred to the other component of the heterojunction and subsequently to the electrolyte, where they participate in reduction reactions. In this way, type II heterojunctions not only increase the charge separation efficiency, reducing recombination, but also enable directional and selective charge transport across the interface.[107–113]

The concepts presented in this chapter provide the theoretical framework for understanding the charge carrier dynamics and interfacial processes in semiconductor photoelectrochemical systems. In particular, the kinetic competition between charge transfer and recombination, together with the role of surface states and heterojunctions, constitutes the basis for the interpretation of experimental results discussed in the following chapters.

Chapter 3

Structural, morphological, and optical characterisation

Summary

This chapter introduces the techniques used for the structural, morphological, and optical characterisation of the investigated materials, focusing on their underlying principles and analytical capabilities. Particular emphasis is placed on how these approaches enable the assessment of crystallinity, morphology, and light-matter interaction, which are key to understanding the physicochemical behaviour of the materials. The concepts described in this chapter establish the basis for the interpretation of the experimental results discussed in **Chapters 6**, **7**, and **8**.

3.1. Scanning electron microscopy (SEM)

Scanning electron microscopy (SEM) is a widely used technique for the morphological characterisation of solid materials, based on the interaction between a focused electron beam and the surface of a sample. In a conventional SEM, the electron beam is generated by an electron source, accelerated under high vacuum, and focused into a fine probe by a system of electromagnetic lenses, including condenser and objective lenses. The beam is raster-scanned across the sample by means of deflection coils, enabling spatially resolved signal generation and image formation. A schematic representation of the main components of an SEM instrument is shown in **Figure 3.1**.[114–118]

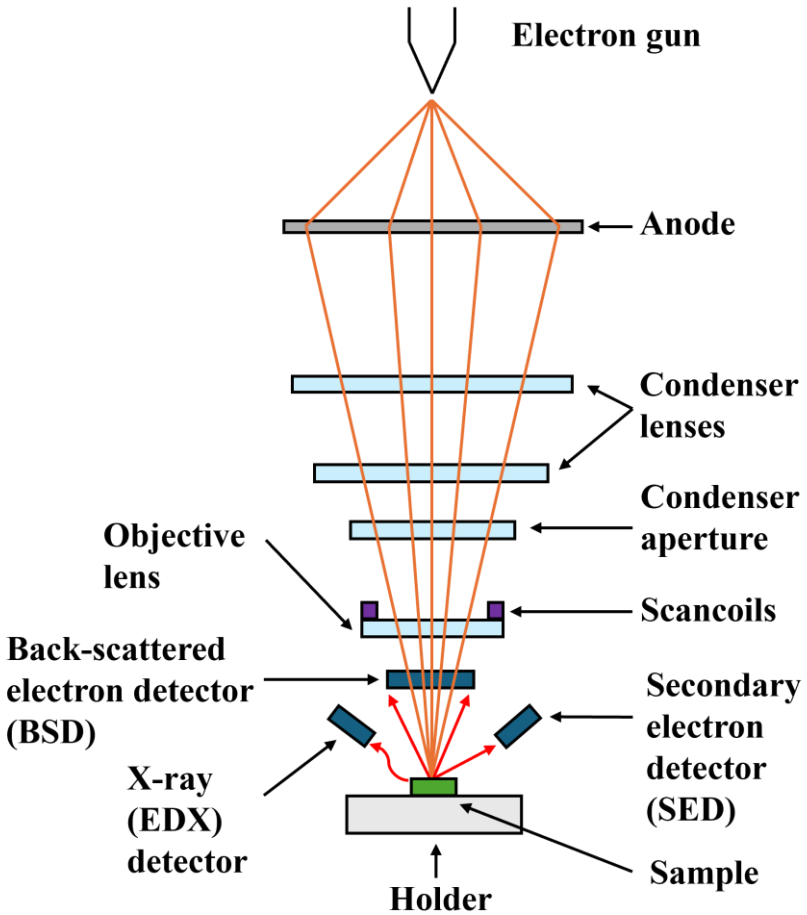

Figure 3.1. Schematic illustration of an SEM showing the main instrumental components and electron beam pathway.

Upon interaction of the incident electron beam with the material, a variety of signals are generated as a result of elastic and inelastic scattering processes. Among these, secondary electrons (SE) and backscattered electrons (BSE) are the most used for imaging. SE originate from inelastic interactions with weakly bound electrons and possess low kinetic energy, providing high-resolution information on surface topography. BSE result from elastic collisions with atomic nuclei and retain a large fraction of the incident electron energy; their yield is strongly dependent on the atomic number, enabling compositional contrast.[114–118]

In this thesis, a field-emission scanning electron microscope (FE-SEM) was used. FE-SEM employs a field emission electron source, which provides a highly coherent beam with a reduced energy spread and a smaller probe size. This results in improved spatial resolution, particularly at low accelerating voltages, and enhanced imaging performance for materials that are sensitive to electron beam damage or charging effects.[114–118]

For electrically insulating or poorly conductive materials, the accumulation of surface charge under electron irradiation can lead to image distortion, reduced resolution, and signal instability. To mitigate these effects, samples are often coated with a thin conductive layer before observation. This coating, typically consisting of a few nanometres of a noble metal such as gold, platinum, or palladium, facilitates charge dissipation and improves signal collection, thereby enhancing image quality and contrast. The use of such conductive coating is particularly relevant when operating at low accelerating voltages or when analysing beam-sensitive materials.[114–118] This approach was selectively applied to the PCN-222 samples studied in **Chapter 6**, which exhibit lower electrical conductivity than metal oxides, to ensure stable imaging conditions and improved surface definition.

In this thesis, SEM analysis was performed using both top-view and cross-sectional configurations, enabling a comprehensive assessment of the sample morphology. Top-view imaging was employed to evaluate particle size, shape, and surface distribution, as well as the overall

morphology of the deposited layers. In addition, cross-sectional observations provided direct information on layer thickness and structural organisation across the film depth, allowing a complete characterisation of the material architecture.

3.2. Energy dispersive X-ray spectroscopy (EDX)

Energy dispersive X-ray spectroscopy (EDX) is an analytical technique commonly coupled to SEM that enables elemental identification and spatially resolved compositional analysis. In addition to the electron signals described in the previous section, the interaction of the incident electron beam with the sample can also induce inner-shell ionisation of atoms. The subsequent relaxation of electrons from higher energy levels results in the emission of characteristic X-ray photons, whose energies are specific to each element, allowing their identification. The intensity of these signals provides qualitative and semi-quantitative information on the elemental composition of the material.[114–118]

The emitted X-rays are detected using semiconductor-based detectors, which convert photon energy into electrical signals, producing spectra composed of a characteristic peak superimposed on a continuous background. Besides point analysis, EDX can be employed to generate elemental maps by collecting spectra over a defined area of the sample, enabling visualization of the spatial distribution of elements across the surface.[114–118] However, the spatial resolution of the technique is limited by the electron-matter interaction volume, and its quantitative accuracy may be affected by factors such as matrix effects, absorption phenomena, and peak overlap.

3.3. X-ray diffraction (XRD)

X-ray diffraction (XRD) is a standard non-destructive technique used for the structural characterisation of crystalline materials, providing information on crystal structure, phase composition, and lattice

parameters. The technique is based on the diffraction of X-rays by periodically arranged atomic planes within a crystal. When an incident X-ray beam interacts with a crystalline material, elastic scattering occurs, and constructive interference arises only for specific directions that satisfy the geometric conditions imposed by the crystal structure.[119,120] A schematic representation of the XRD process is shown in **Figure 3.2**.

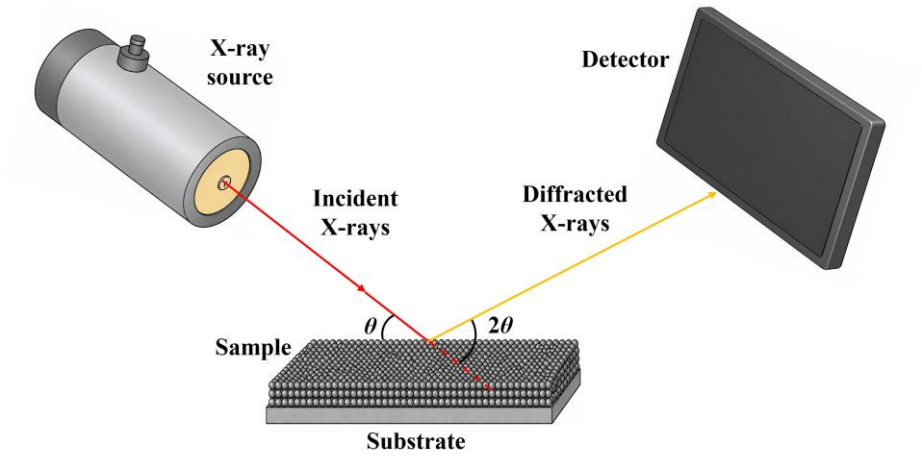

Figure 3.2. Schematic representation of the XRD measurements, illustrating the interaction of incident radiation with a crystalline surface and the detection of the diffracted beam.

The condition for constructive interference is described by Bragg's law:

$$m\lambda = 2d\sin\theta \tag{3.1}$$

Where m is the order of reflection, λ is the wavelength of the incident radiation, d is the interplanar spacing, and θ is the Bragg angle between the incident beam and the crystallographic planes. When this condition is fulfilled, the scattered waves interfere constructively, producing diffraction peaks that are characteristic of the crystal structure.

In addition, XRD can be used to estimate the average crystallite size (D) through peak broadening analysis, typically using the Scherrer equation:

$$D = \frac{K\lambda}{\beta\cos\theta} \tag{3.2}$$

Where K is the Scherrer constant, and β is the full width at half maximum (FWHM) of the diffraction peak. This approach provides an estimation of the coherent diffraction domain size, which is particularly useful for nanostructured materials.

In a typical XRD experiment, the intensity of the diffracted X-rays is recorded as a function of the scattering angle (2θ), generating a diffraction pattern in which each peak corresponds to a specific set of crystallographic planes. The position and intensity of these peaks provide information on phase identification, crystallinity, and preferred orientation. Comparison with the reference database allows the identification of crystalline phases and the assessment of structural properties of the material.[119–121]

In addition, grazing angle X-ray diffraction (GAXRD) was employed for the analysis of thin films and powders (PXRD). In this configuration, the incident X-ray beam is directed onto the sample at a very low angle, typically below a few degrees, thereby reducing the penetration depth and enhancing the contribution from the near-surface region.

3.4. X-ray photoelectron spectroscopy (XPS)

X-ray photoelectron spectroscopy (XPS) is a surface-sensitive analytical technique widely employed to investigate the elemental composition, chemical states, and electronic structure of materials. The method relies on the photoelectric effect, whereby irradiation with monochromatic X-rays induces the emission of core-level electrons from atoms within the material.[122–124]

The kinetic energy of the emitted photoelectrons is measured using an electron energy analyser, allowing the determination of their binding energy (BE) according to:

$$BE = h\nu - (E_{kin} + \Phi) \tag{3.3}$$

Where E_{kin} is the measured kinetic energy, and Φ is the work function of the spectrometer. Since the BE is characteristic of each element and

sensitive to its chemical state, XPS enables both elemental identification and analysis of oxidation states and chemical bonding.

XPS spectra are typically represented as the intensity of detected electrons as a function of binding energy, where distinct peaks correspond to specific electronic levels of the element present. Variation in peak position and shape provides information on the local chemical state, including oxidation states and coordination. Due to the limited inelastic mean free path of electrons in solids, typically on the order of a few nanometres, XPS is inherently surface-sensitive, probing only the near-surface region of the material.[122–124]

In addition, depth profiling can be achieved by sequential removal of surface layers, commonly through ion sputtering, allowing the investigation of compositional variations along the sample depth. This approach is particularly useful for the analysis of thin films and layered structures.

3.5. Dynamic light scattering (DLS)

Dynamic light scattering (DLS) is a technique for determining particle size distributions in colloidal suspensions and nanoparticle dispersions, based on the analysis of temporal fluctuation in the intensity of light scattered by particles undergoing Brownian motion in a liquid medium. When a coherent light source, typically a laser, illuminates the dispersion, the suspended particles scatter light, and their continuous random motion leads to time-dependent variations in the scattered intensity. These fluctuations are analysed through an autocorrelation function, from which the translational diffusion coefficient of the particles can be obtained.[125,126]

The particle size is expressed in terms of the hydrodynamic diameter (D_h) defined as the diameter of a hypothetical hard sphere that diffuses at the same rate as the particle under investigation. This parameter reflects the effective size of the diffusing entity in the liquid, including contributions from solvation layers and surface-bound species, and may therefore differ from dimensions obtained by microscopy-based

techniques. The D_h is calculated from the diffusion coefficient using the Stokes-Einstein equation, expressed in terms of the particle diameter:

$$D_h = \frac{k_B T}{3\pi\eta D_t} \tag{3.4}$$

Where η is the viscosity of the medium, and D is the translational diffusion coefficient. In a system where aggregation occurs, the measured size corresponds to the hydrodynamic diameter of the aggregates, and even a small fraction of larger particles can significantly influence the result due to the strong dependence of scattering intensity on the particle size.[125–127]

In addition to particle size, the polydispersity index (*PDI*) is obtained from cumulant analysis of the autocorrelation function and measures the width of the size distribution. Low *PDI* values indicate narrow size distributions, whereas higher values are associated with broader distributions or the presence of aggregates.[127]

The zeta potential (ζ) is determined from electrophoretic mobility measurements, typically obtained by laser Doppler anemometry (LDA), providing information on the surface charge of the particles and allowing the assessment of colloidal stability.[128]

3.6. UV-Visible spectroscopy (UV-Vis)

Ultraviolet-visible (UV-Vis) spectroscopy provides information on the optical absorption properties of materials as a function of wavelength, arising from electronic transitions within the material.

For colloidal dispersion, optical properties were evaluated through transmission measurements. The transmittance, $T(\lambda)$, is defined as the ratio between transmitted, $I(\lambda)$, and incident light intensity, $I_0(\lambda)$, as

$$T(\lambda) = \frac{I(\lambda)}{I_0(\lambda)} \tag{3.5}$$

The absorbance is then obtained from the transmittance according to:

$$Abs(\lambda) = -\log_{10}(T(\lambda)) \tag{3.6}$$

The optical processes involved upon UV-Vis irradiation of a solid sample are schematically illustrated in **Figure 3.3**. The measured response arises from the relative contributions of transmission, reflection, and scattering.[129,130]

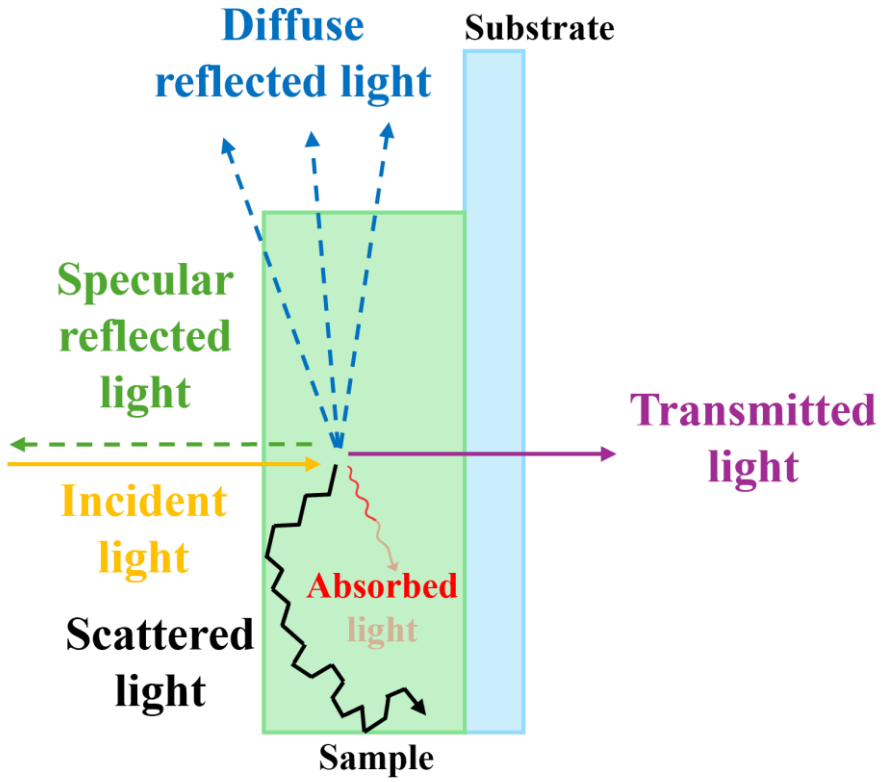

Figure 3.3. Schematic representation of the different optical processes occurring upon irradiation of a solid sample.

For films deposited on a substrate, optical characterisation was performed using diffuse reflectance spectroscopy (DRS). In this configuration, an integration sphere is employed to collect both specular and diffuse components of the reflected light, providing a measurement of the total reflectance. The total reflectance $R_T(\lambda)$ is calculated as:

$$\boldsymbol{R}_T(\lambda) = \frac{R_{sample}(\lambda)}{R_{reference}(\lambda)} 100 \tag{3.7}$$

where the reference corresponds to the bare substrate. In this configuration, as shown in **Figure 3.4**, the sample is placed on a diffusively reflective holder, made of the same material as the integration sphere, which redirects transmitted light back towards the sample. As a result, light that is not collected as reflected is assumed to be absorbed, allowing the absorptance, $A(\lambda)$, to be estimated as

$$A(\lambda) = 100 - R_T(\lambda) \tag{3.8}$$

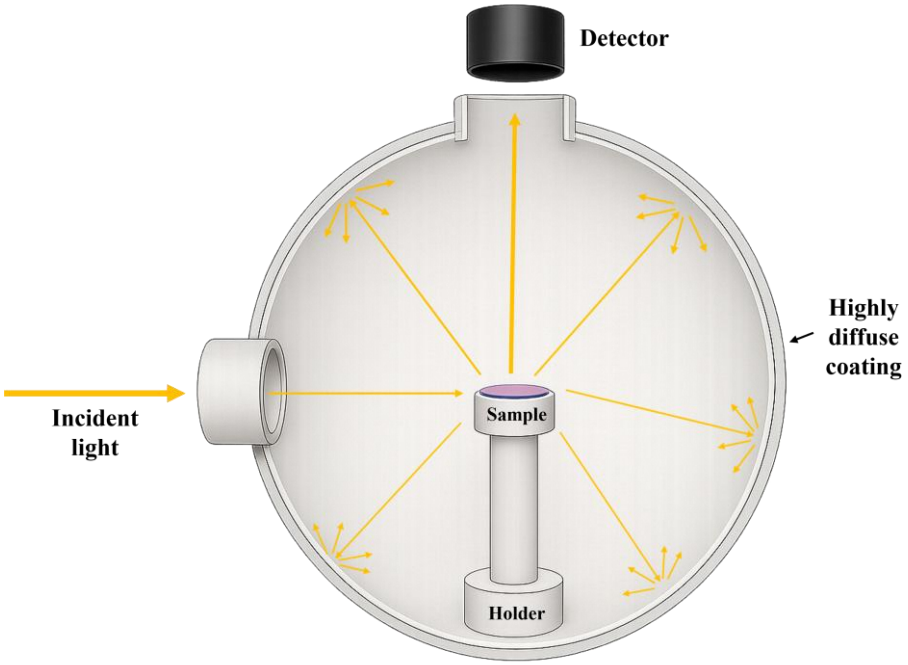

Figure 3.4. Integration sphere configuration for DRS measurements, with the sample mounted on a high-reflectance diffuse holder.

Under these conditions, the absorptance approximates the light-harvesting efficiency (*LHE*), representing the fraction of incident photons absorbed at each wavelength.[130]

The optical bandgap of the materials can be estimated from UV-Vis measurements using the Tauc method, which relates the absorption coefficient to the photon energy. For materials analysed in transmission, the absorption coefficient (α) can be used to construct a Tauc plot according to

$$(\alpha h\nu)^{\gamma} = B(h\nu - E_g) \tag{3.9}$$

where B is the proportionality constant, and γ depends on the nature of the electronic transition, $\gamma = ½$ for indirect transitions, and $\gamma = 2$ for direct transitions. The bandgap is determined by extrapolating the linear region of the plot to $(\alpha h\nu)^{\gamma} = 0$.[64,69,70,131]

For films analysed by DRS, the absorption coefficient is not directly accessible. In this case, the Kubelka-Munk function, $F(R)$ is used as an approximation:

$$F(R_\infty) = \frac{(1 - \frac{R_T(\lambda)}{100})^2}{2\frac{R_T(\lambda)}{100}} \tag{3.10}$$

Where $F(R_\infty)$ is proportional to the absorption coefficient under the assumption of an optically thick and diffusively scattering sample. Therefore, Tauc plots can be constructed by replacing α with $F(R_\infty)$, allowing the estimation of the optical bandgap from reflectance data.[132]

In this thesis, transmission measurements were employed to determine the absorbance of particle dispersions, while DRS measurements were used to evaluate the optical properties of films.

3.7. Fourier transform infrared spectroscopy (FTIR)

Fourier transform infrared (FTIR) spectroscopy is a vibrational spectroscopic technique used to identify chemical bonds and functional groups in materials through their interaction with infrared radiation. The technique is based on the absorption of infrared light by molecular vibrations, which occur when the frequency of the incident radiation matches the natural vibrational frequencies of chemical bonds.

In an FTIR experiment, a broadband infrared source is directed through an interferometer, which modulates the radiation as a function of the optical path difference. The resulting interferogram is recorded as a function of time and subsequently converted into a conventional

spectrum of intensity versus wavenumber by applying a Fourier transform. This approach enables the simultaneous acquisition of all wavelengths.

The obtained FTIR spectrum represents the absorbance (or transmittance) as a function of wavenumber, where characteristic absorption bands correspond to specific vibrational modes of the chemical bonds present in the material. These bands provide qualitative information on molecular structure, functional groups, and chemical compositions.[133,134]

In this thesis, FTIR spectroscopy was employed to analyse functional groups attached to the surface of the photocatalytic material.

The physicochemical properties of semiconductor materials strongly influence their behaviour under photoelectrochemical operating conditions. In this context, the characterisation methods presented in this chapter provide insight into the structure, morphology, composition, surface chemistry, and optical response of investigated systems. The information obtained through these approaches constitutes a fundamental basis for understanding the experimental results discussed in the following chapters.

Chapter 4

(Photo)electrochemical characterisation

Summary

This chapter describes the (photo)electrochemical characterisation techniques employed throughout this thesis. It provides an overview of the methodologies used to evaluate the charge carrier dynamics. In addition, the fundamental principles of small-perturbation (opto)electronic techniques are introduced, enabling a deeper understanding of the processes governing the photoelectrochemical performance. The concepts presented in this chapter support the interpretation of the experimental result discussed in **Chapters 6**, **7**, and **8**.

4.1. Current density-potential (*J-E*) curves

Current density-potential (*J-E*) curves constitute one of the most widely used tools for the photoelectrochemical characterisation, as they provide general insight into the electrode performance. These curves are typically obtained through linear sweep voltammetry (LSV) or cyclic voltammetry (CV) by recording the current response as a function of applied potential under controlled illumination conditions, normalised by the active area.

J-E curves enable the extraction of key parameters that describe the (photo)electrochemical behaviour of the system. In particular, they provide information on the photocurrent density and energy conversion efficiency as functions of the applied potential, as well as the corresponding dark current response. The analysis of these curves also allows the determination of the photocurrent onset and plateau and identification of their sign, distinguishing between anodic and cathodic behaviour, as illustrated in **Figure 4.1**.[64] Experimentally, *J-E* curves were obtained by sweeping the applied potential at a constant rate of 20 mV s^{-1} in this thesis, either in the dark, under continuous illumination, or by switching the light on and off at a fixed frequency during the measurement.

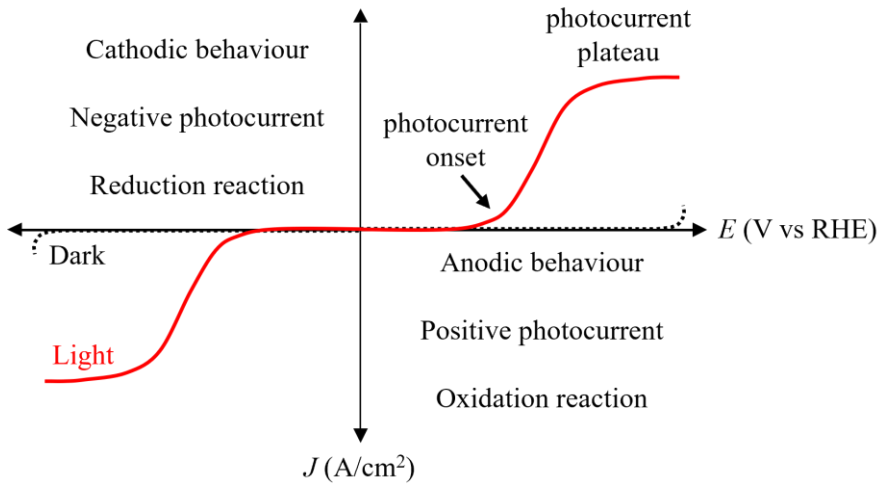

Figure 4.1. Schematic steady-state *J-E* curve for cathodic (left) and anodic (right) behaviour under dark (black dashes) and illumination (red line) conditions.

In addition, characteristic features in the curves can be associated with the redox processes at the electrode/electrolyte interface. Furthermore, *J-E* measurements can give insight into charge transport limitation within the system, for instance by comparing front- and back-side illumination conditions.[64,135]

When measurements are performed under chopped illumination, transient features such as current spikes or delayed responses upon light on/off switching may be observed, as is schematised in **Figure 4.2**, where representative transient photocurrent behaviours are illustrated. This transient response can be monitored either during potential sweeps (*J-E*) or under fixed potential conditions via chronoamperometry, where the photocurrent is recorded as a function of time (*J-t*), providing a direct assessment of steady-state behaviour and enabling the evaluation of the temporal stability of the photoelectrode under operational conditions.

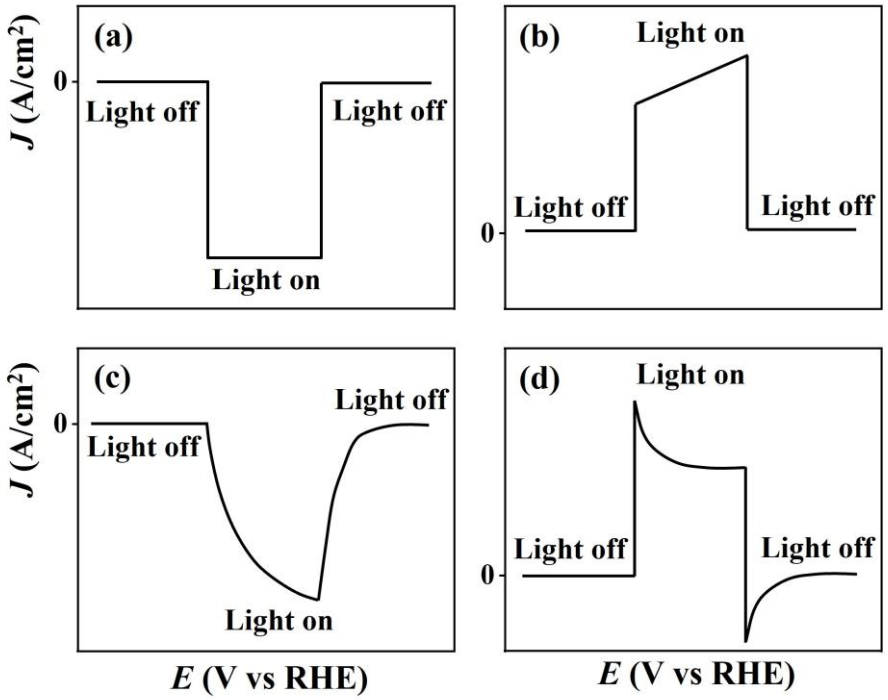

Figure 4.2. Schematic representation of the origin of transient photocurrent response under chopped illumination, including (a) electron (for photocathode) photocurrent without surface recombination, (b) hole (for photoanode) photocurrent increasing the applied potential,

(c) surface electron-hole recombination due to accumulation of hole (for photoanode) at the surface, inducing band edge unpinning, (d) surface trapped electron (for photocathode). This schematic is valid for both photoanode and photocathode behaviours with opposite photocurrent signals (positive photocurrent for photoanode and negative photocurrent for photocathode). The different profiles illustrate typical responses associated with charge separation, accumulation, recombination, and trapping processes at the electrode surface.

Upon illumination, the photocurrent often exhibits an initial spike followed by a decay towards a quasi-steady value. This transient response is commonly attributed to the rapid generation of charge carriers and their temporal accumulation at the electrode surface or within trap states, before slower processes such as charge transfer and recombination reach the equilibrium. The magnitude of the spike and the rate of decay can therefore provide information about charge separation efficiency and recombination kinetics. When the light is switched off, the decays back to the dark value. The shape and timescale of this decay are indicative of the lifetime of accumulated charges and the extent of recombination processes. A rapid decay suggests fast recombination or efficient charge extraction, whereas a slower decay may indicate charge trapping or delayed recombination processes.[96,99,101,136–140] Therefore, the analysis of these transient features allows a qualitative assessment of charge carrier dynamics, as is discussed in more detail in **Chapter 6**.

The measured current can arise from different contributions or processes that may occur simultaneously within the system. In photoelectrochemical systems, the dominant contribution typically originates from light-induced processes in the photoactive material. Upon illumination, photon absorption generates electron-hole pairs, whose separation and transport, in competition with recombination processes, determine the flux of charge carriers reaching the semiconductor/electrolyte interface. Once these photogenerated carriers reach the interface and are transferred, they can participate in oxidation or reduction reactions, leading to a Faradaic contribution to the current.[141]

In addition to these contributions, the measured current may also include non-Faradaic components. In particular, the charging and discharging of the electrical double layer give rise to a capacitive current, which is particularly relevant in potential regions where no interfacial reactions occur. Furthermore, surface-related phenomena such as charge accumulation, trap states, or adsorption processes can also contribute to the overall current response, modifying the shape of the *J-E* curve and, in some cases, complicating their interpretation.[141]

All potentials (*E*) are reported with respect to the reversible hydrogen electrode (RHE) scale and were converted from the Ag/AgCl (3 M KCl) reference electrode according to:

$$E_{RHE} = E_{Ag/AgCl} + 0.059\ \text{pH} + E^{\circ}_{Ag/AgCl} \tag{4.1}$$

where $E^{o}_{\text{Ag/AgCl}}$ is the standard potential of the reference electrode. *J-E* and *J-t* curves are analysed and discussed in more detail in **Chapters 6, 7,** and **8**.

4.2. External quantum efficiency (*EQE*)

In photoelectrochemical systems, the energy conversion efficiency can be evaluated by correlating the generated photocurrent with the incident photon flux. In this context, the external quantum efficiency (*EQE*), also referred to as incident photon-to-current conversion efficiency (*IPCE*), quantifies the fraction of incident photons that contribute to the measured photocurrent at a given monochromatic wavelength, and is expressed as:

$$EQE = \frac{J}{P_{light}} \frac{h\,c}{e\,\lambda} 100 = \frac{\dfrac{J_{photoelectrode}}{A_{photoelectrode}}}{\dfrac{J_{photodiode}}{SR_{photodiode}\,A_{photodiode}}} \frac{h\,c}{e\,\lambda} 100 \tag{4.2}$$

Where *J* corresponds to the photocurrent (A) measured for both the photoelectrode and the photodiode under the same conditions, P_{light} is the light power intensity (W m^{-2}), *A* is the active area (m^2) of the photoelectrode and photodiode, *SR* is the spectral response (A W^{-1}) of the photodiode, *h* is Planck's constant (J s), *c* is the speed of light (m s^{-1}),

e is the elementary charge (C) and λ is the wavelength (m) of the incident light used for the measurement.

Since *EQE* is based on the total number of incident photons, it reflects the overall efficiency of the system, including optical losses such as reflection or transmission. When only the absorbed photons are considered, the internal quantum efficiency (*IQE*), also referred to as absorbed photon-to-current conversion efficiency (*APCE*), can be defined as

$$IQE = \frac{EQE}{LHE} \tag{4.3}$$

The *IQE* provides an intrinsic measure of the efficiency of the charge carrier dynamics, excluding optical effects.

4.3. Small-signal perturbation techniques

Small-signal perturbation techniques are essential for a better understanding of the processes and mechanisms that limit the photoelectrode performance. In these methods, either the applied potential or the incident light intensity is sinusoidally modulated over a wide frequency range, the system response is measured, and a transfer function is defined. For the analysis to be valid, several conditions must be fulfilled: (i) the photoelectrode must remain stable during the measurement and operate under steady-state conditions (stability); (ii) the measured response must be a direct consequence of the applied perturbation (causality); and (iii) the response must be linearly related to the perturbation amplitude (linearity).[26] The small-perturbation techniques used in this thesis are electrochemical impedance spectroscopy (EIS), where the transfer function is given by the ratio between the modulated potential and the resulting current, and intensity-modulated photocurrent spectroscopy (IMPS), where, at a constant applied potential, the modulated photocurrent is normalised to the modulated light intensity. These techniques are closely related, and their combined use can provide a consistent description of the system, as shown in **Chapter 8**.[142,143]

The validity of this small-signal approach can be experimentally assessed through time-domain representations of the system response. The sinusoidal response of the system, either in terms of voltage or photocurrent, is characterised by its amplitude and phase shift with respect to the applied perturbation, as shown in **Figure 4.3**. The relationship between the frequency-dependent response and the perturbation signal can be described through a transfer function, which provides insight into the dynamic response of the system under small perturbations.

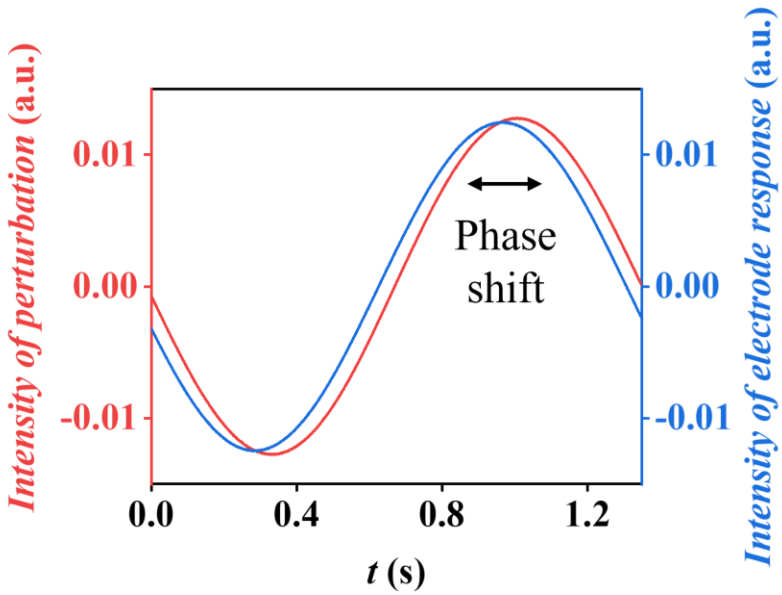

Figure 4.3. Sinusoidal output (blue line) of a linear system in response to a sinusoidal input (red line) in the time domain.

The spectrum is measured over a broad frequency range, typically from 10^5 Hz to 10^{-2} Hz. This range is selected to probe different timescales associated with electronic and kinetic processes occurring in the electrode. In practice, the frequency window is also limited by instrumental constraints, such as the potentiostat response and the measurement setup. The amplitude of the perturbation must be carefully controlled: it should be sufficiently small to ensure a linear response of the system, while remaining large enough to produce a measurable signal above the noise level. In this thesis, perturbation amplitudes on the order

of 10% of the bias light intensity for IMPS and 10 mV for EIS were employed.[64,144–146]

To verify that the systems operate within the linear regime, the relationship between the applied AC perturbation and the resulting electrode response can be visualised in the time domain. In this context, the Lissajous plot provides a convenient representation: when the response is linear, the resulting figure appears as a symmetric ellipse or straight line, reflecting the proportionality between input and output signals, as is shown in **Figure 4.4**.

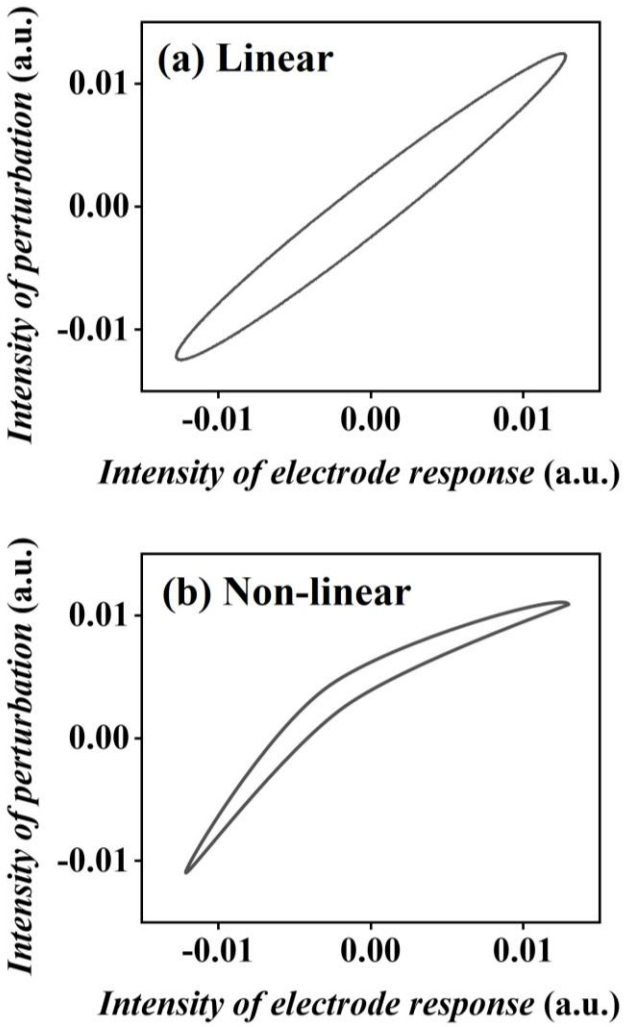

Figure 4.4. Lissajous plot showing the linear AC (a) linear and (b) non-linear response of the electrode

In addition, to ensure that the photoelectrode remains stable throughout the measurement, a *J-E* curve is recorded at the beginning and at the end of each experiment to verify that no significant changes occur in the electrode performance during the measurement. Furthermore, a chronoamperometric measurement is performed for 15 min prior to each EIS or IMPS data point to confirm the stability of the photocurrent and the absence of transient effects, ensuring that the electrode is in a steady state before perturbation is applied.

The frequency-dependent response of the electrode can be represented in different forms to extract complementary information. The Nyquist plot (**Figure 4.5a**) shows the imaginary versus the real component of the response, the Cole-Cole plot (**Figure 4.5b**) displays the imaginary component as a function of frequency, and the Bode plot (**Figure 4.5c**) presents the magnitude and phase of the response as a function of frequency. These representations together allow a clear overview of the system's dynamic behaviour.

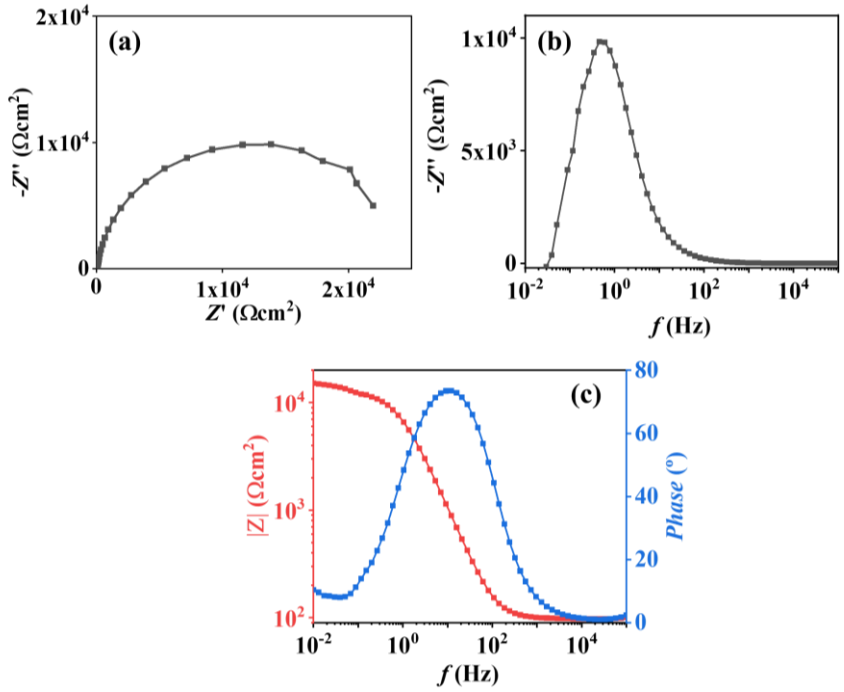

Figure 4.5. Different representations of the frequency-dependent response: (a) Nyquist, (b) Cole-Cole, and (c) Bode plots extracted from EIS measurement.

4.3.1. Electrochemical impedance spectroscopy (EIS)

In EIS technique, a small-amplitude sinusoidal AC voltage perturbation is superimposed on a DC bias, and the resulting current response is measured as a function of angular frequency (ω) [144,145,147–150] as

$$\omega = 2\pi f \tag{4.4}$$

By analysing the relationship between the applied voltage (V) and the measured current (I), the impedance (Z) (i.e., the resistance, R) of the system is obtained as their ratio, in analogy with Ohm's law, as

$$R = \frac{V}{I} \tag{4.5}$$

The applied voltage perturbation can be expressed as

$$V(t) = V_0 \cos(\omega t) \tag{4.6}$$

Where the V_0 is the amplitude of the voltage perturbation. The resulting current response also varies sinusoidally, but with a phase shift related to the applied voltage perturbation as

$$I(t) = I_0 \cos(\omega t - \varphi) \tag{4.7}$$

Where I_0 is the amplitude of the current response, and φ is the phase shift between voltage and current. Thus, the impedance is defined as the complex ratio of the modulated voltage, $\tilde{V}$, to modulated current, $\tilde{I}$, in the frequency domain, extending Ohm's law to describe the electrochemical systems as a frequency-dependent transfer function

$$Z(\omega) = \frac{\tilde{V}(\omega)}{\tilde{I}(\omega)} = \frac{V_0 \cos(\omega t)}{I_0 \cos(\omega t - \varphi)} \tag{4.8}$$

$Z(\omega)$ can be represented as a complex number

$$Z(\omega) = Z'(\omega) + iZ''(\omega) \tag{4.9}$$

Where Z' and Z'' represent the real and the imaginary component of the impedance, and i is the imaginary unit ($i = \sqrt{1}$) .

Equivalent circuit modelling is a common approach to interpret EIS data, providing a simplified representation of complex dynamic processes. In this context, the frequency-dependent response is reproduced using a network of resistors, capacitors, and non-ideal capacitive elements, each representing specific physical processes such as charge transport, recombination, or interfacial charge storage.

The simplest Randles-type equivalent circuit, shown in **Figure 4.6a**, consists of a series resistance (R_s) combined in series with a parallel *RC* element, whose total impedance can be expressed as

$$Z(\omega) = R_s + \frac{1}{i\omega C + \frac{1}{R}} \tag{4.10}$$

This expression gives rise to a complete loop in the Nyquist plot, with its intercept on the real axis defined by R_s, the diameter corresponding to *R,* and a characteristic frequency defined by the *RC* time constant.

When a second loop appears in the Nyquist plot, an additional *RC* element must be included, as shown in **Figure 4.6b**, thus **Eq. 4.10** can be rewritten as

$$Z(\omega) = R_s + \frac{1}{i\omega C_1 + \frac{1}{R_1 + \frac{1}{i\omega C_2 + \frac{1}{R_2}}}} \tag{4.11}$$

In real (photo)electrochemical systems, ideal capacitive behaviour is rarely observed, as deviations from ideality arise from factors such as surface roughness, interfacial heterogeneity, and distributed reaction pathways at the semiconductor/electrolyte interface. Consequently, ideal capacitors often fail to accurately describe experimental impedance response, and are therefore replaced by constant phase elements (*CPEs*).[145,151–153] In this case, the impedance of an ideal capacitor, is substituted by that of a *CPE*

$$Z_{CPE} = \frac{1}{Q(i\omega)^{n_{CPE}}} \tag{4.12}$$

Where Q is a pseudo-capacitance ($s^{nCPE}\ \Omega^{-1}$) and n_{CPE} (with $0 < n_{CPE} \leq 1$) is the exponent indicating the deviation from ideal capacitive behaviour. When $n_{CPE} = 1$, the *CPE* corresponds to an ideal capacitor, while decreasing values of n_{CPE} correspond to progressively greater deviation from ideal capacitive behaviour. Exponents below approximately 0.90 indicate a pronounced non-ideal response.

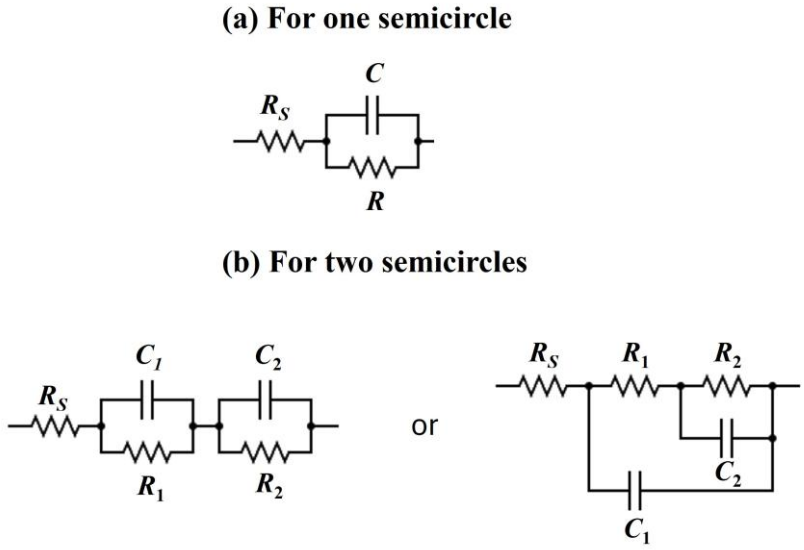

Figure 4.6. (a) Randles-type equivalent circuit used when only one semicircle is observed, and (b) simplified equivalent circuit applied when two semicircles are visible.

When *CPE* is connected in parallel with a *R*, an effective capacitance (C_{eff}) can be introduced to a better physical interpretation and to enable direct comparison with the behaviour of an ideal *RC* circuit. The C_{eff} is typically expressed as

$$C_{eff} = (QR^{1-n_{CPE}})^{\frac{1}{n_{CPE}}} \tag{4.13}$$

The experimental EIS spectra in this thesis were analysed and fitted using Zview4. The EIS analysis and the corresponding equivalent circuits used in this thesis are discussed in more detail in **Chapter 8**.

4.3.2. Intensity-modulated photocurrent spectroscopy (IMPS)

This section focuses on the use of IMPS to characterise n-type metal oxide photoelectrodes, following the kinetic approach of Laurence M. Peter and co-workers, as discussed in **Section 2.6** of this thesis.[42,96,98–101,136,147,154,155] In this technique, a small sinusoidal modulation is superimposed onto a constant light intensity, and the resulting modulated photocurrent is quantified as a function of frequency (**Eq. 4.4**).

IMPS results are typically interpreted through the transfer function, $H(\omega)$, which is defined as the ratio of modulated photocurrent, $\tilde{j}_{ph}$, to the modulated light intensity, $\tilde{I}_{ligh}$, in the frequency domain

$$H(\omega) = \frac{\tilde{j}_{ph}(\omega)}{\tilde{I}_{ligh}(\omega)} = \frac{j_{ph}\sin(\omega t+\varphi)}{j_0\sin(\omega t)} \tag{4.14}$$

When an LED with a specific wavelength is used, the amplitude of the modulated light intensity, j_0, can be described in terms of photon flux (cm^{-2} s^{-1}), while the amplitude of the modulated photocurrent, j_{ph}, is converted to electron flux (cm^{-2} s^{-1}). As a result, $H(\omega)$ represents the complex, small-signal, frequency-dependent *EQE*, and quantitative values can be obtained through normalisation against a calibrated photodiode, as is shown in **Eq. 4.2**.

$H(\omega)$ can be represented as a complex number

$$H(\omega) = \mathrm{Re}(H) + i\mathrm{Im}(H) \tag{4.15}$$

Where Re(H) and Im(H) represent the real and imaginary components of the transfer function, respectively. The AC component of the $H(\omega)$ is

$$H(\omega) = \frac{j_{ph}}{j_0}\,\frac{k_{tr}+i\omega}{k_{tr}+k_{rec}+i\omega}\,\frac{\frac{C_T}{C_{sc}}}{1+i\omega RC_T} \tag{4.16}$$

where

$$C_T = \frac{C_{sc}C_H}{C_{sc}+C_H} \tag{4.17}$$

In the limiting case that $C_{sc} << C_H$, **Eq. (4.16)** can be rewritten as

$$H(\omega) = \frac{j_{ph}}{j_0} \frac{k_{tr}+i\omega}{k_{tr}+k_{rec}+i\omega} \frac{1}{1+i\omega RC_T} \tag{4.18}$$

Figure 4.7 illustrates the different loop shapes observed in IMPS measurements for an n-type semiconductor, which can be described based on **Eqs. 4.16** and **4.18**.

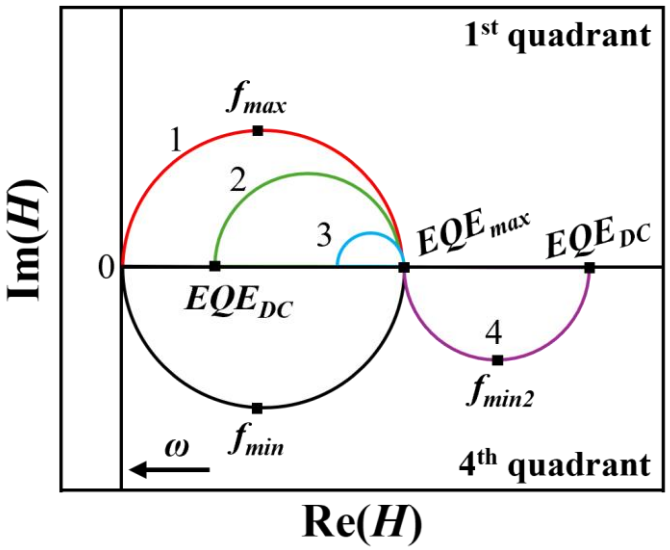

Figure 4.7. Schematic IMPS spectra under different kinetic regimes for n-type semiconductors. (1) $k_{rec} >> k_{tr}$, (2) $k_{rec} = k_{tr}$, (3) for $k_{rec} < k_{tr}$, all under the condition $C_{sc} << C_H$ and $(RC)^{-1} << k_{tr} + k_{rec}$, and (4) $k_{rec} << k_{tr}$ with C_{sc} and C_H of similar magnitude. The presence of a small curl is indicative of surface states. The arrow indicates the direction of increasing frequency.

At high frequencies ($\omega \rightarrow \infty$), the system cannot follow the modulated illumination, and the IMPS transfer function tends to zero ($H(\omega) \rightarrow 0$). In this regime, the modulated photocurrent is strongly attenuated, giving rise to a semicircle in the lower quadrant of the complex plane associated with the RC time constant of the system. The characteristic frequency at the minimum of this loop is defined as f_{min}, normally related to charge transport, charge separation and bulk recombination before separation.

As the frequency decreases, the influence of the *RC* term becomes less significant, and the response transitions towards the regime governed by interfacial kinetics. In this intermediate region, where $\omega >> k_{tr} + k_{rec}$ but $\omega << 1 / (1 + RC_T)$, the transfer function approaches (j_{ph} / j_0), defined as maximum external quantum efficiency (EQE_{max}).

Upon further decreasing the frequency ($\omega \approx k_{tr} + k_{rec}$), the system response is governed by the competition between charge transfer and surface recombination processes. In this regime, the imaginary component of the photocurrent reaches a maximum at $f_{max} = k_{tr} + k_{rec}$, giving rise to a semicircle in the upper quadrant of the complex plane.

In the low-frequency limit ($\omega \rightarrow 0$), the system reaches steady-state conditions, and the transfer function simplifies to $(j_{ph} / j_0)(k_{tr} / (k_{tr} + k_{rec}))$, which corresponds to the small-signal DC external quantum efficiency (EQE_{DC}) of the system at the potential and light intensity applied. The term $(k_{tr} / (k_{tr} + k_{rec}))$ is defined as the relative charge transfer efficiency (η_{tr}), representing the fraction of photogenerated carriers that are successfully transferred rather than recombined.

The previous analysis assumes the limiting case of $C_{sc} << C_H$, where the IMPS response exhibits a well-defined semicircle in the upper quadrant associated with charge transfer and recombination processes. However, when C_{sc} and C_H are of comparable magnitude and $k_{rec} << k_{tr}$, the IMPS response can develop an additional semicircle in the lower quadrant of the complex plane, with a characteristic minimum frequency of the loop denoted as f_{min2}. This feature originates from the coupling between interfacial kinetics and capacitive effects.

From a physical standpoint, the origin of the modulated photocurrent can be attributed to two main mechanisms: (i) the separation of photogenerated charge carriers at the semiconductor/electrolyte interface, and (ii) their separation driven by an internal electric field within the material. In practice, distinguishing between these contributions is not always straightforward. The overall photoelectrochemical response is governed by a combination of semiconductor and electrolyte properties. On the semiconductor side, relevant factors include the bandgap, doping density, and film characteristics such as morphology, porosity, particle size, and thickness.

On the electrolyte side, key parameters include the nature of the solvent, dielectric constant, ionic strength, pH, and the presence of appropriate redox species capable of interacting with the semiconductor. As a result, the system exhibits a wide range of possible behaviours depending on the interplay of these variables.[26] The IMPS analysis and its application to probe charge carrier dynamics are discussed in more detail in **Chapters 7** and **8**.

The techniques described in this chapter provide complementary information on the processes governing the behaviour of semiconductor photoelectrodes under operating conditions. In particular, the combination of steady-state and frequency-resolved measurements enables the analysis of charge separation, transport, recombination and interfacial transfer occurring at different timescales. These methodologies constitute the experimental basis for the discussion of charge carrier dynamics presented in the following chapters.

Chapter 5

Photoelectrochemical system

Summary

This chapter introduces the general photoelectrochemical cell configuration employed throughout this thesis, followed by the fabrication of photoelectrodes based on semiconductor materials deposited onto fluorine-dope tin oxide (FTO) substrates. Different deposition techniques are presented and discussed in terms of their ability to control film properties such as thickness, homogeneity, and surface coverage. These strategies provide the basis for the photoelectrodes fabrication for the photoelectrochemical studies discussed in detail in **Chapters 6**, **7**, and **8**.

5.1. Photoelectrochemical cell configuration

The (photo)electrochemical measurements carried out in this thesis were performed using a conventional three-electrode configuration, as schematically illustrated in **Figure 5.1**. The system consists of a main electrolyte compartment containing the working electrode (WE), based on an FTO substrate coated with semiconductor materials, and a counter electrode (CE) consisting of a Pt wire. The WE is positioned directly behind a quartz window, which allows light to pass through without absorption, enabling direct irradiation of the electrode surface. This configuration allows both front-side and back-side illumination geometries.

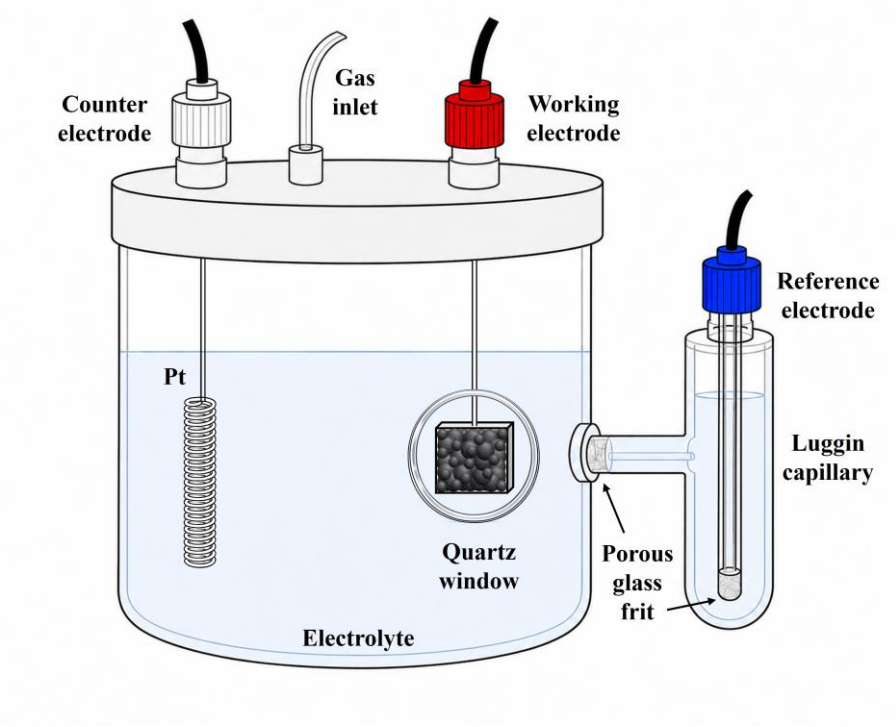

Figure 5.1. Schematic illustration of the photoelectrochemical cell with a three-electrode configuration.

The reference electrode (RE), an Ag/AgCl electrode (3 M KCl), is placed in a separate compartment and electrically connected to the cell via a Luggin capillary equipped with a porous glass frit, which ensures ionic

conductivity while preventing cross-contamination between compartments. The potential was converted to RHE scale using **Eq. 4.1**.

The cell is further equipped with a gas inlet, allowing the electrolyte to be purged with an inert gas (e.g., N_2), thereby enabling control over dissolved species and ensuring well-defined and reproducible experimental conditions.

Under operation, current flows between the WE and the CE through the external circuit and in measured using an Autolab PGSTAT302 potentiostat, while ionic charge transport occurs within the electrolyte to maintain electroneutrality, thus completing the electrochemical circuit. The corresponding electrochemical reactions take place at the electrode/electrolyte interfaces. The potential of the WE is measured with respect to the RE, which provide a stable reference with a well-defined electrochemical potential.

5.2. Deposition techniques

5.2.1. Spin coating

Spin coating is a solution-based deposition technique in which a liquid precursor is deposited onto a substrate and subsequently spread by centrifugal force during high-speed rotation. As the substrate spins, excess solution is expelled, and the remaining liquid forms a thin film whose thickness is determined by the balance between viscous forces, solvent evaporation, and rotational speed. A schematic representation of the spin coating process is shown in **Figure 5.2**. This method enables the fabrication of uniform coatings with controlled thickness and is widely used for the preparation of thin films from colloidal dispersion or low-viscosity precursor solution.[156,157]

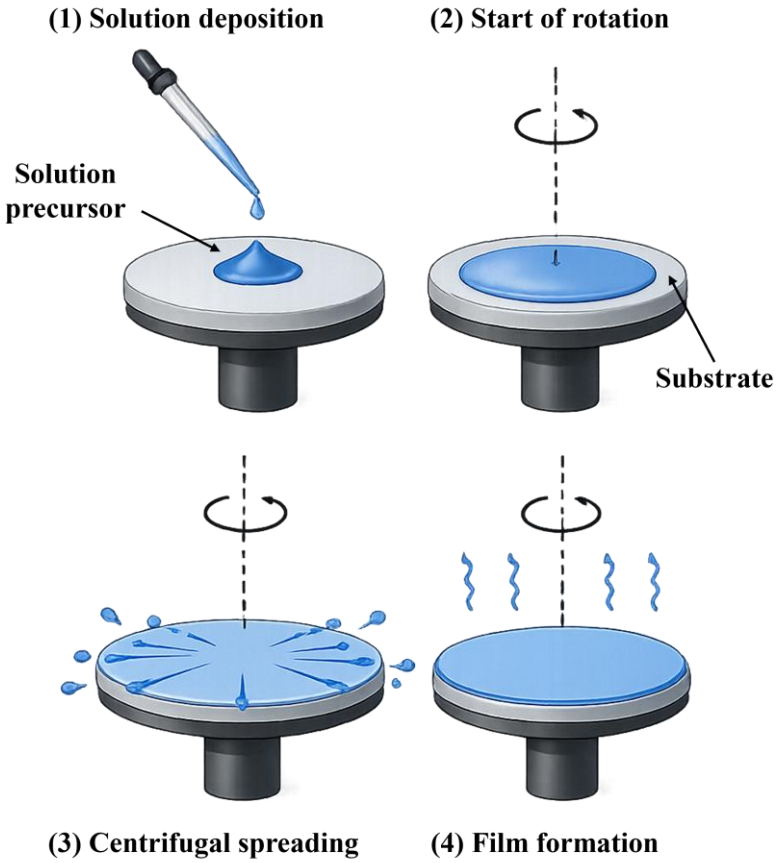

Figure 5.2. Schematic representation of the spin coating process, illustrating the deposition of a liquid precursor onto a rotating substrate and the subsequent thinning of the film due to centrifugal spreading.

5.2.2. Screen printing

In screen printing, a paste or ink is deposited onto a substrate by passing it through a patterned mesh using a mechanical action, typically applied with a squeegee. The geometry of the mesh determines the shape and dimension of the resulting film, enabling a high degree of control over the deposited layer. A schematic representation of the screen-printing process is shown in **Figure 5.3**. This technique is commonly employed for the fabrication of structured coatings and is particularly well suited

for producing relatively thick and porous film from particle-based pastes.[158,159]

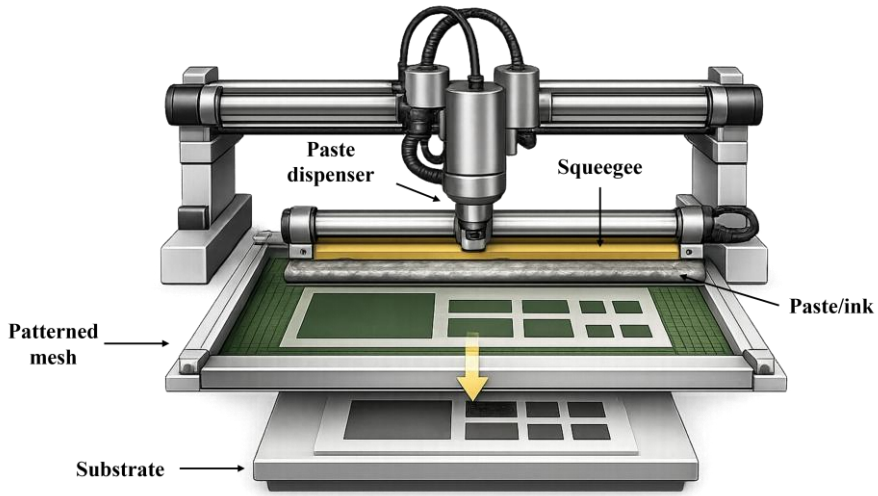

Figure 5.3. Schematic illustration of the screen-printing technique, showing the transfer of paste through a patterned mesh onto a substrate using a squeegee.

5.2.3. Spray pyrolysis

Spray pyrolysis is a deposition technique in which a precursor solution is atomised into fine droplets and directed towards a heated substrate. Upon reaching the substrate, the solvent rapidly evaporates, and the precursor undergoes thermal deposition, leading to the formation of a solid film. A schematic representation of the spray pyrolysis process is shown in **Figure 5.4**. This technique is particularly well suited for the deposition of metal oxide films and allows the preparation of coatings over relatively large areas with good compositional control.[160,161]

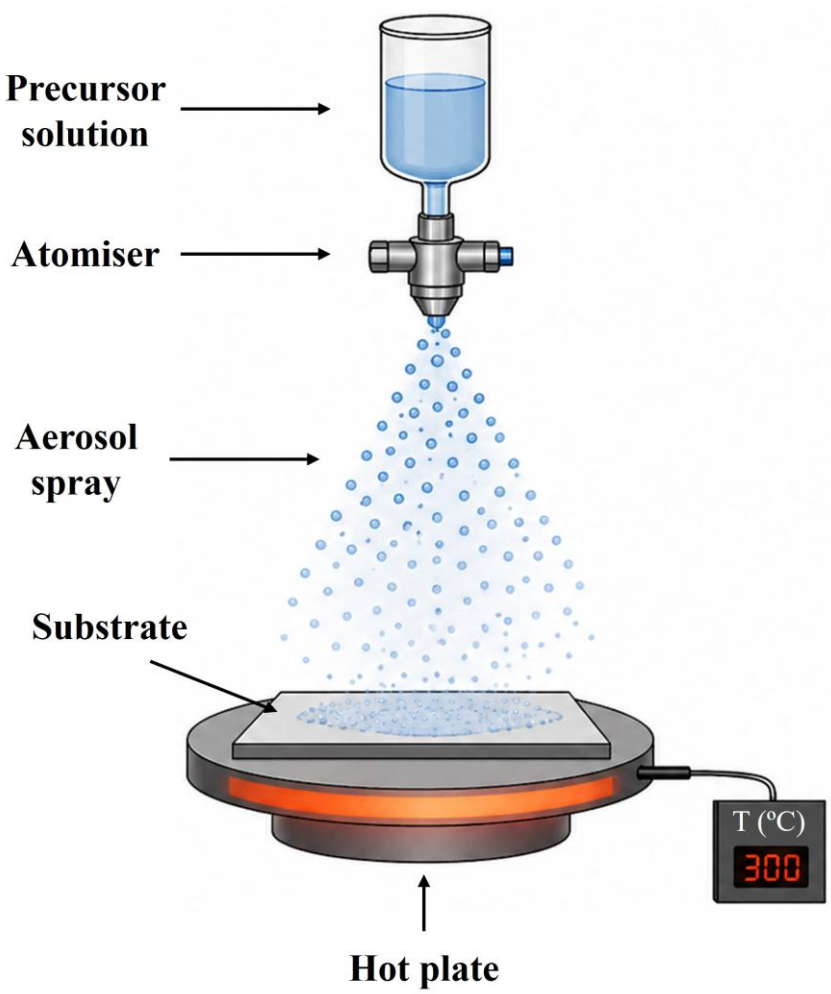

Figure 5.4. Schematic illustration of the spray pyrolysis process, showing the atomisation of a precursor solution and its deposition onto a heated substrate, where solvent evaporation and thermal decomposition occur.

5.2.4. Sputter deposition

Sputter deposition is a physical vapour deposition (PVD) technique based on the interaction between a plasma and a solid target material. Energetic ions (e.g., Ar^+) generated in the plasma impact the target surface, causing the emission of atoms that subsequently travel through

the gas phase and condense onto a substrate, forming a thin film. A schematic representation of the sputter deposition process is shown in **Figure 5.5**. This technique is widely employed for the preparation of compact and uniform coatings with good adhesion and enables precise control over film thickness.[162,163]

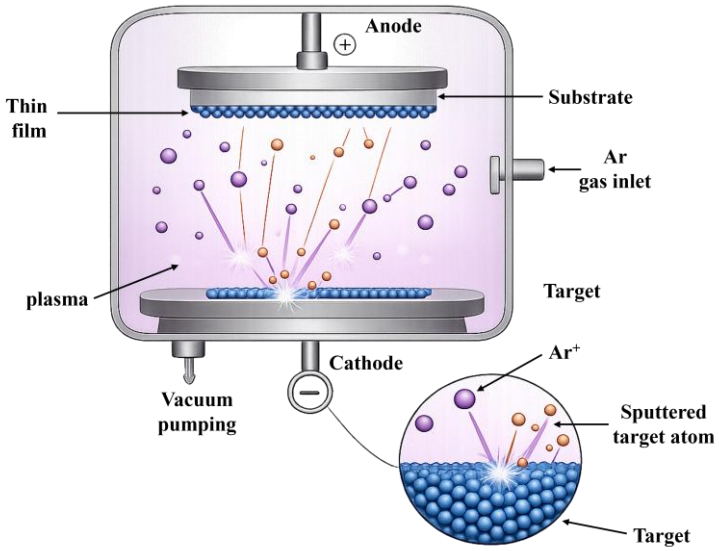

Figure 5.5. Schematic representation of the sputter deposition process, showing the interaction between a plasma and a target material and the deposition of atoms onto the substrate.

The deposition techniques presented in this chapter enable the fabrication of semiconductor photoelectrodes with controlled thickness, morphology, porosity, and surface coverage on conductive substrates. Since these parameters strongly influence the charge carrier dynamics, careful control over the fabrication procedure is essential for obtaining reproducible and well-defined photoelectrodes. The methodologies described here form the basis of the material systems investigated in the following chapters.

Chapter 6

Tuning the photoelectrochemical properties of Ti/W-modified PCN-222 using charge-selective interfaces

Summary

Metal-organic frameworks (MOFs) have attracted growing interest for PEC applications, including visible-light photocatalysis, CO_2 reduction, and hydrogen evolution, owing to their structural tunability and hybrid inorganic-organic nature. The Zr-based porphyrinic framework PCN-222 combines strong visible light absorption from its porphyrin linkers with robust Zr_6 clusters that act as structural and electronic backbones. This chapter reports a modular strategy to tailor and optimise the PEC behaviour of PCN-222 through postsynthetic metal-node substitution with Ti, pore encapsulation of phosphotungstic acid (PTA), and integration with charge-selective interfaces. The resulting PCN-222 materials exhibit photoelectrochemical activity across the entire visible range. Whereas pristine PCN-222(Zr) exhibits photocathodic behaviour (photoelectron transfer to the solution and photohole collection at the FTO substrate), partial substitution of Zr with Ti inverts the current to

photoanodic. Encapsulation of PTA further enhances the anodic photocurrent due to its electrocatalytic properties. Furthermore, charge-selective TiO_2 and NiO_x interlayers deposited between the FTO substrate and the metal-organic framework (MOF) films enable selective extraction of photoelectrons or holes, respectively. This strategy results in a significant photocurrent enhancement, which can be attributed to effective competition of charge extraction and recombination. For PCN-222(Zr), the cathodic photocurrent increases by a factor of 7 using a NiO_x interlayer, while the current switches to photoanodic upon TiO_2 integration, illustrating the importance of efficient charge extraction. Similarly, the current direction is reversed to photocathodic for PCN-222(Zr/Ti) and PCN-222(Zr/Ti/W) when using NiO_x. This chapter discusses the interfacial charge extraction, charge transfer and trapping mechanisms in detail, providing strategies for the design of multicomponent MOF-based systems for photoelectrochemical devices. The contents of this chapter have been published in ACS Applied Materials & Interfaces.[107]

6.1. Introduction

Photoelectrocatalysis has been touted as one of the most promising strategies for the synthesis of chemical fuels and value-added products. By coupling light absorption with charge transport and surface redox processes, photoelectrocatalytic systems can drive reactions such as water splitting, CO_2 reduction, or selective organic oxidation reactions using sunlight as the only energy source. Significant advances have been achieved with inorganic semiconductors, including n-type semiconductors TiO_2, Fe_2O_3, WO_3 and $BiVO_4$, and p-type materials Cu_2O, CuO and $CuBi_2O_4$; however, these materials often suffer from limited spectral absorption, poor stability (p-type), and limited tunability of their electronic properties.[63,164]

Consequently, a central challenge in PEC research is the rational design of materials that combine broad light absorption with efficient charge separation and transport, while offering structural and chemical flexibility.

Controlling how a photoactive material behaves, whether it acts as an n-type or p-type semiconductor, how its band edges align with the electrolyte redox potentials, and how efficiently charges are transferred through interfacial layers, largely determines the overall PEC performance. The type of semiconductor determines the direction of the photogenerated current: n-type materials typically drive oxidation reactions (photoanodes), while p-type materials favour reduction processes (photocathodes).[165] Beyond bulk composition, interfacial engineering has proven crucial. Selective charge transport layers or molecular interlayers can promote directional transport, suppress recombination, and tune band bending at the semiconductor/electrolyte junction.[166,167] Nevertheless, achieving precise control of such behaviour in complex hybrid materials remains a major materials science challenge.

MOFs have emerged over the past decade as a powerful platform to address these issues. MOFs combine crystalline order, chemical modularity, and high surface area, allowing simultaneous control of composition, topology, and functionality.[168] Their use in photocatalysis and PEC conversion is particularly appealing because both the organic linker and the metal node can contribute to light absorption and charge transport. Pioneering studies have demonstrated that several MOFs, particularly those based on Ti, Fe, or Zr clusters, can display semiconductor-like bandgaps and stable photoactivity in water.[169–172] The semiconductor behaviour of other MOFs, such as MOF-5, was also demonstrated in early studies.[173] Still, most MOFs are intrinsically insulating, and long-range charge migration is hindered by large intermetallic distances and weak orbital overlap between linkers. Overcoming these limitations through structural design and compositional engineering is therefore an active area of research.

Among all families of photoactive MOFs, porphyrinic frameworks are particularly attractive. The extended π-conjugation of the porphyrin macrocycle affords strong visible-light absorption through Soret and Q bands, while its central metal ion can be exchanged to tailor redox properties.[174] The archetypal Zr-based PCN-222 exemplifies this concept: it features one-dimensional mesochannels lined with metalloporphyrins and robust $Zr_6O_4(OH)_4$ nodes that provide exceptional chemical and thermal stability.[175] PCN-222 and related

frameworks have been explored for visible-light photocatalysis, CO_2 reduction, and hydrogen evolution.[176–179] Their porphyrinic units act as light harvesters and redox centres, whereas the inorganic nodes serve as electron transport materials and structural supports.

However, despite their favourable optical characteristics, porphyrinic MOFs suffer from rapid charge recombination and poor electronic conductivity across crystals and films. The intrinsic separation between metal clusters and organic linkers hampers delocalisation of charge carriers, and the alignment of the frontier orbitals often prevents efficient injection of electrons into external substrates such as FTO.[180] Considerable effort has therefore been devoted to enhancing the electronic coupling in these systems. Strategies include linker functionalisation with donor or acceptor groups[170,176] and incorporation of conductive guests.[181] However, targeted modification of the inorganic node, either by partial metal substitution or by controlled defect generation, has emerged as the most powerful approach to reshape the electronic landscape and enhance charge transport. Mixed-metal substitution has been successfully employed to tailor band-edge positions and improve electronic coupling in Zr-based MOFs,[182] while defect engineering strategies have been widely explored to enhance conductivity and catalytic activity in these robust frameworks.[183–185]

Ti-doping or partial substitution of Zr by Ti in PCN-222 is particularly promising because Ti centres possess 3d orbitals of appropriate energy to mediate ligand-to-metal charge transfer (LMCT) processes and enhance electronic communication between porphyrins and the inorganic cluster. In analogy to mixed-metal oxides, introducing Ti into the Zr-oxo cluster can lower the conduction-band edge, improve electron mobility, and enable stronger coupling with conductive supports.[180,182,186] Moreover, Ti species can act as active sites for interfacial reactions, favouring electron extraction and decreasing the recombination rate at the MOF/FTO interface. Such controlled substitution thus offers a versatile route to modulate the semiconductor character and directionality of the photoresponse.

Complementary to cationic substitution, the incorporation of redox-active molecular guests within MOF pores provides an internal pathway

for charge delocalisation and temporary electron storage. Polyoxometalates (POMs), and particularly Keggin-type phosphotungstates ($PW_{12}O_4^{3-}$), are well-known electron sponges capable of fast, reversible multielectron reduction while maintaining structural integrity.[187] When confined inside MOFs, POMs can interact electronically with the framework through hydrogen bonding or coordination to node hydroxyls, forming hybrid materials with synergistic photoactivity.[188] Encapsulation of an electron-rich POM within MOF matrices and their integration with semiconductor photoanodes has been shown to enhance visible-light-driven charge separation and interfacial electron transfer, thereby improving photocurrent generation and stability in photoelectrochemical water splitting systems.[189]

On the other hand, photoelectrochemical systems exhibit parallel characteristics with third-generation solar cells. For many systems, the solar cell can be considered to consist of an active layer sandwiched between two selective contacts, one for electrons and one for holes. In this case, the charge extraction efficiency at these selective contacts determines the photocurrent rather than the potential distribution.[190–193] In photoelectrochemical systems, one selective contact is the electrolyte solution, which is generally characterised by slow charge transfer. Hence, efficient extraction of carriers at the FTO contact becomes crucial, which has led to heterojunction systems with the specific goal of improving charge extraction at the FTO contact side. A typical example is the FTO/WO_3/$BiVO_4$ system, where WO_3 functions as a selective contact with a high electron extraction rate, thus significantly diminishing recombination in the $BiVO_4$ absorber layer.[194,195]

These observations highlight how subtle modifications, either intrinsic (via Ti substitution or POM incorporation) or extrinsic (through interfacial contacts), may provide opportunities to tailor the operational mode of a porphyrinic MOF electrode. Within this broad context, the present work investigates the interplay between composition, electronic structure, and photoelectrochemical characteristics in thin films of the porphyrinic MOF PCN-222(Zr), with a special emphasis on the influence of charge-selective interlayers on their performance. Three representative systems were fabricated on FTO substrates (or FTO

substrates incorporating interfacial transport layers): pristine PCN-222(Zr), a mixed-metal analogue with partial substitution of Zr by Ti PCN-222(Zr/Ti), and a subsequent composite containing encapsulated phosphotungstic acid, $H_3PW_{12}O_{40}$, PCN-222(Zr/Ti/W). By combining UV-Vis spectroscopy, transient photocurrent, and LSV under chopped illumination, this chapter analyses how each structural modification alters the optical response, charge-separation efficiency, and directionality of the photocurrent. The results reveal that Ti incorporation and subsequent $H_3PW_{12}O_{40}$ encapsulation collectively shift the photoelectrode behaviour from photocathodic to photoanodic under visible-light illumination, with a strong dependence on the nature of the interfacial layer. Together, these findings provide fundamental insight into how rational chemical modification of MOF nodes, pores, and interfaces can tailor semiconductor behaviour in hybrid photoelectrodes, bridging the gap between molecular light-harvesting units and extended solid-state architectures.

6.2. Experimental section

6.2.1. Synthesis of PCN-222 (Zr) nanoparticles

Nanoparticles of PCN-222 were synthesised in an Initiator Classic Microwave reactor (Biotage) by using a microwave-assisted (MW) method previously optimised in our group.[196] First, the Zr_6 clusters, $[Zr_6(\mu_3\text{-}O)_4(\mu_3\text{-}OH)_4]$, were prepared according to a previously reported method.[197] For the nanoparticle synthesis, 76 mg (28.4 μmol) of Zr_6 clusters and 22.5 mg (28.5 μmol) of tetrakis(4-carboxyphenyl)porphyrin (BD168635, BLD Pharmatech) were dissolved in 8 mL of anhydrous N, N-dimethylformamide (DMF) (481785, Panreac) and placed into a 10 mL MW vial. Next, 100 μL of trifluoroacetic acid (302031, Sigma-Aldrich) was added to the vial. The mixture was subjected to an initial MW power of 250 W, reaching 100 °C within minutes, and further maintained for 10 min. After this time, the reaction was rapidly quenched by forced air cooling to suppress further crystal growth. The obtained nanoparticles were collected by centrifugation (10 000 RCF, 15 min), washed twice with fresh DMF and twice with methanol (131091,

Panreac). The purified product was redispersed in methanol to obtain a 5 mg mL^{-1} suspension, which was stored at 4 °C until use.

6.2.2. Preparation of PCN-222(Zr/Ti) nanoparticles: metal-exchange at the nodes

The incorporation of Ti into PCN-222 nanoparticles was performed using a newly optimised microwave-assisted method aimed at maximising the amount of Ti incorporated. The previously prepared PCN-222 was dried and thermally activated in an oven at 120 °C for 6 h before performing the postsynthetic modification (PSM) to introduce Ti into the structure. For this purpose, 20 mg (8.5 μmol) of activated PCN-222 and 10 mg (40 μmol) of bis(cyclopentadienyl)titanium(IV) dichloride ($TiCp_2Cl_2$) (234826, Sigma-Aldrich) were dissolved in 6 mL of anhydrous DMF and transferred into a 10 mL MW vial. The mixture was heated to 150 °C by MW irradiation and maintained at this temperature for 30 min. After this period, the modified PCN-222(Zr/Ti) nanoparticles were collected by centrifugation (10 000 RCF, 15 min), washed twice with fresh DMF and twice with methanol. The purified product was redispersed in methanol to obtain a 5 mg mL^{-1} suspension, which was stored at 4 °C until use.

6.2.3. Preparation of PCN-222(Zr/Ti/W) nanoparticles: encapsulation of $H_3PW_{12}O_{40}$ into the pores

PCN-222 was dried and thermally activated in an oven at 120 °C for 6 h before performing the PSM to load $H_3PW_{12}O_{40}$ molecules into the pores of the framework via an impregnation method under mild temperature conditions. Specifically, 20 mg (8.5 μmol) of activated PCN-222 and 80 mg (27.8 μmol) of phosphotungstic acid hydrate (79690, Sigma-Aldrich) were dissolved in 6 mL of anhydrous DMF and placed into a 10 mL microwave vial. The mixture was allowed to soak for 30 min and then incubated at 60 °C under continuous stirring for 48 h. Afterwards, the modified PCN-222(Zr/Ti/W) nanoparticles were collected by centrifugation (10 000 RCF, 15 min), washed three times with methanol,

and finally redispersed in methanol to obtain a 5 mg mL^{-1} suspension. The sample was stored at 4 °C until use.

6.2.4. Photoelectrode fabrication

The FTO-coated conductive glass substrates (SnO_2:F, 12-15 Ω sq^{-1}, TEC 15 Xop Glass) were sequentially cleaned using an ultrasonic bath for 20 min in each of the following solvents: Milli-Q water containing Hellmanex III (Z805939, Sigma-Aldrich), Milli-Q water, ethanol (20821, VWR), isopropanol (278475, Sigma-Aldrich), and acetone (20067, VWR). After solvent cleaning, the substrates were dried using a nitrogen stream and subsequently treated in a UV ozone cleaner (Ossila, L2002A3-EU) for 30 min at room temperature.

TiO_2 and NiO_x layers were deposited on FTO substrates via spray pyrolysis with the substrate at 300 °C under N_2 flow. The precursors were 0.14 M titanium diisopropoxide bis(acetylacetonate) (325252, Sigma-Aldrich) in isopropanol and 0.05 M nickel(II) nitrate hexahydrate (203874, Sigma-Aldrich) in water, respectively. A total of 20 and 15 layers were deposited, respectively, with a 30 s interval between each deposition step. After reaching the desired number of layers, the films were kept at 300 °C for 30 min and allowed to cool to room temperature.

The photoelectrodes were prepared by depositing 20 µL of a 5 mg mL^{-1} PCN-222(Zr, Zr/Ti, and Zr/Ti/W) previously sonicated dispersion in methanol onto FTO, FTO/TiO_2, and FTO/NiO_x substrates via a two-step spin-coating process: first at 500 rpm for 10 s to ensure covering the FTO substrate, followed by 3000 rpm for 30 s. This procedure was repeated for a total of 3 sequential deposition steps, with each layer left to dry at room temperature for 5 min to ensure solvent evaporation before the next coating step (see **Figure 6.1**).

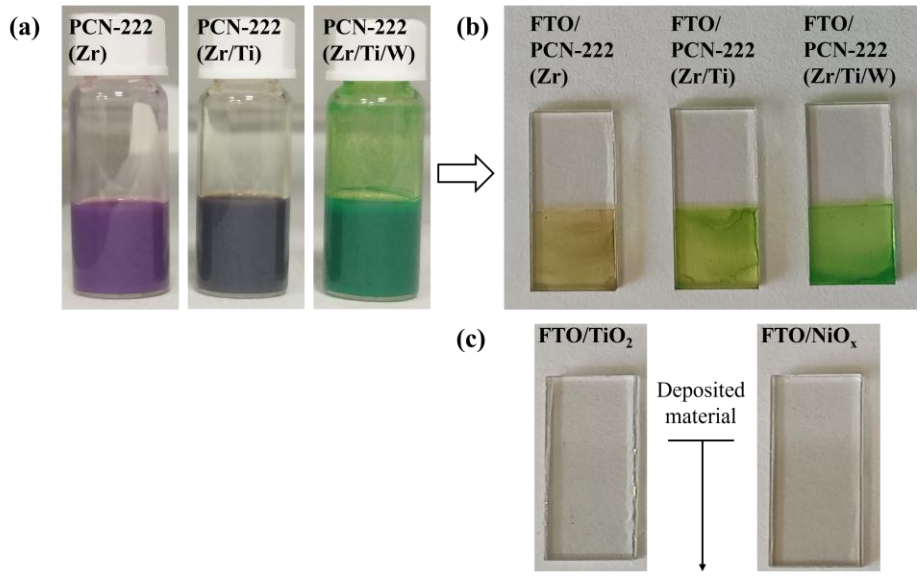

Figure 6.1. (a) Photographs of PCN-222(Zr), PCN-222(Zr/Ti), and PCN-222(Zr/Ti/W) dispersed in methanol (5 mg mL^{-1}). (b) Photographs of the photoelectrodes prepared by deposition of the different PCN-222 material on FTO by spin coating technique, and (c) compact layers of TiO_2 and NiO_x deposited on FTO by spray pyrolysis.

6.2.5. Structural, morphological, and optical characterisation

SEM to evaluate the morphology and homogeneity of the nanoparticles was performed on a HITACHI S4800 FE-SEM operating at 2 kV. Samples were prepared by drying a diluted suspension of the particles in methanol on a silicon wafer substrate. Elemental composition of the nanoparticles (e.g., relative metal ratios Ti/Zr or W content) was estimated by semiquantitative EDX using the same FE-SEM instrument coupled to a Bruker-X Flash-4010EDX detector and operating at 10 kV.

PXRD of the crystalline powder of the samples was performed using a Bruker D8-Advance Diffractometer. Cu Kα X-ray radiation was used and the measurement range was 1.5°−30° (2θ) with a step of 0.02°. GAXRD was performed using an incidence angle of 2°, in the 2θ range 2°−60° with a step size of 0.01° per 0.2 s was used to determine the

crystalline structure of the PCN-222 films. All measurements were collected in 2D mode using a Bruker EIGER2 R 250 K Detector. DLS measurements on the nanoparticles in suspension (in methanol) were carried out using a Malvern Zetasizer Nano ZSP equipped with a 10 mW He−Ne laser operating at a wavelength of 633 nm and fixed scattering angle of 173°. The ζ-potential of the nanoparticles dispersed in water was measured with LDA using the same Malvern Zetasizer Nano ZSP instrument.

XPS spectra were recorded in a Phoibos-100 spectrometer with a non-monochromatized X-ray source (Al Kα; 1486.6 eV) and the power source was 230 W. The electron energy hemispherical analyser was operated in the constant pass energy mode. Low-resolution survey spectra were obtained with a pass energy of 50 eV, while high-energy resolution spectra of detected elements were obtained with a pass energy of 20 eV. The spectra were analysed with the "CASA XPS" software (version 2.3.16.Dev52). Binding energies were calibrated using C 1s signal as an internal standard at 284.8 eV. Shirley-type backgrounds were used to determine the areas under the peaks.

The homogeneity, film thickness, and surface morphology were examined in both top-view and cross-section modes using a Zeiss Gemini 300 FE-SEM, with an accelerating voltage of 15 kV. EDX was used to estimate the elemental distribution of photoelectrode materials using the same FE-SEM system. The films were previously coated with a 10 nm gold layer using a Vac Coat sputtering system (model DSCT) to improve surface conductivity and minimise charging effects during SEM measurements.

The absorbance spectrum of a diluted suspension (0.03 mg mL^{-1}) of PCN-222 in methanol was measured using an Agilent UV-Vis Cary 100 spectrophotometer (model G9821A), in the range of 350−800 nm. To determine the optical properties of the films, DRS was performed using a UV/Vis/NIR FSL1000-DD-STM Edinburgh Instruments spectrophotometer equipped with an integrating sphere and an Xe lamp as the light source in the 350−800 nm range, with a dwell time of 1 s and step size of 1 nm.

6.2.6. Photoelectrochemical characterisation

PEC measurements were carried out using a three-electrode setup with front-side illumination (i.e., from the electrolyte side) in a single-compartment electrochemical cell equipped with a quartz window. A Pt wire served as the counter electrode, while an Ag/AgCl electrode (3 M KCl) (P3911, Sigma-Aldrich) was used as the reference. The electrolyte was a 0.1 M acetate buffer (1.06267, Supelco and 211008, Panreac) solution at pH 4.5, which was purged with N_2 for 20 min before the measurement to remove dissolved gases, such as O_2. Measurements were performed with an Autolab PGSTAT302N system and a solar simulator (ABET 1100) equipped with an AM 1.5G filter, calibrated to 1 sun (100 mW cm^{-2}) using a silicon photodiode (Newport model 91150), and under high-power monochromatic LED illumination of different wavelengths: UV (λ = 400 nm), blue (λ = 455 nm), green (λ = 535 nm) and red (λ = 670 nm) calibrated with a Si-photodiode (Hamamatsu S12698-2) at the same photon flux of 1.6×10^{16} cm^{-2} s^{-1}. Both for the solar simulator and LED illumination, a chopper was used to modulate the light intensity at a frequency of 0.18 Hz. The emission spectra of the LEDs were obtained using an Ocean Optics (USB 4000) spectrometer equipped with an optical fibre. The applied potential was converted to the RHE at pH 4.5. The illuminated area in contact with the electrolyte was 1 cm^2, and the scan rate was 20 mV s^{-1}. The photoelectrochemical characteristics remained unchanged over multiple days and numerous measurements.

A solution of 0.1 M acetic acid/sodium acetate buffer with 0.01 M $[Fe(CN)_6]^{4-}$ (P3289, Sigma-Aldrich) and other with 0.01 M $[Fe(CN)_6]^{3-}$ (26810, VWR) both at pH = 4.5, and a nonaqueous solution 0.1 M $TBAPF_6$ (86874, Sigma-Aldrich) and 0.01 M p-benzoquinone (A13162, Thermo Scientific) in propylene carbonate (310328, Sigma-Aldrich) under dark conditions were used to verify the compactness of the TiO_2 and NiO_x charge-selective layers, respectively.

6.3. Result and discussion

6.3.1. Synthesis and structural characterisation of Ti/W-modified PCN-222

In a first step, PCN-222(Zr/Ti) was obtained by a postsynthetic metal-node exchange using a newly developed method, not previously reported for the incorporation of Ti into MOFs. It consists of employing $TiCp_2Cl_2$ in DMF under controlled microwave heating to take advantage of microwave irradiation, achieving high incorporation efficiency while drastically reducing reaction times from several days, as typically reported in the literature, to only 30 min.[198] The method relies on the high hydrolytic and thermal stability of PCN-222(Zr) and on the similar coordination chemistry of Zr(IV) and Ti(IV), enabling an efficient exchange of Zr by Ti without compromising the structural integrity of the material. Thus, this postsynthetic modification strategy also overcomes one of the main challenges associated with the direct synthesis of Ti-based MOFs, namely the severe hydrolysis of most Ti precursors and the poor reversibility of Ti-ligand coordination, which often prevents the formation of well-defined crystalline frameworks. Following Ti incorporation, the colour of the material changes from purple to brown (**Figure 6.2a**), a transformation attributed to perturbations in the electronic structure induced by metal substitution within the metal nodes, a phenomenon previously rationalised and proposed as a strategy for tuning the electronic structure in MOFs.[182] SEM reveals that the characteristic nanorod morphology of PCN-222 is largely preserved (**Figure 6.2b**), with an average lateral dimension of approximately 180 nm. Some changes in aspect ratio and surface texture are observed, likely as a consequence of the intense MW heating applied. In particular, the slightly roughened surface may indicate the formation of structural defects or the presence of localised Ti-rich domains at the particle surface. Reducing the MW heating temperature to 100 °C prevented such morphological alterations but also markedly decreased the Ti incorporation efficiency. Therefore, MW heating at 150 °C for 30 min was selected as the optimal condition, maximising Ti incorporation while preserving acceptable morphological characteristics.

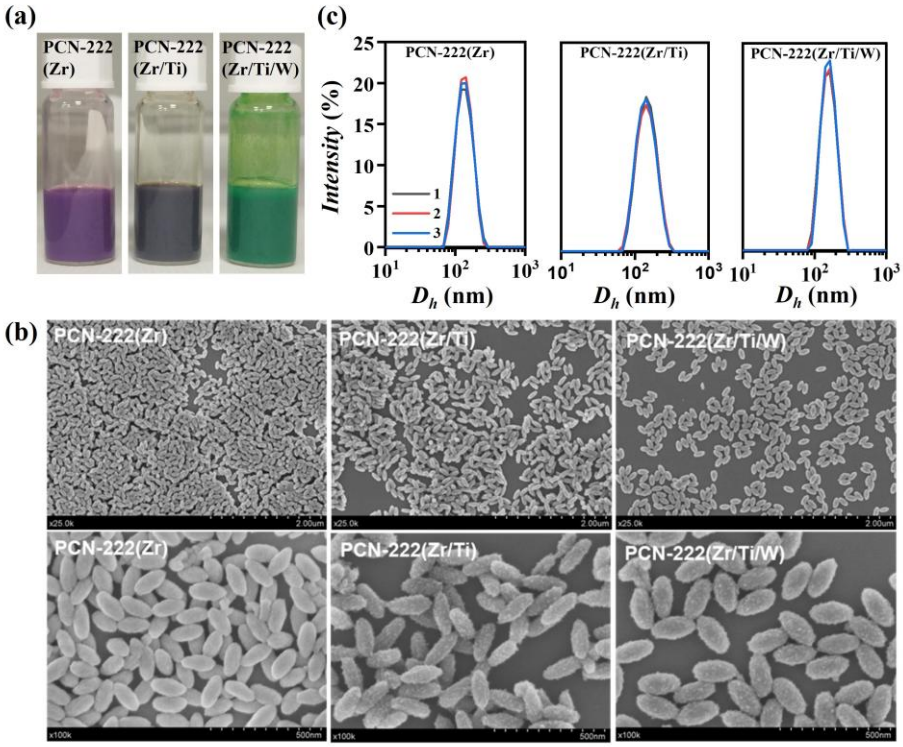

Figure 6.2. (a) Photographs of the as-prepared samples: PCN-222(Zr), PCN-222(Zr/Ti), and PCN-222(Zr/Ti/W) dispersed in methanol. (b) SEM images at different magnifications of pristine PCN-222(Zr) nanoparticles and after Ti/W modifications. (c) DLS size distribution by intensity of the as-prepared PCN-222 nanoparticles dispersed in methanol (for 3 independent measurements).

In a second step, the well-defined mesoporosity of PCN-222 was exploited to encapsulate a Keggin-type polyoxometalate species (POM), specifically $H_3PW_{12}O_{40}$, into the framework cavities via a straightforward impregnation method using, yielding the composite material denoted as PCN-222(Zr/Ti/W). Given the size mismatch between the 3.6 nm mesochannels of PCN-222 and the 1 nm Keggin anion, PTA incorporation is expected to only partially occupy the pore volume. The $[PW_{12}O_{40}]^{3-}$ clusters are strongly retained within the mesopores due to favorable electrostatic interactions with the positively charged Zr/Ti-oxo nodes and coordinated aquo/hydroxo ligands at the

metal clusters, as previously reported for other MOF systems, specifically NU-1000.[199] SEM images of the resulting PCN-222(Zr/Ti/W) nanoparticles reveal minimal morphological changes, with a slight variation in the aspect ratio of the nanorods, which appear more rounded. The colour changes to green observed after encapsulation of $H_3PW_{12}O_{40}$ (**Figure 6.2a**) arise from the characteristic optical properties of the Keggin type polyoxometalate. When confined within the MOF structure, additional ligand-to-metal charge-transfer transitions, particularly from oxygen to tungsten (O → W) are induced, leading to enhanced absorption in the visible region and giving the material its distinctive green colour. This behaviour aligns with prior reports, where photochromic effects have been observed after incorporating a Keggin anion into UiO-66 and UiO-67 frameworks, attributed to charge-transfer effects and guest-induced band modulation.[200,201]

The atomic composition of the modified PCN-222 materials was estimated by EDX (semiquantitative) (**Table 6.1**), supporting efficient incorporation of Ti and W into the structure. For PCN-222(Zr/Ti), the Ti content was 48% relative to the total (Zr + Ti) atomic fraction, indicating substantial Zr-to-Ti exchange within the clusters. Notably, the achieved Ti-incorporation value is considerably higher than that reported for Ti-doped PCN-224 after 48 h of reaction, which reached only around 36%.[198] In the fully modified PCN-222(Zr/Ti/W) sample, the Ti content was 46% of the total metal content (Ti/Zr = 0.88), showing that the subsequent Keggin-type polyoxometalate $[PW_{12}O_{40}]^{3-}$ encapsulation did not displace the incorporated Ti. The W content corresponds to 0.6 PW_{12} units per Zr_6 node, which is close to the theoretical maximum expected for full occupation of the mesopores (based on geometric constraints and pore volume analysis of PCN-222). The high encapsulation level achieved here reflects both the strong electrostatic affinity between the anionic POM clusters and the cationic metal centres in the PCN framework, as well as the accessibility of the large mesoporous channels. Comparable high loadings have been reported for NU-1000-based systems, typically in the range of 0.6-0.8 PW_{12}/Zr_6 node.[199,202] These compositional estimates are consistent with the structural (PXRD) and chemical-state (XPS) signatures discussed below, which support mixed Zr/Ti-oxo node formation and PTA incorporation.

Table 6.1. EDX analysis of the samples, showing the atomic percentage (at.%) of Zr, Ti, and W, the corresponding atomic ratios, and the calculated amounts per Zr_6 cluster.

Sample	Zr (at.%)	Ti (at.%)	W (at.%)	Ti/Zr ratio	Ti per Zr_6	PW_{12} per Zr_6
PCN-222(Zr)	100	-	-	-	-	-
PCN-222(Zr/Ti)	51.9	48.1	-	0.927	5.54	-
PCN-222(Zr/Ti/W)	32.4	28.6	38.9	0.883	5.30	0.6

DLS analysis of the as-prepared nanoparticles dispersed in methanol reveals only slight changes in the hydrodynamic size after Ti- and W-modifications (**Figure 6.2c** and **Table 6.2**), consistent with the SEM observations. The moderate increase observed for PCN-222(Zr/Ti/W) may be attributed to slight particle aggregation induced by POM encapsulation. Importantly, the *PDI* values remain low after both PSM steps ($PDI \leq 0.1$), indicating good particle uniformity and the absence of aggregation. Zeta-potential measurements show a slight increase in surface positive charge following Ti-incorporation (from +27.2 mV for PCN-222(Zr) to +34.6 mV for PCN-222(Zr/Ti), likely due to the formation of Ti-rich domains at the particle surface. The subsequent encapsulation of $[PW_{12}O_{40}]^{3-}$ species produces only a very minimal change in surface charge (**Table 6.2**), supporting the conclusion that these species are mainly confined within the internal mesopores rather than adsorbed onto the particle surface. Overall, PTA incorporation reduces the free pore volume, but the mesoporous channels remain sufficiently open to allow electrolyte access and ionic transport under the photoelectrochemical conditions used in this work.

Table 6.2. Hydrodynamic diameter D_h (mean value ± SD), as derived from intensity distributions, and *ζ-potential* (mean value ± SD) of the different PCN-222 dispersed in methanol (for DLS) and water (for *ζ-potential*). Polydispersity index (*PDI*) is also given.

Sample	D_h (nm)	*PDI*	*ζ-potential* (mV)
PCN-222(Zr)	138.5 ± 0.2	0.061	27.2 ± 0.3
PCN-222(Zr/Ti)	149.5 ± 1.4	0.102	34.6 ± 0.3
PCN-222(Zr/Ti/W)	160.9 ± 0.9	0.098	31.8 ± 0.9

The PXRD pattern of pristine PCN-222 matches well with the simulated pattern (**Figure 6.3a**)**.** After Ti-incorporation via metal-node exchange, the diffraction peak at 2θ ≈ 2.4°, assigned to the (100) crystallographic plane, exhibits a clear splitting. This effect suggests lattice distortion induced by the substitution of Zr(IV) by the smaller Ti(IV) ion, potentially lowering the framework symmetry or giving rise to coexisting structural domains. Similar PXRD peak splitting in MOFs has previously been attributed to symmetry reduction and framework distortion, as reported for the NTU-9 MOF.[203,204]

The (200) reflection at 2θ−4.8° also shows splitting along with a marked decrease in intensity, which can be ascribed to increased microstrain, reduced crystallographic coherence, and/or compositional heterogeneity introduced in the PCN-222(Zr/Ti) sample. In contrast, the PXRD pattern of the PCN-222(Zr/Ti/W) reveals a notable increase in the intensity of the (211) and (201) reflections (at 2θ−6.65° and 7.06°, respectively). This enhancement arises from the extra electron density of $[PW_{12}O_{40}]^{3-}$ species confined within the mesopores, which increases the X-ray scattering contrast along specific crystallographic directions.[202] In this case, the selective intensification of these reflections supports the successful and uniform encapsulation of the $[PW_{12}O_{40}]^{3-}$ guests while preserving the structural integrity of the host framework.

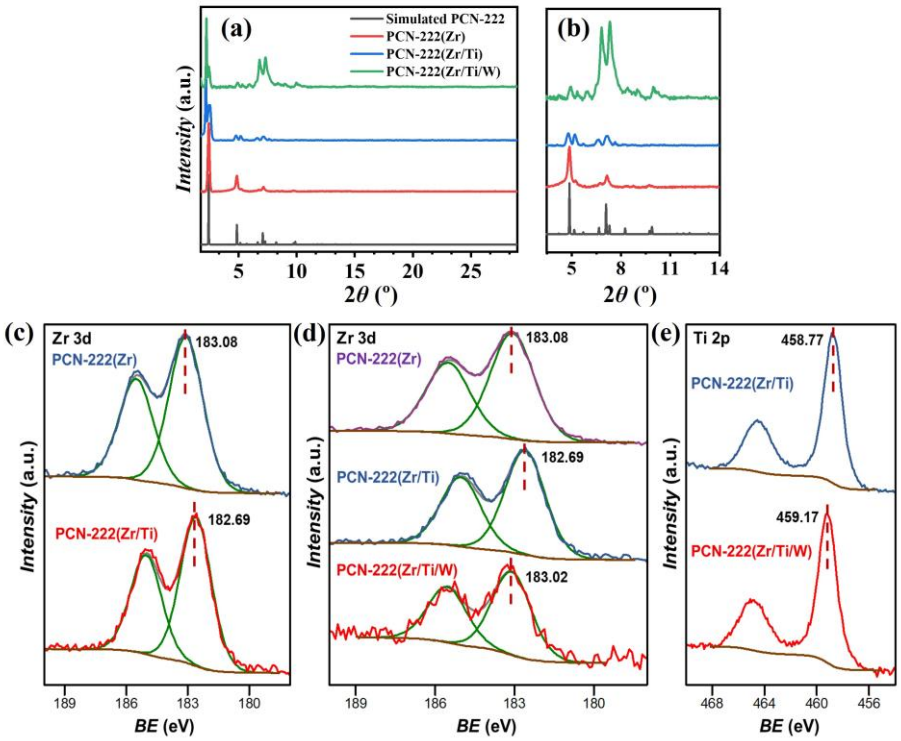

Figure 6.3. (a) PXRD patterns of the as-prepared nanoparticles, including the simulated pattern for PCN-222 (CCDC 893545), within the range of (a) 2θ = 1.7−29°, and (b) magnification of the 2θ = 3.5−14° region to more clearly visualise the changes. (c) Zr 3d XPS spectra of PCN-222(Zr) (top, blue) and PCN-222(Zr/Ti) (bottom, red). (d) Comparison of Zr 3d XPS spectra of PCN-222(Zr) (top, purple), PCN-222(Zr/Ti) (middle, blue) and PCN-222(Zr/Ti/W) (bottom, red). (e) Comparison of Ti 2p XPS spectra of PCN-222(Zr/Ti) (top, blue) and PCN-222(Zr/Ti/W) (bottom, red).

XPS analysis were carried out to investigate the surface composition and chemical states of the as-prepared nanoparticles. **Figure 6.4a** displays the high-resolution spectra of the Zr 3d, O 1s, and C 1s regions for PCN-222(Zr) nanoparticles. The Zr 3d spectrum exhibits two peaks at *BE* of 183.08 and 185.51 eV, with a spin-orbit splitting (SOS) of 2.43 eV, corresponding to Zr $3d_{5/2}$ and Zr $3d_{3/2}$, respectively. These values are characteristic of Zr(IV) cations within Zr_6 clusters commonly observed

in this class of MOFs.[205,206] The O 1s spectrum was deconvoluted into three components located at 531.15, 532.10, and 533.61 eV, assigned to Zr−O−Zr, Zr−O−C, and Zr−OH environments, respectively, with the central peak being the dominant contribution.[207] The C 1s region was well fitted with four components at 284.77, 285.49, 288.82, and 292.67 eV, attributed to C=C (aromatic), C−O, O−C=O, and a shakeup satellite feature, respectively.[45] The N 1s signal appears as a broad feature centred at 399.95 eV, consistent with the porphyrinic nitrogen environment (**Figure 6.4c**).

The successful incorporation of Ti into PCN-222(Zr/Ti) is confirmed by the Ti 2p doublet (**Figures 6.3e** and **6.4b**) at 458.77 eV (Ti 2p3/2) and 464.31 eV (Ti 2p1/2). The observed SOS of 5.54 eV, along with the *BE* positions and full width at half maximum (FWHM) values, is consistent with the Ti(IV) oxidation state, as expected for materials prepared under ambient conditions. The Zr 3d signal shows peaks at 182.69 eV (Zr $3d_{5/2}$) and 185.12 eV (Zr $3d_{3/2}$) *BE*. Notably, a negative shift in binding energy (ΔBE = −0.39 eV) was observed, compared to PCN-222(Zr), **Figure 6.3c**. This shift reflects a modified local electronic environment at the Zr centres upon Ti incorporation, consistent with a reduced electron-withdrawing character within the Zr_6 clusters when Ti(IV) is introduced, leading to the formation of mixed Zr/Ti-oxo nodes.[205,207,208] In the O 1s region, two main components at 532.31 and 530.38 eV are resolved and assigned to Zr−O and Ti−O bonds, respectively, further supporting the formation of mixed-metal oxo nodes. The N 1s signal remains essentially unchanged (400.05 eV), indicating that the chemical environment of the porphyrinic nitrogen atoms is unaffected by Ti incorporation (**Figure 6.4c**). These findings indicate that Ti atoms are not coordinated to the porphyrinic macrocycle linkers but are instead incorporated into the inorganic nodes, resulting in mixed Ti−Zr clusters.[209] Notably, these XPS signatures correlate with the structural distortions inferred from PXRD (shown in **Figure 6.3a**), where the splitting of the (100) reflection at 2θ−2.4° and the concomitant changes at the (200) reflection (2θ−4.8°) point to symmetry lowering and microstrain in the framework. The chemical shift of Zr 3d toward lower *BE* and the emergence of a distinct Ti−O contribution in O 1s are fully consistent with such lattice perturbations and with the coexistence of Zr-rich and Ti-perturbed local

environments at the nodes, an electronic/structural heterogeneity that rationalises the PXRD peak splitting previously discussed for PCN-222(Zr/Ti).

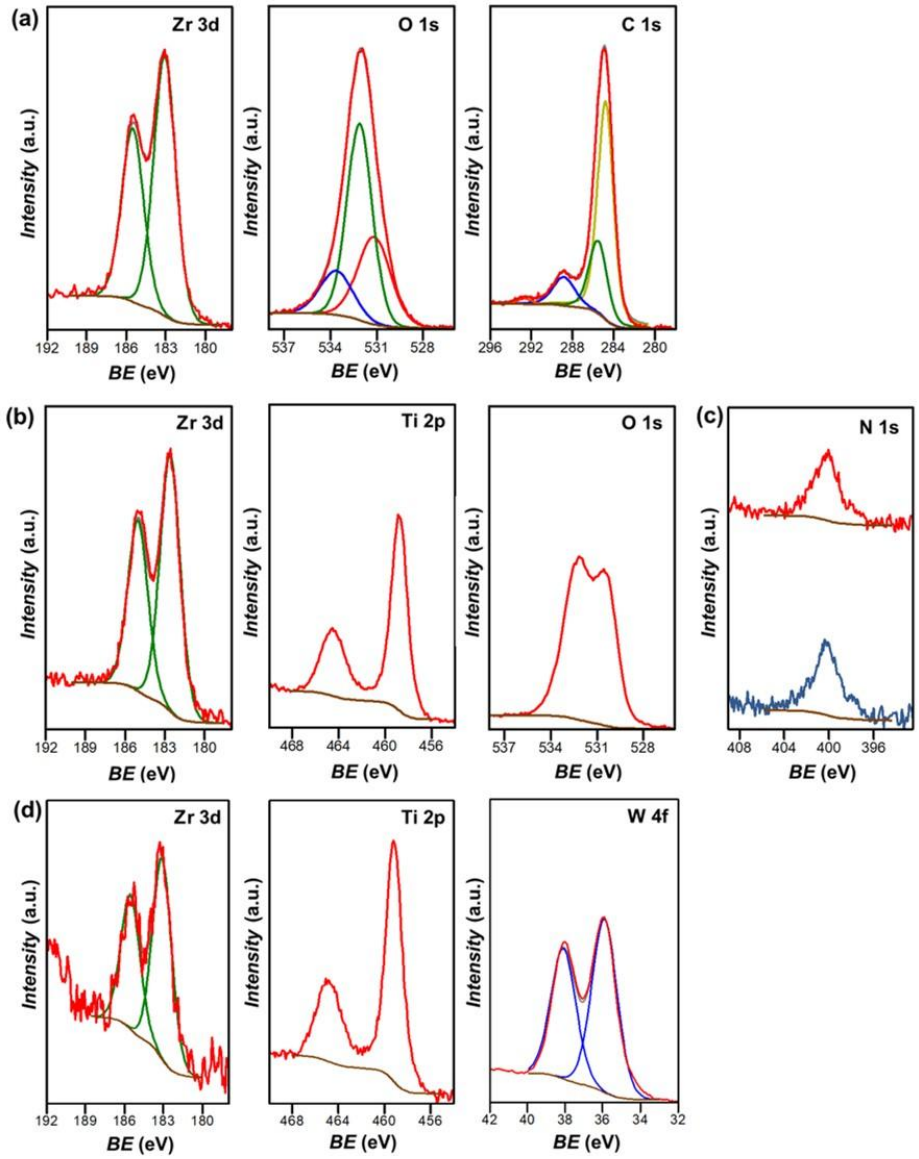

Figure 6.4. (a) Zr 3d, O 1s and C 1s XPS spectra for PCN-222(Zr) sample. (b) (c) Zr 3d, Ti 2p and O 1s XPS spectra for PCN-222(Zr/Ti) sample. (c) Comparison N 1s region XPS spectra of PCN-222(Zr) (top), and PCN-222(Zr/Ti) (bottom). (d) Zr 3d, Ti 2p and W 4f XPS spectra for PCN-222(Zr/Ti/W) sample.

For the PCN-222(Zr/Ti/W) sample, the survey spectrum confirmed the presence of P and W elements along with Zr, Ti, O, N, and C. The high-resolution W 4f spectrum (**Figure 6.4d**) exhibits two peaks at 35.90 and 38.08 eV *BE*, assigned to W $4f_{7/2}$ and W $4f_{5/2}$, with a SOS of 2.18 eV, consistent with the W(VI) oxidation state of encapsulated $H_3PW_{12}O_{40}$ species.[210]

The Zr 3d region spectrum (**Figure 6.3d**) shows two peaks at 183.02 and 185.45 eV *BE*, corresponding to the Zr $3d_{5/2}$ and Zr $3d_{3/2}$ photoemission. These values are slightly higher than those recorded for PCN-222(Zr/Ti), likely due to the strong electron-withdrawing effect of the PTA moieties, which reduce the electron density around the Zr centres. Similarly, the Ti 2p peaks shifted to higher binding energies (459.17 and 464.71 eV), reflecting the same effect (Figure 2e). Finally, the O 1s spectrum displays two components at 532.55 eV (Zr−O) and 530.93 eV (Ti−O), while the N 1s peak remained almost unchanged at 400.60 eV (400.42 eV in PCN-222(Zr/Ti/W)), indicating preservation of the porphyrinic fragment. These electronic shifts observed by XPS correlate with PXRD observations. The increased intensity of the (111) and (201) reflections in PCN-222(Zr/Ti/W) (**Figure 6.3a**) is consistent with the higher electron density introduced by $[PW_{12}O_{40}]^{3-}$ encapsulation. Together, the data confirm strong interaction of the POM with the metal-oxo nodes, which perturbs the electronic structure while preserving the crystallinity of the framework.

Based on these characterisation results, from this chapter can be concluded that the proposed stepwise PSM approach, taking full advantage of the structural robustness, chemical tunability, and hierarchical porosity of PCN-222, enables dual-site functionalisation at both the metal nodes and the mesopores, thereby creating multicomponent hybrid MOF materials.

6.3.2. Characterisation of the photoelectrodes containing the active Ti/W-modified PCN-222

The deposition process of the Ti/W-modified PCN-222 materials onto FTO substrates as well as FTO covered with the charge-selective interfacial layers, FTO/TiO_2 and FTO/NiO_x, was optimised for the fabrication of reproducible photoelectrodes. SEM images of PCN-222(Zr) spin-coated film on FTO are shown in **Figure 6.5a** (top-view) and **Figure 6.5b** (cross-section), revealing a homogeneous layer with complete coverage of the FTO substrate, and an average thickness of 1.1 µm. Similar results were obtained for PCN-222(Zr/Ti) and PCN-222(Zr/Ti/W). EDX analysis confirms a uniform distribution of the elements comprising PCN-222 (i.e., O, C, and Zr), as well as the presence of Ti and W in the samples where these metals were incorporated into the PCN-222 particles (see **Figures 6.6**, **6.7** and **6.8**).

The intensity of this peak decreases upon incorporation of Ti, and further with Ti/W. It should be noted that the absolute peak intensities in these GAXRD patterns (thin films on FTO, at an incidence angle of 2°) are not directly comparable to the powder PXRD patterns in **Figure 6.3a**, because they are strongly influenced by the effective diffracting volume (film thickness/areal mass), preferred orientation, surface roughness, and the background/scattering contribution from the FTO substrate, particularly at low angles. Therefore, the lower (100) peak height observed for FTO/PCN-222(Zr/Ti/W) reflects the combined effects of thin-film measurement conditions and peak broadening/microstrain upon Ti/W modification, rather than a loss of the PCN-222 structure. The remaining peaks at 26.5°, 33.8°, 37.9°, and 51.7° are attributed to the FTO substrate (COD 1534785). In the case of FTO/TiO_2 and FTO/NiO_x, the layers were too thin to yield reliable XRD data or accurate thickness measurements; however, this did not affect the optical properties of the film.

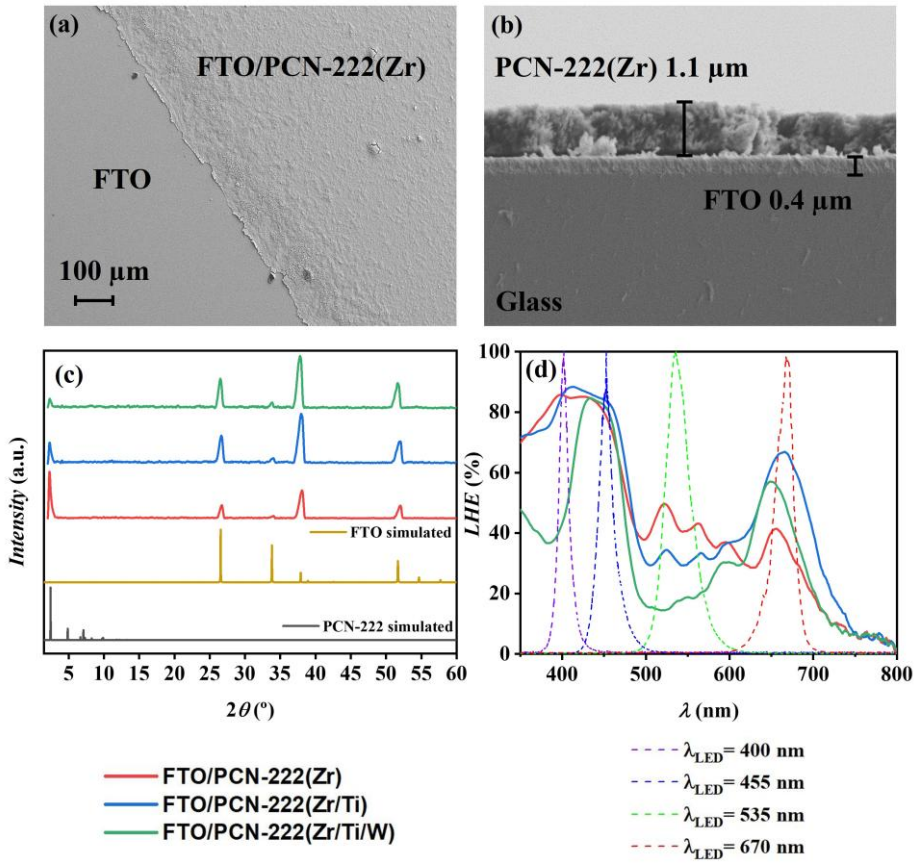

Figure 6.5. (a) SEM top-view image, and (b) cross-section image of FTO/PCN-222(Zr) photoelectrode. (c) GAXRD diffractograms of spin-coated PCN-222 on FTO and simulated patterns for comparison (FTO: COD 1534785 and PCN-222: CCDC 893545). (d) *LHE* spectra (lines) of FTO/PCN-222 and illumination spectra (dashed lines) of each LED used in photoelectrochemical measurements.

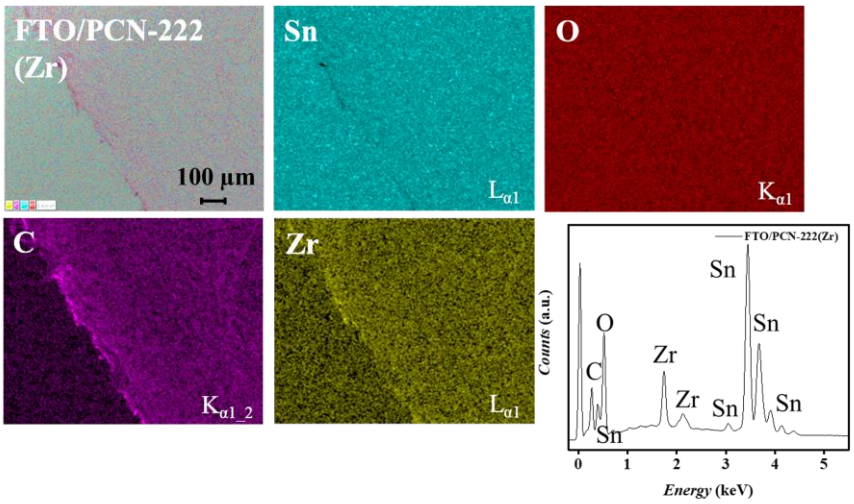

Figure 6.6. EDX mapping of PCN-222(Zr) layer deposited by spin coating on FTO.

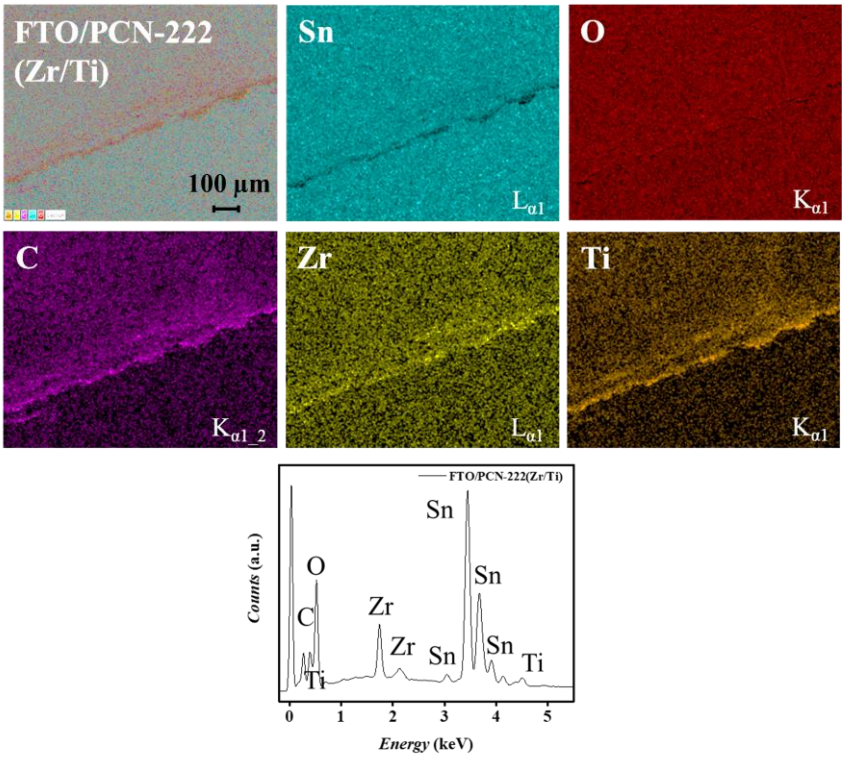

Figure 6.7. EDX mapping of PCN-222(Zr/Ti) layer deposited by spin coating on FTO.

Figures 6.9 and **6.10** reveal that Ti and Ni are the only detected elements, apart from O, in the FTO/TiO_2 and FTO/NiO_x thin layers, respectively, along with Sn from the FTO substrate. **Figure 6.5c** displays the GAXRD patterns of the PCN-222 electrode, showing the characteristic peak at 2θ−2.4° corresponding to the (100) plane of PCN-222 (CCDC 893545).

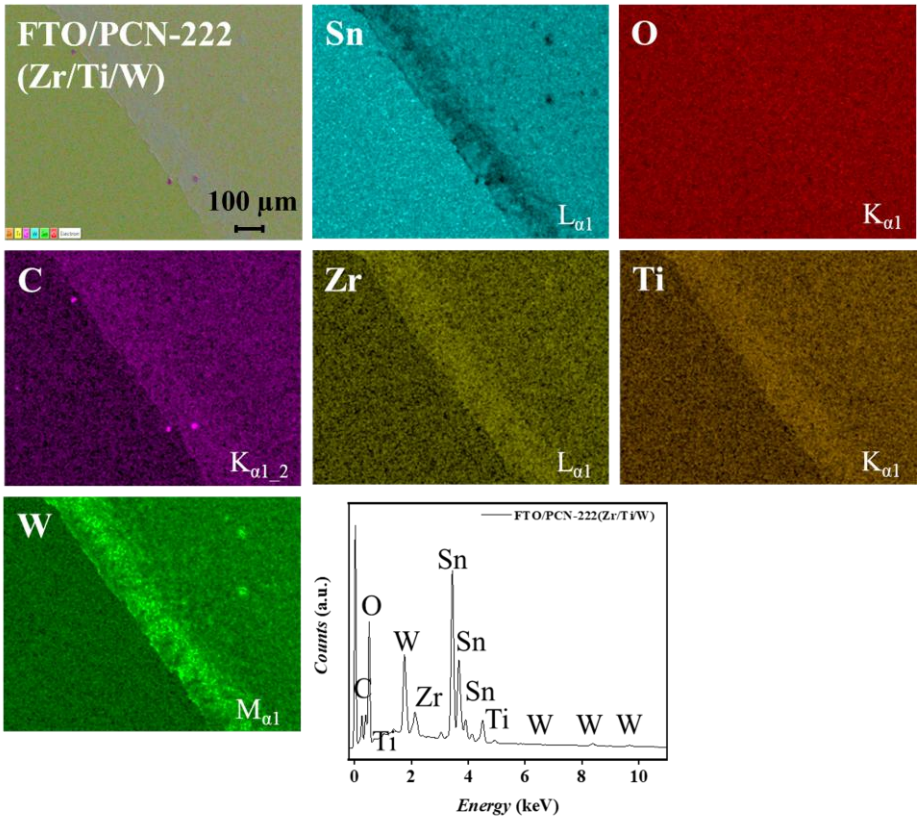

Figure 6.8. EDX mapping of PCN-222(Zr/Ti/W) layer deposited by spin coating on FTO.

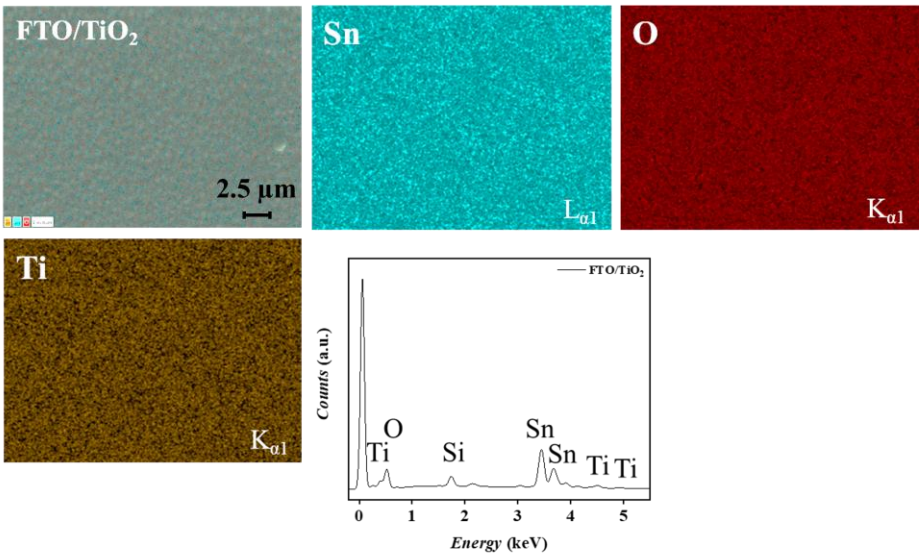

Figure 6.9. EDX mapping of the TiO_2 layer deposited by spray pyrolysis on FTO.

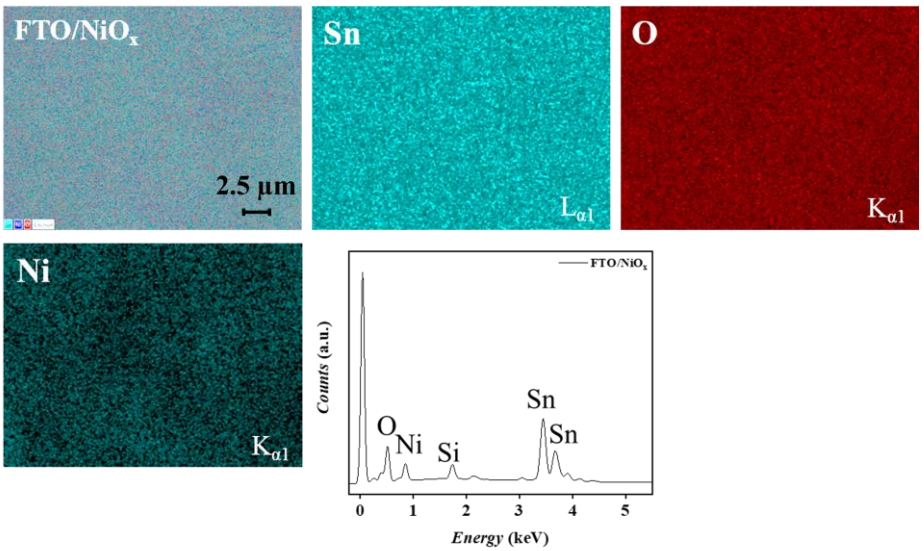

Figure 6.10. EDX mapping of the NiO_x layer deposited by spray pyrolysis on FTO.

Figure 6.11 shows the absorbance spectra of both dispersed and FTO-deposited PCN-222 samples. In dispersion (**Figure 6.11a**), the characteristic Soret band appears at 412 nm, along with the four Q-bands at 510, 545, 585, and 640 nm.[211,212] Upon deposition on FTO (**Figure 6.11b-e**), a red-shift is observed, 7 nm for PCN-222(Zr), 21 nm for PCN-222(Zr/Ti), and 34 nm for PCN-222(Zr/Ti/W), accompanied by a peak broadening, as evidenced by a 20 nm increase in the FWHM. These spectral changes can be attributed to several factors: first, the red-shift may arise from π-π interactions between neighbouring PCN-222 self-assembled during film formation, which leads to excitonic coupling and lowers the energy of the electronic transitions. Second, changes in the coordination environment of the PCN-222 once deposited or changes in the local dielectric environment at the PCN/FTO interface can influence the energy and width of the Soret band. Notably, this red-shift is significantly more pronounced for the Ti- and Ti/W-modified samples; however, the corresponding FWHM values remain comparable across all samples. This observation suggests that dielectric effects at the PCN/FTO interface, rather than particle assemblies, are the dominant factor governing the magnitude of the observed spectral shifts. In the case of the dispersed PCN-222(Zr/Ti/ W), two peaks are observed in the Soret band region; the first corresponds to the Soret absorption of the porphyrin units from well-dispersed MOF particles, while the second arises from the characteristic absorption of the encapsulated $H_3PW_{12}O_{40}$ species within the mesopores. Note that $H_3PW_{12}O_{40}$ in aqueous solution displays two absorption bands centred at 355 and 480 nm.[213]

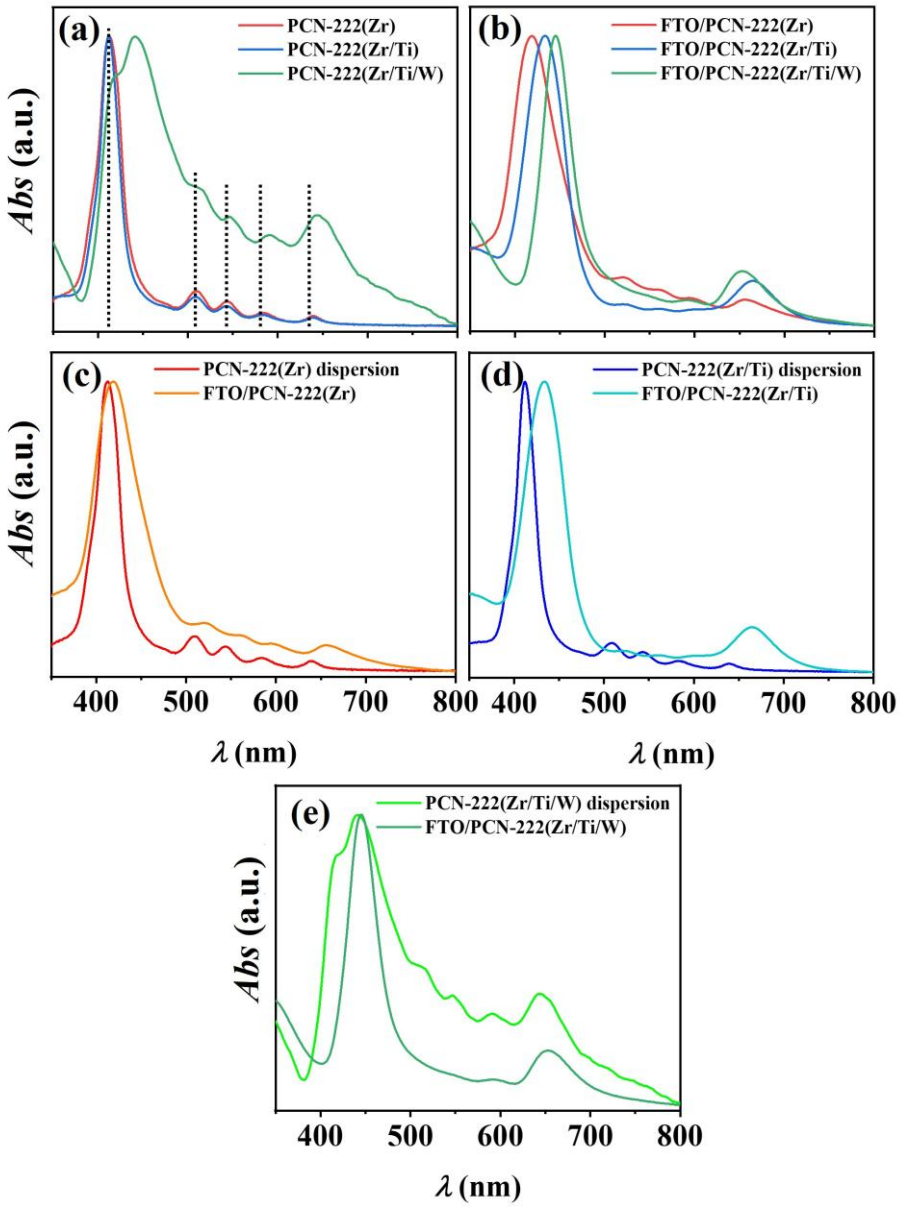

Figure 6.11. Absorbance spectra of (a) dispersed PCN-222 with a concentration of 0.03 mg mL^{-1} in methanol, and (b) FTO/PCN-222 electrode. Comparison between dispersed (light colour) and deposited on FTO (dark colour) of (c) PCN-222(Zr), (d) PCN-222(Zr/Ti), and (e) PCN-222(Zr/Ti/W).

As a result of the red-shift of the optical transitions observed for the Ti- and Ti/W-modified samples relative to pristine PCN-222(Zr), a slight reduction in the bandgap energy occurs. For PCN-222(Zr), (Zr/Ti), and (Zr/Ti/W), the estimated optical bandgaps in dispersion were 1.89, 1.89, and 1.82 eV, respectively. After film formation, independent of whether the indirect (**Figure 6.12**) or direct (**Figure 6.13**) Tauc plot analysis was applied, the estimated bandgap decreased to 1.75 eV for all photoelectrodes due to interparticle interactions, light scattering, and morphological effects in films. These values were estimated using both the Tauc plot analysis (from the absorbance spectra in **Figure 6.11**) and Kubelka-Munk analysis (from the DRS in **Figure 6.14**).[64,69,70,131,214,215] **Figure 6.5d** shows the *LHE* values (obtained from **Figure 6.14**) of the FTO/PCN-222 photoelectrodes and the illumination spectra of the monochromatic LEDs used for photoelectrochemical measurements.

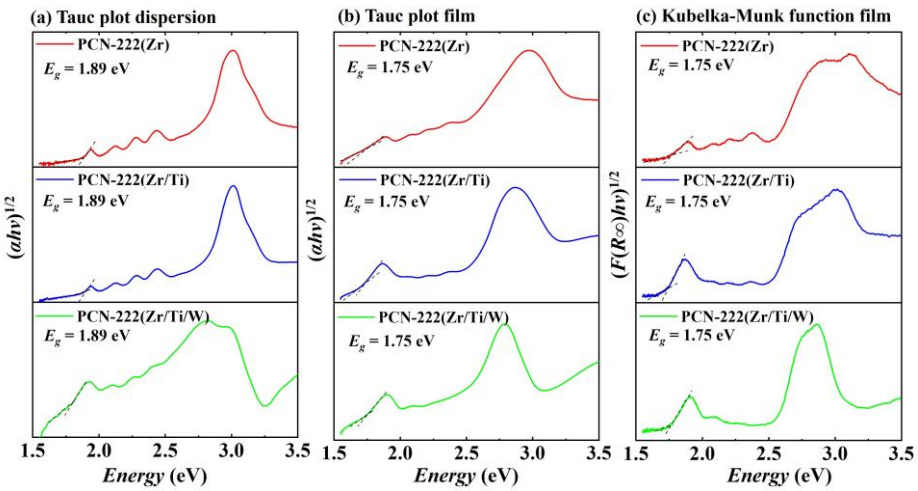

Figure 6.12. Indirect bandgap estimation of (a) dispersed PCN-222 with a concentration of 0.03 mg mL^{-1} in methanol and (b,c) spin-coated on FTO, using different estimation methods as (a,b) Tauc plot from absorbance spectroscopy and (c) Kubelka-Munk analysis from DRS.

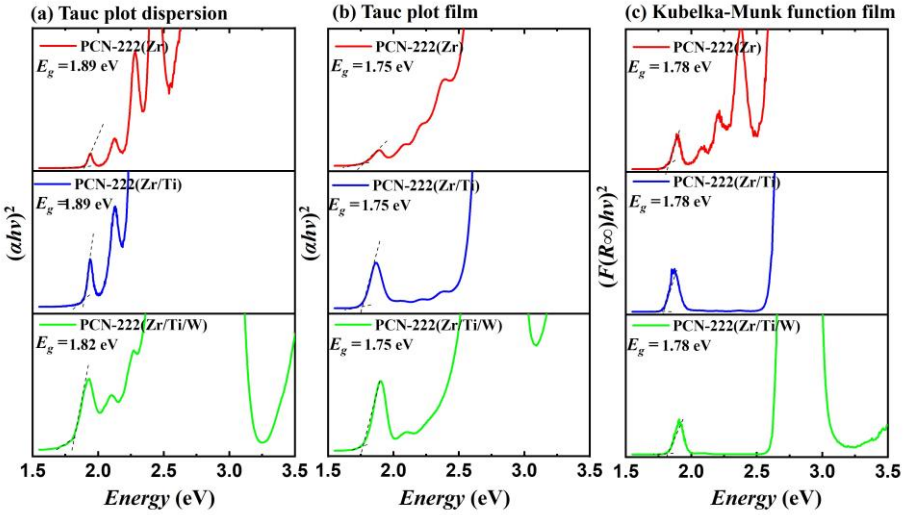

Figure 6.13. Direct bandgap estimation of (a) dispersed PCN-222 with a concentration of 0.03 mg mL^{-1} in methanol and (b,c) spin-coated on FTO, using different estimation methods as (a,b) Tauc plot from absorbance spectroscopy and (c) Kubelka-Munk analysis from DRS.

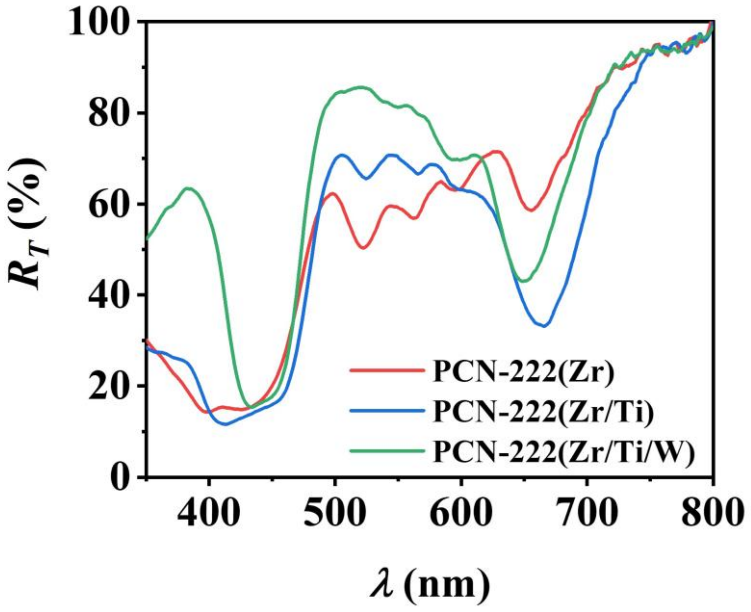

Figure 6.14. DRS of FTO/PCN-222(Zr), FTO/PCN-222(Zr/Ti), and FTO/PCN-222(Zr/Ti/W), electrodes measured using an integration sphere.

6.3.3. Tailoring the photoelectrochemical activity in PCN-222-based electrodes

Figure 6.15 illustrates LSV curves for FTO/PCN-222(Zr), FTO/PCN-222(Zr/Ti), and FTO/PCN-222(Zr/Ti/W) photoelectrodes compared with bare-FTO in 0.1 M acetate buffer as electrolyte at a scan rate of 20 mV s^{-1} with chopped front side illumination using different monochromatic LED wavelengths: UV (λ = 400 nm), blue (λ = 455 nm), green (λ = 535 nm) and red (λ = 670 nm) at the same photon flux of 1.6×10^{16} cm^{-2} s^{-1}.

The FTO/PCN-222(Zr) film acts as a photocathode, generating cathodic (negative) photocurrent with an onset potential of 0.45 V vs RHE. Under illumination, photogenerated electrons are transferred to the electrolyte, where two electrons participate in the reduction of water to hydrogen, as described by the water reduction half-reaction **Eq. (6.1a)**. The photocurrent measured in the external circuit corresponds to the flux of photoelectrons to the solution, and photoholes to the FTO contact; the circuit is closed by the corresponding oxidation reaction at the counter electrode.

Upon incorporation of Ti and Ti/W into the PCN-222(Zr) structure, the photoelectrochemical behaviour changes significantly. The FTO/PCN-222(Zr/Ti) and FTO/PCN-222(Zr/Ti/W) photoelectrodes exhibit anodic (positive) photocurrent generation as photoanodes with onset potential at 0.70 and 0.80 V vs RHE, respectively. In this case, photogenerated holes are transferred to the electrolyte, driving the oxidation of water ideally to produce molecular oxygen, as described by the water oxidation half-reaction in **Eq. (6.1b)**. In this case, the measured photocurrent corresponds to the net flux of photogenerated electrons to the FTO, and the flux of photoholes to the solution.[64]

$$2H_2O_{(l)} + 2e^- \rightarrow 2OH^-_{(aq)} + H_{2(g)} \quad (6.1a)$$

$$2H_2O_{(l)} + 4h^+ \rightarrow 4H^-_{(aq)} + O_{2(g)} \quad (6.1b)$$

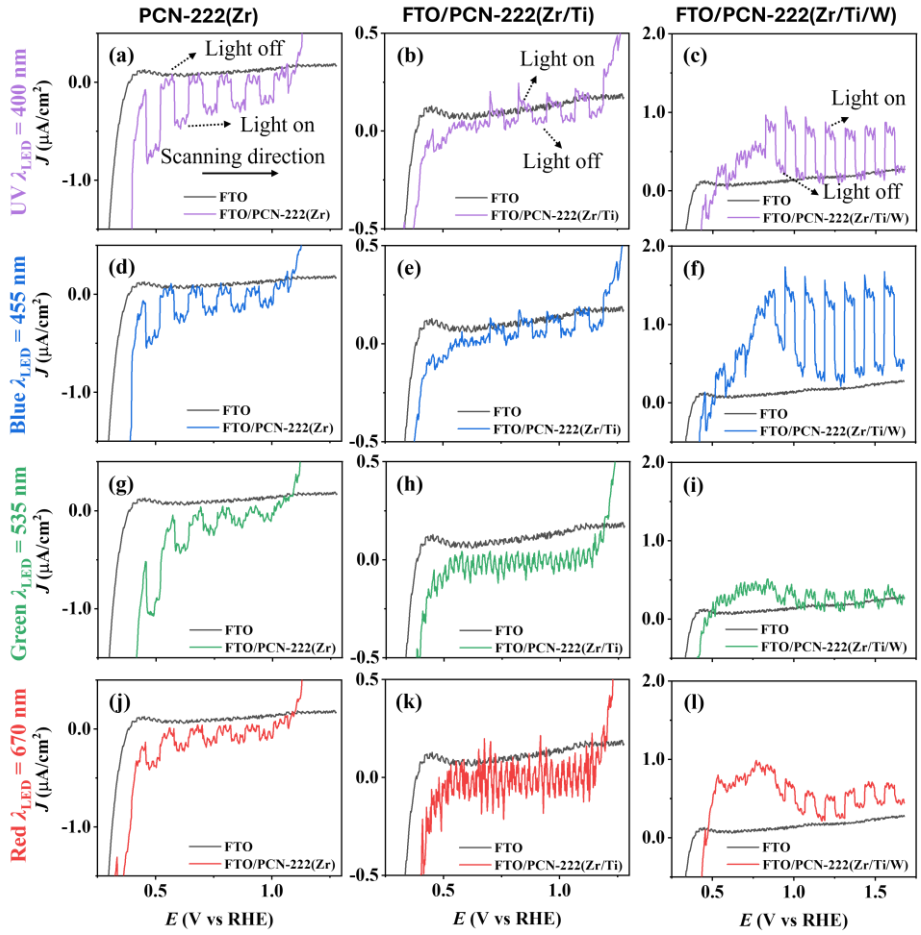

Figure 6.15. LSV curves with chopped front-side LED illumination under (a-c) λ_{LED} = 400 nm (UV), (d-f) λ_{LED} = 455 nm (blue), (g-i) λ_{LED} = 535 nm (green), and (j-l) λ_{LED} = 670 nm (red) at the same photon flux of 1.6×10^{16} cm^{-2} s^{-1} in 0.1 M acetate buffer as electrolyte with a scan rate of 20 mV s^{-1} for (a,d,g,j) FTO/PCN-222(Zr), (b,e,h,k) FTO/PCN-222(Zr/Ti), and (c,f,i,l) FTO/PCN-222(Zr/Ti/W). The scan direction was from negative to positive potentials, and the potentials where the light was switched on and switched off, respectively, are indicated.

All absorption bands of the measured porphyrin-based MOFs, including the Soret band (λ_{max} = 412 nm) and the four Q-bands (λ_{max} = 510-640 nm), are photoelectrochemically active, as evidenced by the photocurrent generation upon illumination at the respective wavelengths. The highest

photocurrent response is obtained under LED illumination corresponding to the Soret band, highlighting its dominant contribution to the overall photoresponse. In contrast, under green and red LED illumination, the FTO/PCN-222(Zr/Ti) electrode exhibits a noisy signal and negligible photocurrent, which may be attributed to limited charge separation efficiency at these wavelengths.

The FTO/PCN-222(Zr/Ti/W) photoelectrodes (**Figure 6.15c,f,i,l**) appear to behave similarly to WO_3 semiconductor electrodes, exhibiting a broad anodic feature centred at about 0.8 V vs RHE.[50,216] The reoxidation potential, however, is markedly more positive than reported for WO_3, where W^{4+} and W^{5+} centres were reoxidised at 0.18 and 0.38 V vs RHE, respectively. The positive shift, and the broader and less-defined peak, can be attributed to the unique properties of the modified PCN-222(Zr/Ti/W) composite material, resulting in an increase of the overpotential required to fully convert tungsten to W^{6+}. This may be related to changes in local coordination and electronic structure associated with Ti/W incorporation within PCN-222(Zr/Ti/W), which is supported by XPS.

Figure 6.16 presents the *J-E* curves of FTO electrodes covered with thin oxide layers deposited by spray pyrolysis. The FTO/TiO_2 electrodes were measured in a redox solution consisting of 0.01 M $K_4Fe(CN)_6$ (**Figure 6.16a**) and 0.01 M $K_3Fe(CN)_6$ (**Figure 6.16b**) in the 0.1 M acetate buffer. The FTO/NiO_x electrodes were evaluated in a non-aqueous solution of 0.01 M p-benzoquinone in propylene carbonate with 0.1 M $TBAPF_6$ as inert electrolyte (**Figure 6.16c**). The absence of redox peaks for both FTO/TiO_2 and FTO/NiO_x, thin films, in contrast to the results for bare FTO, indicates the compactness of both layers, preventing oxidation or reduction of the redox couple at uncovered FTO, thus confirming their role as compact blocking layers.

More importantly, beyond their blocking behaviour, these thin oxide interlayers also serve as selective contacts that enhance the charge separation efficiency and lower recombination losses. TiO_2 and NiO_x were selected due to their well-established use as charge-selective interfaces, particularly in hybrid perovskite solar cells, and their chemical stability and good compatibility with FTO substrates. TiO_2 is

an n-type semiconductor that may act as an electron transport layer, selectively extracting photogenerated electrons and blocking holes. Conversely, NiO_x is a p-type semiconductor that may function as a hole transport layer, enabling photogenerated hole extraction while suppressing electron transfer to FTO.[108–113]

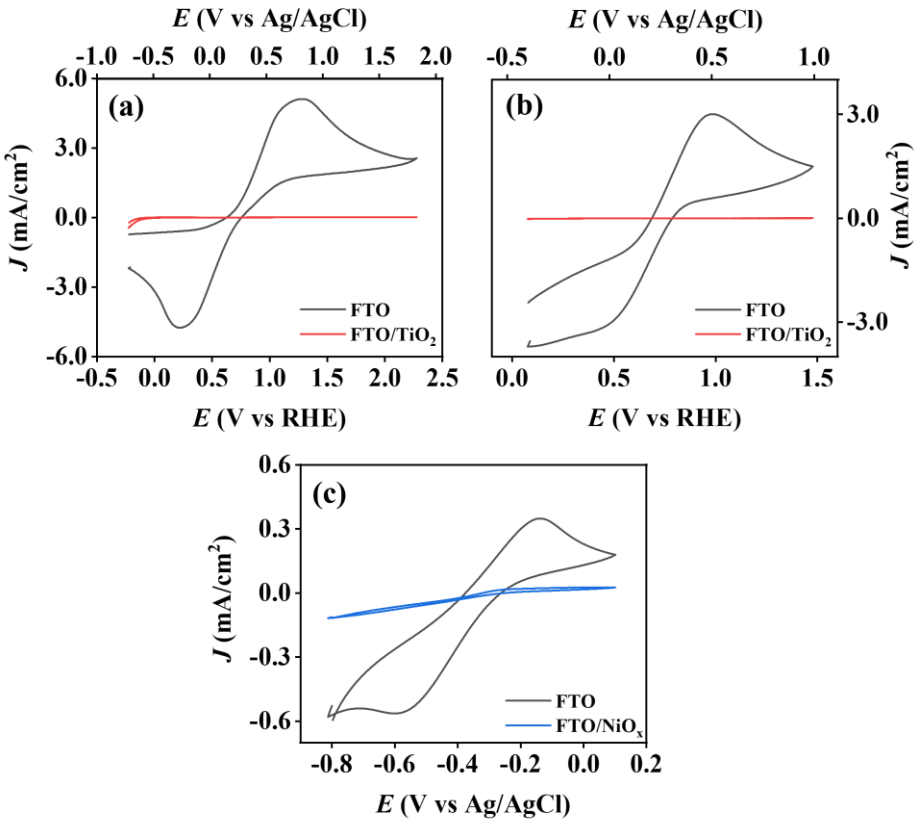

Figure 6.16. *J-E* curves under dark conditions at scan rate of 20 mV s^{-1} of thin films (a) FTO/TiO_2 with 0.1 M acetate buffer with 0.01 M $[Fe(CN)_6]^{4-}$ and (b) FTO/TiO_2 with 0.1 M acetate buffer with 0.01 M $[Fe(CN)_6]^{3-}$ both at pH = 4.5 as electrolytes, and (c) FTO/NiO_x with non-aqueous solution of 0.1 M propylene carbonate with 0.1 M $TBAPF_6$ with 0.01 M p-benzoquinone as electrolyte. Both films deposited by spray pyrolysis on FTO and compared with bare-FTO.

Figure 6.17 shows the LSV curves for PCN-222(Zr), PCN-222(Zr/Ti), and PCN-222(Zr/Ti/W) films spin-coated on FTO, FTO/TiO_2, and FTO/NiO_x, employed as electron- or hole-selective interlayers, respectively. Measurements were carried out in aqueous 0.1 M acetate buffer at a scan rate of 20 mV s^{-1} with chopped 1 sun AM1.5 G illumination. A significant increase in photocurrent is observed in all cases, which can be attributed to enhanced charge separation efficiency and suppressed recombination due to the interfacial charge selectivity provided by the ETL (TiO_2) and HTL (NiO_x) layers.[108–113]

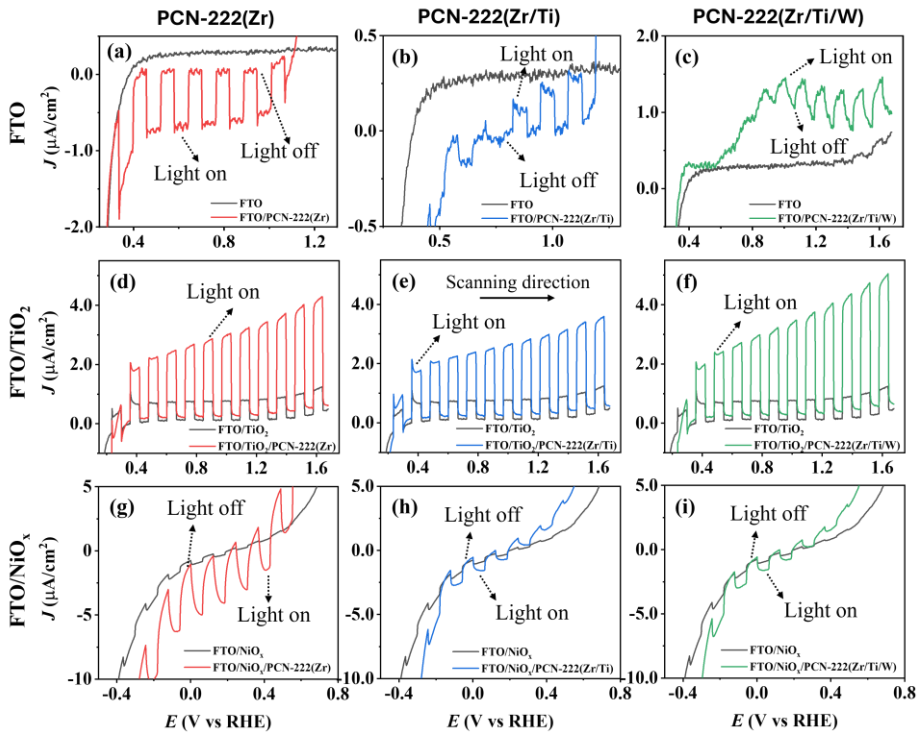

Figure 6.17. LSV curves with chopped front-side 1 sun AM 1.5G illumination in 0.1 M acetate buffer as electrolyte with a scan rate of 20 mV s^{-1} for (a,d,g) PCN-222(Zr), (b,e,h) PCN-222(Zr/Ti), and (c,f,i) PCN-222(Zr/Ti/W) spin-coated on (a,b,c) FTO, (d,e,f) FTO/TiO_2, and (g,h,i) FTO/NiO_x as different selective layers. The scan direction was from negative to positive potentials, and the potentials where the light was switched on and switched off, respectively, are indicated.

When TiO_2 is used as the ETL, photocurrent enhancements of 5-, 10- and 6-fold are observed for PCN-222(Zr), PCN-222(Zr/Ti) and PCN-222(Zr/Ti/W), respectively. In the case of NiO_x as the HTL, improvements of 7-, 4- and 3-fold are observed, respectively. Hence, the PCN-222 system demonstrates the interesting property of tunable photoelectrochemical polarity, acting either as a photoanode or a photocathode depending on the interfacial layer. This corresponds to either transferring electrons to FTO/TiO_2 or holes to FTO/NiO_x related to the charge-extraction selectivity of the interlayer.

Notably, encapsulation of $H_3PW_{12}O_{40}$ within the PCN-222(Zr/Ti) framework further enhances the photocurrent by a factor of 2-5 (depending on the wavelength of illumination) when deposited on FTO. When deposited on FTO/TiO_2 or FTO/NiO_x, this enhancement is more modest (about 1.5-fold). The enhancement may be attributed to the presence of W centres, which may alter interfacial charge dynamics by introducing surface states or contributing to electrocatalytic activity. The electrocatalytic activity corresponds to improved charge transfer kinetics to the solution resulting in reduced recombination losses.[217–219] Concomitantly, due to the effect of W-modification, the incorporation of the charge-selective interlayers results in a less-pronounced relative improvement.

Figure 6.18 schematically illustrates the characteristic shapes of the photocurrent transients shown in **Figure 6.17**, which are applicable to both photoanode and photocathode behaviours, but with opposite photocurrent polarities. The initial photocurrent spike observed upon illumination corresponds to the fast separation of photogenerated electron-hole pairs. For a photocathode, electrons are driven toward the electrolyte interface, while holes are collected in the external circuit. In the case of FTO/PCN-222(Zr), the photocurrent under illumination reaches a steady-state condition without significant losses, resulting in a rectangular-shaped transient. This shape is characteristic for the situation where recombination does not occur on the time scale of the measurement (see **Figure 6.18a**).

A similar transient behaviour is observed for FTO/TiO_2/PCN-222 at applied potentials more positive than 0.5 V vs RHE. However, in this

case, as the steady-state hole photocurrent increases with potential, the rectangular shape becomes deformed (see **Figure 6.18b**).

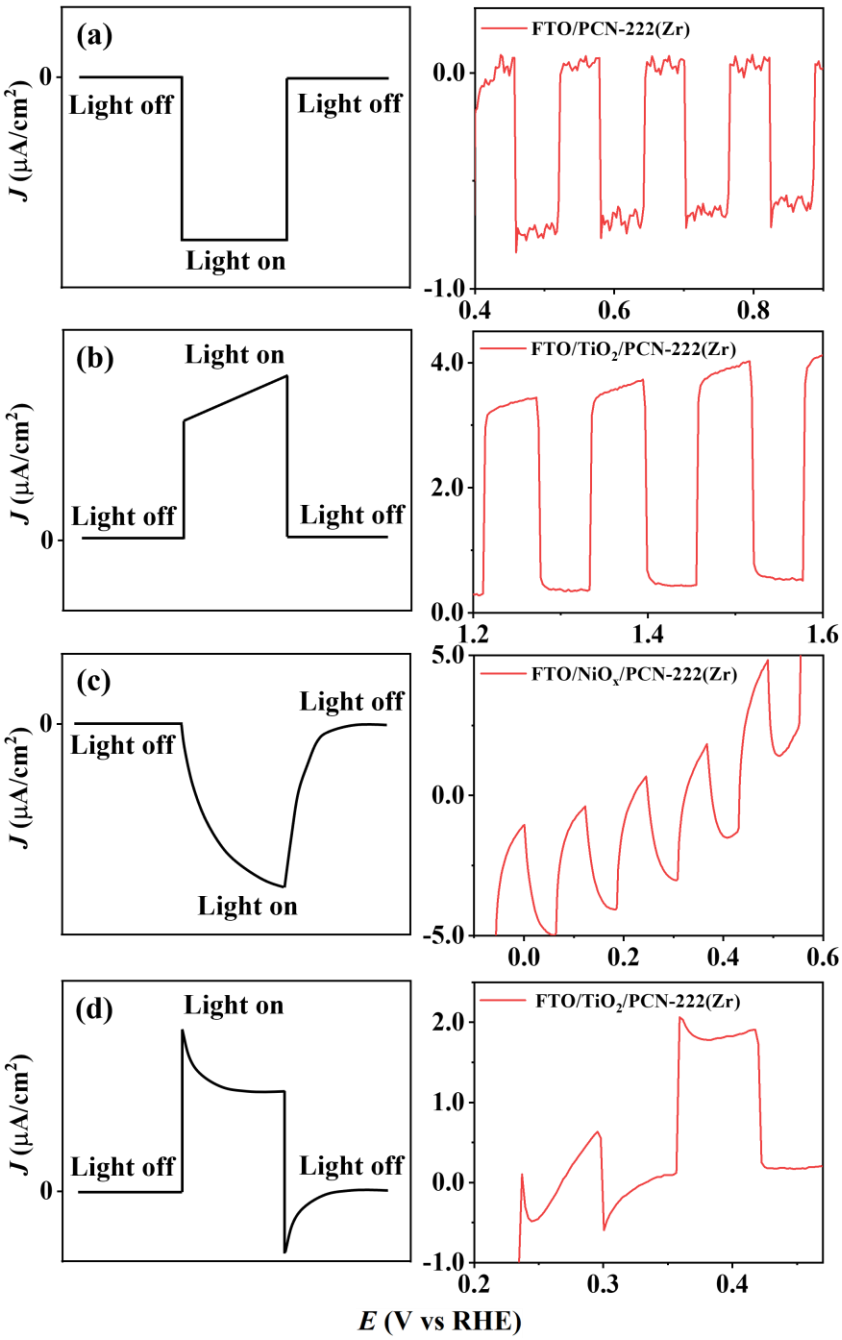

Figure 6.18. Schematic of the origin of transient photocurrent responses under chopped illumination, along with the representative experimental

behaviours. (a) Electron (for photocathode) photocurrent without surface recombination, (b) hole (for photoanode) photocurrent increasing the applied potential, (c) surface electron-hole recombination due to accumulation of hole (for photoanode) at the surface, inducing band edge unpinning, (d) surface trapped electron (for photocathode). This schematic is valid for both photoanode and photocathode behaviours with opposite photocurrent signals (positive photocurrent for photoanode and negative photocurrent for photocathode).

For FTO/NiO_x/PCN-222 and FTO/PCN-222(Zr/Ti/W), a slow increase in photocurrent is observed upon illumination until steady-state is reached, followed by a slow decay after switching off the light. This behaviour is indicative of electron trapping during illumination. When the light is switched on, photogenerated electrons first fill trap states within the material before a measurable current appears. The density of such traps, which often depends on the applied potential and light intensity, can be estimated from the "missing" current and the time required to reach steady-state conditions. Upon light off, the gradual release of trapped charges occurs as the Fermi level slowly returns to equilibrium (see **Figure 6.18c**).

For PCN-222(Zr/Ti), and especially for FTO/TiO_2/PCN-222 at low applied potential, a photocurrent peak and subsequent decay is observed before reaching steady-state conditions, followed by an overshoot of the same intensity but opposite sign upon switching the light off. This transient behaviour can be attributed to the accumulation of photogenerated holes at or near the electrolyte interface, which promotes interfacial recombination, resulting in a decrease in the net photocurrent. However, if the overshoot upon light-off is absent or differs in magnitude compared to the light-on, it may indicate that accumulation of holes at the interface alters the potential distribution at the electrolyte junction, as observed at more positive potentials (see **Figure 6.18d**).[96,99,101,136–140,187] Note that these current vs potential measurements are not suitable for the determination of recombination kinetics, which can be obtained from current vs time transients or EIS or IMPS.

6.3.4. Band alignment and mechanistic interpretation of photocurrent directionality

Figure 6.19 presents a schematic illustration of the charge carrier dynamics under illumination for the different electrode configurations, along with the corresponding band alignments relative to the water redox potentials. The diagrams illustrate the processes of photogeneration, charge separation, and transport of photogenerated electrons and holes at the electrode/electrolyte interface. In all configurations, PCN-222 serves as the principal photoactive layer, while TiO_2 and NiO_x, although capable of absorbing light in the UV region and generating photocurrent (as shown in **Figure 6.17d-i**), mainly function as ETL and HTL, respectively.

In the FTO/PCN-222 configuration (**Figure 6.19a**), photoinduced electron-hole pairs are generated within the PCN-222 material, with FTO acting as a non-selective contact. Depending on the specific PCN-material deposited on the FTO, the electrode behaves either as a photocathode (when using pristine PCN-222(Zr)) or as a photoanode (when using PCN-222(Zr/Ti) and PCN-222(Zr/Ti/W)), promoting water reduction or oxidation, respectively.

Applying the postsynthetic metal node exchange method reported here to produce Ti- and W-modified PCN-222(Zr) materials significantly alters the electronic and optical properties of the pristine framework. The incorporation of Ti leading to mixed Zr/Ti-oxo nodes, the formation of Ti-rich surface domains as discussed above, and the encapsulation of $H_3PW_{12}O_{40}$ within the mesopores all contribute to an increased local electron density within the framework. These modifications influence the band structure through changes in the coordination environment of the metal ions, as supported by XPS, and may introduce new surface states, thereby affecting the optical transitions and charge carrier dynamics. Optical characterisation reveals a bandgap narrowing upon Ti and W-modification, likely due to shifts in the conduction or valence band edge. Given that the band edge positions in PCN-222(Zr) are close to the redox potentials of water (**Figure 6.19a**), even slight shifts induced by Ti-/W-modification can alter the alignment with respect to the water oxidation or reduction levels. This alignment is critical in determining

the thermodynamic favourability of the redox processes and, consequently, the direction of photoinduced charge transfer.[180,219,220] Indeed, the negative shift of Zr 3d binding energy upon Ti incorporation, together with the positive shifts of both Zr and Ti signals after POM encapsulation (indicated by XPS), highlight the electronic perturbations at the metal-oxo clusters, which correlate with the polarity switching and photocurrent enhancement observed in the photoelectrochemical experiments. It should be noted that the band alignment is expected to depend on the surface chemistry of both the ETL/HTL and the PCN-222 materials, which in turn depends on the applied potential and illumination conditions; hence, at this point, it has not been able to determine band edge positions under working conditions, but rather focus on the charge extraction characteristics.

An additional explanation for the change in photocurrent polarity may involve the electrocatalytic role of the incorporated Ti and W species. Ti and W are known as photoanodic materials for water oxidation, and their presence at the PCN-222/electrolyte interface may generate catalytically active sites or induce surface states that lower the kinetic barrier for hole transfer. This change in the semiconductor/electrolyte interface selectivity ultimately determines the direction of the photocurrent flow. In the FTO/TiO_2/PCN-222 system (**Figure 6.19b**), the TiO_2 layer improves charge separation by efficiently extracting photogenerated electrons from PCN-222 and transporting them toward the FTO back contact. This reduces charge recombination and promotes hole transfer to the electrolyte, thereby favouring oxidation reactions. Notably, this strategy is effective even for PCN-222(Zr) which, when deposited directly on FTO, operates as a photocathode. Conversely, in the FTO/NiO_x/PCN-222 configuration (**Figure 6.19c**), the NiO_x layer selectively extracts photogenerated holes from the PCN-222 photoactive layer, transporting them toward the FTO substrate. This facilitates electron transfer from PCN-222 to the electrolyte, thus promoting reduction reactions. As a result, this architecture reinforces the photocathodic response not only for PCN-222(Zr) but also for PCN-222(Zr/Ti) and PCN-222(Zr/Ti/W), regardless of their intrinsic photoelectrochemical behaviour when deposited on bare FTO.

Hence, these results indicate that the overall photoelectrochemical behaviour is governed not by the doping density and dopant properties of the PCN-222 material, which behaves as an intrinsic semiconductor, but rather by the selectivity of the contact with the external circuit. While differences in oxidation and reduction kinetics at the electrolyte interface could, in principle, affect the direction of current flow, our findings clearly show that the nature of the contact at the FTO substrate plays a dominant role in determining the photoelectrochemical properties and the photoresponse polarity.

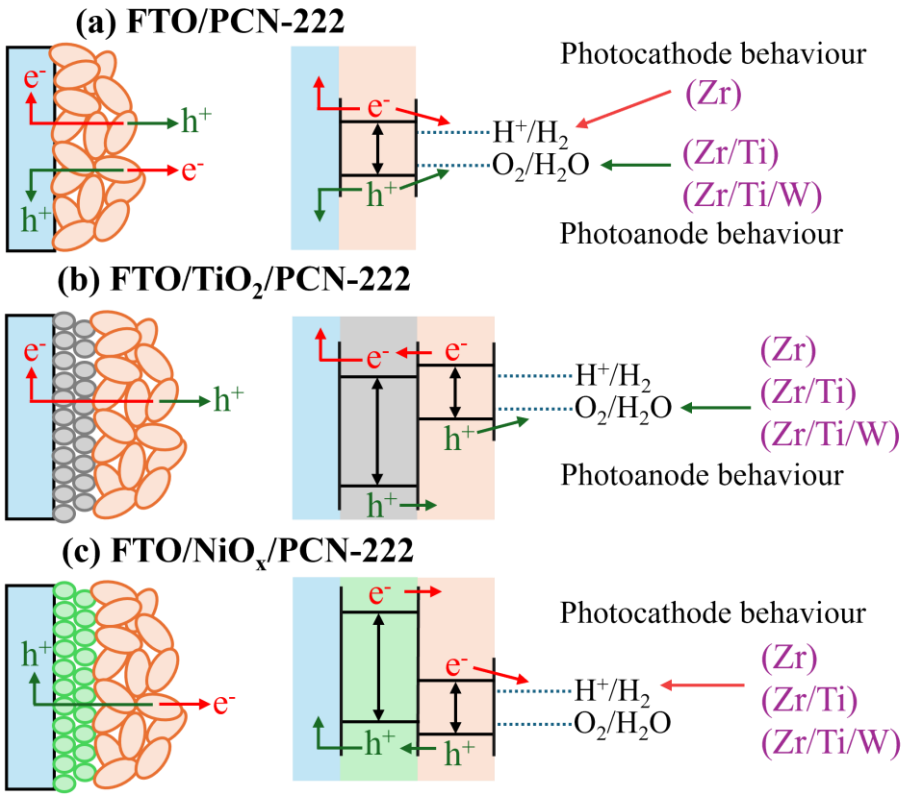

Figure 6.19. Schematic representation of charge carriers dynamics under illumination and in contact with an electrolyte for (a) FTO/PCN-222, (b) FTO/TiO_2/PCN-222 acting as a photoanode, and (c) FTO/NiO_x/PCN-222 acting as a photocathode. FTO acts as a non-selective contact, while TiO_2 and NiO_x function as ETL and HTL, respectively.

In addition, the incorporation of Ti- and W- within the PCN-222(Zr) structure may further modulate this behaviour through their potential electrocatalytic activity. In particular, the phosphotungstate material incorporated in the mesopores exhibits redox reactions involving W^{4+} and/or W^{5+} centres, and upon applying a more positive potential, the reoxidised POM improves hole extraction, thus imposing selectivity at the electrolyte interface and reducing the impact of the oxide interlayer. The ability to switch the photoelectrode response from photocathodic to photoanodic (or vice versa) enables the same MOF-based materials to be selectively operated under either reductive or oxidative conditions. This polarity control is particularly relevant for photoelectrochemical systems where the target reaction depends on the dominant charge carrier, allowing the electrode function to be adapted through interfacial engineering rather than material replacement.

6.4. Conclusions

This chapter demonstrates a stepwise strategy to modulate the photoelectrochemical properties of the mesoporous PCN-222 through a combination of metal-node substitution and pore encapsulation, followed by integration into functional photoelectrodes with charge-selective extraction layers. Ti was successfully incorporated into the framework via postsynthetic metal node exchange, preserving the crystallinity and nanorod morphology, while introducing lattice distortion and band structure modification. Subsequent encapsulation of the polyoxometalate $H_3PW_{12}O_{40}$ within the PCN mesopores further altered the optical properties and enhanced photocurrent generation. These chemical modifications collectively shifted the photoelectrode behaviour from photocathodic to photoanodic under visible light illumination, attributed to changes in band edge positions and electrocatalytic contributions. Moreover, the directionality of the photocurrent was found to be strongly dependent on the nature of the interfacial layer (TiO_2 or NiO_x), overriding the intrinsic semiconductor character of the PCN-222 and enabling tunable photoelectrode architectures. This polarity control highlights the potential of PCN-222-based electrodes for versatile photoelectrochemical configurations,

where charge directionality can be tailored to match specific reaction environments. These findings provide valuable insights into the design of multicomponent MOF-based systems with tailored optoelectronic properties and open new avenues for their application in photoelectrochemical devices.

This chapter has shown that chemical modification and charge selective contacts can be used to control charge extraction and photocurrent directionality in a hybrid MOF-based system. The following chapter moves to a more conventional metal oxide photoanode, WO_3, to examine a complementary aspect of charge carrier dynamics: the influence of morphology on charge transport, recombination, and surface reactivity. By comparing WO_3 nanoparticles and nanofibres under photocatalytic and photoelectrochemical conditions, the next chapter evaluates whether the increased surface area typically associated with nanostructuring is sufficient to improve water oxidation performance, or whether it also introduces additional limitations for charge collection.

Chapter 7

Comparing the performance of WO_3 nanoparticles and nanofibres: photocatalytic dye degradation versus photoelectrochemical water oxidation

Summary

Nanostructured WO_3 is a widely studied, attractive material for photocatalysis applications, ranging from degradation of organic contaminants to water photooxidation, related to its relatively small bandgap, good stability, and adequate charge transport and charge transfer efficiencies. In catalysis, a large surface-to-volume ratio generally improves activity; however, this is not always the case for photoelectrochemical systems. This chapter compares the photocatalytic and photoelectrochemical performance of commercial WO_3 nanoparticles with that of WO_3 nanofibres prepared by centrifugal spinning. The photocatalytic dye degradation kinetics are faster for the

nanofibres, related to their larger specific surface area. On the other hand, the photoelectrochemical performance is essentially the same for both materials. This fundamental difference in performance is demonstrated to be due to the influence of trap-limited electron transport on the collection efficiency of photoelectrons, required for the observation of photocurrent in the external circuit, whereas photocatalysis is more surface-driven. The contents of this chapter have been published in Electrochimica Acta.[50]

7.1. Introduction

Stable semiconductor nanomaterials consisting of abundant and inexpensive elements form an attractive family of materials suitable for photocatalysis-based technologies, ranging from remediation of contaminated water to the generation of green hydrogen from water as a clean fuel and feedstock for the chemical industry.[45,221–223] Metal oxides are particularly interesting for these applications owing to their inherent stability to further oxidation, although a disadvantage is that the band gap is generally too large to absorb a significant part of the solar spectrum. WO_3 is a widely studied material for photoelectrochemical applications due to its relatively low band gap of 2.5–2.8 eV, allowing the absorption of up to 12 % of the solar spectrum, a decent hole diffusion length of around 150 nm, and electron mobility of about 12 $cm^2\ V^{-1}\ s^{-1}$, which is better than for many other materials.[221–223] Several morphologies such as nanorods[45], nanopyramids[46], nanoflakes[224], and nanoflowers[47] have been examined for a variety of photo-processes. Other improvement strategies have also been explored, such as the creation of oxygen vacancies[225–228], dopant insertion[229,230], heterojunctions with several semiconductors[231–237], WO_3-based compounds[195,238–241], or the use of rapid thermal annealing to improve crystallinity.[242–244] WO_3 may also be an interesting alternative as an electron transporting layer in the third-generation solar cell applications.[245] In addition, several reports focusing on the stability and electronic characteristics of WO_3 in dye-sensitized[246] and perovskite solar cells[247] have recently been published. Although much progress has

been made in the development of this material, the maximum theoretical performance has not yet been achieved.

The suitability of a nanomaterial or system design depends on the process, for example, for the photocatalytic degradation of organic contaminants, such as dyes, a dispersion of nanoparticles can be used. In this case, the photogenerated electron-hole pair is separated within the particle, and the charge carriers are transferred to the solution (at suitable electrocatalysts, if necessary). The reaction with oxygen, hydroxyl groups and water produce reactive oxygen species (ROS), such as superoxide radical anions ($\cdot O_2^-$) and hydroxyl radicals (·OH), which are responsible for the degradation of pollutants in water.[245,246] On the other hand, for systems where half-reactions are used in an electrochemical cell, a film deposited on a conducting substrate is the preferred design. The electron-hole pair is separated within the film, with one carrier transferred to the solution and the other collected in the external circuit and directed to a counter electrode, where it reacts, and closes the electrical circuit. Depending on the applied potential, the WO_3/electrolyte interface is characterised by a range of surface states with different electronic properties, generally related to W^{4+} and W^{5+} surface states.[216] These states may significantly influence not just the charge transfer but also transport properties.

The morphology, particle size, and specific surface area of nanomaterials are important parameters in heterogeneous catalysis to optimise the catalytic activity.[248,249] The challenge is to understand how these factors affect the performance. In this study, two WO_3 materials of different morphology are compared in both photocatalytic dye degradation and photoelectrochemical oxidation of water: (i) nanostructured, mesoporous WO_3 fibres synthesised by centrifugal spinning[250]; and (ii) commercial WO_3 nanopowder. For this purpose, an in-depth IMPS study is presented to elucidate the complex charge dynamics processes involved in both materials and explain the differences in performance.

7.2. Experimental methods

7.2.1. Photoelectrode fabrication

WO_3 nanofibres were prepared by centrifugal spinning, according to the previously published work.[250] In brief, the solution of W precursor and carrying polymer was spun and the fibres were annealed to obtain crystalline WO_3 fibres. WO_3 nanopowder (550086, Sigma-Aldrich, particle size below 100 nm), was finely ground in an agate mortar to ensure particle homogeneity and 0.1 g was dispersed in 10 mL isopropanol in an ultrasonic bath for 20 min. Subsequently, 1 mL terpineol (86480, Sigma-Aldrich) was added and the dispersion was magnetically stirred for 20 min. On the other hand, 0.03 g ethyl cellulose (247499, Sigma-Aldrich) was dissolved in 10 mL isopropanol and magnetically stirred at 70 ºC for 1 h. Finally, the WO_3 dispersion and the ethyl cellulose solution were mixed, magnetically stirred, and sonicated for 20 min. The excess solvent was removed in a rotary evaporator until the desired density and viscosity of the paste were reached. The procedure was repeated independently for WO_3 nanofibres, however, without the sonication processes in order to avoid mechanical damage to the nanofibres.

FTO substrates were sequentially cleaned and sonicated for 20 min with Hellmanex III®, de-ionised water, alcohol, and lastly, isopropanol. A thin, compact WO_3 layer was sputter-deposited onto FTO-coated conductive glass substrates (SnO_2:F, TEC 15 $\Omega\ sq^{-1}$) using a 2-inch target prepared from 99 % pure WO_3 powder (95410, Sigma-Aldrich), and a power of 40 W and argon flow rate of 20 sccm. The substrates were sintered at 500 ºC for 2 h. The film thickness was determined to be 54 nm using mechanical profilometry.

The FTO/compact-WO_3/mesoporous-WO_3 photoelectrodes were prepared by screen printing, depositing successive layers using a screen with a mesh opening of 46 μm, nominal thread diameter of 55 μm, open area of about 17.2 %, mesh thickness of 97 μm, theoretical ink volume of about 16.7 $cm^3\ m^{-2}$ and deposition area of 1 cm^2. The substrate was placed on a hot plate at 100 ºC for 10 min between deposition steps. After finishing the desired number of deposition steps, the WO_3 films were

sintered at 550 ºC for 1 h using a 3 h temperature ramp. From here on, this chapter will distinguish between the nanoparticle and nanofibre photoelectrodes, keeping in mind that both were fabricated the same way with the compact layer, unless otherwise mentioned.

7.2.2. Structural and optical characterisation

XRD analysis with Bruker D8 Discover diffractometer at 50 kV and 1 mA for Cu $K\alpha$ (λ = 1.5418 Å) and K = 0.89 with a collimator of 2 mm and micro slit of 1 mm, in the 2θ range 20 º to 65 º with an increment step of 0.015 º per 0.05 s was used to determine the crystalline structure for the WO_3 commercial and WO_3 fibre films, furthermore, GAXRD was used to determine the crystalline structure in the WO_3 compact layer thin film fixing the incidence angle at 2º with an increment step of 0.015º per 0.75 s. The crystallite size was measured for all peaks using the Scherrer equation.

The surface morphology and particle size were evaluated through a FE-SEM model Zeiss Gemini300, and EDX was used to examine the atomic weight ratio of the samples with an accelerating voltage of 15 kV.

DRS was employed to determine the optical properties of the films, using a UV/Vis/NIR spectrophotometer model FSL1000-DD-STM Edinburgh Instruments equipped with an integrating sphere using a Xe lamp in the range of 300 nm to 800 nm, with a dwell time of 0.5 s, step of 1 nm, bandwidth excitation of 3 nm and bandwidth emission of 0.05 nm.

7.2.3. Photocatalytic measurements

The photocatalytic activities of both types of WO_3 nanomaterial used in this work were examined using photocatalytic decomposition of methylene blue (MB; initial concentration = 1×10^{-5} M). Before the measurements, materials were sonicated for 5 min at 50% power at 37 kHz (FB11203, Fisherbrand) in deionised water, and subsequently separated by centrifugation (Optima MAX-XP, Beckman Coulter) at 5000 g for 5 min at room temperature using a fixed-angle rotor (MLA-150). Materials were immersed in the MB solution (30 mL) for 1 h under constant stirring to achieve the dye adsorption-desorption equilibrium. Afterwards, the materials were separated from the MB solution by

centrifugation at 5000 g for 5 min. Subsequently, 80 mg of material was irradiated by an LED-based UV lamp (λ = 365 nm ± 5 nm) and Vis light (Vis lamp; λ = 400–410 nm) and the absorbance of the MB solution was periodically measured (6 × 10 min and 2 × 30 min steps, respectively) by a UV-Vis spectrophotometer (S-200, Boeco) at a wavelength of 670 nm to monitor the decomposition rate. Repeatedly, prior to absorbance measurements, 4 mL aliquots of MB solution were taken from the reaction solution and the sample was separated from the MB solution by centrifugation at 5000 g for 5 min at 25 ºC. The measured solutions were always returned to the base solution for further experiments.

7.2.4. Photoelectrochemical measurements

Photoelectrochemical measurements were carried out using a three-electrode electrochemical cell with Pt wire as a counter electrode and Ag/AgCl (3 M KCl) as a reference, with 1 M $HClO_4$ (pH ≈ 0) as an electrolyte solution, using an Autolab system (PGSTAT302N). A Xe arc lamp (Thermo Oriel 69921 500 W) was used as light source and was calibrated at 100 mW cm^{-2} with Si-photodiode (Gentec-eo Turner 280857). Both UV (λ = 370 nm) and blue (λ = 435 nm) high-power LEDs (see **Figure 7.1** for the spectra) were used as photon source for the IMPS measurements and were calibrated with a Si photodiode (Hamamatsu S12698-2). The applied potential was converted to the potential versus RHE at pH = 0.

The IMPS measurements were performed using a sinusoidal intensity modulation on top of a bias light intensity in the frequency range from 10^5 Hz to 10^{-2} Hz. The modulation amplitude was about 10 % of the base light intensity, and the response linearity was tested and confirmed through Lissajous plots. Normalisation was carried out by determining the number density of incident photons and calculating the corresponding maximum photocurrent assuming that each incident photon generates one electron-hole pair; hence, *EQE* is obtained as a function of frequency.

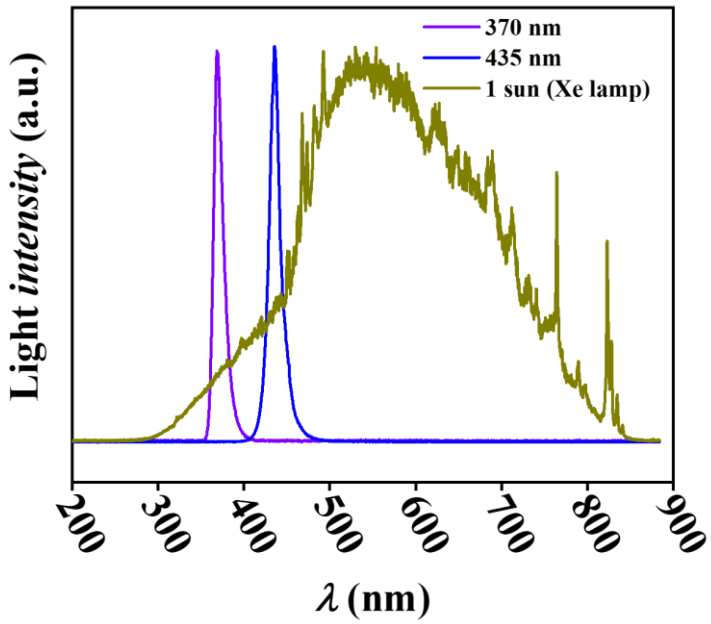

Figure 7.1. Emission spectra of the 370 nm and 435 nm LEDs and the Xe arc lamp.

7.3. Results and discussion

7.3.1. Structure, morphology, and optical properties

Screen printing provides a convenient and reproducible film deposition method, and the film thickness can be controlled by changing the number of printed layers. The presence of the sputter-deposited WO_3 underlayer resulted to be essential to achieve well-adhered, homogeneous films. **Figure 7.2** in the Supporting Information shows photos of the films using 5 printed layers of each material. **Figure 7.3a** shows the XRD patterns for the WO_3 nanoparticles, the synthesised WO_3 nanofibres and the sputter-deposited WO_3 compact layer. All diffractograms correspond to monoclinic WO_3 (γ-WO_3), nanoparticles and nanofibres correspond to COD 2311041 with the space group P1 21/c 1 and compact layer corresponds to COD 2106382 with different space group P1 21/n 1. The

diffraction peaks at approximately 38º and 52º correspond to underlying FTO substrate. These peaks are less intense for the nanofibres and nanoparticles electrodes compared to the compact WO_3 layer, since both architectures already include the compact layer and additionally present thicker WO_3 coatings. The crystallite size was determined using the Scherrer equation (measured for all peaks) and found to be about 39 ± 9 nm for the nanofibres and 53 ± 16 nm for the nanoparticles, respectively. The thin compact layer (54 nm) is also nanocrystalline, the wide diffraction peaks evidence the smaller particle size due to the preparation method (sputtering) with an estimated crystallite size of 10 nm.

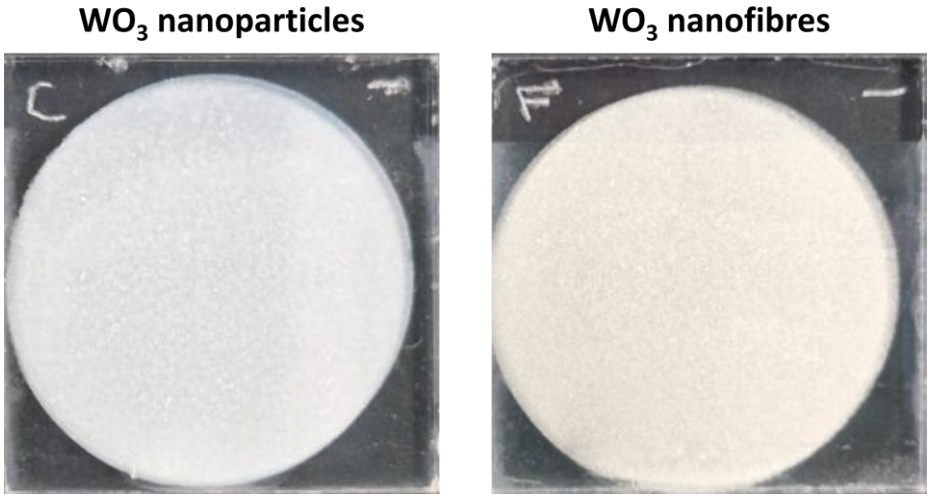

Figure 7.2. Photographs of screen-printed WO_3 nanoparticulate and nanofibre photoelectrodes (5 deposition steps).

The optical properties are shown in **Figure 7.3b**, which shows the *LHE*, obtained from the DRS measurements versus wavelength in the range from 325 to 475 nm. Kubelka-Munk analysis results in an indirect bandgap energy of 2.6 eV for both WO_3 nanomaterials and 2.8 eV for the WO_3 compact layer, this variation is related to the higher density of defects due to the smaller particle size (see **Figure 7.4**).[251,252] The *LHE* is similar for both materials, indicating that comparative measurements can be performed. IMPS measurements were carried out at 370 nm, a wavelength close to the maximum *LHE* peak of WO_3 and at 435 nm where the *LHE* values for the nanostructured WO_3 are similar, while the

compact layer does not significantly absorb. At wavelengths larger than 475 nm, the apparent slight increase in the *LHE* values for the nanostructured films does not represent absorption, but is rather due to scattering. The very thin compact layer on the other hand shows negligible scattering.

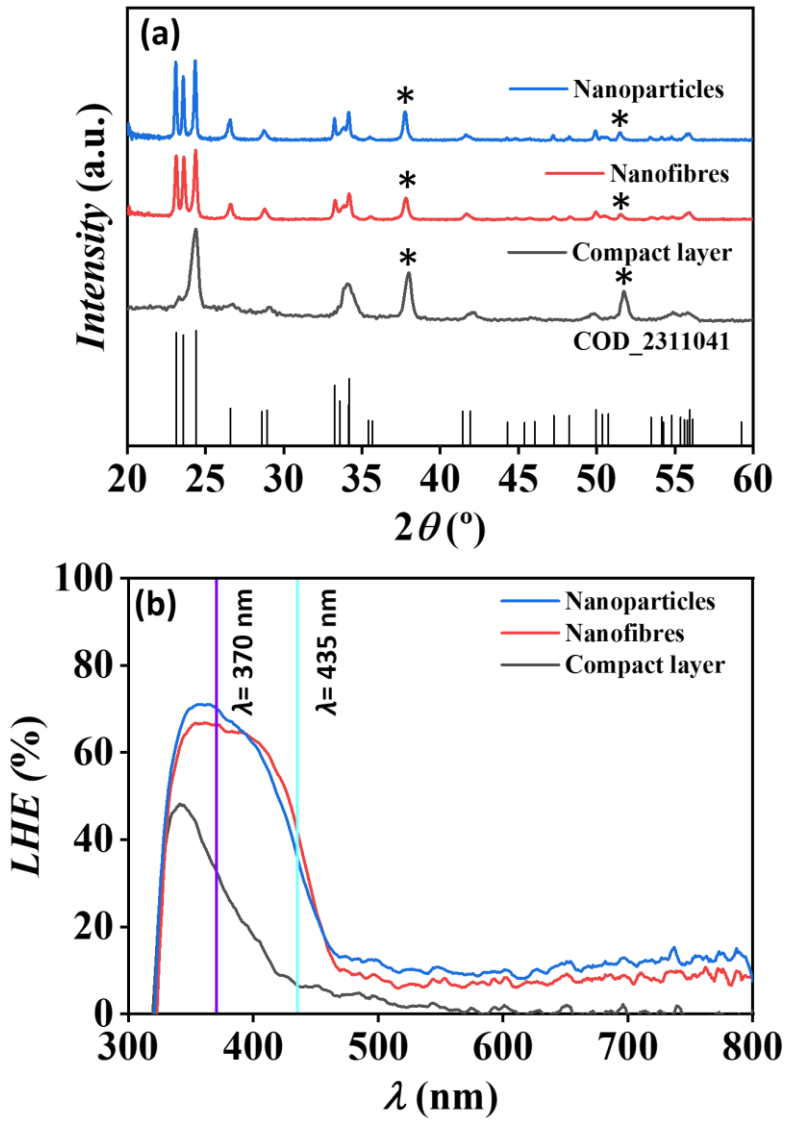

Figure 7.3. (a) XRD patterns of WO_3 films deposited by screen printing onto a compact WO_3 thin film (prepared by sputter deposition) on FTO;

the peaks at 38º and 52º correspond to FTO and are indicated by an asterisk; (b) *LHE* spectra obtained from DRS.

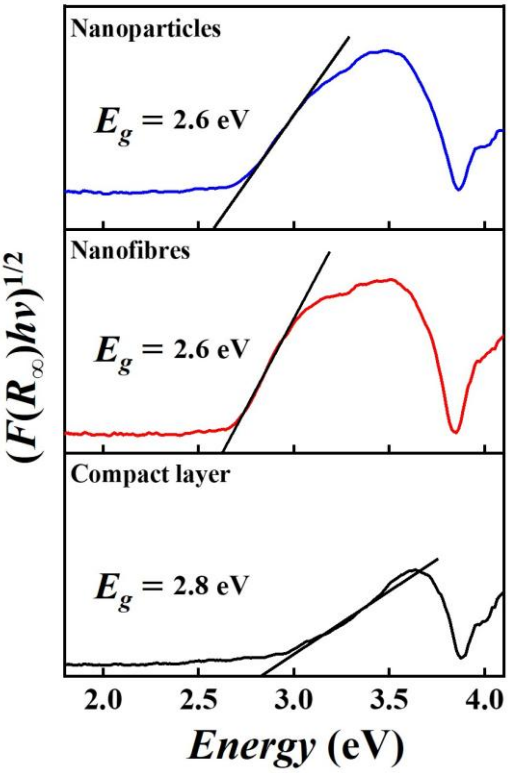

Figure 7.4. Kubelka-Munk analysis of the DRS measurements of WO_3 nanoparticles and nanofibres deposited onto the WO_3 compact layer on FTO, indicating the indirect bandgap values.

The morphology of screen-printed films was examined using SEM, and **Figure 7.5** shows the corresponding images at different magnifications obtained for nanoparticulate (**Figure 7.5a-c**) and nanofibre (**Figure 7.5d-f)** films. The nanoparticulate film shows a homogeneous distribution of particles with an average size of about 84 ± 35 nm, which is somewhat larger than the crystallite size from XRD, indicating that small agglomerates are present. The fibres are also distributed homogeneously on the surface, with the nanoparticles that make up the

nanofibres distinctively smaller at around 57 ± 37 nm. The fibres are partially hollow with a highly porous interior.

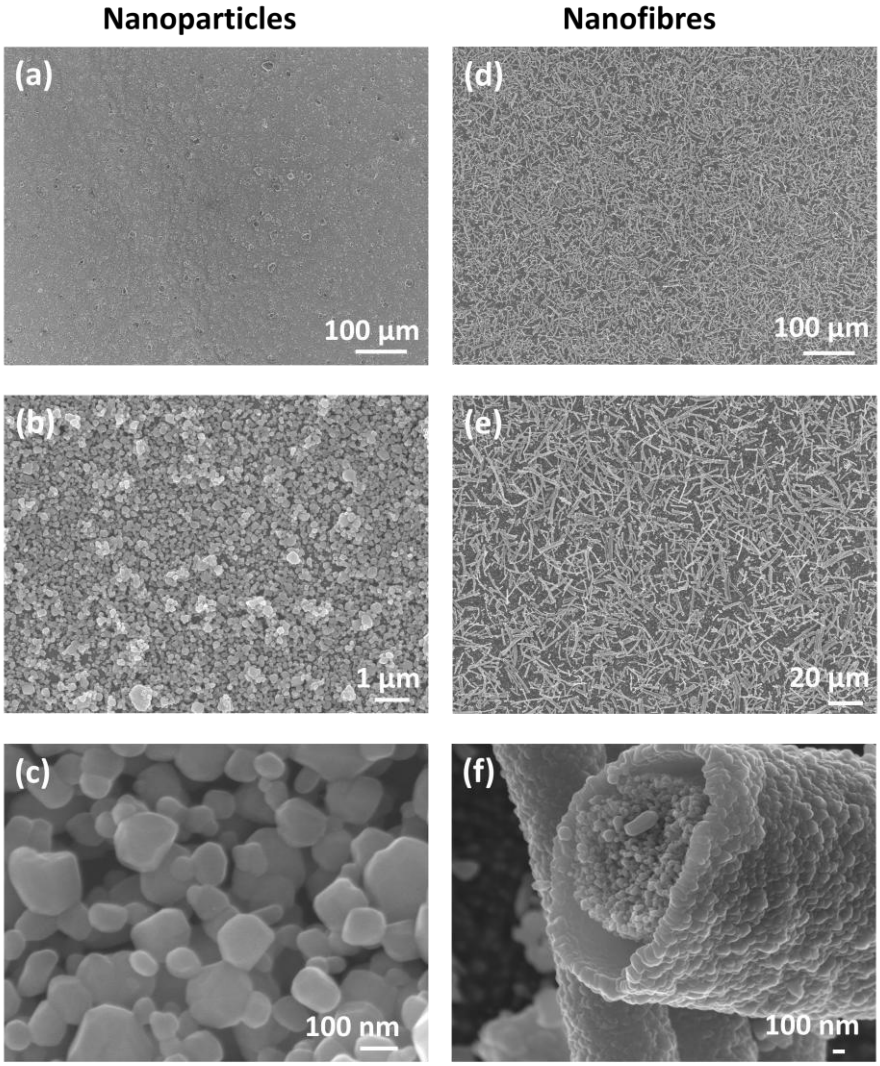

Figure 7.5. SEM images of: (a–c) screen-printed WO_3 nanoparticulate film; (d–f) screen-printed WO_3 nanofibre film. Both films were deposited onto a compact WO_3 thin film prepared by sputter deposition on FTO.

EDX analysis reveals that the atomic weight ratios of tungsten (60%) compared to oxygen (20%) and tin (20%) are the same for the nanoparticulate and the nanofibre samples (**Figures 7.6, 7.7** and **7.8**).

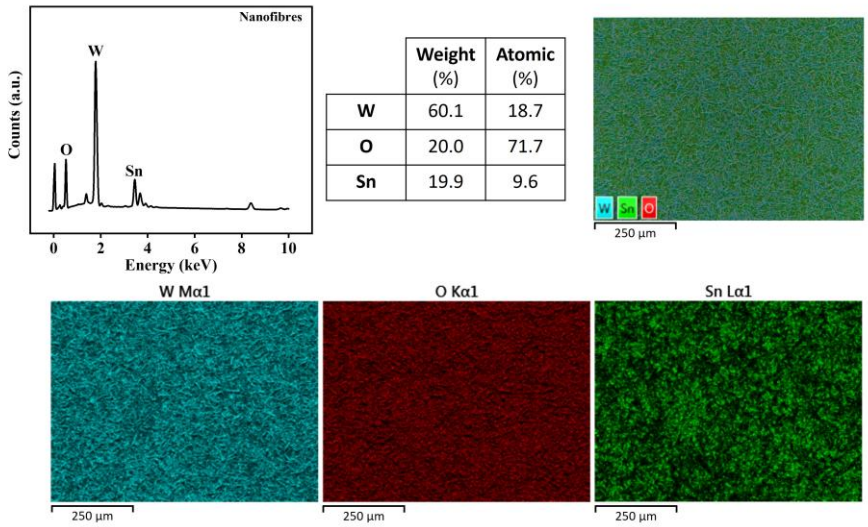

Figure 7.6. EDX analysis of WO_3 nanofibres on a WO_3 compact layer on FTO.

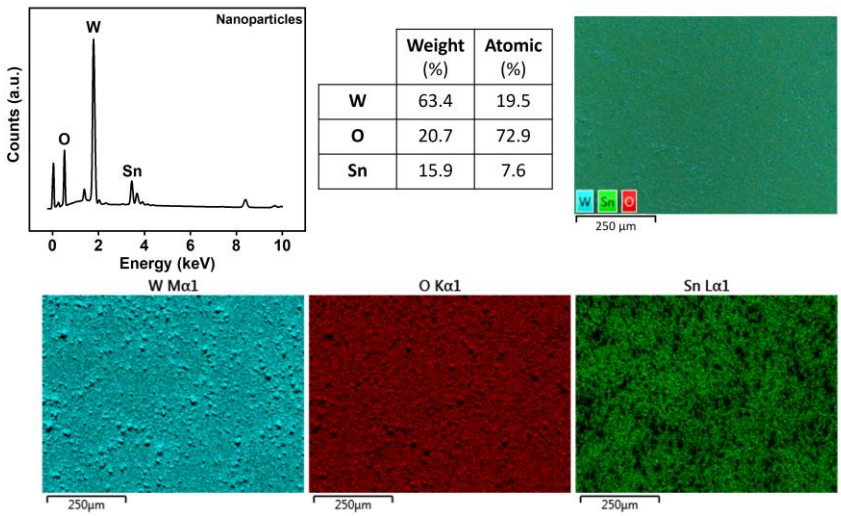

Figure 7.7. EDX analysis of WO_3 nanoparticles on the WO_3 compact layer on FTO.

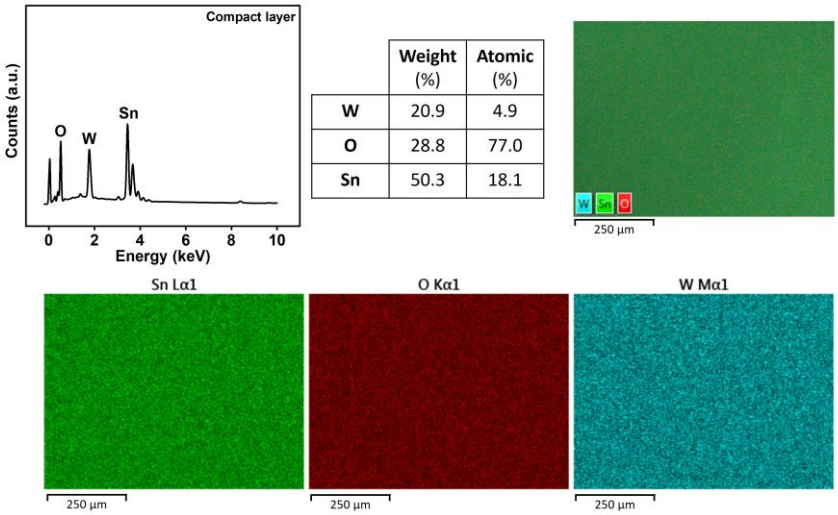

Figure 7.8. EDX analysis of WO_3 compact layer on FTO.

It was found that the nanofibre film contained on average about 20% more WO_3 than the nanoparticulate film. It can be concluded that the amount of material is similar, but that the nanofibre films have a total surface area that is expected to be about double that of the nanoparticulate films. On the other hand, the difference in morphology leads to almost equal values for the *LHE*, which provides optimal conditions to compare the photoelectrochemical properties at the same absorbed light intensity. The amount of WO_3 deposited was determined by weighing the electrodes both before and after deposition, and by scraping off the WO_3 and subsequent weighing. (see **Figure 7.9**).

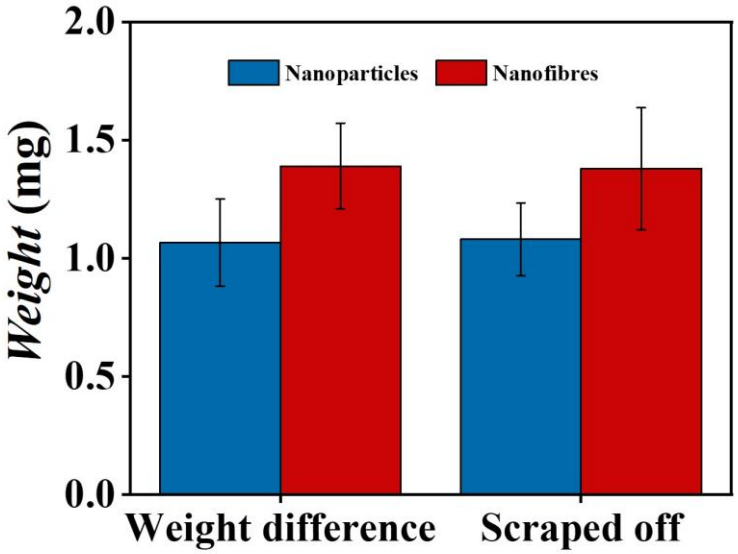

Figure 7.9. Analysis of the amount of WO_3 material deposited for the fabrication of the photoanodes, where the weight difference was determined using an analytical balance before and after deposition (and the full sintering procedure), while the second set of columns corresponds to the weight of the WO_3 scraped off afterwards. At least 5 films were independently analysed, and the error bar indicates the standard deviation.

7.3.2. Photocatalysis vs photoelectrochemistry

Figure 7.10a illustrates the photocatalytic degradation of MB using the same weight of dispersed WO_3 nanofibres and nanoparticles under UV illumination: it can be clearly observed that the nanofibres result in significantly faster degradation than the nanoparticles, which correlates with the larger surface area in contact with the electrolyte solution, as previously reported.[250] **Figure 7.10b** shows CV curves for WO_3 nanoparticulate and nanofibre electrodes prepared using 5 subsequent deposition steps onto the WO_3 compact layer (on FTO) in 1 M $HClO_4$ (pH ≈ 0) under front side illumination (i.e. from the electrolyte solution side).

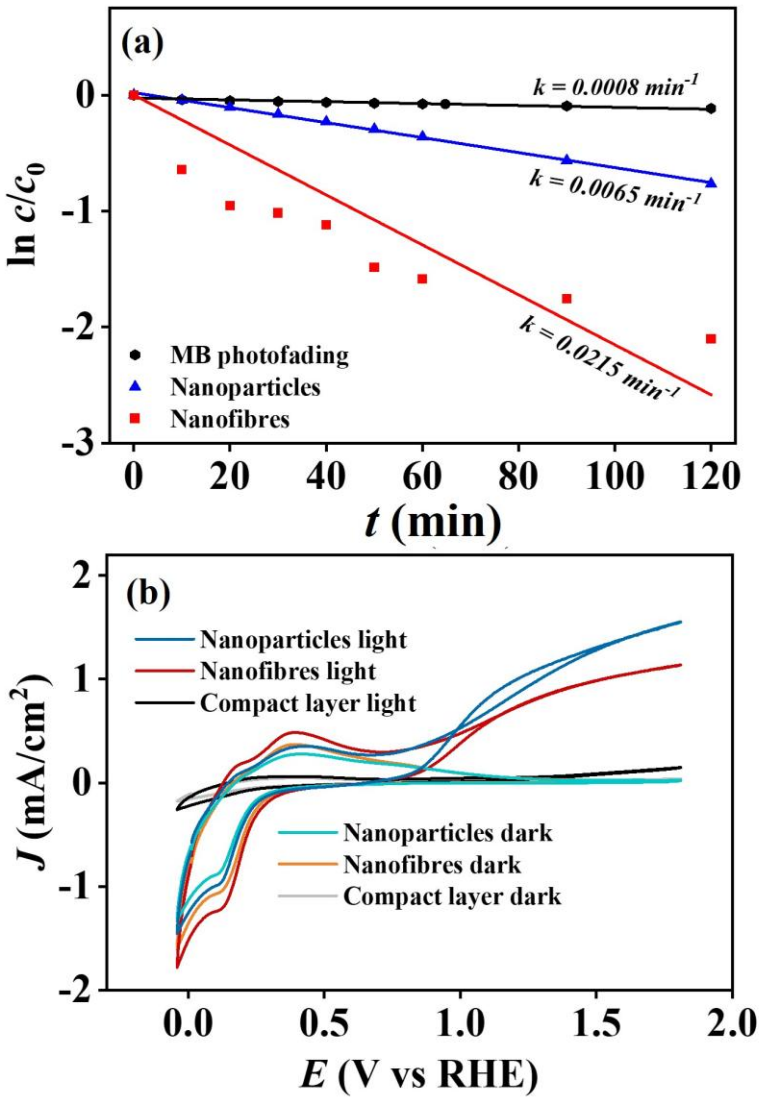

Figure 7.10. (a) Absorbance of a MB solution with WO_3 nanofibres and nanoparticles dispersed versus illumination time using a 365 nm UV lamp; (b) *J-E* curves for the sputter-deposited compact layer and the screen-printed nanofibre and nanoparticulate WO_3 photoelectrodes (on top of the WO_3 compact layer) under 1 sun front side illumination in 1 M $HClO_4$ (pH ≈ 0) at 1 sun (AM1.5 G; 100 mW cm^{-2}). The photoelectrodes were prepared using 5 consecutive deposition steps (see **Figures 7.12** and **7.13**).

The photocurrent onset is at 0.8 V vs RHE, and the photocurrent stabilises at approximately 1.3 V vs RHE. The maximum photocurrent is 0.15 mA cm^{-2}, 1 mA cm^{-2} and 1.5 mA cm^{-2} under 1 sun illumination (AM1.5 G; 100 mW cm^{-2}) for the compact layer, the nanofibre and the nanoparticulate photoelectrodes, respectively. The photocurrent increases to 1.6 mA cm^{-2} and 2.2 mA cm^{-2} for the nanofibre and nanoparticle electrodes, respectively, under irradiance of 10.2 mW cm^{-2} (photon flux of 1.9×10^{16} cm^{-2} s^{-1}) using an LED emitting UV at 370 nm. However, the photocurrent decreases at the same photon flux corresponding to an irradiance of 8.7 mW cm^{-2} of an LED emitting at 435 nm to 0.6 mA cm^{-2} and 0.7 mA cm^{-2} (see **Figure 7.11**).

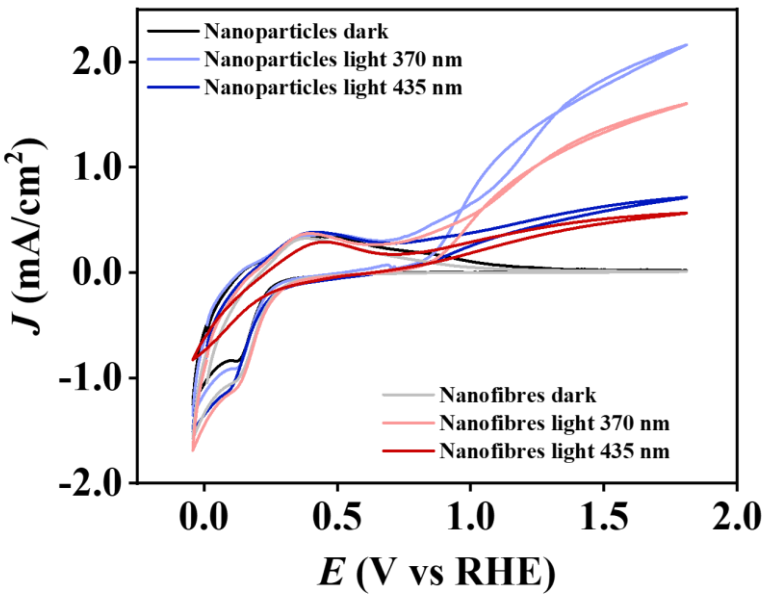

Figure 7.11. *J-E* curves for screen-printed WO_3 nanoparticulate and nanofibre photoelectrodes deposited onto the WO_3 compact layer on FTO for illumination at different wavelengths (370 nm and 435 nm) at same photon flux of 1.9 x 10^{16} cm^{-2} s^{-1} in a 1 M $HClO_4$ (pH ≈ 0) electrolyte solution.

This is mainly due to a 50% decrease in the *LHE* (**Figure 7.3b**); however, the collection efficiency also appears to be smaller at 435 nm. **Figures 7.12** and **7.13** illustrate the reproducibility and improvement of the photocurrent with the thickness for neutral pH solutions, illustrating that the maximum photocurrent begins to saturate after 3 or 4 deposition steps.

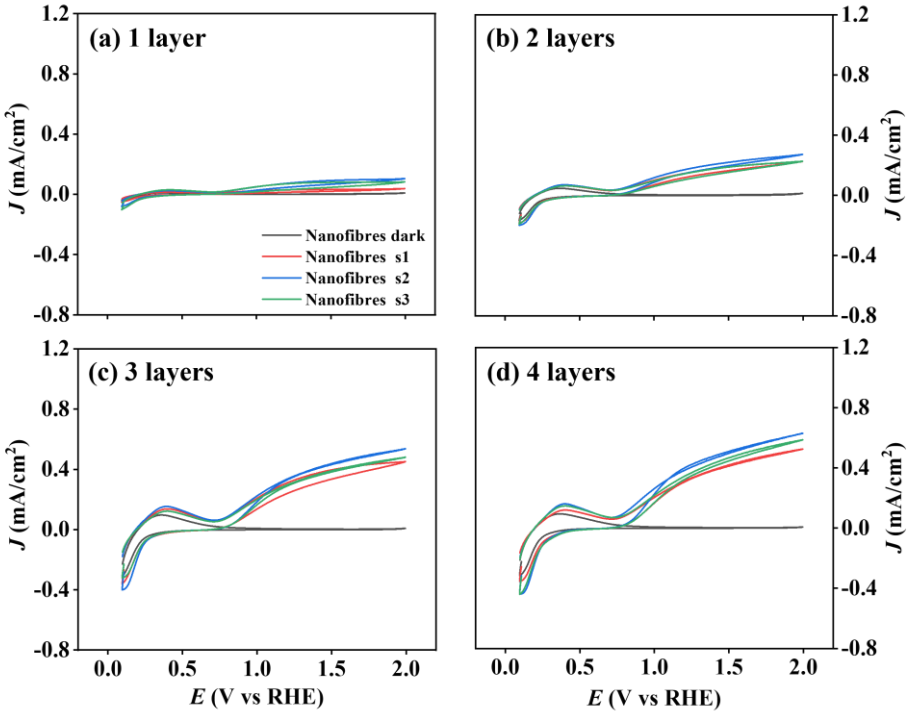

Figure 7.12. *J-E* curves for screen-printed WO_3 photoelectrodes using WO_3 nanofibres on FTO for three samples and as a function of the number of subsequent deposition steps, illustrating the reproducibility and improvement of the photocurrent with thickness up to a saturation value, under illumination at 100 mW cm^{-2} using a Xe lamp and in 0.1 M phosphate buffer solution (pH = 6.5).

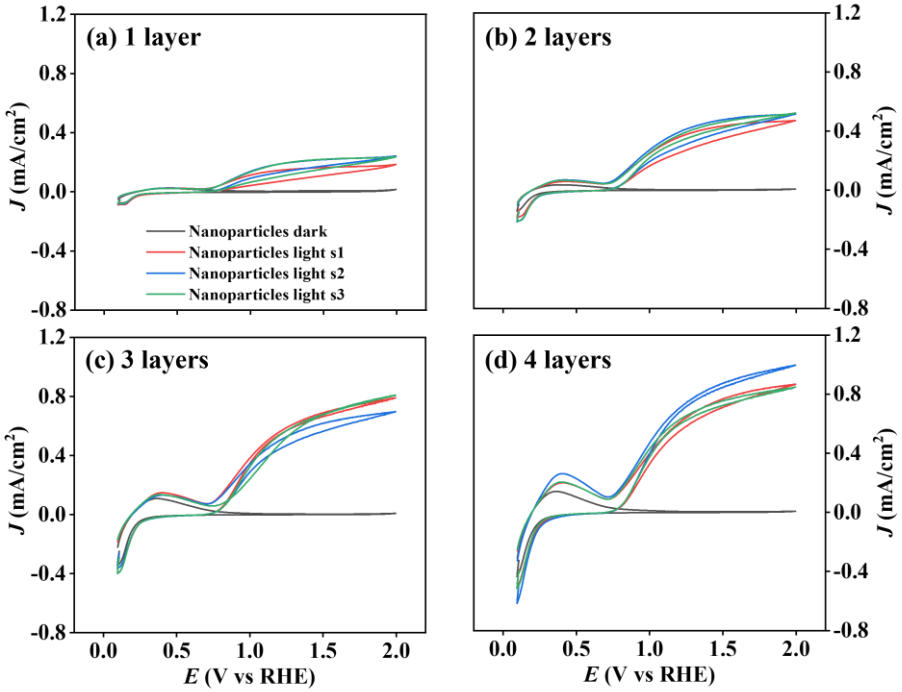

Figure 7.13. *J-E* curves for screen-printed WO_3 photoelectrodes using WO_3 nanoparticles on FTO for three samples and as a function of the number of subsequent deposition steps, illustrating the reproducibility and improvement of the photocurrent with thickness up to a saturation value, under illumination at 100 mW cm^{-2} using a Xe lamp and in 0.1 M phosphate buffer solution (pH = 6.5).

Figure 7.14 demonstrates the stability of WO_3 nanofibre and nanoparticle films under operational conditions with 1 M $HClO_4$ as electrolyte at pH ≈ 0 for at least 15 min, showing that steady-state conditions are reached and maintained, suitable for reliable IMPS measurements.

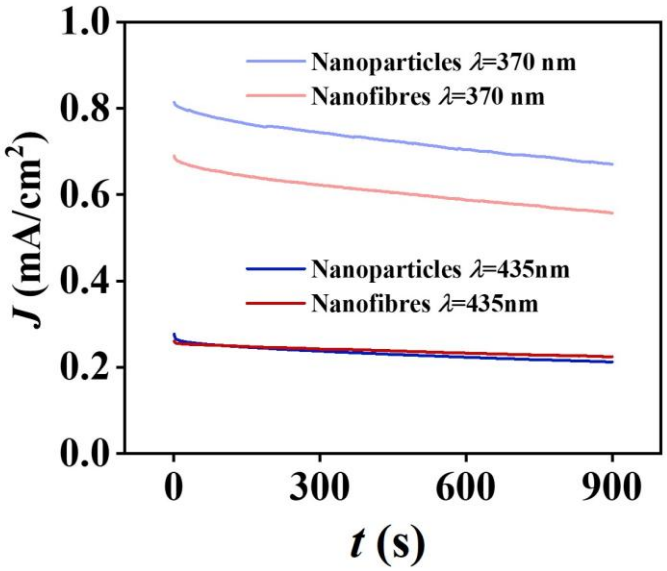

Figure 7.14. *J-t* curves for screen-printed WO_3 nanoparticulate and nanofibre photoelectrodes deposited onto the WO_3 compact layer on FTO for illumination at different wavelengths (370 nm and 435 nm) at same photon flux of 1.9 x 10^{16} cm^{-2} s^{-1} in 1 M $HClO_4$ (pH ≈ 0) electrolyte solution at 1.23 V vs RHE.

Between 0.10 V and 0.15 V vs RHE, a cathodic peak is observed corresponding to the reduction of W^{6+}-sites to W^{5+}-sites[216,253], while on the return sweep the reoxidation peak is observed at 0.15 V vs RHE to 0.20 V vs RHE. These processes do not depend on illumination, i.e., these reactions also occur in the dark. Multiple reduction-reoxidation peaks are only observed under acidic conditions, indicating the participation of protons. However, the reoxidation peak at 0.4 V vs RHE is observed independent of pH. **Figure 7.15** shows that the peak current at 0.4 V vs RHE is linear with the number of deposition steps for both the nanofibre and the nanoparticulate WO_3 photoelectrodes. These results indicate that the current maximum scales with the molar amount of WO_3 material that composes the films. Under illumination, the current value at 0.4 V vs RHE increases somewhat, although the trend is the same. Note that the linear tendency continues after 4 deposition steps,

which is not the case for the photocurrent at 1.5 V vs RHE, which is found to saturate after 3 or 4 deposition steps.

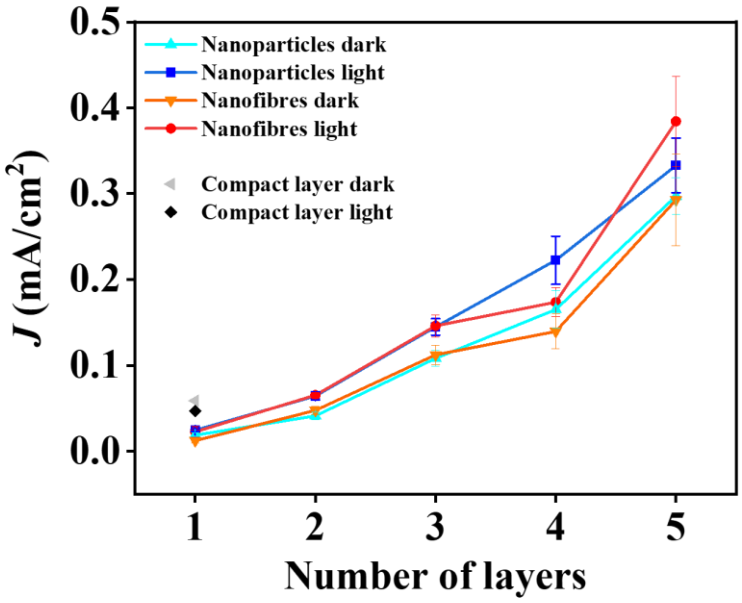

Figure 7.15. The current density peak at 0.4 V vs RHE as a function of the number of layers; 1-4 layers measured in a 0.1 M phosphate buffer (pH = 6.5), and 5 deposits in 1 M $HClO_4$ (pH ≈ 0) for nanoparticles and nanofibres.

It can be concluded that although the surface area of the nanofibre photoelectrodes is about double that of the nanoparticulate electrodes, the photocurrent corresponding to water oxidation is, in fact, larger for the nanoparticulate photoelectrodes. This is in strong contrast to the results obtained for the photocatalytic degradation of MB in the dispersed system, where the larger surface area of the nanofibres (for essentially the same molar amount of WO_3) results in much faster degradation kinetics (**Figure 7.10a**). These results indicate that charge separation and charge transport in nanostructured films affect performance in a different way than in photocatalysis using dispersions of the same nanomaterials.

7.3.3. Intensity-modulated photocurrent spectroscopy

To better understand the charge carrier dynamics IMPS was applied to explain the contrasting results obtained for the two different morphologies in the two applications, photocatalytic dye degradation and PEC water oxidation.[98,154,254–260]

IMPS measurements were performed for nanoparticulate and nanofibre films screen-printed on top of the WO_3 compact layer (on FTO) in 1 M $HClO_4$ (pH ≈ 0) as a function of applied potential, and using the same photon flux of 1.9×10^{16} cm^{-2} s^{-1} with LEDs with emission maxima at 370 nm and 435 nm, respectively. **Figure 7.16** shows the IMPS spectra obtained using the 435 nm LED in both a Nyquist-type representation (**Figure 7.16a,b**), and in a Cole-Cole plot (**Figure 7.16c,d**). Both materials present similar characteristics, with the Nyquist plot dominated by one loop in the 4th quadrant (**Figure 7.16a,b**) except for at 0.8 V vs RHE, which corresponds to the onset potential. At high frequencies, $H(EQE) = 0$, and the loop develops upon decreasing the modulation frequency. The apex of the loop defines a characteristic frequency, f_{min}, and upon further decreasing the frequency, the loop ends on the $Re(EQE)$ axis giving the low-frequency external quantum efficiency, EQE_{max}. Hence, the charge carrier dynamics are essentially described by a single time constant, which corresponds to the competition between charge separation or collection and recombination. The size of the arc increases with applied potential, and the low-frequency *EQE* obtained from IMPS and plotted against the applied potential results in graphs that mirror the *J-E* curves, indicating that EQE_{max} provides a good measure for the steady-state *EQE*. Hence, the IMPS plots confirm that the nanoparticulate and nanofibre films perform similarly in photoelectrochemical water oxidation.

At 0.8 V vs RHE, corresponding to the onset potential in *J-E* curve, a double arc is observed in the 4th quadrant, which indicates a competition between the recombination and the hole transfer to the solution, that limits the charge separation and collection dynamics. In addition, a very small upper loop is observed in the 1st quadrant, which classically

corresponds to surface recombination in the presence of a (small) built-in potential. At more positive potentials only one arc is present, indicating that one process limits performance, in this case, the charge collection.

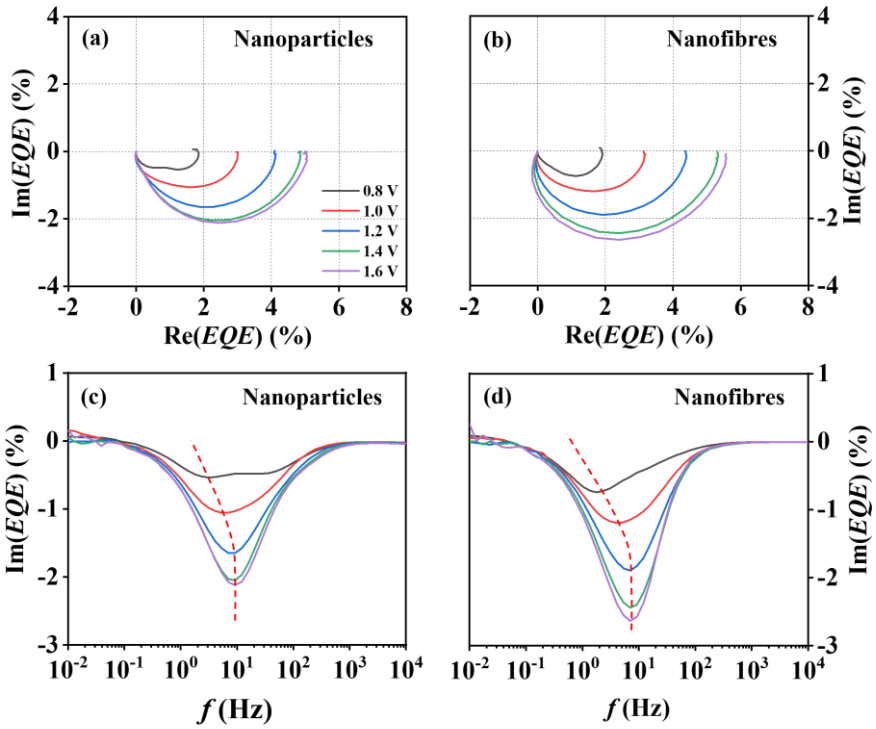

Figure 7.16. Nyquist (a,b) and Cole-Cole (c,d) plots for screen-printed films of: (a,c) WO_3 nanoparticulate films; (b,d) WO_3 nanofibre films, all under LED illumination at 435 nm at the same photon flux of 1.9×10^{16} cm^{-2} s^{-1}.

Figure 7.17a shows f_{min} versus applied potential for both WO_3 photoelectrodes. In range of 0.8–1.2 V vs RHE, that corresponds to the region, where the photocurrent increases to a plateau value in the *J-E* curves (**Figure 7.10b**), f_{min} increases with potential, while at more positive potentials f_{min} is essentially a constant. These results indicate that the increase of EQE_{max} in the onset region with more positive applied potential is caused by improving charge extraction at the WO_3/electrolyte

solution interface. Apart from at 0.8 V vs RHE, surface recombination is not distinguished from the bulk recombination, and the loop in the 4th quadrant describes the dynamics of the competition between collection mediated by charge transport and recombination, either inside the nanoparticles or at their surface. At more positive potentials, the charge collection is limited by the diffusive electron transport in the nanostructured film. Therefore, the increase in photocurrent observed between 0.8 and 1.2 V vs RHE is mainly associated with improved charge separation and reduced surface recombination at the WO_3/electrolyte interface. At more positive potentials, where the photocurrent reaches a plateau, further improvements become less significant, indicating that electron transport collection within the nanostructured WO_3 films becomes the dominant limiting factor.[42,96,98–101,136,147,154,155]

Figure 7.17b shows f_{min} as a function of the photon flux at an applied potential of 1.23 V vs RHE, i.e. light intensity, and it can be observed that f_{min} increases with increasing photon flux for both the nanofibre and the nanoparticulate photoelectrodes.

In general terms, the driving force for diffusion-limited transport in materials is given by the quasi-Fermi level gradient, and this is independent of the light intensity and varies little with the relative position. However, in disordered semiconductors, the transport mechanism is more complex often involving a distribution of trap states. This has been previously observed for nanostructured TiO_2 photoelectrodes as well as other materials: the observed dependence is attributed to trap-limited charge transport, represented schematically in **Figure 7.18**, in which electrons are photogenerated near the electrolyte solution and collected at the FTO back contact.[254–260] Different types of band gap states may be present, and localization of electrons in states around the quasi-Fermi level has the strongest attenuation effect on the electron transport.[216] Upon increasing the light intensity, the quasi-Fermi level moves to higher energy resulting in shallower traps determining the transport kinetics. The model has been validated by one key result: that the value of f_{min} is dependent on the charge density in the film, hence the incident light intensity. If the trap density distribution is assumed to be

exponential, f_{min} depends on the light intensity through a power-law dependence, which is exactly what has been observed for these nanostructured, mesoporous WO_3 photoelectrodes.

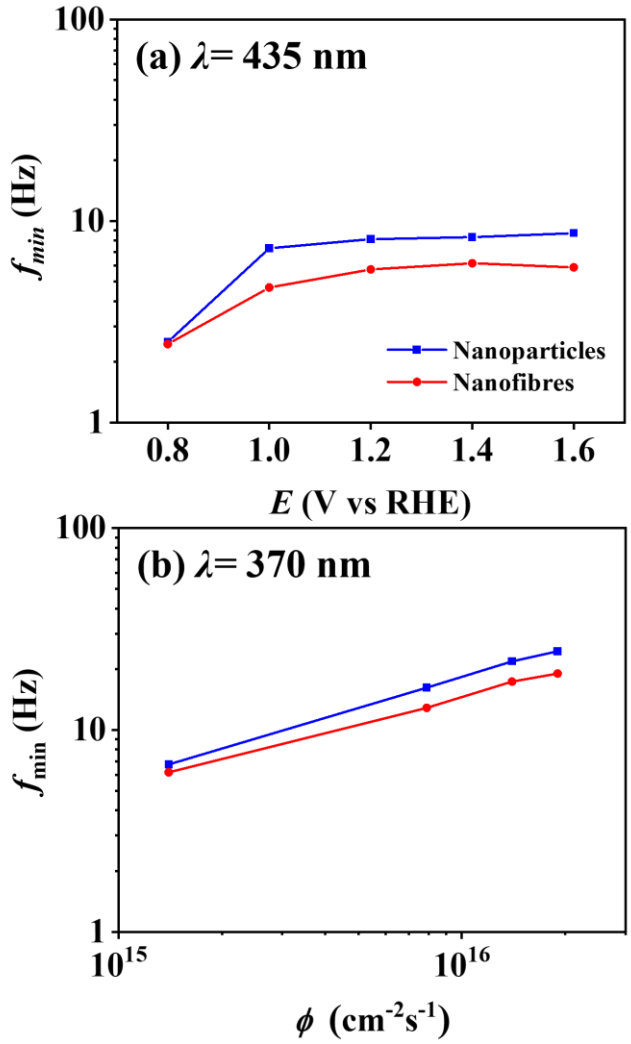

Figure 7.17. (a) f_{min} versus applied potential for WO_3 nanoparticles and nanofibres films at 435 nm at a photon flux of 1.9×10^{16} cm^{-2} s^{-1}. (b) Dependence of f_{min} as a function of the light intensity for both WO_3 photoelectrodes under LED illumination at 370 nm at 1.23 V vs RHE.

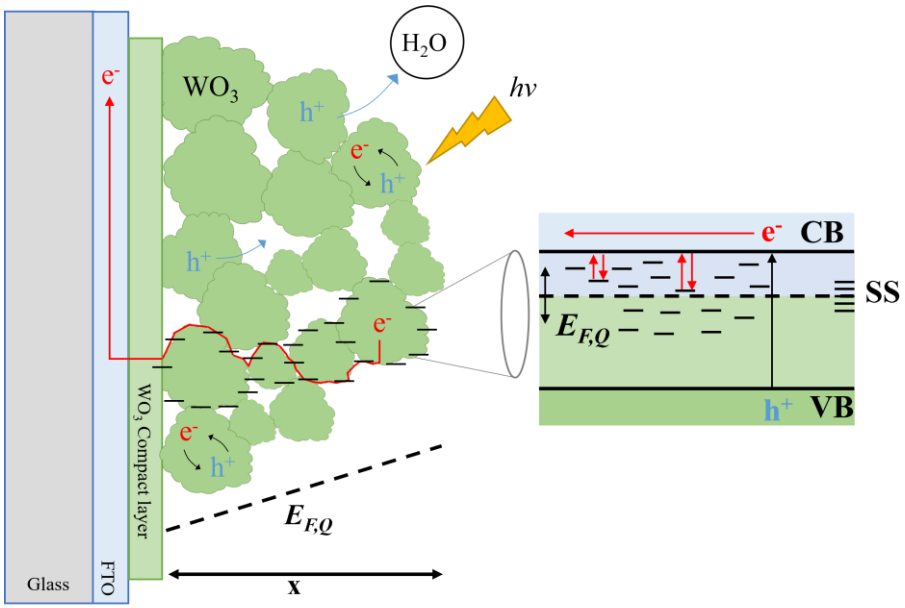

Figure 7.18. Electron transport in the WO_3 conduction band model under steady-state conditions. Electrons are photogenerated by front-side illumination near the electrolyte solution (x = 0) and collected by the FTO back contact (x = d) at a constant rate.

Interestingly, the value of f_{min} is smaller for the nanofibre film, which could be interpreted as being caused by a larger density of trap states. Following the argument of references that for this type of electrodes the trap states are in fact at the surface, this may be attributed to the larger surface area of the nanofibres.[254,256] A second possible explanation could be that the non-optimal orientation of the nanofibres with respect to the FTO surface leads to a longer travel path for the electrons to be collected. The dependence of the time constant on photon flux or, more appropriately, the charge density accumulated in the WO_3 nanostructured films, also affects the comparison of the performance at different wavelengths. **Figure 7.17** shows that at the same photon flux the charge carrier dynamics are faster using illumination with 370 nm (**Figure 7.17b** at the highest photon flux) as compared to 435 nm (**Figure 7.17a**). At the same photon flux, the effective charge density under 370 nm illumination is larger due to the larger fraction of absorbed photons. This

can be inferred from **Figure 7.3b**, where the *LHE* is much larger for 370 nm than 435 nm. Additionally, the observation that the process dynamics are faster at higher charge density also affects the collection efficiency, thus explaining the more than proportionally lower photocurrent observed in the *J-E* curves obtained using 435 nm (see **Figure 7.11**). Hence, these results indicate that in both the nanoparticulate and the nanofibre films trap-limited electron transport strongly affects the photoelectrode performance. It can also be concluded that the 1D nanofibre morphology does not translate in faster electron collection, which may be ascribed to the larger surface area, and hence larger trap density, but may also be related to the number of inter-nanoparticle contacts electrons need to pass before reaching the FTO, where grain boundaries may further hinder electron transport, and the observation that the fibres do not exhibit perpendicular directionality to the WO_3 compact underlayer, thus preventing faster, directed electron transport. To conclude, a long-range electron transport is not required in photocatalysis, while a larger surface area provides better photocatalytic activity. In contrast, for these WO_3 nanomaterials, this is not the case for photoelectrochemical water oxidation.

7.4. Conclusions

The photocatalytic activity of WO_3 nanomaterials suspended in an aqueous MB solution depends on the morphology of the material, showing an improvement for the nanofibres with a larger surface area related to the smaller size of the particles that constitute the fibres. However, the same improvement is not observed for the photoelectrochemical oxidation of water at screen-printed, mesoporous films. The light intensity dependence of the time constant corresponding to charge collection obtained with IMPS shows that this is related to the observation that trap-limited electron transport in the interconnected, nanostructured films determines the dynamics, rather than hole transfer to the solution. As a consequence, the surface area is no longer a determining factor in the performance of the WO_3 nanomaterials for water oxidation. These results illustrate the intricacies of photocatalytic processes and indicate that the nanomaterial morphology needs to be

optimised for each specific application, keeping in mind the charge carrier dynamics that govern performance.

After focusing on WO_3 as a model oxide to examine morphology-dependent photoelectrochemical behaviour, the next chapter broadens the discussion to metal vanadate semiconductors and alloys. This transition allows the analysis to move from structural effects in a single material system to a comparative evaluation of charge carrier dynamics across related metal oxides. In the next chapter, EIS and IMPS are used to resolve how differences in composition influence the processes contributing to photocurrent generation, providing a more detailed kinetic framework for interpreting photoelectrochemical performance.

Chapter 8

Charge dynamics as probed by small signal-modulated photocurrent and impedance spectroscopy of metal vanadate semiconductors and alloys

Abstract

This chapter presents the combined and complementary use of two techniques, namely, IMPS and PEIS for the study of partially or wholly replacing copper with an alkaline earth metal (Mg, Ca) in a metavanadate compound matrix (MV_2O_6). To this end, the three reference compounds (CuV_2O_6, CaV_2O_6, MgV_2O) and two alloy compositions ($Mg_{0.1}Cu_{0.9}V_2O_6$ and $Ca_{0.1}Cu_{0.9}V_2O_6$), obtained from a solution combustion technique, were screen-printed on FTO substrates. Wavelength discrimination for optical excitation of these semiconductor samples was provided by using high-power LED (front-side) illumination with different wavelengths, UV (λ = 370 nm), blue (λ = 455 nm), green (λ = 535 nm), and red (λ = 670 nm). A nonunity

photogeneration yield of mobile charge carriers was seen in a trend reminiscent of previous data on binary oxides or even for other types of ternary copper oxides from other laboratories. The dynamic aspects of charge transfer and carrier recombination are discussed using the combined IMPS-PEIS data along with other optical (e.g., DRS) and PEC data. The contents of this chapter have been published in ACS Applied Optical Materials.[91]

8.1. Introduction

Tuning the chemical composition or alloying metallic elements within a compound semiconductor framework is a powerful method in a materials chemist's toolbox to tweak its properties for a targeted application. Cases in point are the semiconductor alloys in the group III−V (13−15) family where the energy bandgaps are tuned for optoelectronic device (e.g., diode lasers, displays, solar cells) use by alloying the cationic component. However, other than perhaps ternary oxide perovskites, examples of chemical modification or alloying of ternary oxide semiconductors are only emerging of late.[261–273] This chapter explores the dynamic consequences of partially or wholly replacing copper with an alkaline earth metal (Mg, Ca) in a metavanadate compound matrix (MV_2O_6). This is a companion study that builds on our previous efforts on both *ortho*- and *pyro*-vanadates ($M_2V_2O_7$).[274,275] Closely related studies in other laboratories on a variety of ternary copper vanadates are also noted here. This alloying strategy was motivated by the potential of alkaline earth metals, such as Mg and Ca, to enhance water adsorption properties and alter the electronic structure in a way that could reduce recombination losses, thereby improving photocarrier generation and injection efficiency.[274,275]

Time-dependent perturbation is very effective for studying the dynamic behaviour of semiconductor/electrolyte interfaces. The two most common types of perturbation are illumination with modulated intensity at a fixed electrode potential or modulation of the electrode potential at constant illumination. The corresponding techniques, namely IMPS and PEIS, have been thoroughly reviewed in a monograph.[147] In what

follows, (P)EIS was used for the cases when the EIS technique was used with or without illumination of the semiconductor surface (i.e., in the dark). The complementarity of IMPS and PEIS for gleaning insights into dynamic processes such as carrier recombination or interfacial charge transfer is well exemplified by the results reported by other authors on binary compound semiconductors such as GaAs, CdS, and InP,[100,276] as well as metal oxides.[142,260]

One of us has previously used IMPS for the study of a ternary oxide semiconductor, namely, $CuBi_2O_4$.[277] Interfacial hole transfer and carrier recombination were also studied as a function of potential for β-$Cu_2V_2O_7$/electrolyte interfaces in a previous collaboration.[278] The present chapter specifically shows that the recently discussed reinterpretation of declining photogeneration efficiency with wavelength in terms of being rooted in nonmobile charge carriers (rather than carrier recombination) applies to the metavanadates under discussion as well.[279] In this context, potential issues with localised (e.g., d−d) light absorption resulting in subunity quantum yields, may be more widely prevalent than previously envisioned.

8.2. Experimental section

8.2.1. Photoanode fabrication

The metal vanadates CuV_2O_6, CaV_2O_6, MgV_2O_6, and the alloy compositions $Mg_{0.1}Cu_{0.9}V_2O_6$ and $Ca_{0.1}Cu_{0.9}V_2O_6$ were prepared in polycrystalline powder form by solution combustion synthesis (SCS) according to previously reported work, where detailed characterisation and elemental analysis confirmed their exact composition.[274,275,280] In brief, stoichiometric amounts of the corresponding metal nitrates, ammonium vanadate, and malic acid were dissolved in water to form a homogeneous precursor solution, where malic acid acted both as complexing agent and combustion fuel. The precursor mixtures were thermally treated in a preheated furnace at 300 ºC, leading to dehydration, ignition, and subsequent combustion. The obtained

powders were finally annealed at 600 ºC for 1 h to improve crystallinity and remove residual organic species.

The photoelectrodes were fabricated using a semiautomatic screen-printing system (ATMA AT-45PA). The printing paste was formulated using 0.1 g of the SCS-derived powder, which was finely ground in an agate mortar to ensure particle size homogeneity and then dispersed in 10 mL isopropanol in an ultrasonic bath for 20 min. Subsequently, 1 mL terpineol (86480, Sigma-Aldrich) was added and the dispersion was magnetically stirred for 20 min. Separately, 0.03 g ethyl cellulose 100 cP (247499, Sigma-Aldrich) was dissolved in 10 mL isopropanol and magnetically stirred at 90 °C for 1 h. Finally, the powder dispersion and the ethyl cellulose solution were combined, magnetically stirred, and sonicated for 20 min. The excess solvent was removed in a rotatory evaporator until the paste reached the desired density and viscosity.[50,281] The procedure was independently repeated for each material.

Screen printing was performed employing a screen with a mesh opening of 68 μm, nominal thread diameter of 40 μm, open area of 37.6%, mesh thickness of 65 μm, theoretical ink volume of 24.4 cm^3 m^{-2} and deposition area of 1 cm^2. Prior to deposition, the FTO substrates (Xop Glass, FTO TEC 15, 12−15 Ω sq^{-1}) were cleaned in an ultrasonic bath for 20 min in each of the following solvents, in the given order: Milli-Q water with Hellmanex III (Z805939 Sigma-Aldrich), Milli-Q water, ethanol, isopropanol, and acetone. Finally, the substrates were dried under a nitrogen stream. To obtain the optimal film thickness of about 6 μm (see below), as defined by reaching saturation of the photocurrent upon increasing the thickness, 5 layers were subsequently printed; between deposition steps, the films were heated on a hot plate at 125 °C for 10 min. The films were finally heated to 550 °C using a linear 40 min ramp and sintered at that temperature for 1 h. The samples were left to cool down to room temperature before use.

8.2.2. Structural, morphological, and optical characterisation

PXRD was performed on a Bruker D8 Discover diffractometer operating at 50 kV and 1 mA for Cu Kα (λ = 0.15418 nm), in the range of 12.5° to

60° with an increment step of 0.01° per 0.05 s. The surface morphology and film thickness were examined using a Zeiss Gemini 300 FE-SEM in both top-view and cross-section modes.

DRS was performed using a UV/Vis/NIR spectrophotometer model FSL1000-DD-STM Edinburgh Instruments equipped with an integrating sphere and an Xe lamp as illumination source in the range of 300 to 800 nm, with a dwell time of 1 s and step size of 1 nm.

The emission spectra of the LEDs were obtained through an optical fibre using an Ocean Optics (USB 4000) spectrometer. ATR-FTIR was performed on a JASCO FTIR-4700 instrument in the 4000−400 cm^{-1} wavenumber range.

8.2.3. Photoelectrochemical measurements and photocurrent-electrochemical impedance spectroscopy

The PEC measurements were performed using a three-electrode cell configuration and front-side illumination (i.e., from the electrolyte solution side) in a single-compartment electrochemical cell equipped with a quartz window, using a Pt wire as counter electrode and Ag/AgCl (3 M KCl) as reference. The electrolyte used was 0.1 M phosphate buffer at pH 6.5. The measurements were performed using an Autolab system (PGSTAT302N) and a solar simulator (ABET 1100) with an AM 1.5G filter as the light source, which was calibrated at 100 mW cm^{-2} using a Si photodiode (Newport model 91150), at a scan rate of 20 mV s^{-1}. The applied potential was converted to RHE at pH 6.5. The submerged area in contact with the electrolyte was 0.785 cm^2.

The IMPS measurements were carried out in the frequency range from 10^5 Hz to 10^{-2} Hz under high-power LED illumination using different wavelengths: UV (λ = 370 nm), blue (λ = 455 nm), green (λ = 535 nm), and red (λ = 670 nm). Front-side illumination was employed with the LED photon source calibrated with a Si-photodiode (Hamamatsu S12698-2) at the same photon flux of 1.6×10^{16} cm^{-2} s^{-1} at different applied potentials, and at different photon fluxes at a fixed applied potential of 1.8 V vs RHE. The modulation amplitude was about 10% of

the base light intensity, and the response linearity was tested and confirmed through Lissajous plots. Before each IMPS measurement, a 15 min chronoamperometry measurement was performed to establish a steady-state condition and confirm the response stability. Normalisation was performed by determining the number density of incident photons to obtain real values of the *EQE*.[26,40,50,98,99,154,240,281–285]

EIS was performed with a potential perturbation amplitude of 10 mV (p/p) in the range from 10^5 Hz to 10^{-2} Hz under dark and high-power LED blue (λ = 455 nm) illumination at a photon flux of 1.6×10^{16} cm^{-2} s^{-1} as a function of the applied potential. The latter technique variant is referred to as photoelectrochemical EIS or PEIS in what follows. The C_{eff} was calculated from the *CPE*.[152,153]

8.3. Result and discussion

8.3.1. Structural, morphological, and optical attributes

Photographs of the 5-layer screen-printed electrodes are presented in **Figure 8.1** in the Supporting Information. The films present good homogeneity, with different colours for CaV_2O_6 and MgV_2O_6, and the same colour with different hues for CuV_2O_6 and the alloy modifications, $Mg_{0.1}Cu_{0.9}V_2O_6$ and $Ca_{0.1}Cu_{0.9}V_2O_6$.

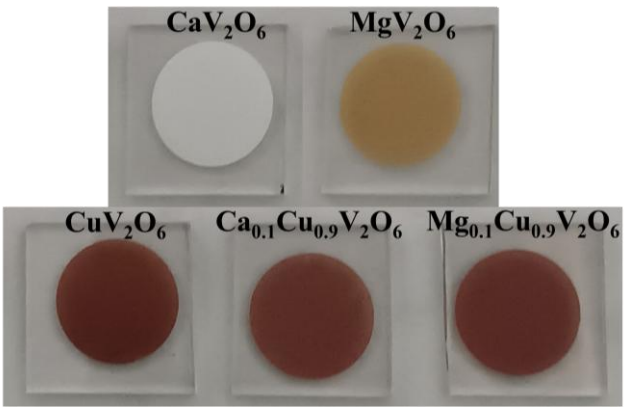

Figure 8.1. Photos of 5-layer films deposited on FTO using the screen-printing technique.

Figure 8.2 shows the XRD patterns for each vanadate compound deposited on FTO. The CaV_2O_6 and MgV_2O_6 films present a monoclinic structure (PDF #73-0186 and PDF #71-1651, respectively), while the CuV_2O_6 film and the alloy modifications $Mg_{0.1}Cu_{0.9}V_2O_6$ and $Ca_{0.1}Cu_{0.9}V_2O_6$ adopt a triclinic structure (PDF #75-1054). The last two samples have grains with preferred orientation as diagnosed by the peak located at 29.3° in the (201) plane. The peaks at 26.5°, 33.8°, 37.9° and 51.7° correspond to the FTO substrate. The film pattern data agree very well with those of the corresponding SCS-derived powder samples used for film deposition. In previous work, elemental analysis using XPS confirmed the stoichiometry of the compounds, and detailed Rietveld analysis was performed on the XRD patterns of the powder materials, confirming the phase purity of the materials.[274]

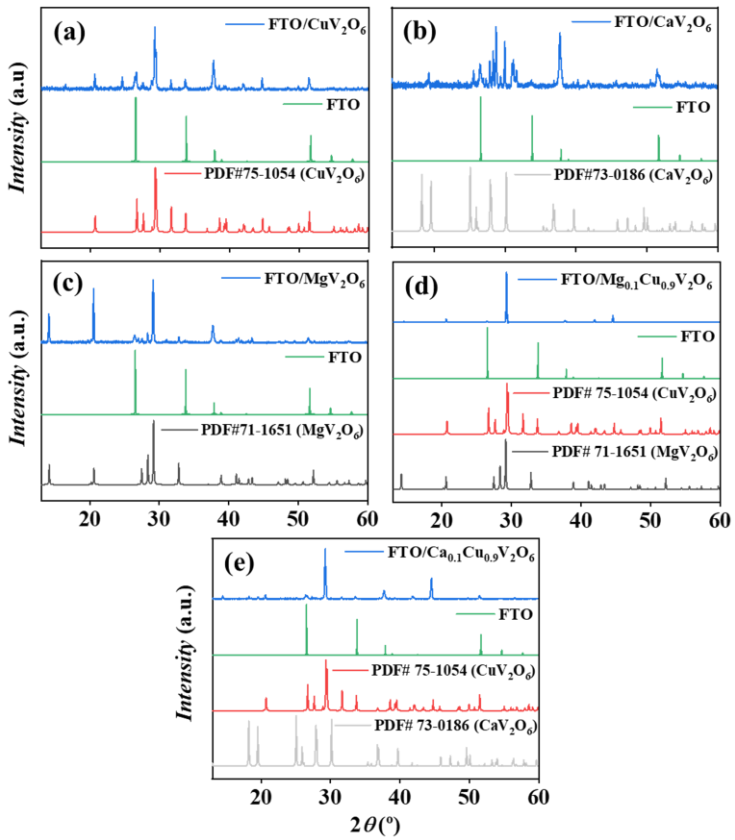

Figure 8.2. PXRD patterns for (a) CuV_2O_6, (b) CaV_2O_6, (c) MgV_2O_6, (d) $Mg_{0.1}Cu_{0.9}V_2O_6$, and (e) $Ca_{0.1}Cu_{0.9}V_2O_6$ and photoanodes screen-printed on FTO.

SEM images of the photoelectrodes are presented in **Figure 8.3** (top-view) and **Figure 8.4** (cross-section) revealing that the morphology and particle shape of CuV_2O_6, $Mg_{0.1}Cu_{0.9}V_2O_6$ and $Ca_{0.1}Cu_{0.9}V_2O_6$ films are similar, with a particle size of about 2 μm and a homogeneous distribution.

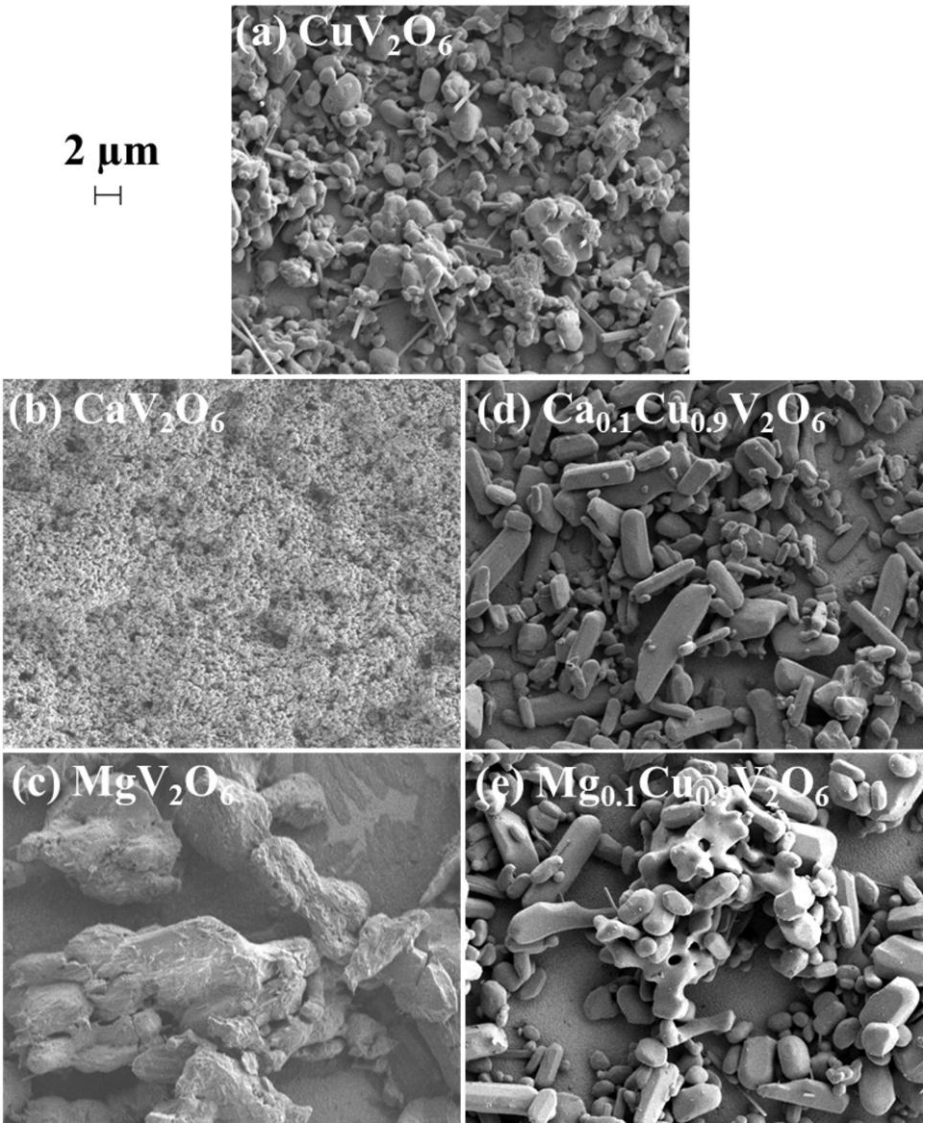

Figure 8.3. SEM top-view images of (a) CuV_2O_6, (b) CaV_2O_6, (c) MgV_2O_6, (d) $Ca_{0.1}Cu_{0.9}V_2O_6$, and (e) $Mg_{0.1}Cu_{0.9}V_2O_6$ electrodes screen-printed on FTO.

In contrast, the MgV_2O_6 film exhibits larger and more agglomerated particles, while the CaV_2O_6 film shows the smallest particle size of about 0.4 μm. The film thickness is approximately 6 μm for all samples, obtained by screen-printing 5 layers. The films are generally porous, which implies that in the electrochemical experiments the FTO and the metal oxide semiconductor are both in contact with the electrolyte solution.

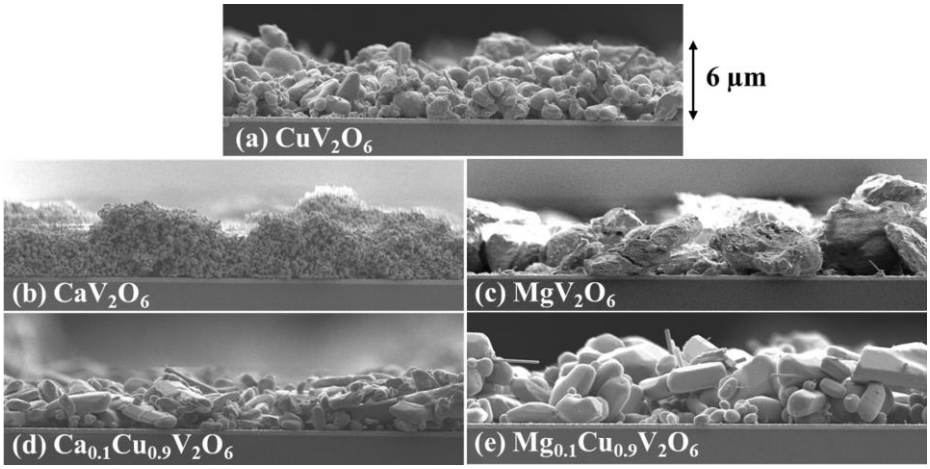

Figure 8.4. SEM cross-section images of (a) CuV_2O_6, (b) CaV_2O_6, (c) MgV_2O_6, (d) $Ca_{0.1}Cu_{0.9}V_2O_6$, and (e) $Mg_{0.1}Cu_{0.9}V_2O_6$ electrodes screen-printed on FTO, with 6 µm thickness.

Figure 8.5a shows the DRS data for the five samples under study. **Figure 8.5b** illustrates the corresponding *LHE* spectra derived from these measurements. The higher *LHE* values are obtained for CuV_2O_6, with 74% for UV (λ = 370 nm), 83% for blue (λ = 455 nm), and 82% for green (λ = 535 nm) illumination. The $Mg_{0.1}Cu_{0.9}V_2O_6$ and $Ca_{0.1}Cu_{0.9}V_2O_6$ alloy samples exhibit a decrease of about 5% in *LHE* relative to CuV_2O_6, while CaV_2O_6 and MgV_2O_6 absorb significantly less. **Figure 8.5c** presents the light penetration depth for the samples of interest compared to the three high-power LED spectra of different wavelengths used in the PEC measurement.

The penetration depth is about 4 μm for all materials and increases somewhat in the UV and toward the NIR. Comparing to the film

thickness of 6 μm, this implies that a small fraction of light is not absorbed, as also observed in the *LHE* graph. Note that the inhomogeneous morphology and the partial coverage of the FTO substrate complicates the *LHE* analysis, leading to a relatively large uncertainty in the parameter values extracted. UV light exhibits a somewhat larger penetration depth, related to an increase in reflectance in this region (**Figure 8.5a**), corresponding to a decrease of the effective absorptance; this observation is consistent with similar trends reported for related metal oxide semiconductors. This phenomenon either reflects a decrease of the absorption coefficient, or complications determining absorption due to combined effects of surface reflectivity, optical interference within the film attributed to the porous nature of the material and surface roughness. For the experiments reported here, the *LHE* and penetration depth can be considered to be similar for the three LEDs used. The increase in *LHE* at wavelengths larger than 550 nm corresponds to absorption to midgap states, which is further addressed in the discussion of **Figure 8.22**.

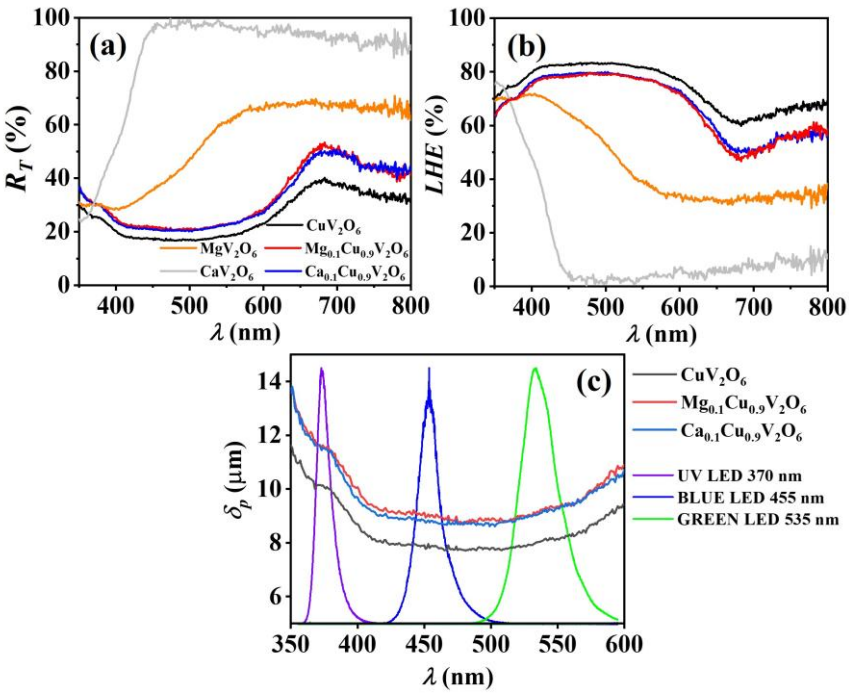

Figure 8.5. (a) DRS data (b) *LHE* and (c) δ_p for CuV_2O_6, CaV_2O_6, MgV_2O_6, $Ca_{0.1}Cu_{0.9}V_2O_6$ and $Mg_{0.1}Cu_{0.9}V_2O_6$ films screen-printed on FTO.

Energy bandgap values are estimated using Kubelka-Munk analysis (**Figure 8.6**) from the DRS data on the five film samples, presenting similar values for $Mg_{0.1}Cu_{0.9}V_2O_6$, $Ca_{0.1}Cu_{0.9}V_2O_6$ and CuV_2O_6.[286,287] The absence of Cu in the pure CaV_2O_6 and MgV_2O_6 samples greatly enlarges the band gap of these photoelectrodes, resulting in a much lower *LHE*. The DRS data on the five film samples are in good agreement with the trends presented in our earlier study on the corresponding SCS-derived powder samples.[275]

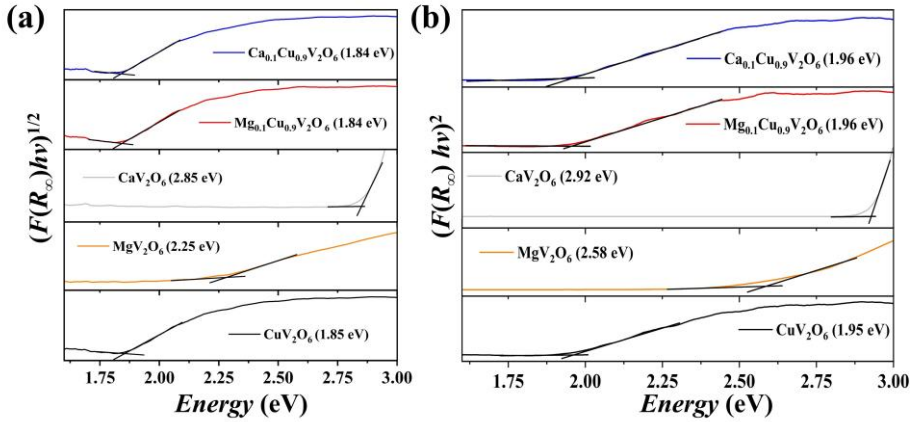

Figure 8.6. Kubelka-Munk analysis of the DRS measurement of the films deposited onto FTO, indicating the (a) indirect and (b) direct optical bandgap values for CuV_2O_6, CaV_2O_6, MgV_2O_6, $Ca_{0.1}Cu_{0.9}V_2O_6$, and $Mg_{0.1}Cu_{0.9}V_2O_6$ electrodes screen-printed on FTO.

8.3.2. Photoelectrochemical measurements

Figure 8.7 shows LSV curves for CuV_2O_6, $Mg_{0.1}Cu_{0.9}V_2O_6$ and $Ca_{0.1}Cu_{0.9}V_2O_6$ photoelectrodes in 0.1 M phosphate buffer as electrolyte at a potential scan rate of 20 mV s^{-1} with chopped front side illumination using different light sources: 1 sun AM 1.5G, UV (λ = 370 nm), blue (λ = 455 nm) and green (λ = 535 nm) illumination, at the same LED photon flux of 1.6×10^{16} cm^{-2} s^{-1}. The photocurrent generated by CaV_2O_6 and MgV_2O_6 electrodes is very small, hence, these electrodes were excluded from further analysis. Also, measurements under red LED illumination result in negligible photocurrent for all electrodes. The photocurrent onset is located at 1.0 V vs RHE, and the CuV_2O_6 film exhibits the

highest photocurrent, reaching 0.26 mA cm^{-2} at 1.8 V vs RHE compared to 0.17 mA cm^{-2} and 0.15 mA cm^{-2} for $Ca_{0.1}Cu_{0.9}V_2O_6$ and $Mg_{0.1}Cu_{0.9}V_2O_6$, respectively. The disparity in photocurrent decreases with increasing wavelength, with the CuV_2O_6 electrode achieving twice the photocurrent under UV illumination, 1.5 times higher under blue light and comparable performance under green light conditions in comparison with the two alloy vanadates. This behaviour is not correlated with the light penetration depth, where the larger penetration depth in the UV region corresponds to lower light absorption. A possible explanation for this phenomenon, related to the electronic band structure of α-CuV_2O_6, will be provided in **Section 8.3.5**. On the other hand, the higher photocurrent observed for the CuV_2O_6 film can be partially attributed to the higher *LHE*, but also implies better kinetic properties in comparison with the alloy modifications.

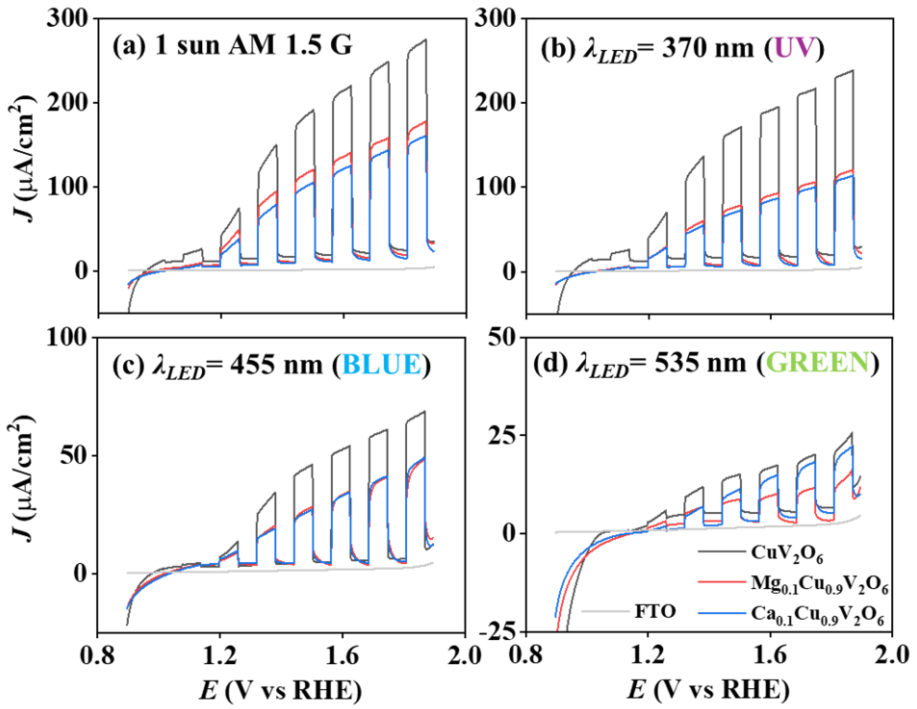

Figure 8.7. LSV curves with chopped front side illumination at (a) 1 sun AM 1.5G (b) λ_{LED} = 370 nm (UV), (c) λ_{LED} = 455 nm (blue) and (d) λ_{LED} = 535 nm (green) at the same photon flux of 1.6×10^{16} cm^{-2} s^{-1} in 0.1 M phosphate buffer as electrolyte with a potential scan rate of 20 mV s^{-1}

for CuV_2O_6, $Mg_{0.1}Cu_{0.9}V_2O_6$ and $Ca_{0.1}Cu_{0.9}V_2O_6$ photoanodes screen-printed on FTO.

Figure 8.8 shows LSV curves under chopped light with 1 sun AM 1.5G filter as light source with 0.1 M phosphate buffer and 0.1 M Na_2SO_3 as hole scavenger for CuV_2O_6, CaV_2O_6, MgV_2O_6, $Ca_{0.1}Cu_{0.9}V_2O_6$ and $Mg_{0.1}Cu_{0.9}V_2O_6$ electrodes. Except for the CaV_2O_6 film, a large current corresponding to the oxidation of sulfite is observed even in the dark, which is attributed to direct charge transfer from the FTO, due to only partial coverage of the FTO by the metal oxide material, consistent with the porous morphology observed in the SEM images. Hence, the use of a hole scavenger in this system is unsuitable for studying photo-generated hole transfer kinetics and was not further explored.

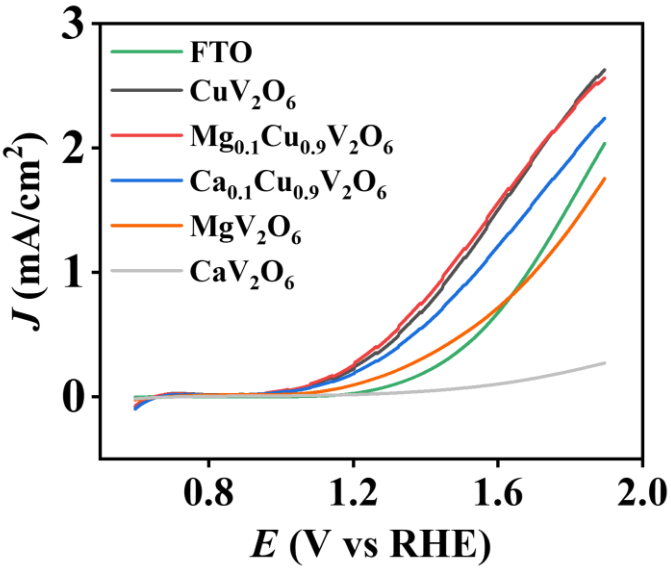

Figure 8.8. LSV curves with chopped light under 1 sun illumination with AM1.5 G filter with 0.1 M phosphate buffer and 0.1 M Na_2SO_3 as hole scavenger at a scan rate of 20 mV s^{-1} for CuV_2O_6, CaV_2O_6, MgV_2O_6, $Ca_{0.1}Cu_{0.9}V_2O_6$, and $Mg_{0.1}Cu_{0.9}V_2O_6$ films screen-printed on FTO.

The potential distribution at the semiconductor/electrolyte solution interface and interfacial charge transfer kinetics play a crucial role in

photocurrent generation, directly influencing the efficiency of charge separation, transport, charge transfer and recombination in the material. It should be kept in mind that water oxidation to oxygen involves the transfer of 4 holes and 4 protons, and the interfacial kinetics are expected to be very complex. Recent work on photoelectrochemical water oxidation at hematite illustrates these aspects, detailing the challenges to determine the reaction mechanism, the molecularity and reaction order of the rate-determining step, light intensity dependence, band edge unpinning and interfacial chemistry.[89] Charge transfer therefore does not simply correspond to hole transfer to the solution, but rather involves interfacial reactions at the semiconductor surface.

Carrier recombination may occur in the bulk or at the surface on localised states that may correspond to reaction intermediates or even charge transport states. Hence, the competition between charge transfer, recombination and charge transport depends on many factors. Therefore, when detailed information on the mechanisms cannot be accessed, it is preferred to use a simple model. The most generally used model considers that charge separation competes with bulk recombination on a short time scale, while surface recombination competes with charge transfer at longer times.[99] In addition, it is often assumed that charge transfer occurs via surface states corresponding to reaction intermediates, which also act as recombination centres.[99,288] Note that for porous, mesoscopic photoelectrodes the potential distribution is expected to be significantly different from classical single crystal semiconductors, which affects the driving force for charge separation and transport, thus complicating the interpretation of experimental results.[26]

To gain a more comprehensive understanding of these processes, a concurrent use of (P)EIS and IMPS techniques was employed in this study.[100,147] As discussed below, these complementary techniques provide valuable insights into the dynamic behaviour of charge carriers under operational conditions, enabling a detailed analysis of the factors affecting efficiency loss. In (P)EIS, the modulated applied potential is applied to the FTO substrate, and the partial coverage of the FTO indicates that the total impedance contained contributions from both the semiconductor/electrolyte solution and the FTO/electrolyte solution

interface. On the other hand, the modulated light intensity used in IMPS is only absorbed in the semiconductor. Thus, the effect of uncovered FTO may be smaller, providing an additional and complementary analysis of this complex system.

8.2.3. (Photo)electrochemical impedance spectroscopy

Figure 8.9 shows the (P)EIS plots as a function of applied potential under dark and blue (λ = 455 nm) LED illumination at a photon flux of 1.6×10^{16} cm^{-2} s^{-1} in 0.1 M phosphate buffer as electrolyte for FTO, CuV_2O_6, $Mg_{0.1}Cu_{0.9}V_2O_6$ and $Ca_{0.1}Cu_{0.9}V_2O_6$. The Nyquist graphs present similar characteristics in all cases, with one loop dominating the upper quadrant. On the other hand, the $Mg_{0.1}Cu_{0.9}V_2O_6$ and $Ca_{0.1}Cu_{0.9}V_2O_6$ electrodes show a second arc in the dark (refer to the Bode plots in **Figure 8.10**). Hence, surprisingly, the complex photoelectrode impedance can be characterised by one time constant for most cases; two time constants are only needed for the doped systems in the dark.

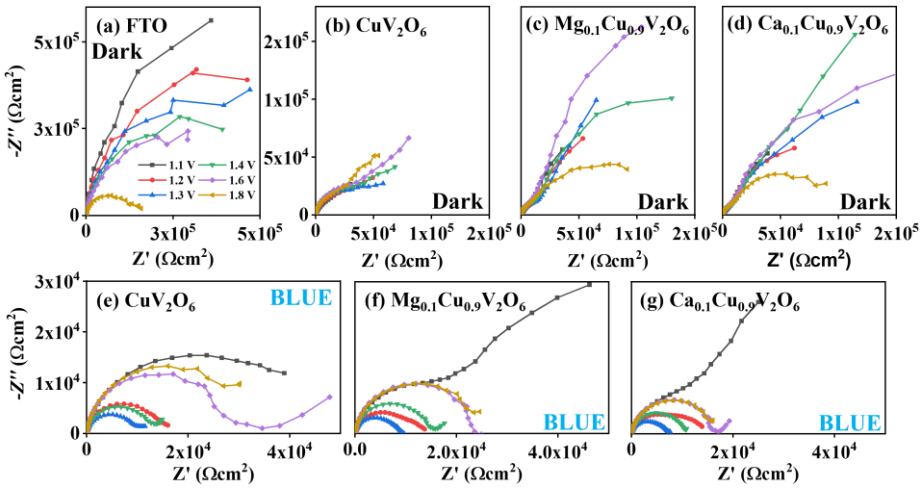

Figure 8.9. (P)EIS data plotted in Nyquist format at different applied potentials under (a-d) dark and (e-g) blue (λ = 455 nm) LED illumination at photon flux of 1.6×10^{16} cm^{-2} s^{-1} in 0.1 M phosphate buffer as electrolyte for (b,e) CuV_2O_6, (c,f) $Mg_{0.1}Cu_{0.9}V_2O_6$ and (d,g) $Ca_{0.1}Cu_{0.9}V_2O_6$ photoelectrodes screen-printed on FTO. The data for the FTO substrate as reference is shown in frame (a).

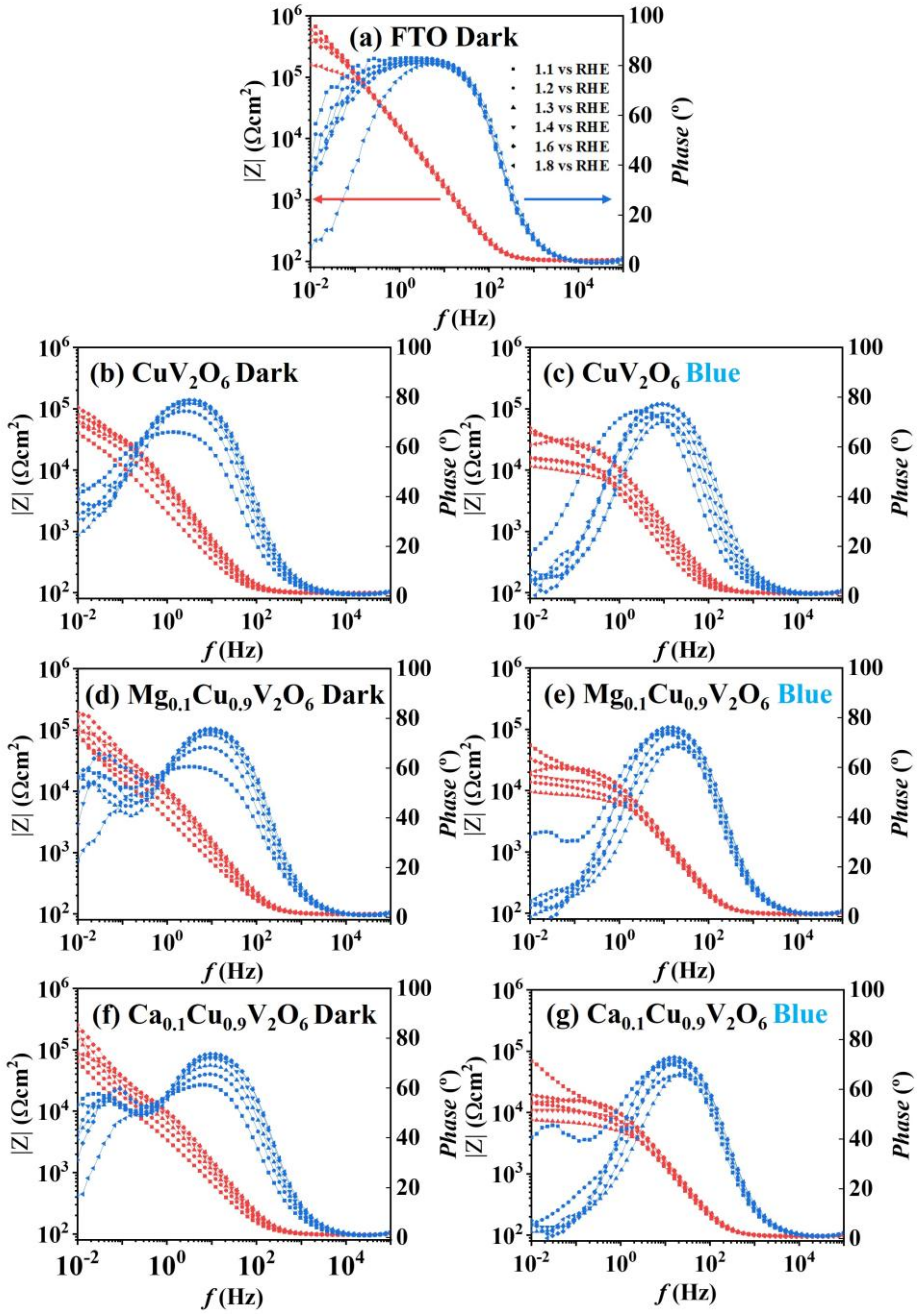

Figure 8.10. EIS Bode plots at different applied potentials under (a-d) dark and (e-g) blue (λ = 455 nm) LED illumination at photon flux of 1.6 x 10^{16} cm^{-2} s^{-1} in 0.1 M phosphate buffer as electrolyte for (b,c) CuV_2O_6, (d,e) $Mg_{0.1}Cu_{0.9}V_2O_6$ and (f,g) $Ca_{0.1}Cu_{0.9}V_2O_6$ photoanodes screen-printed on FTO and (a) FTO as reference.

Figure 8.11 shows an equivalent circuit that aims to illustrate the complexity of the photoelectrode electrical properties related to the morphology of the porous metal oxide film, considering that the FTO substrate is also in direct contact with the electrolyte solution. The FTO/electrolyte interface impedance appears in parallel to that corresponding to the metal oxide/electrolyte interface, and may be represented by a simple circuit, with an effective capacitance corresponding to the FTO capacitance in series with the Helmholtz capacitance at the electrolyte side, in parallel to a resistance that describes charge transfer.

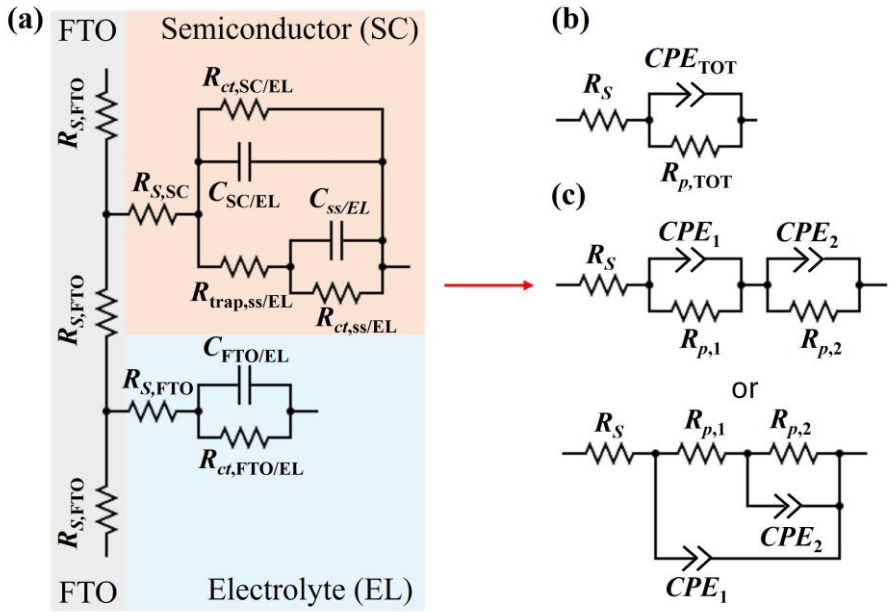

Figure 8.11. (a) Equivalent circuit for a typical photoelectrode with porous morphology and FTO in contact with the electrolyte solution. (b) Randles-type circuit used when only one loop is observed; and (c) simplified equivalent circuit applied when two loops are visible. R_{ct} represents the charge transfer resistance and R_p the parallel resistance.

The metal oxide/electrolyte impedance generally needs to be represented by a complex equivalent circuit, where the semiconductor capacitance is expected to be smaller than that of the Helmholtz layer, and additional processes involving electronic surface states that may also act as

recombination centres and charge transfer states need to be considered.[288] In addition, if trap-limited charge transport within the semiconductor affects the total impedance, a transmission line impedance is often used to model the system. However, if only one time constant (one semicircle) is observed in the EIS spectra, this complex total circuit is modelled by a reduced equivalent circuit shown in **Figure 8.11b**: the total capacitance contains contributions from the semiconductor, possibly including interfacial trap states, and the Helmholtz layer. The total parallel resistance comprises the resistances corresponding to generation, transport, trapping, interfacial charge transfer, and is proportional to the potential-dependent inverse slope of the *J-E* curve.

The R_s obtained from fitting the spectra to these circuits, shown in **Figure 8.12a**, is found to be essentially independent of material, and the same in the dark and under illumination, and is principally dominated by the FTO substrate.

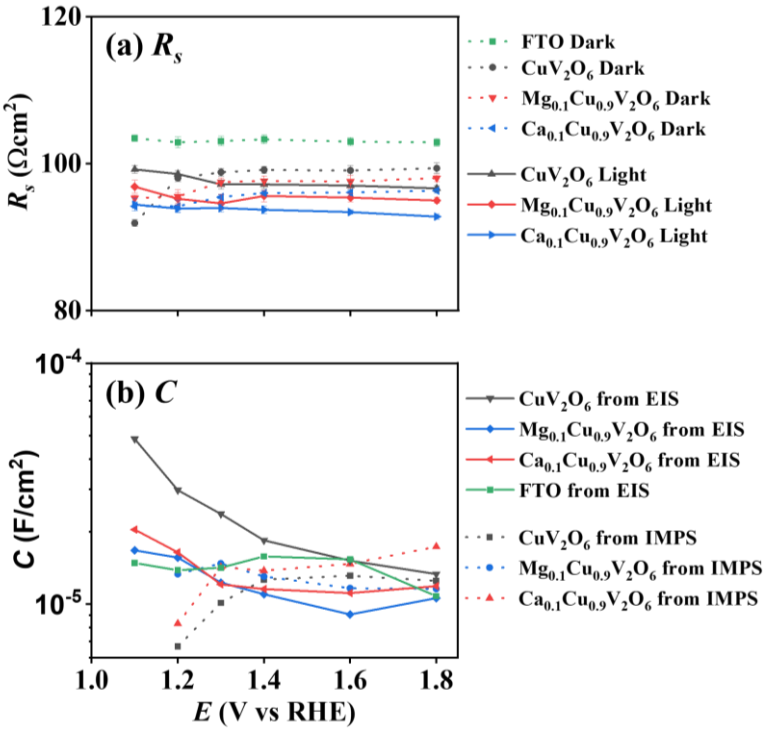

Figure 8.12. (a) R_S extracted from EIS; (b) C extracted from EIS and IMPS (calculated using f_{min} from IMPS and R_S from EIS) at different

applied potentials using a blue (λ = 455 nm) LED at a photon flux of 1.6 x 10^{16} cm^{-2} s^{-1} in 0.1 M phosphate buffer as electrolyte for FTO, CuV_2O_6, $Mg_{0.1}Cu_{0.9}V_2O_6$, and $Ca_{0.1}Cu_{0.9}V_2O_6$ screen-printed on FTO.

Figure 8.13 illustrates the quality of the fits at a representative potential (1.8 V vs RHE) under dark and light conditions, and the extracted impedance parameters along with the errors are summarised in **Table 8.1**.

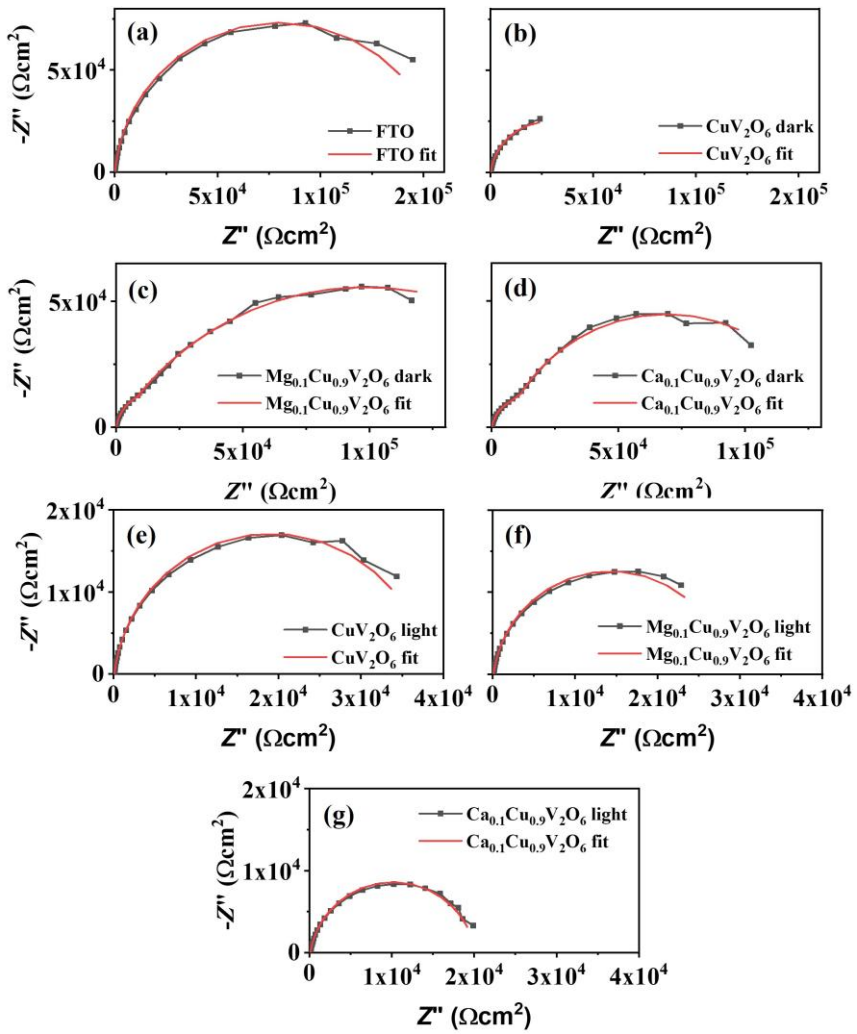

Figure 8.13. EIS Nyquist fitting at applied potentials of 1.8 V vs RHE in (a-d) dark and (e-g) blue (λ = 455 nm) LED illumination at photon flux

of 1.6 x 10^{16} cm^{-2} s^{-1} in 0.1 M phosphate buffer as electrolyte for (a) FTO as reference, (b,e) CuV_2O_6, (c,f) $Mg_{0.1}Cu_{0.9}V_2O_6$ and (d,g) $Ca_{0.1}Cu_{0.9}V_2O_6$ screen-printed on FTO.

Table 8.1. Equivalent circuit fitting parameters extracted from EIS measurements at 1.8 V vs RHE in dark and blue (λ = 455 nm) LED illumination at photon flux of 1.6 x 10^{16} cm^{-2} s^{-1} in 0.1 M phosphate buffer as electrolyte.

Material	Condition at 1.8 V vs RHE	R_s	R_{tr}	Q (CPE)	n_{CPE}	C_{eff}
		Ω cm^2	kΩ cm^2	$\mu s^n \Omega^{-1}$	-	μF cm^{-2}
FTO	Dark	102.9 ± 0.5	125.3 ± 1.2	8.4 ± 0.1	0.95	8.6 ± 0.0
CuV_2O_6	Dark	99.4 ± 0.7	44.0 ± 1.0	22.1 ± 0.2	0.92	22.5 ± 0.1
CuV_2O_6	Blue	96.6 ± 0.4	29.8 ± 0.2	11.3 ± 0.1	0.93	10.6 ± 0.0
$Mg_{0.1}Cu_{0.9}V_2O_6$	Dark HF loop	98.0 ± 0.4	25.7 ± 0.6	11.4 ± 0.1	0.91	10.3 ± 0.0
$Mg_{0.1}Cu_{0.9}V_2O_6$	Dark LF loop	-	175.6 ± 2.4	24.7 ± 0.4	0.72	44.9 ± 0.2
$Mg_{0.1}Cu_{0.9}V_2O_6$	Blue	95.0 ± 0.4	22.3 ± 0.2	9.5 ± 0.1	0.92	8.5 ± 0.0
$Ca_{0.1}Cu_{0.9}V_2O_6$	Dark HF loop	96.3 ± 0.3	21.6 ± 0.4	12.0 ± 0.1	0.91	10.6 ± 0.0
$Ca_{0.1}Cu_{0.9}V_2O_6$	Dark LF loop	-	100.8 ± 3.4	28.5 ± 0.6	0.78	41.4 ± 0.1
$Ca_{0.1}Cu_{0.9}V_2O_6$	Blue	92.8 ± 0.3	15.8 ± 0.1	11.3 ± 0.1	0.90	9.6 ± 0.0

Figure 8.14 shows $R_{p,TOT}$ for the spectra with one arc, and $R_{p,1}$ or $R_{p,2}$ for the results with two arcs (**Figure 8.11**), and the C_{eff} under dark and blue illumination conditions for FTO (as a reference), CuV_2O_6, $Mg_{0.1}Cu_{0.9}V_2O_6$ and $Ca_{0.1}Cu_{0.9}V_2O_6$ screen-printed onto FTO. The largest difference in R_p obtained from the high-frequency loop between dark and light is observed for the CuV_2O_6 photoelectrode, which is in concordance with the results observed in **Figure 8.7**. In the dark, R_p is essentially independent of potential, while under illumination R_p first decreased when changing the applied potential in the positive direction up to 1.3 V vs RHE, coinciding with the observation of the onset and increase of the photocurrent. Hence, in this potential regime, the parallel resistance is determined by the charge transfer resistance and its decrease translates into a larger photocurrent.[289–292] At more positive potential, R_p increases again, in agreement with the decreasing slope of the *J-E* curve reaching a saturated photocurrent. In this regime, the photocurrent is limited by the balance between generation, recombination and charge transfer.

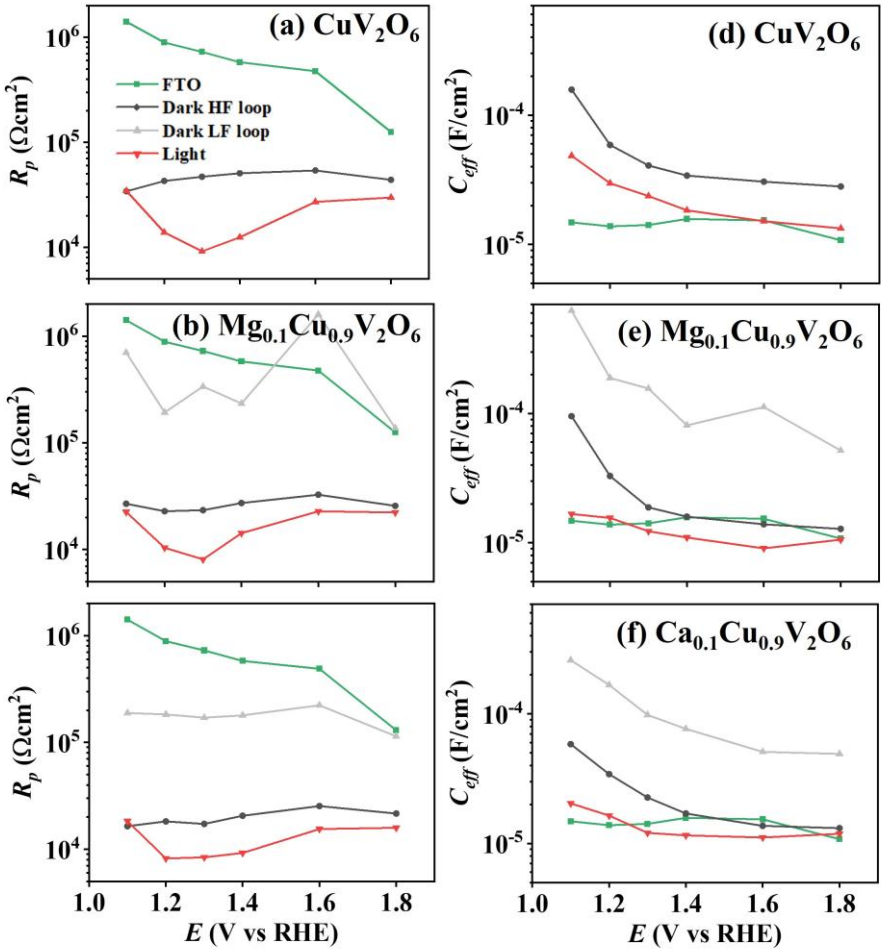

Figure 8.14. (a-c) Values for R_p and (d-f) C_{eff} extracted from the (P)EIS data at different applied potentials under dark and light conditions with blue (λ = 455 nm) LED at a photon flux of 1.6×10^{16} cm^{-2} s^{-1} in 0.1 M phosphate buffer as electrolyte for FTO as reference and (a,d) CuV_2O_6, (b,e) $Mg_{0.1}Cu_{0.9}V_2O_6$ and (c,f) $Ca_{0.1}Cu_{0.9}V_2O_6$ electrodes screen-printed on FTO.

Although the charge transfer resistance likely no longer dominates the total parallel resistance, slower charge transfer kinetics could also occur due to surface poisoning. Phosphate groups adsorbed to the photoelectrode surface are capable of passivating the catalytically active sites or reaction intermediates, thereby limiting hole transfer.[293,294]

Support for this hypothesis is provided by the FTIR-ATR spectra for films before and after PEC measurement (**Figure 8.15**), where new bands in the 1300 to 900 cm^{-1} regions appear exclusively for the photoelectrochemically treated films. These bands are consistent with phosphate groups either directly adsorbed onto the surface or bound to surface hydroxyls to form phosphorylated −OH species.[295,296]

On the other hand, the charge transfer resistance obtained from the low-frequency loop observed for $Mg_{0.1}Cu_{0.9}V_2O_6$ and $Ca_{0.1}Cu_{0.9}V_2O_6$ is very similar to that for bare FTO and can be attributed to the photoelectrode morphology. In this case, the FTO/electrolyte interface impedance is observed as a second arc at low frequencies.

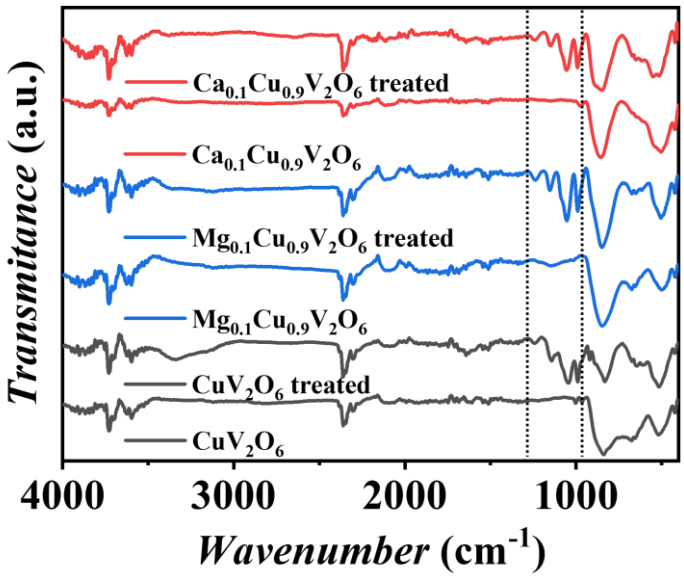

Figure 8.15. ATR-FTIR spectra of CuV_2O_6, $Mg_{0.1}Cu_{0.9}V_2O_6$, and $Ca_{0.1}Cu_{0.9}V_2O_6$ screen-printed on FTO, before and after photoelectrochemical measurements with phosphate buffer 0.1 M as electrolyte. The dotted lines indicate the region of interest at 1200-940 cm^{-1}.

The C_{eff} for bare FTO in contact with the electrolyte is about 15 $\mu F\ cm^{-2}$, in agreement with the expected value of the C_H.[64] The capacitance of the photoelectrodes is larger under dark conditions in the potential range up

to 1.4 V vs RHE, which indicates that the larger surface area for the $Mg_{0.1}Cu_{0.9}V_2O_6$ and $Ca_{0.1}Cu_{0.9}V_2O_6$ electrodes contributes to the differential capacitance. At more positive potentials, the capacitance is very similar to that of FTO implying the mixed oxides are depleted. For the CuV_2O_6 photoelectrode, the capacitance in the dark remains larger than for FTO, indicating that the CuV_2O_6 film still contributes to the measured capacitance, and that the surface remains in electronic contact with the FTO substrate.[297,298] Under illumination, the capacitive properties follow a similar trend; however, the effective capacitance is generally smaller than in the dark and closer to the value obtained for FTO. Combined, these results indicate that the impedance of the semiconductor is smaller under illumination.

8.3.4. Intensity-modulated photocurrent spectroscopy

Figure 8.16 shows the IMPS spectra as a function of the applied potentials under front side illumination using three LEDs: UV (λ = 370 nm), blue (λ = 455 nm) and green (λ = 535 nm) with the photon flux constant at 1.6×10^{16} cm^{-2} s^{-1} for CuV_2O_6, $Mg_{0.1}Cu_{0.9}V_2O_6$ and $Ca_{0.1}Cu_{0.9}V_2O_6$ photoanodes in a 0.1 M phosphate buffer electrolyte. The Nyquist-type plot of the CuV_2O_6 electrode is dominated principally by one loop in the 4th quadrant, with the characteristic f_{min}. For the $Mg_{0.1}Cu_{0.9}V_2O_6$ and $Ca_{0.1}Cu_{0.9}V_2O_6$ electrodes, at applied potentials more positive than 1.4 V vs RHE, a second loop appears in the 4th quadrant. The size of this second loop increases with more positive applied potential. Interestingly, the second loop is absent in the CuV_2O_6 film for any tested wavelength. It is also absent for $Mg_{0.1}Cu_{0.9}V_2O_6$ and $Ca_{0.1}Cu_{0.9}V_2O_6$ films under UV illumination. However, it do appear and develop upon increasing the wavelength; the frequency at the minimum of this second arc, f_{min2}, is observed at lower frequency than f_{min}.

The high-frequency loop in IMPS spectra is generally attributed to the cell's *RC* time constant, which is determined by the total (effective) capacitance and the series cell resistance.[98,284] For a photoelectrode on FTO, the series resistance would correspond to the FTO substrate, while the total capacitance would be determined by the semiconductor capacitance, the surface state capacitance and the Helmholtz layer

capacitance. **Figure 8.12b** shows the capacitance versus applied potential calculated from $C = (2\pi f_{\min} R_s)^{-1}$, where R_s is obtained from the EIS measurement (shown in **Figure 8.12a**). It can be observed that the capacitance increases upon shifting the applied potential from 1.2 to 1.4 V, and it saturates at about 15 μF cm^{-2} at more positive potentials. This relatively high value indicates that the semiconductor capacitance is similar in magnitude to that of the Helmholtz layer. This also implies that the applied potential is distributed between the semiconductor and the Helmholtz layer, resulting in a shift of the band edges upon changing the applied potential, i.e. band edge unpinning. The initial increase of the capacitance from 1.2 to 1.4 V vs RHE could indicate a buildup of hole density at the interface upon shifting the applied potential positively but may also result from surface recombination as observed at lower frequencies in this potential range (see below).

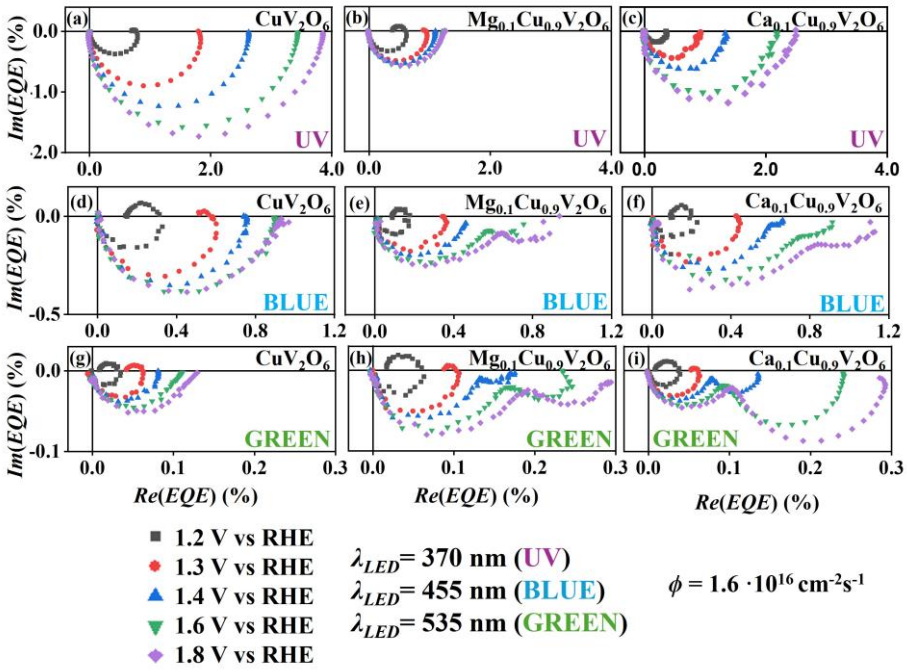

Figure 8.16. IMPS data in Nyquist plot format at different applied potentials under different wavelength LED illumination (a-c) UV $\lambda = 370$ nm, (d-f) blue $\lambda = 455$ nm, (g-i) green $\lambda = 535$ nm, at the same photon flux 1.6×10^{16} cm^{-2} s^{-1} in front side illumination with 0.1 M phosphate

buffer as electrolyte for (a,d,g) CuV_2O_6, (b,e,h) $Mg_{0.1}Cu_{0.9}V_2O_6$ and (c,f,i) $Ca_{0.1}Cu_{0.9}V_2O_6$ electrodes screen-printed on FTO.

For the high-frequency loop, in absence of a second loop in the 4th quadrant, the intersection with the real axis corresponds to the maximum *EQE*, excluding surface processes losses (i.e., unattenuated *EQE*), which increases with more positive applied potential. The *EQE* and therefore, the charge separation efficiency, decreases with larger wavelengths, reflecting the behaviour observed above in the *J-E* curves shown in **Figure 8.7**. At applied potentials more negative than 1.3 V vs RHE, a low-frequency loop appears in the 1st quadrant, where the frequency of the maximum reflects the competition between the hole transfer and surface recombination, according to the simple model where electrons in the conduction band may still reach the surface to recombine with (trapped) holes. However, this loop quickly disappeared at more positive potential, indicating that either fast electron extraction at the FTO interface or the internal field prevents surface recombination at these potentials. Moreover, it does not reappear under varying illumination intensity or for different wavelengths.

Consequently, the rate constants for k_{tr} and k_{rec} cannot be determined at more positive potentials. Notably, this behaviour is consistent with the photocurrent transients under chopped illumination (see **Figure 8.7**), which do not exhibit significant overshoot and delays, indicating minimal surface recombination.[99] These observations suggest that the photoresponse is not limited by surface recombination processes.

Figure 8.17 presents the IMPS spectra as a function of photon flux using different LEDs under front side illumination: UV (λ = 370 nm), blue (λ = 455 nm) and green (λ = 535 nm), at a constant applied potential of 1.8 V vs RHE for CuV_2O_6, $Mg_{0.1}Cu_{0.9}V_2O_6$ and $Ca_{0.1}Cu_{0.9}V_2O_6$ photoanodes.

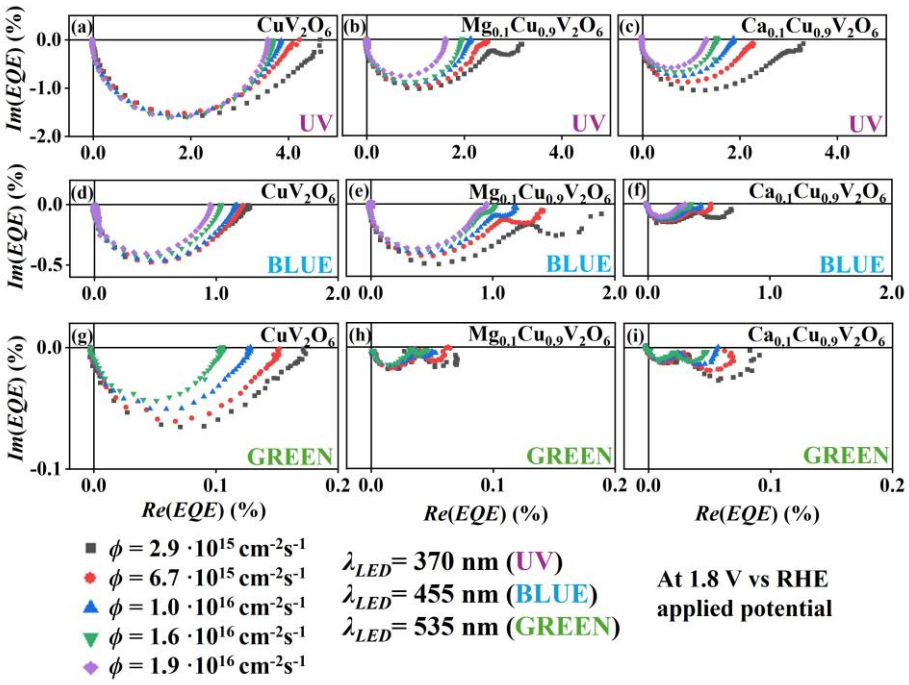

Figure 8.17. IMPS data in Nyquist plot format at varying photon flux under different wavelength LED illumination (a-c) UV λ = 370 nm, (d-f) blue λ = 455 nm, (g-i) green λ = 535 nm, at a fixed applied potential of 1.8 V vs RHE in 0.1 M phosphate buffer as electrolyte for (a,d,g) CuV_2O_6, (b,e,h) $Mg_{0.1}Cu_{0.9}V_2O_6$ and (c,f,i) $Ca_{0.1}Cu_{0.9}V_2O_6$ films screen-printed on FTO.

The *EQE* at the intersection on the real axis at low frequency decreases with increasing photon flux, indicating that efficiency losses due to bulk recombination become more significant at higher light intensities, i.e., larger charge densities. **Figure 8.18** shows a sublinear intensity dependence with a slope of about −0.5 for the Ca- and Mg-containing CuV_2O_6 samples. Similar sublinear trends have been reported in solar cells, where this observation is associated with the recombination mechanism.[299–303] Within this interpretation, the slope of about −0.5 points to second-order (bimolecular) recombination kinetics for the Ca- and Mg-containing samples. In contrast, the pure CuV_2O_6 material

shows a much weaker intensity dependence, closer to first order (monomolecular) kinetics.

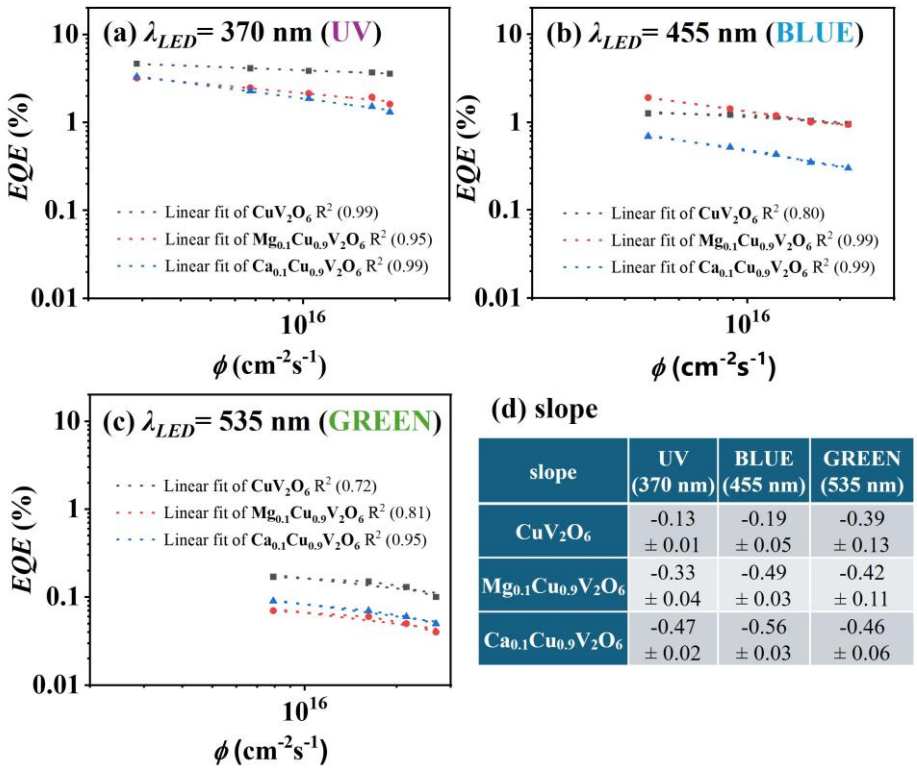

(d) slope

slope	UV (370 nm)	BLUE (455 nm)	GREEN (535 nm)
CuV_2O_6	-0.13 ± 0.01	-0.19 ± 0.05	-0.39 ± 0.13
$Mg_{0.1}Cu_{0.9}V_2O_6$	-0.33 ± 0.04	-0.49 ± 0.03	-0.42 ± 0.11
$Ca_{0.1}Cu_{0.9}V_2O_6$	-0.47 ± 0.02	-0.56 ± 0.03	-0.46 ± 0.06

Figure 8.18. *EQE* as a function of photon flux at an applied potential of 1.8 V vs RHE with 0.1 M phosphate buffer as an electrolyte at different wavelength LED illumination (a) UV λ = 370 nm, (b) blue λ = 455 nm, (c) green λ = 535 nm, and (d) extracted slope from linear fit for CuV_2O_6, $Mg_{0.1}Cu_{0.9}V_2O_6$ and $Ca_{0.1}Cu_{0.9}V_2O_6$ screen-printed on FTO. R^2 denotes the coefficient of determination and it is shown for each fit.

Once again, the second semicircle is absent for CuV_2O_6 film under any photon flux tested. In contrast, when the photon flux is sufficiently low, the magnesium and calcium copper vanadate electrodes develop a second arc, even under UV illumination. This second loop decreases as the light intensity increases.

Figure 8.19 shows f_{min} as a function of (**Figure 8.19a-c**) of the applied potential at the same photon flux of 1.6 × 10^{16} cm^{-2} s^{-1} and varying

photon flux (**Figure 8.19d-f**) at an applied potential of 1.8 V vs RHE, under different wavelength LED illumination for CuV_2O_6, $Mg_{0.1}Cu_{0.9}V_2O_6$ and $Ca_{0.1}Cu_{0.9}V_2O_6$ electrodes, respectively.

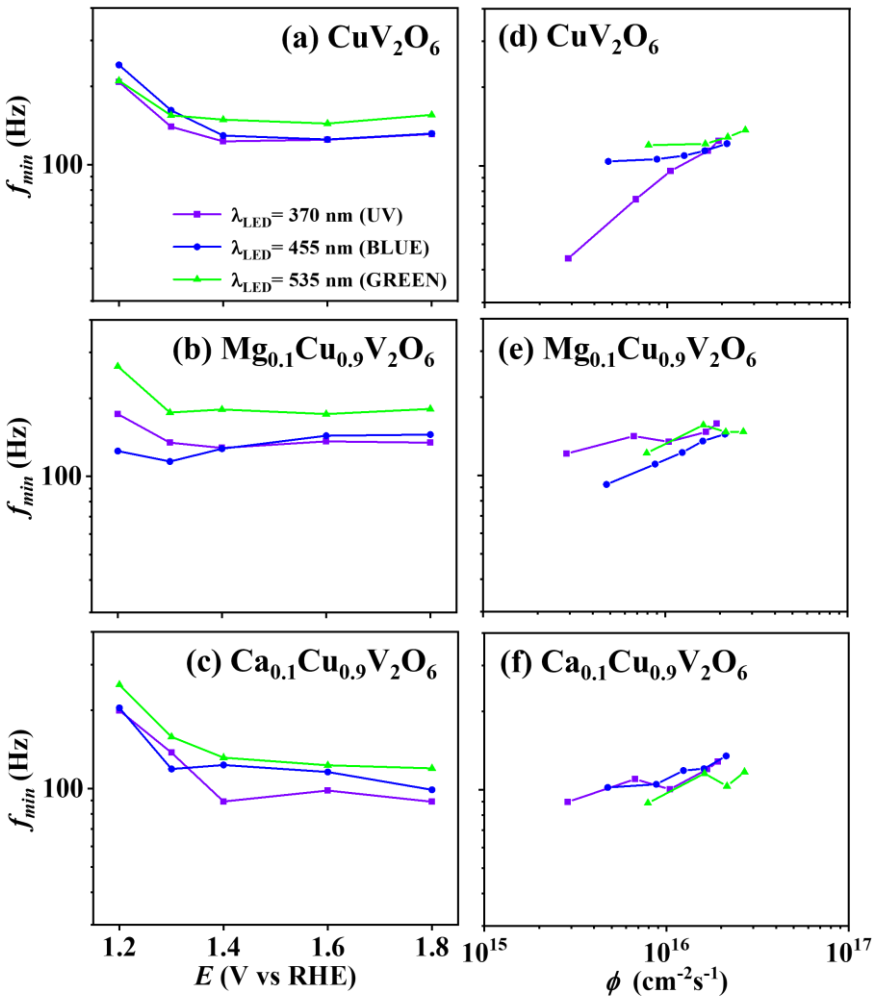

Figure 8.19. IMPS parameter f_{min} under different wavelength LED illumination, with 0.1 M phosphate buffer as electrolyte for (a-c) different applied potentials at the same photon flux 1.6×10^{16} cm^{-2} s^{-1} and for (d-f) different photon fluxes at an applied potential of 1.8 V vs RHE for (a,d) CuV_2O_6, (b,e) $Mg_{0.1}Cu_{0.9}V_2O_6$ and (c,f) $Ca_{0.1}Cu_{0.9}V_2O_6$ photoelectrodes screen-printed on FTO.

The f_{min} value is similar for all samples and is independent of the illumination wavelength and the external potential, except for the applied potential below 1.3 V vs RHE, which is influenced by the loop in the 1st quadrant in the Nyquist plot. In contrast, f_{min} shows a weak dependence on the photon flux and increases with increasing light intensity. There are several possible explanations for this observation, including the slight decrease of R_p under illumination. On the other hand, a similar light intensity dependence of f_{min} has been previously reported for nanostructured, mesoscopic TiO_2 and WO_3 photoelectrodes, among other materials. The observed dependence is generally attributed to trap-limited charge transport: as the light intensity increases, deeper traps are filled up, leading to shallower traps to govern the transport kinetics.[50,254–260] This effect is well-known in dye-sensitised solar cells, but it is not exclusive to nanostructured systems. Recent studies have demonstrated that trap-limited transport also occurs in bulk metal oxide photoanodes with larger particle sizes, such as $BiVO_4$.[304,305]

Figure 8.20 shows the parameter f_{min2} as a function of applied potential **(Figure 8.20a,b)** at a fixed photon flux of 1.6×10^{16} cm^{-2} s^{-1} and varying photon flux (**Figure 8.20c,d**) at an applied potential of 1.8 V vs RHE, under different wavelength LED illumination for $Mg_{0.1}Cu_{0.9}V_2O_6$ (**Figure 8.20a,c**) and $Ca_{0.1}Cu_{0.9}V_2O_6$ (**Figure 8.20b,d**) electrodes. The values of f_{min2} are similar for both electrodes and do not depend on the applied potential. On the other hand, f_{min2} decreased with increasing wavelength and depended strongly on the photon flux, increasing rapidly with increasing light intensity.

A second loop in the 4th quadrant has been shown to occur when the semiconductor and Helmholtz capacitance are of similar magnitude, with the total capacitance given by $(C_{sc}\ C_H)$ / $(C_{sc} + C_H)$, and the charge transfer constant becomes larger than the surface recombination constant;[98,284] this may be the case upon shifting the potential more positive, in the presence of a hole scavenger, or at larger photon flux.

The accumulation of photogenerated holes at higher light intensities near the surface may induce a modification in the potential drop across the Helmholtz layer, which may result in an increase of the hole transfer rate constant. This interpretation is consistent with prior work on light-

induced modulation of interfacial potentials in photoelectrochemical systems.[89,138,155,306] Interestingly, the second loop is only observed for the Mg- and Ca-modified copper vanadates, indicating modifications in the electronic structure upon partial substitution of Cu^{2+} with Mg^{2+} or Ca^{2+}. This may affect Cu−O hybridisation and lead to the formation of oxygen vacancies, which can act as trapping or recombination centres for charge carriers.[274,275,307] These defects increase the charge transfer kinetics to the solution, resulting in the second loop in the IMPS spectra; however, the DC photocurrent is actually smaller than for copper vanadate, indicating that the charge separation efficiency is smaller due to enhanced (bulk) recombination as confirmed by the smaller high-frequency loop.

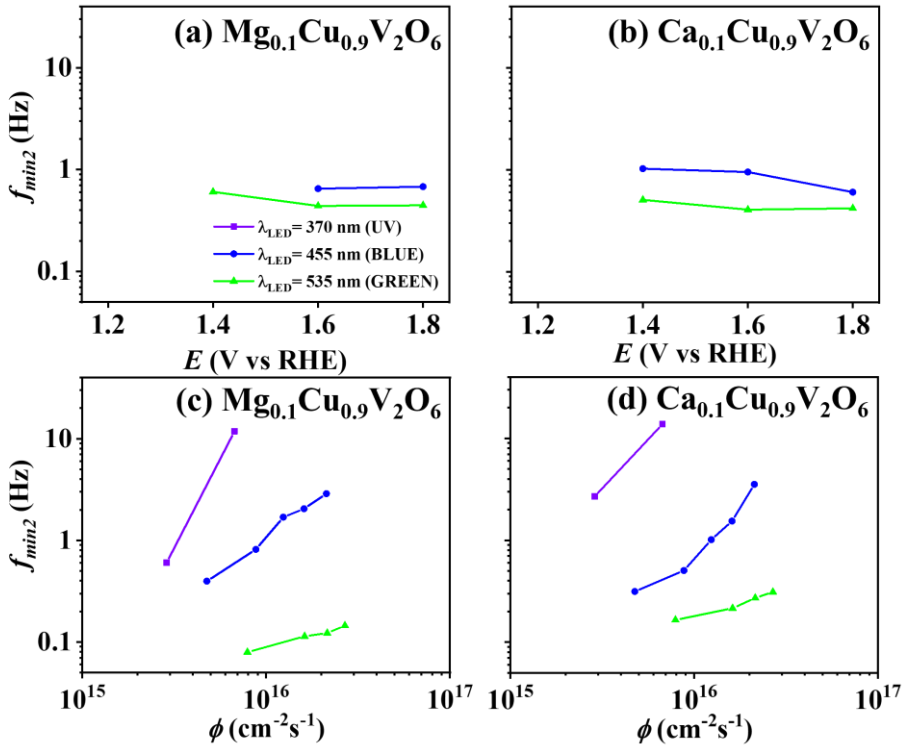

Figure 8.20. f_{min2} under different wavelength LED illumination with 0.1 M phosphate buffer as an electrolyte at (a,b) different applied potentials at the same photon flux 1.6×10^{16} cm^{-2} s^{-1} and at (c,d) different photon fluxes at an applied potential of 1.8 V vs RHE for (a,c) $Mg_{0.1}Cu_{0.9}V_2O_6$ and (b,d) $Ca_{0.1}Cu_{0.9}V_2O_6$ photoanodes screen-printed on FTO. Note that a second loop was not observed for CuV_2O_6, which was also the case for

several potentials and light intensities for the modified materials, hence f_{min2} could not be determined under these conditions.

8.3.5. Putting the (P)EIS and IMPS data together

The characteristic frequencies of the different interfacial processes considered in this chapter are summarised in **Figure 8.21**.

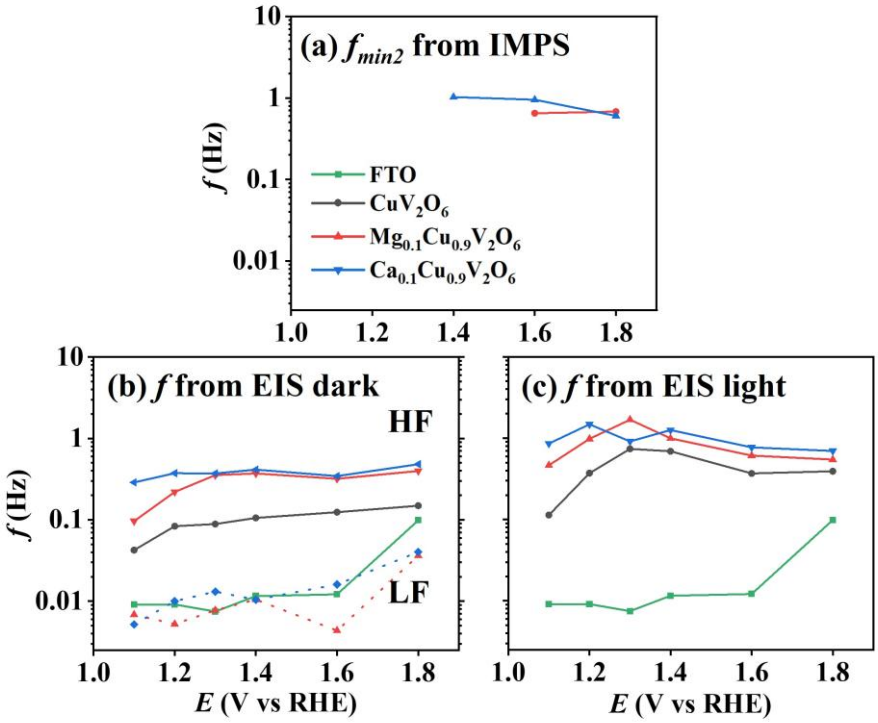

Figure 8.21. *f* extracted from (a) IMPS (b) EIS in dark conditions and (c) PEIS under illumination. The photon flux was fixed at 1.6×10^{16} cm^{-2} s^{-1} with blue (λ = 455 nm) LED in 0.1 M phosphate buffer as electrolyte for FTO as reference, CuV_2O_6, $Mg_{0.1}Cu_{0.9}V_2O_6$, and $Ca_{0.1}Cu_{0.9}V_2O_6$ films screen-printed on FTO.

Under dark conditions, the low-frequency loop in the EIS spectra of magnesium and calcium vanadate samples is attributed to the FTO substrate. In contrast, under illumination, the inverse time constant

extracted from PEIS matched with the low-frequency loop characterised by f_{min2} in IMPS measurement, under the same conditions. Hence, the low-frequency time constant from IMPS and the time constant in PEIS describe the charge transfer kinetics at the photoelectrode interface. IMPS results in additional information on the potential distribution and total capacitance in the high-frequency loop. Furthermore, the surface recombination feature observed in the 1st quadrant of IMPS spectra in the potential range of 1.2 to 1.4 V vs RHE cannot be distinguished in the PEIS measurements, indicating the complementary character of the two small-signal modulation techniques.

Finally, the two parameters *LHE* and the *EQE*, of critical importance to practical applications of these materials (e.g., energy conversion), as extracted from chronoamperometry and IMPS data, may be compared. This is shown in **Figure 8.22** as a function of wavelength for CuV_2O_6, $Mg_{0.1}Cu_{0.9}V_2O_6$ and $Ca_{0.1}Cu_{0.9}V_2O_6$ photoelectrodes at a potential of 1.8 V vs RHE and the same photon flux of 1.6×10^{16} cm^{-2} s^{-1} for each LED.

Although the *LHE* increases up to 400 nm and remains constant until 600 nm, both *EQE*, extracted from chronoamperometry and from IMPS, decreased with increasing wavelength, which mirrors the behaviour observed in **Figure 8.5**.

This observation is attributed to the electronic band structure of α-CuV_2O_6.[274] The top of the valence band is primarily composed of strongly hybridised Cu 3d−O 2p orbitals, whereas the bottom of the conduction band is dominated by V 3d states with a minor contribution from O 2p orbitals. At shorter wavelengths (UV illumination), the photon energy is sufficiently high to drive direct transitions from the valence band to the conduction band, leading to efficient charge carrier generation and, consequently, a high *EQE*. In contrast, at larger wavelengths, even though the material continues to absorb light (as indicated by the constant *LHE*), the lower photon energies are insufficient to effectively promote electrons via a direct optical transition. Instead, any excitation involves the midgap states, primarily Cu 3d e_g states hybridised with O 2p, which require an O-p to O-p transition that is intrinsically less favourable. This results in a reduced

efficiency in generating free carriers and can account for the observed decrease in *EQE* with increasing wavelength.[274,275,280,308]

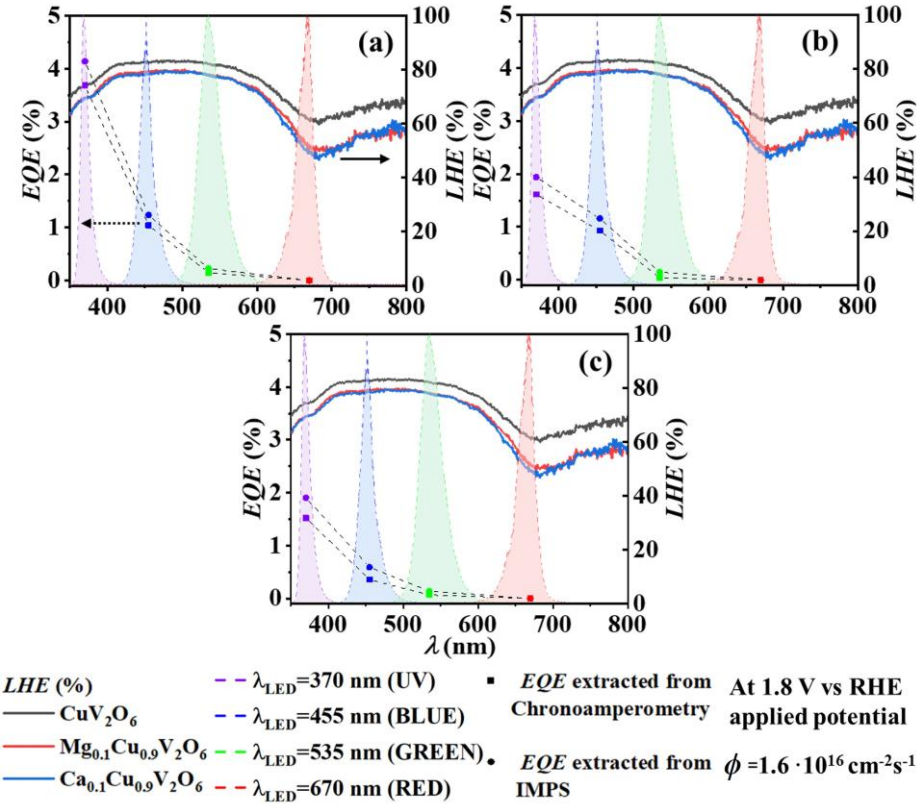

Figure 8.22. *LHE* and *EQE* extracted from chronoamperometry (circles) and IMPS (squares) vs illumination wavelength for (a) CuV_2O_6, (b) $Mg_{0.1}Cu_{0.9}V_2O_6$, and (c) $Ca_{0.1}Cu_{0.9}V_2O_6$ screen-printed on FTO, at an applied potential of 1.8 V vs RHE and photon flux of 1.6×10^{16} cm^{-2} s^{-1}. The emission spectrum of each used LED in the PEC measurements is represented by dashed lines.

It has been noted (**Figures 8.5** and **8.22**) that a significant portion of the absorbed photons do not generate mobile charge carriers seems to be prevalent for several metal oxide semiconductors as recently reviewed by other authors.[279] Interestingly, this group indeed includes copper vanadates as well (cf., see **Figure 8.7** cited in their review), and four separate sets of data on declining *EQE* (or *IQE*) vs wavelength for copper vanadates were cited by these authors.[279] This alloying strategy was

motivated by the potential of alkaline earth metals, such as Mg and Ca, to enhance water adsorption properties and alter the electronic structure in a way that could reduce recombination losses, thereby improving photocarrier generation and injection efficiency.[274,275,308] However, the optimistic projection by these authors[279] that photocarrier generation yield losses can be possibly mitigated by alloying does not seem to be borne out by the trends in this study on alloying Cu with either Mg or Ca within the vanadate compound framework.

Nevertheless, the results presented in this chapter provide valuable insights into how alkaline earth substitution affects the optical and interfacial properties of multinary vanadates. These findings contribute to a broader understanding of the challenges in designing efficient photoelectrodes and highlight the need for further exploration of compositional tuning strategies in complex metal oxides.

8.4. Conclusions

The combined use of IMPS and (P)EIS in this chapter has furnished useful insights into the dynamic consequences of partially or wholly replacing copper with an alkaline earth metal (Mg, Ca) in a metavanadate compound matrix (MV_2O_6). Our new data on these compounds and alloys also show that the phenomenon of nonunity photogeneration yield of mobile charge carriers pervades many transition metal oxide semiconductors (both binary and ternary compounds) and in this sense, is more prevalent than may have been envisioned. Indeed, the notion of optoelectronic behaviour akin to “bound excitons” may be evoked for photocarriers generated from localised optical transitions of the d−d type. Mitigating this trend and improving *EQE* (or *IQE*), and thereby the overall photoconversion efficiencies of devices based on these materials, would require research beyond the scope of the present study.

Together with the preceding results chapters, the analysis presented here completes the progression from interface engineering, through morphology-dependent behaviour, to composition-dependent charge carrier dynamics in metal oxide photoelectrodes. These chapters converge on the central idea of this thesis: that photoelectrochemical

performance is governed not only by light absorption, surface area, or composition, but by the balance between carrier generation, charge extraction, recombination, and transfer at the semiconductor/electrolyte interface. The following **general conclusions** synthesise these findings across the different material systems and identify the common limitations that must be addressed to improve photoelectrochemical water-splitting devices.

General conclusions

This thesis demonstrates that the performance of semiconductor-based photoelectrochemical systems cannot be understood solely in terms of intrinsic material properties but must be interpreted within the context of the complete photoelectrode architecture and operating conditions. In particular, charge carrier dynamics emerge as the central factor governing efficiency, arising from the competition between generation, transport, interfacial transfer, and recombination processes.

The systems studied in **Chapters 6**, **7**, and **8** provide complementary examples of how interface design, morphology, and composition influence these charge carrier dynamics under different photoelectrochemical conditions.

A key outcome of this work is that strategies commonly used to improve performance, such as compositional modification, nanostructuring, or defect engineering, do not lead to universally beneficial effects. Instead, their impact depends critically on the nature of the material itself and on how these modifications influence the dominant charge carrier pathways under specific operating conditions. As a result, improvements observed in one configuration do not necessarily translate to others, highlighting the importance of evaluating materials within their intended functional environment.

The results further show that interfacial processes play a decisive role in determining the overall photoelectrochemical response. This is particularly evident in the PCN-222-based electrodes, where the use of charge-selective layers modifies the extraction pathways and determines the directionality of the photocurrent. In this case, the interface is not merely a passive boundary, but an active component that can dominate

the observed response of the photoactive material by controlling the balance between charge extraction and recombination losses.

In addition, this thesis reveals that defects and surface states play a dual role in photoelectrochemical systems. While they can facilitate interfacial charge transfer by providing intermediate states, they can also enhance recombination pathways, reducing overall efficiency. The net effect therefore depends on the relative rates of these competing processes, emphasising the need for a controlled and quantitative understanding of defect-mediated charge dynamics. This is particularly relevant for the metal vanadate systems, where capacitance contributions and frequency-resolved kinetic features provide insight into the role of surface states in the measured photoelectrochemical response.

A further important conclusion is that morphology must be considered in relation to the dominant transport regime. The comparison between WO_3 nanoparticles and nanofibres shows that increasing surface area and reducing characteristic dimensions may enhance performance in systems governed by surface reactions, such as photocatalytic systems, but can become detrimental when directional charge transport and carrier collection are required, such as photoelectrochemical systems. This highlights the existence of inherent trade-offs in material design, where optimisation of one parameter may negatively impact another.

Finally, the combined application of steady-state and frequency-resolved techniques has proven to be a powerful approach to disentangle the processes governing photoelectrochemical performance. By enabling the separation of charge transfer and recombination dynamics, this methodology provides a more complete and mechanistic understanding of the system, which is essential for guiding the design of improved materials and device architectures.

Overall, this thesis establishes that the effective improvement of photoelectrochemical systems requires a system-level approach, where material properties, morphology, defects, and interfaces are considered as interconnected factors. By combining the fabrication and evaluation of semiconductor photoelectrodes, material and electrode modification, and steady-state and small-perturbation analysis, the work addresses the specific objectives and identifies common performance-limiting

processes across the systems studied. The insights obtained provide a framework for the development of more efficient and robust photoelectrodes for solar fuel production, based on the controlled management of charge carrier dynamics.

Conclusiones generales

Esta tesis demuestra que el rendimiento de los sistemas fotoelectroquímicos basados en semiconductores no puede entenderse únicamente en términos de las propiedades intrínsecas del material, sino que debe interpretarse en el contexto de la arquitectura completa del fotoelectrodo y de las condiciones de operación. En particular, la dinámica de los portadores de carga emerge como el factor central que gobierna la eficiencia, resultado de la competencia entre los procesos de generación, transporte, transferencia interfacial y recombinación.

Los sistemas estudiados en los **Capítulos 6**, **7**, y **8** proporcionan ejemplos complementarios de cómo el diseño de interfaces, la morfología y la composición influyen en esta dinámica de portadores de carga bajo diferentes condiciones fotoelectroquímicas.

Un resultado clave de esta tesis es que las estrategias comúnmente empleadas para mejorar el rendimiento, como la modificación composicional, la nanoestructuración o la ingeniería de defectos, no conducen a efectos universalmente beneficiosos. Por el contrario, su impacto depende de forma crítica tanto de la naturaleza del propio material como de cómo estas modificaciones influyen en las rutas dominantes de los portadores de carga bajo condiciones específicas de operación. Como consecuencia, las mejoras observadas en una configuración no necesariamente se trasladan a otras, lo que pone de manifiesto la importancia de evaluar los materiales dentro de su entorno funcional previsto.

Los resultados también muestran que los procesos interfaciales desempeñan un papel decisivo en la determinación de la respuesta fotoelectroquímica global. Esto es particularmente evidente en los fotoelectrodos basados en PCN-222, donde el uso de capas selectivas de

carga modifica las rutas de extracción y determina la direccionalidad de la fotocorriente. En este caso, la interfaz no es simplemente un límite pasivo, sino un componente activo que puede dominar la respuesta observada del material fotoactivo al controlar el equilibrio entre la extracción de carga y las pérdidas por recombinación.

Además, este trabajo pone de manifiesto el papel dual de los defectos y de los estados superficiales en los sistemas fotoelectroquímicos. Aunque pueden facilitar la transferencia de carga interfacial al proporcionar estados intermedios, también pueden favorecer rutas de recombinación, reduciendo la eficiencia global. El efecto neto depende, por tanto, de las velocidades relativas de estos procesos en competencia, lo que resalta la necesidad de una comprensión controlada y cuantitativa de la dinámica de carga mediada por defectos. Esto resulta especialmente relevante para los sistemas de vanadatos metálicos, donde las contribuciones capacitivas y los rasgos cinéticos resueltos en frecuencia proporcionan información sobre el papel de los estados superficiales en la respuesta fotoelectroquímica medida.

Otra conclusión relevante es que la morfología debe considerarse en relación con el régimen dominante de transporte. La comparación entre nanopartículas y nanofibras de WO_3 muestra que el aumento del área superficial y la reducción de las dimensiones características pueden mejorar el rendimiento en sistemas dominados por procesos superficiales, como los sistemas fotocatalíticos, pero pueden resultar perjudiciales cuando se requiere transporte direccional de carga y una recolección eficiente de portadores, como ocurre en sistemas fotoelectroquímicos. Esto pone de relieve la existencia de compromisos inherentes en el diseño de materiales, donde la optimización de un parámetro puede afectar negativamente a otros.

Por último, la aplicación combinada de técnicas en estado estacionario y técnicas resueltas en frecuencia ha demostrado ser una herramienta poderosa para desentrañar los procesos que gobiernan el rendimiento fotoelectroquímico. Al permitir separar la dinámica de transferencia de carga y de recombinación, esta metodología proporciona una comprensión más completa y mecanística del sistema, lo cual resulta

esencial para guiar el diseño de materiales y arquitecturas de dispositivo mejoradas.

En conjunto, esta tesis establece que la optimización de los sistemas fotoelectroquímicos requiere un enfoque a nivel de sistema, en el que las propiedades del material, la morfología, los defectos y las interfaces se consideren como factores interconectados. Mediante la combinación de la fabricación y evaluación de fotoelectrodos semiconductores, la modificación de materiales y electrodos, y el análisis mediante técnicas en estado estacionario y de pequeña perturbación, este trabajo responde a los objetivos específicos e identifica procesos comunes que limitan el rendimiento en los sistemas estudiados. Los resultados obtenidos proporcionan un marco para el desarrollo de fotoelectrodos más eficientes y estables para la producción de combustibles solares, basado en el control de la dinámica de los portadores de carga.

References

(1) Smalley, R. E. Future Global Energy Prosperity: The Terawatt Challenge. *MRS Bull.* **2005**, *30* (6), 412–417. https://doi.org/10.1557/mrs2005.124.

(2) Ritchie, H.; Rosado, P.; Roser, M. Energy Production and Consumption. *Our World in Data* **2020**. https://archive.ourworldindata.org/20260508-144950/energy-production-consumption.html

(3) Ritchie, H. How Have the World's Energy Sources Changed over the Last Two Centuries? *Our World in Data* **2021**. https://archive.ourworldindata.org/20260507-171259/global-energy-200-years.html

(4) Scafetta, N. Impacts and Risks of "Realistic" Global Warming Projections for the 21st Century. *Geoscience Frontiers* **2024**, *15* (2), 101774. https://doi.org/10.1016/j.gsf.2023.101774.

(5) Allen, M. R.; Frame, D. J.; Huntingford, C.; Jones, C. D.; Lowe, J. A.; Meinshausen, M.; Meinshausen, N. Warming Caused by Cumulative Carbon Emissions towards the Trillionth Tonne. *Nature* **2009**, *458* (7242), 1163–1166. https://doi.org/10.1038/nature08019.

(6) Van Vuuren, D. P.; Edmonds, J.; Kainuma, M.; Riahi, K.; Thomson, A.; Hibbard, K.; Hurtt, G. C.; Kram, T.; Krey, V.; Lamarque, J.-F.; Masui, T.; Meinshausen, M.; Nakicenovic, N.; Smith, S. J.; Rose, S. K. The Representative Concentration Pathways: An Overview. *Climatic Change* **2011**, *109* (1–2), 5–31. https://doi.org/10.1007/s10584-011-0148-z.

(7) *Solar Hydrogen Generation: Toward a Renewable Energy Future*; Rajeshwar, K., Licht, S., McConnell, R., Eds.; SpringerLink Bücher; Springer New York: New York, NY, **2008**. https://doi.org/10.1007/978-0-387-72810-0.

(8) Cook, T. R.; Dogutan, D. K.; Reece, S. Y.; Surendranath, Y.; Teets, T. S.; Nocera, D. G. Solar Energy Supply and Storage for the Legacy and Nonlegacy Worlds. *Chem. Rev.* **2010**, *110* (11), 6474–6502. https://doi.org/10.1021/cr100246c.

(9) De Castro, C.; Mediavilla, M.; Miguel, L. J.; Frechoso, F. Global Solar Electric Potential: A Review of Their Technical and Sustainable Limits. *Renewable and Sustainable Energy Reviews* **2013**, *28*, 824–835. https://doi.org/10.1016/j.rser.2013.08.040.

(10) Zidanšek, A.; Ambrožič, M.; Milfelner, M.; Blinc, R.; Lior, N. Solar Orbital Power: Sustainability Analysis. *Energy* **2011**, *36* (4), 1986–1995. https://doi.org/10.1016/j.energy.2010.10.030.

(11) Hosenuzzaman, M.; Rahim, N. A.; Selvaraj, J.; Hasanuzzaman, M.; Malek, A. B. M. A.; Nahar, A. Global Prospects, Progress, Policies, and Environmental Impact of Solar Photovoltaic Power Generation. *Renewable and Sustainable Energy Reviews* **2015**, *41*, 284–297. https://doi.org/10.1016/j.rser.2014.08.046.

(12) Green, M. A.; Dunlop, E. D.; Yoshita, M.; Kopidakis, N.; Bothe, K.; Siefer, G.; Hao, X. Solar Cell Efficiency Tables (Version 62). *Progress in Photovoltaics* **2023**, *31* (7), 651–663. https://doi.org/10.1002/pip.3726.

(13) Mdallal, A.; Yasin, A.; Mahmoud, M.; Abdelkareem, M. A.; Alami, A. H.; Olabi, A. G. A Comprehensive Review on Solar Photovoltaics: Navigating Generational Shifts, Innovations, and Sustainability. *Sustainable Horizons* **2025**, *13*, 100137. https://doi.org/10.1016/j.horiz.2025.100137.

(14) Barber, J. Photosynthetic Energy Conversion: Natural and Artificial. *Chem. Soc. Rev.* **2009**, *38* (1), 185–196. https://doi.org/10.1039/B802262N.

(15) Chu, S.; Majumdar, A. Opportunities and Challenges for a Sustainable Energy Future. *Nature* **2012**, *488* (7411), 294–303. https://doi.org/10.1038/nature11475.

(16) Song, H.; Luo, S.; Huang, H.; Deng, B.; Ye, J. Solar-Driven Hydrogen Production: Recent Advances, Challenges, and Future Perspectives. *ACS Energy Lett.* **2022**, *7* (3), 1043–1065. https://doi.org/10.1021/acsenergylett.1c02591.

(17) Alobaid, A.; Adomaitis, R. A. Optimal Design of a Coupled Photovoltaic–Electrolysis-Battery System for Hydrogen Generation.

Sustainable Energy Fuels **2023**, *7* (6), 1395–1414. https://doi.org/10.1039/D2SE01555B.

(18) Khaselev, O. High-Efficiency Integrated Multijunction Photovoltaic/Electrolysis Systems for Hydrogen Production. *International Journal of Hydrogen Energy* **2001**, *26* (2), 127–132. https://doi.org/10.1016/S0360-3199(00)00039-2.

(19) Shaner, M. R.; Atwater, H. A.; Lewis, N. S.; McFarland, E. W. A Comparative Technoeconomic Analysis of Renewable Hydrogen Production Using Solar Energy. *Energy Environ. Sci.* **2016**, *9* (7), 2354–2371. https://doi.org/10.1039/C5EE02573G.

(20) Kudo, A.; Miseki, Y. Heterogeneous Photocatalyst Materials for Water Splitting. *Chem. Soc. Rev.* **2009**, *38* (1), 253–278. https://doi.org/10.1039/B800489G.

(21) Hisatomi, T.; Kubota, J.; Domen, K. Recent Advances in Semiconductors for Photocatalytic and Photoelectrochemical Water Splitting. *Chem. Soc. Rev.* **2014**, *43* (22), 7520–7535. https://doi.org/10.1039/C3CS60378D.

(22) Osterloh, F. E. Inorganic Materials as Catalysts for Photochemical Splitting of Water. *Chem. Mater.* **2008**, *20* (1), 35–54. https://doi.org/10.1021/cm7024203.

(23) Roger, I.; Shipman, M. A.; Symes, M. D. Earth-Abundant Catalysts for Electrochemical and Photoelectrochemical Water Splitting. *Nat Rev Chem* **2017**, *1* (1), 0003. https://doi.org/10.1038/s41570-016-0003.

(24) Jiang, C.; Moniz, S. J. A.; Wang, A.; Zhang, T.; Tang, J. Photoelectrochemical Devices for Solar Water Splitting – Materials and Challenges. *Chem. Soc. Rev.* **2017**, *46* (15), 4645–4660. https://doi.org/10.1039/C6CS00306K.

(25) Van De Krol, R.; Liang, Y.; Schoonman, J. Solar Hydrogen Production with Nanostructured Metal Oxides. *J. Mater. Chem.* **2008**, *18* (20), 2311. https://doi.org/10.1039/b718969a.

(26) Oskam, G.; Coria Quiñones, S. D.; Expósito-Gálvez, J. C.; Jiménez Sandoval, O.; Rodríguez Gutiérrez, I. G. Photoelectrochemical Characterization of Metal Oxide Semiconductors for Solar Water Splitting Using Intensity-Modulated Photocurrent Spectroscopy. In *Photoelectrochemical Engineering*

for Solar Harvesting; Elsevier, **2024**; pp 311–352. https://doi.org/10.1016/B978-0-323-95494-5.00013-6.

(27) Murphy, A.; Barnes, P.; Randeniya, L.; Plumb, I.; Grey, I.; Horne, M.; Glasscock, J. Efficiency of Solar Water Splitting Using Semiconductor Electrodes. *International Journal of Hydrogen Energy* **2006**, *31* (14), 1999–2017. https://doi.org/10.1016/j.ijhydene.2006.01.014.

(28) Weber, M.; Dignam, M. Splitting Water with Semiconducting Photoelectrodes—Efficiency Considerations. *International Journal of Hydrogen Energy* **1986**, *11* (4), 225–232. https://doi.org/10.1016/0360-3199(86)90183-7.

(29) Bolton, J. R.; Strickler, S. J.; Connolly, J. S. Limiting and Realizable Efficiencies of Solar Photolysis of Water. *Nature* **1985**, *316* (6028), 495–500. https://doi.org/10.1038/316495a0.

(30) Hu, S.; Xiang, C.; Haussener, S.; Berger, A. D.; Lewis, N. S. An Analysis of the Optimal Band Gaps of Light Absorbers in Integrated Tandem Photoelectrochemical Water-Splitting Systems. *Energy Environ. Sci.* **2013**, *6* (10), 2984. https://doi.org/10.1039/c3ee40453f.

(31) Chen, S.; Huang, D.; Xu, P.; Xue, W.; Lei, L.; Cheng, M.; Wang, R.; Liu, X.; Deng, R. Semiconductor-Based Photocatalysts for Photocatalytic and Photoelectrochemical Water Splitting: Will We Stop with Photocorrosion? *J. Mater. Chem. A* **2020**, *8* (5), 2286–2322. https://doi.org/10.1039/C9TA12799B.

(32) Bonn, M.; Wang, F.; Shan, J.; Heinz, T. F.; Hendry, E. Ultrafast Scattering of Electrons in TiO_2. In *Femtochemistry and Femtobiology*; Elsevier, **2004**; pp 517–520. https://doi.org/10.1016/B978-044451656-5/50100-6.

(33) Van De Lagemaat, J.; Zhu, K.; Benkstein, K. D.; Frank, A. J. Temporal Evolution of the Electron Diffusion Coefficient in Electrolyte-Filled Mesoporous Nanocrystalline TiO_2 Films. *Inorganica Chimica Acta* **2008**, *361* (3), 620–626. https://doi.org/10.1016/j.ica.2007.03.051.

(34) Bak, T.; Nowotny, M. K.; Sheppard, L. R.; Nowotny, J. Mobility of Electronic Charge Carriers in Titanium Dioxide. *J. Phys. Chem. C* **2008**, *112* (33), 12981–12987. https://doi.org/10.1021/jp801028j.

(35) Fravventura, M. C.; Deligiannis, D.; Schins, J. M.; Siebbeles, L. D. A.; Savenije, T. J. What Limits Photoconductance in Anatase TiO_2 Nanostructures? A Real and Imaginary Microwave Conductance Study. *J. Phys. Chem. C* **2013**, *117* (16), 8032–8040. https://doi.org/10.1021/jp400222t.

(36) Ling, Y.; Wang, G.; Wheeler, D. A.; Zhang, J. Z.; Li, Y. Sn-Doped Hematite Nanostructures for Photoelectrochemical Water Splitting. *Nano Lett.* **2011**, *11* (5), 2119–2125. https://doi.org/10.1021/nl200708y.

(37) Klahr, B.; Gimenez, S.; Fabregat-Santiago, F.; Bisquert, J.; Hamann, T. W. Electrochemical and Photoelectrochemical Investigation of Water Oxidation with Hematite Electrodes. *Energy Environ. Sci.* **2012**, *5* (6), 7626. https://doi.org/10.1039/c2ee21414h.

(38) Dotan, H.; Sivula, K.; Grätzel, M.; Rothschild, A.; Warren, S. C. Probing the Photoelectrochemical Properties of Hematite (α-Fe_2O_3) Electrodes Using Hydrogen Peroxide as a Hole Scavenger. *Energy Environ. Sci.* **2011**, *4* (3), 958–964. https://doi.org/10.1039/C0EE00570C.

(39) Kennedy, J. H.; Frese, K. W. Photooxidation of Water at α-Fe_2O_3 Electrodes. *J. Electrochem. Soc.* **1978**, *125* (5), 709–714. https://doi.org/10.1149/1.2131532.

(40) Gómez-Mejía, D. R.; Expósito-Gálvez, J. C.; Oskam, G.; Olguín-Melo, D.; Jiménez-Sandoval, O. Synthesis, Characterization and Photoelectrochemical Performance of $Bi_2Fe_4O_9$ Thin Films. *Materials Today Chemistry* **2024**, *40*, 102250. https://doi.org/10.1016/j.mtchem.2024.102250.

(41) Xiao, M.; Luo, B.; Wang, Z.; Wang, S.; Wang, L. Recent Advances of Metal-Oxide Photoanodes: Engineering of Charge Separation and Transportation toward Efficient Solar Water Splitting. *Solar RRL* **2020**, *4* (8), 1900509. https://doi.org/10.1002/solr.201900509.

(42) Peter, L. M. Energetics and Kinetics of Light-Driven Oxygen Evolution at Semiconductor Electrodes: The Example of Hematite. *J Solid State Electrochem* **2013**, *17* (2), 315–326. https://doi.org/10.1007/s10008-012-1957-3.

(43) Huang, Q.; Ye, Z.; Xiao, X. Recent Progress in Photocathodes for Hydrogen Evolution. *J. Mater. Chem. A* **2015**, *3* (31), 15824–15837. https://doi.org/10.1039/C5TA03594E.

(44) Yang, W.; Moon, J. Recent Advances in Earth-Abundant Photocathodes for Photoelectrochemical Water Splitting. *ChemSusChem* **2019**, *12* (9), 1889–1899. https://doi.org/10.1002/cssc.201801554.

(45) Fan, X.; Gao, B.; Wang, T.; Huang, X.; Gong, H.; Xue, H.; Guo, H.; Song, L.; Xia, W.; He, J. Layered Double Hydroxide Modified WO_3 Nanorod Arrays for Enhanced Photoelectrochemical Water Splitting. *Applied Catalysis A: General* **2016**, *528*, 52–58. https://doi.org/10.1016/j.apcata.2016.09.014.

(46) Cai, M.; Fan, P.; Long, J.; Han, J.; Lin, Y.; Zhang, H.; Zhong, M. Large-Scale Tunable 3D Self-Supporting WO_3 Micro-Nano Architectures as Direct Photoanodes for Efficient Photoelectrochemical Water Splitting. *ACS Appl. Mater. Interfaces* **2017**, *9* (21), 17856–17864. https://doi.org/10.1021/acsami.7b02386.

(47) Bhosale, N. Y.; Mali, S. S.; Hong, C. K.; Kadam, A. V. Hydrothermal Synthesis of WO_3 Nanoflowers on Etched ITO and Their Electrochromic Properties. *Electrochimica Acta* **2017**, *246*, 1112–1120. https://doi.org/10.1016/j.electacta.2017.06.142.

(48) Le Formal, F.; Pendlebury, S. R.; Cornuz, M.; Tilley, S. D.; Grätzel, M.; Durrant, J. R. Back Electron–Hole Recombination in Hematite Photoanodes for Water Splitting. *J. Am. Chem. Soc.* **2014**, *136* (6), 2564–2574. https://doi.org/10.1021/ja412058x.

(49) Liao, A.; He, H.; Tang, L.; Li, Y.; Zhang, J.; Chen, J.; Chen, L.; Zhang, C.; Zhou, Y.; Zou, Z. Quasi-Topotactic Transformation of FeOOH Nanorods to Robust Fe_2O_3 Porous Nanopillars Triggered with a Facile Rapid Dehydration Strategy for Efficient Photoelectrochemical Water Splitting. *ACS Appl. Mater. Interfaces* **2018**, *10* (12), 10141–10146. https://doi.org/10.1021/acsami.8b00367.

(50) Expósito-Gálvez, J. C.; Hromadko, L.; Sepúlveda, M.; Peón-Díaz, F. J.; Coria-Quiñones, S. D.; Jiménez-Sandoval, O.; Macak, J. M.; Oskam, G. Comparing the Performance of WO_3 Nanoparticles and Nanofibers: Photocatalytic Dye Degradation versus

Photoelectrochemical Water Oxidation. *Electrochimica Acta* **2024**, *474*, 143545. https://doi.org/10.1016/j.electacta.2023.143545.

(51) Osterloh, F. E. Inorganic Nanostructures for Photoelectrochemical and Photocatalytic Water Splitting. *Chem. Soc. Rev.* **2013**, *42* (6), 2294–2320. https://doi.org/10.1039/C2CS35266D.

(52) Tao, S.; Chung, R.; Lin, L. Heteroatom Doping Strategy for Establishing Hematite Homojunction as Efficient Photocatalyst for Accelerating Water Splitting. *Chemistry An Asian Journal* **2020**, *15* (22), 3853–3860. https://doi.org/10.1002/asia.202001021.

(53) Kang, D.; Hill, J. C.; Park, Y.; Choi, K.-S. Photoelectrochemical Properties and Photostabilities of High Surface Area $CuBi_2O_4$ and Ag-Doped $CuBi_2O_4$ Photocathodes. *Chem. Mater.* **2016**, *28* (12), 4331–4340. https://doi.org/10.1021/acs.chemmater.6b01294.

(54) Mary, A. S.; Murugan, C.; Pandikumar, A. Uplifting the Charge Carrier Separation and Migration in Co-Doped $CuBi_2O4/TiO_2$ p-n Heterojunction Photocathode for Enhanced Photoelectrocatalytic Water Splitting. *Journal of Colloid and Interface Science* **2022**, *608*, 2482–2492. https://doi.org/10.1016/j.jcis.2021.10.172.

(55) Hao, L.; Huang, H.; Zhang, Y.; Ma, T. Oxygen Vacant Semiconductor Photocatalysts. *Adv Funct Materials* **2021**, *31* (25), 2100919. https://doi.org/10.1002/adfm.202100919.

(56) Zhuang, G.; Chen, Y.; Zhuang, Z.; Yu, Y.; Yu, J. Oxygen Vacancies in Metal Oxides: Recent Progress towards Advanced Catalyst Design. *Sci. China Mater.* **2020**, *63* (11), 2089–2118. https://doi.org/10.1007/s40843-020-1305-6.

(57) Wang, G.; Ling, Y.; Li, Y. Oxygen-Deficient Metal Oxide Nanostructures for Photoelectrochemical Water Oxidation and Other Applications. *Nanoscale* **2012**, *4* (21), 6682. https://doi.org/10.1039/c2nr32222f.

(58) Gao, Y.; Li, Y.; Yang, G.; Li, S.; Xiao, N.; Xu, B.; Liu, S.; Qiu, P.; Hao, S.; Ge, L. Fe_2TiO_5 as an Efficient Co-Catalyst To Improve the Photoelectrochemical Water Splitting Performance of $BiVO_4$. *ACS Appl. Mater. Interfaces* **2018**, *10* (46), 39713–39722. https://doi.org/10.1021/acsami.8b14141.

(59) Rosman, N. N.; Yunus, R. M.; Shah, N. R. A. M.; Shah, R. M.; Arifin, K.; Minggu, L. J.; Ludin, N. A. An Overview of Co-catalysts

on Metal Oxides for Photocatalytic Water Splitting. *Intl J of Energy Research* **2022**, *46* (9), 11596–11619. https://doi.org/10.1002/er.8001.

(60) Li, D.; Shi, J.; Li, C. Transition-Metal-Based Electrocatalysts as Cocatalysts for Photoelectrochemical Water Splitting: A Mini Review. *Small* **2018**, *14* (23), 1704179. https://doi.org/10.1002/smll.201704179.

(61) Wang, S.; He, T.; Yun, J.; Hu, Y.; Xiao, M.; Du, A.; Wang, L. New Iron-Cobalt Oxide Catalysts Promoting $BiVO_4$ Films for Photoelectrochemical Water Splitting. *Adv Funct Materials* **2018**, *28* (34), 1802685. https://doi.org/10.1002/adfm.201802685.

(62) Kumar, M.; Meena, B.; Subramanyam, P.; Suryakala, D.; Subrahmanyam, C. Recent Trends in Photoelectrochemical Water Splitting: The Role of Cocatalysts. *NPG Asia Mater* **2022**, *14* (1), 88. https://doi.org/10.1038/s41427-022-00436-x.

(63) Fujishima, A.; Honda, K. Electrochemical Photolysis of Water at a Semiconductor Electrode. *Nature* **1972**, *238* (5358), 37–38. https://doi.org/10.1038/238037a0.

(64) *Photoelectrochemical Hydrogen Production*; Van De Krol, R., Grätzel, M., Eds.; Electronic Materials: Science & Technology; Springer US: Boston, MA, **2012**; Vol. 102. https://doi.org/10.1007/978-1-4614-1380-6.

(65) Walter, M. G.; Warren, E. L.; McKone, J. R.; Boettcher, S. W.; Mi, Q.; Santori, E. A.; Lewis, N. S. Solar Water Splitting Cells. *Chem. Rev.* **2010**, *110* (11), 6446–6473. https://doi.org/10.1021/cr1002326.

(66) Yang, W.; Prabhakar, R. R.; Tan, J.; Tilley, S. D.; Moon, J. Strategies for Enhancing the Photocurrent, Photovoltage, and Stability of Photoelectrodes for Photoelectrochemical Water Splitting. *Chem. Soc. Rev.* **2019**, *48* (19), 4979–5015. https://doi.org/10.1039/C8CS00997J.

(67) Kittel, C. *Introduction to Solid State Physics*, 8. ed.; Wiley: Hoboken, NJ, **2005**.

(68) Neamen, D. A. *Semiconductor Physics and Devices: Basic Principles*, 4th ed.; McGraw-Hill: New York, NY, **2012**.

(69) Yu, P. Y.; Cardona, M. *Fundamentals of Semiconductors*; Graduate Texts in Physics; Springer Berlin Heidelberg: Berlin, Heidelberg, **2005**. https://doi.org/10.1007/b137661.
(70) Klingshirn, C. F.; Klingshirn, C. F. *Semiconductor Optics*, 4th ed.; Graduate texts in physics; Springer: Berlin New York, **2012**.
(71) Smets, A. *Solar Energy: The Physics and Engineering of Photovoltaic Conversion, Technologies and Systems*; Bloomsbury Publishing Plc: London, **2016**.
(72) Morrison, S. R. *Electrochemistry at Semiconductor and Oxidized Metal Electrodes*, Nachdruck.; Springer: New York, **2011**.
(73) Pierret, R. F. *Advanced Semiconductor Fundamentals*; Modular series on solid state devices; Addison-Wesley Pub. Co: Reading, Mass, **1987**.
(74) Sze, S. M.; Ng, K. K. *Physics of Semiconductor Devices*, 3rd ed.; Wiley-Interscience: Hoboken, N.J, **2007**.
(75) Brus, L. E. Electron–Electron and Electron-Hole Interactions in Small Semiconductor Crystallites: The Size Dependence of the Lowest Excited Electronic State. *The Journal of Chemical Physics* **1984**, *80* (9), 4403–4409. https://doi.org/10.1063/1.447218.
(76) Nellist, M. R.; Laskowski, F. A. L.; Lin, F.; Mills, T. J.; Boettcher, S. W. Semiconductor–Electrocatalyst Interfaces: Theory, Experiment, and Applications in Photoelectrochemical Water Splitting. *Acc. Chem. Res.* **2016**, *49* (4), 733–740. https://doi.org/10.1021/acs.accounts.6b00001.
(77) Gerischer, H. Charge Transfer Processes at Semiconductor-Electrolyte Interfaces in Connection with Problems of Catalysis. *Surface Science* **1969**, *18* (1), 97–122. https://doi.org/10.1016/0039-6028(69)90269-6.
(78) Memming, R.; Schwandt, G. Potential and Charge Distribution at Semiconductor-electrolyte Interfaces. *Angew. Chem. Int. Ed. Engl.* **1967**, *6* (10), 851–861. https://doi.org/10.1002/anie.196708511.
(79) Memming, R. *Semiconductor Electrochemistry*, 2nd edition.; Wiley-VCH Verlag GmbH & Co. KGaA: Weinheim, **2015**.
(80) The Electrified Interface. In *Modern Electrochemistry 2A*; Kluwer Academic Publishers: Boston, **2002**; pp 771–1033. https://doi.org/10.1007/0-306-47605-3_1.

(81) Kamat, P. V. Quantum Dot Solar Cells. Semiconductor Nanocrystals as Light Harvesters. *J. Phys. Chem. C* **2008**, *112* (48), 18737–18753. https://doi.org/10.1021/jp806791s.
(82) Vanmaekelbergh, D.; De Jongh, P. E. Driving Force for Electron Transport in Porous Nanostructured Photoelectrodes. *J. Phys. Chem. B* **1999**, *103* (5), 747–750. https://doi.org/10.1021/jp9840883.
(83) Kelly, J. J.; Vanmaekelbergh, D. Charge Carrier Dynamics in Nanoporous Photoelectrodes. *Electrochimica Acta* **1998**, *43* (19–20), 2773–2780. https://doi.org/10.1016/S0013-4686(98)00018-8.
(84) Soedergren, S.; Hagfeldt, A.; Olsson, J.; Lindquist, S.-E. Theoretical Models for the Action Spectrum and the Current-Voltage Characteristics of Microporous Semiconductor Films in Photoelectrochemical Cells. *J. Phys. Chem.* **1994**, *98* (21), 5552–5556. https://doi.org/10.1021/j100072a023.
(85) Chen, Z.; Dinh, H. N.; Miller, E. *Photoelectrochemical Water Splitting: Standards, Experimental Methods, and Protocols*; SpringerBriefs in Energy; Springer New York: New York, NY, **2013**. https://doi.org/10.1007/978-1-4614-8298-7.
(86) Genscher, H. Electrochemical Behavior of Semiconductors under Illumination. *J. Electrochem. Soc.* **1966**, *113* (11), 1174. https://doi.org/10.1149/1.2423779.
(87) Peter, L. M.; Li, J.; Peat, R. Surface Recombination at Semiconductor Electrodes. *Journal of Electroanalytical Chemistry and Interfacial Electrochemistry* **1984**, *165* (1–2), 29–40. https://doi.org/10.1016/S0022-0728(84)80084-4.
(88) Schmickler, W.; Santos, E. *Interfacial Electrochemistry*; Springer Berlin Heidelberg: Berlin, Heidelberg, 2010. https://doi.org/10.1007/978-3-642-04937-8.
(89) Peter, L. M. An Exploratory Kinetic Analysis of Photoelectrochemical Oxygen Evolution on Hematite. *J Solid State Electrochem* **2025**, *29* (6), 2141–2155. https://doi.org/10.1007/s10008-025-06221-4.
(90) Bisquert, J. Theory of the Impedance of Electron Diffusion and Recombination in a Thin Layer. *J. Phys. Chem. B* **2002**, *106* (2), 325–333. https://doi.org/10.1021/jp011941g.
(91) Expósito-Gálvez, J. C.; Rawat, A.; Rajeshwar, K.; Oskam, G. Charge Dynamics as Probed by Small Signal-Modulated

Photocurrent and Impedance Spectroscopy of Metal Vanadate Semiconductors and Alloys. *ACS Appl. Opt. Mater.* **2025**, *3* (8), 1684–1695. https://doi.org/10.1021/acsaom.5c00154.

(92) Zachäus, C.; Abdi, F. F.; Peter, L. M.; Van De Krol, R. Photocurrent of $BiVO_4$ Is Limited by Surface Recombination, Not Surface Catalysis. *Chem. Sci.* **2017**, *8* (5), 3712–3719. https://doi.org/10.1039/C7SC00363C.

(93) Klahr, B.; Hamann, T. Water Oxidation on Hematite Photoelectrodes: Insight into the Nature of Surface States through In Situ Spectroelectrochemistry. *J. Phys. Chem. C* **2014**, *118* (19), 10393–10399. https://doi.org/10.1021/jp500543z.

(94) Klotz, D.; Grave, D. A.; Dotan, H.; Rothschild, A. Empirical Analysis of the Photoelectrochemical Impedance Response of Hematite Photoanodes for Water Photo-Oxidation. *J. Phys. Chem. Lett.* **2018**, *9* (6), 1466–1472. https://doi.org/10.1021/acs.jpclett.8b00096.

(95) Hagfeldt, A.; Björkstén, U.; Grätzel, M. Photocapacitance of Nanocrystalline Oxide Semiconductor Films: Band-Edge Movement in Mesoporous TiO_2 Electrodes during UV Illumination. *J. Phys. Chem.* **1996**, *100* (20), 8045–8048. https://doi.org/10.1021/jp9518567.

(96) Cummings, C. Y.; Marken, F.; Peter, L. M.; Tahir, A. A.; Wijayantha, K. G. U. Kinetics and Mechanism of Light-Driven Oxygen Evolution at Thin Film α-Fe_2O_3 Electrodes. *Chem. Commun.* **2012**, *48* (14), 2027. https://doi.org/10.1039/c2cc16382a.

(97) Hwang, Y. J.; Boukai, A.; Yang, P. High Density N-Si/n-TiO_2 Core/Shell Nanowire Arrays with Enhanced Photoactivity. *Nano Lett.* **2009**, *9* (1), 410–415. https://doi.org/10.1021/nl8032763.

(98) Ponomarev, E. A.; Peter, L. M. A Generalized Theory of Intensity Modulated Photocurrent Spectroscopy (IMPS). *Journal of Electroanalytical Chemistry* **1995**, *396* (1–2), 219–226. https://doi.org/10.1016/0022-0728(95)04115-5.

(99) Peter, L. M.; Wijayantha, K. G. U.; Tahir, A. A. Kinetics of Light-Driven Oxygen Evolution at α-Fe_2O_3 Electrodes. *Faraday Discuss.* **2012**, *155*, 309–322. https://doi.org/10.1039/C1FD00079A.

(100) Ponomarev, E. A.; Peter, L. M. A Comparison of Intensity Modulated Photocurrent Spectroscopy and Photoelectrochemical

Impedance Spectroscopy in a Study of Photoelectrochemical Hydrogen Evolution at P-InP. *Journal of Electroanalytical Chemistry* **1995**, *397* (1–2), 45–52. https://doi.org/10.1016/0022-0728(95)04148-9.

(101) Peter, L. M. Dynamic Aspects of Semiconductor Photoelectrochemistry. *Chem. Rev.* **1990**, *90* (5), 753–769. https://doi.org/10.1021/cr00103a005.

(102) Gärtner, W. W. Depletion-Layer Photoeffects in Semiconductors. *Phys. Rev.* **1959**, *116* (1), 84–87. https://doi.org/10.1103/PhysRev.116.84.

(103) Sharma, B. L.; Purohit, R. K. *Semiconductor Heterojunctions*, 1st ed.; International series of monographs in the science of the solid state; Pergamon Press: Oxford, New York, **1974**.

(104) Low, J.; Yu, J.; Jaroniec, M.; Wageh, S.; Al-Ghamdi, A. A. Heterojunction Photocatalysts. *Advanced Materials* **2017**, *29* (20), 1601694. https://doi.org/10.1002/adma.201601694.

(105) Yang, H. A Short Review on Heterojunction Photocatalysts: Carrier Transfer Behavior and Photocatalytic Mechanisms. *Materials Research Bulletin* **2021**, *142*, 111406. https://doi.org/10.1016/j.materresbull.2021.111406.

(106) Wang, H.; Zhang, L.; Chen, Z.; Hu, J.; Li, S.; Wang, Z.; Liu, J.; Wang, X. Semiconductor Heterojunction Photocatalysts: Design, Construction, and Photocatalytic Performances. *Chem. Soc. Rev.* **2014**, *43* (15), 5234. https://doi.org/10.1039/C4CS00126E.

(107) Expósito-Gálvez, J. C.; Vattier, F.; Pedrosa, J. M.; Carrillo-Carrión, C.; Oskam, G. Tuning the Photoelectrochemical Properties of Ti/W-Modified PCN-222 Using Charge–Selective Interfaces. *ACS Appl. Mater. Interfaces* **2026**, *18* (6), 9877–9891. https://doi.org/10.1021/acsami.5c22732.

(108) You, Y.; Tian, W.; Min, L.; Cao, F.; Deng, K.; Li, L. TiO_2/WO_3 Bilayer as Electron Transport Layer for Efficient Planar Perovskite Solar Cell with Efficiency Exceeding 20%. *Adv Materials Inter* **2020**, *7* (1), 1901406. https://doi.org/10.1002/admi.201901406.

(109) Wang, H.; Zhao, C.; Yin, L.; Li, X.; Tu, X.; Lim, E. G.; Liu, Y.; Zhao, C. Z. W-Doped TiO_2 as Electron Transport Layer for High Performance Solution-Processed Perovskite Solar Cells. *Applied*

Surface Science **2021**, *563*, 150298. https://doi.org/10.1016/j.apsusc.2021.150298.

(110) Che Halin, D. S.; Azhari, A. W.; Mohd Salleh, M. A. A.; Muhammad Nadzri, N. I.; Vizureanu, P.; Abdullah, M. M. A. B.; Wahab, J. A.; Sandu, A. V. Metal-Doped TiO_2 Thin Film as an Electron Transfer Layer for Perovskite Solar Cells: A Review. *Coatings* **2022**, *13* (1), 4. https://doi.org/10.3390/coatings13010004.

(111) Mann, D. S.; Singh, J.; Thakur, S.; Kwon, S.; Jeong, K.; Na, S. Influence of Fluorine Doping on Hole Transport Properties of NiO_x for High-Efficiency Perovskite Solar Cells. *Solar RRL* **2025**, *9* (12), 2500152. https://doi.org/10.1002/solr.202500152.

(112) Li, H.; Yin, M.; Li, X.; Mo, R. Enhanced Photoelectrochemical Water Oxidation Performance in Bilayer TiO_2/α-Fe_2O_3 Nanorod Arrays Photoanode with Cu:NiO_x as Hole Transport Layer and Co−Pi as Cocatalyst. *ChemSusChem* **2021**, *14* (11), 2331–2340. https://doi.org/10.1002/cssc.202100363.

(113) Kuo, D.-W.; Chen, C.-T. A Dual Layer of NiO_x Hole-Transporting Material Boosting the Efficiency of Inverted Perovskite Solar Cells up to 20.7%. *ACS Appl. Energy Mater.* **2025**, *8* (8), 5309–5316. https://doi.org/10.1021/acsaem.5c00312.

(114) Zhou, W.; Wang, Z. L. *Scanning Microscopy for Nanotechnology: Techniques and Applications*; Springer Science+Business Media, LLC Springer e-books: New York, NY, **2007**.

(115) Oura, K.; Katayama, M.; Zotov, A. V.; Lifshits, V. G.; Saranin, A. A. *Surface Science*; Advanced Texts in Physics; Springer Berlin Heidelberg: Berlin, Heidelberg, **2003**. https://doi.org/10.1007/978-3-662-05179-5.

(116) Egerton, R. F. *Physical Principles of Electron Microscopy*; Springer International Publishing: Cham, **2016**. https://doi.org/10.1007/978-3-319-39877-8.

(117) Ul-Hamid, A. *A Beginners' Guide to Scanning Electron Microscopy*; Springer International Publishing: Cham, **2018**. https://doi.org/10.1007/978-3-319-98482-7.

(118) Goldstein, J. I.; Newbury, D. E.; Michael, J. R.; Ritchie, N. W. M.; Scott, J. H. J.; Joy, D. C. *Scanning Electron Microscopy and X-*

Ray Microanalysis; Springer New York: New York, NY, **2018**. https://doi.org/10.1007/978-1-4939-6676-9.

(119) Cullity, B. D.; Stock, S. R. *Elements of X-Ray Diffraction*, 3. ed.; Prentice Hall: Upper Saddle River, NJ, **2001**.

(120) Klug, H. P.; Alexander, L. E. *X-Ray Diffraction Procedures for Polycrystalline and Amorphous Materials*, 2d ed.; Wiley: New York, **1974**.

(121) Patterson, A. L. The Scherrer Formula for X-Ray Particle Size Determination. *Phys. Rev.* **1939**, *56* (10), 978–982. https://doi.org/10.1103/PhysRev.56.978.

(122) *Surface Analysis by Auger and X-Ray Photoelectron Spectroscopy*; Briggs, D., Grant, J. T., Eds.; Surface Spectra [u.a.]: Manchester, UK, **2003**.

(123) Hüfner, S. *Photoelectron Spectroscopy*; Advanced Texts in Physics; Springer Berlin Heidelberg: Berlin, Heidelberg, **2003**. https://doi.org/10.1007/978-3-662-09280-4.

(124) *Handbook of X-Ray Photoelectron Spectroscopy: A Reference Book of Standard Spectra for Identification and Interpretation of XPS Data*, Update.; Moulder, J. F., Chastain, J., Eds.; Perkin-Elmer Corporation: Eden Prairie, Minn, **1992**.

(125) Berne, B. J.; Pecora, R. *Dynamic Light Scattering: With Applications to Chemistry, Biology, and Physics*, Dover ed.; Dover Publications: Mineola, NY, **2000**.

(126) Chu, B. *Laser Light Scattering: Basic Principles and Practice*, 2. ed.; Dover Publications: Mineola, N.Y, **2007**.

(127) Stetefeld, J.; McKenna, S. A.; Patel, T. R. Dynamic Light Scattering: A Practical Guide and Applications in Biomedical Sciences. *Biophys Rev* **2016**, *8* (4), 409–427. https://doi.org/10.1007/s12551-016-0218-6.

(128) Hunter, R. J. *Zeta Potential in Colloid Science: Principles and Applications*, 3. printing.; Colloid science; Academic Pr: London, **1988**.

(129) Skoog, D. A.; Holler, F. J.; Crouch, S. R. *Principles of Instrumental Analysis*, 7. edition.; Cengage Learning: Boston, MA, **2018**.

(130) Fox, M. *Optical Properties of Solids*, Second edition, reprinted (with corrections).; Oxford master series in condensed matter physics; Oxford University Press: Oxford New York, NY, **2011**.
(131) Tauc, J. Optical Properties and Electronic Structure of Amorphous Ge and Si. *Materials Research Bulletin* **1968**, *3* (1), 37–46. https://doi.org/10.1016/0025-5408(68)90023-8.
(132) Escobedo-Morales, A.; Ruiz-López, I. I.; Ruiz-Peralta, M. deL.; Tepech-Carrillo, L.; Sánchez-Cantú, M.; Moreno-Orea, J. E. Automated Method for the Determination of the Band Gap Energy of Pure and Mixed Powder Samples Using Diffuse Reflectance Spectroscopy. *Heliyon* **2019**, *5* (4), e01505. https://doi.org/10.1016/j.heliyon.2019.e01505.
(133) Colthup, N. B.; Daly, L. H.; Wiberley, S. E. *Introduction to Infrared and Raman Spectroscopy*, 3rd ed.; Academic Press: Boston, **1990**.
(134) Larkin, P. J. *Infrared and Raman Spectroscopy: Principles and Spectral Interpretation*, Second edition.; Elsevier: Amsterdam, **2018**.
(135) Lindquist, S. -E.; Finnström, B.; Tegnér, L. Photoelectrochemical Properties of Polycrystalline TiO_2 Thin Film Electrodes on Quartz Substrates. *J. Electrochem. Soc.* **1983**, *130* (2), 351–358. https://doi.org/10.1149/1.2119710.
(136) Peter, L. M.; Vanmaekelbergh, D. Time and Frequency Resolved Studies of Photoelectrochemical Kinetics. In *Advances in Electrochemical Sciences and Engineering*; Alkire, R. C., Kolb, D. M., Eds.; Wiley, **1999**; Vol. 6, pp 77–163. https://doi.org/10.1002/9783527616800.ch2.
(137) Spadavecchia, F.; Ardizzone, S.; Cappelletti, G.; Falciola, L.; Ceotto, M.; Lotti, D. Investigation and Optimization of Photocurrent Transient Measurements on Nano-TiO_2. *J Appl Electrochem* **2013**, *43* (2), 217–225. https://doi.org/10.1007/s10800-012-0485-2.
(138) Peter, L. M.; Walker, A. B.; Bein, T.; Hufnagel, A. G.; Kondofersky, I. Interpretation of Photocurrent Transients at Semiconductor Electrodes: Effects of Band-Edge Unpinning. *Journal of Electroanalytical Chemistry* **2020**, *872*, 114234. https://doi.org/10.1016/j.jelechem.2020.114234.
(139) Hagfeldt, A.; Lindström, H.; Södergren, S.; Lindquist, S.-E. Photoelectrochemical Studies of Colloidal TiO_2 Films: The Effect of

Oxygen Studied by Photocurrent Transients. *Journal of Electroanalytical Chemistry* **1995**, *381* (1–2), 39–46. https://doi.org/10.1016/0022-0728(94)03622-A.

(140) Dholam, R.; Patel, N.; Santini, A.; Miotello, A. Efficient Indium Tin Oxide/Cr-Doped-TiO_2 Multilayer Thin Films for H_2 Production by Photocatalytic Water-Splitting. *International Journal of Hydrogen Energy* **2010**, *35* (18), 9581–9590. https://doi.org/10.1016/j.ijhydene.2010.06.097.

(141) Holze, R. C.M.A. Brett, A.M.O. Brett: Electrochemistry — Principles, Methods and Applications, OXford University Press, Oxford, ISBN 0-19-855388-9, 1993, 427 Pages, *Ber Bunsenges Phys Chem* **1994**, *98* (10), 1350–1350. https://doi.org/10.1002/bbpc.19940981033.

(142) Klotz, D.; Ellis, D. S.; Dotan, H.; Rothschild, A. Empirical in Operando Analysis of the Charge Carrier Dynamics in Hematite Photoanodes by PEIS, IMPS and IMVS. *Phys. Chem. Chem. Phys.* **2016**, *18* (34), 23438–23457. https://doi.org/10.1039/C6CP04683E.

(143) Bertoluzzi, L.; Bisquert, J. Investigating the Consistency of Models for Water Splitting Systems by Light and Voltage Modulated Techniques. *J. Phys. Chem. Lett.* **2017**, *8* (1), 172–180. https://doi.org/10.1021/acs.jpclett.6b02714.

(144) *Impedance Spectroscopy: Theory, Experiment, and Applications*, 1st ed.; Barsoukov, E., Macdonald, J. R., Eds.; Wiley, **2018**. https://doi.org/10.1002/9781119381860.

(145) Lasia, A. *Electrochemical Impedance Spectroscopy and Its Applications*; Springer New York: New York, NY, **2014**. https://doi.org/10.1007/978-1-4614-8933-7.

(146) Von Hauff, E.; Klotz, D. Impedance Spectroscopy for Perovskite Solar Cells: Characterisation, Analysis, and Diagnosis. *J. Mater. Chem. C* **2022**, *10* (2), 742–761. https://doi.org/10.1039/D1TC04727B.

(147) Peter, L. M. *Electrochemical Impedance Spectroscopy and Related Techniques: From Basics to Advanced Applications*; Advanced Textbooks in Chemistry; WORLD SCIENTIFIC (EUROPE), **2024**; Vol. a. https://doi.org/10.1142/q0428.

(148) Orazem, M. E.; Tribollet, B. *Electrochemical Impedance Spectroscopy*; The Electrochemical Society series; Wiley: Hoboken, N.J, **2008**. https://doi.org/10.1002/9780470381588.
(149) Wang, S.; Zhang, J.; Gharbi, O.; Vivier, V.; Gao, M.; Orazem, M. E. Electrochemical Impedance Spectroscopy. *Nat Rev Methods Primers* **2021**, *1* (1), 41. https://doi.org/10.1038/s43586-021-00039-w.
(150) Dias, P.; Mendes, A. Hydrogen Production from Photoelectrochemical Water Splitting. In *Encyclopedia of Sustainability Science and Technology*; Meyers, R. A., Ed.; Springer New York: New York, NY, **2018**; pp 1–52. https://doi.org/10.1007/978-1-4939-2493-6_957-1.
(151) Townley, D. Comment on "Evaluation of Kramers-Kronig Transforms for Electrochemical Impedance Data. *J. Electrochem. Soc.* **1990**, *137* (10), 3305–3306. https://doi.org/10.1149/1.2148725.
(152) Hirschorn, B.; Orazem, M. E.; Tribollet, B.; Vivier, V.; Frateur, I.; Musiani, M. Determination of Effective Capacitance and Film Thickness from Constant-Phase-Element Parameters. *Electrochimica Acta* **2010**, *55* (21), 6218–6227. https://doi.org/10.1016/j.electacta.2009.10.065.
(153) Brug, G. J.; Van Den Eeden, A. L. G.; Sluyters-Rehbach, M.; Sluyters, J. H. The Analysis of Electrode Impedances Complicated by the Presence of a Constant Phase Element. *Journal of Electroanalytical Chemistry and Interfacial Electrochemistry* **1984**, *176* (1–2), 275–295. https://doi.org/10.1016/S0022-0728(84)80324-1.
(154) Dloczik, L.; Ileperuma, O.; Lauermann, I.; Peter, L. M.; Ponomarev, E. A.; Redmond, G.; Shaw, N. J.; Uhlendorf, I. Dynamic Response of Dye-Sensitized Nanocrystalline Solar Cells: Characterization by Intensity-Modulated Photocurrent Spectroscopy. *J. Phys. Chem. B* **1997**, *101* (49), 10281–10289. https://doi.org/10.1021/jp972466i.
(155) Peter, L. M.; Bevan, K. H.; Ponomarev, E. A Kinetics-Based Approach to the Steady-State and Impedance Response of Photoelectrodes. *Electrochimica Acta* **2024**, *493*, 144422. https://doi.org/10.1016/j.electacta.2024.144422.

(156) Mendhe, A. C. Spin Coating: Easy Technique for Thin Films. In *Simple Chemical Methods for Thin Film Deposition*; Sankapal, B. R., Ennaoui, A., Gupta, R. B., Lokhande, C. D., Eds.; Springer Nature Singapore: Singapore, **2023**; pp 387–424. https://doi.org/10.1007/978-981-99-0961-2_9.

(157) Seshan, K. *Handbook of Thin-Film Deposition Processes and Techniques: Principles, Methods, Equipment, and Applications*, 2nd ed.; Materials science and process technology series. Electronic materials and process technology; Noyes Publications: Norwich, N.Y, **2002**.

(158) Bommineedi, L. K.; Upadhyay, N.; Minnes, R. Screen Printing: An Ease Thin Film Technique. In *Simple Chemical Methods for Thin Film Deposition*; Sankapal, B. R., Ennaoui, A., Gupta, R. B., Lokhande, C. D., Eds.; Springer Nature Singapore: Singapore, **2023**; pp 449–507. https://doi.org/10.1007/978-981-99-0961-2_11.

(159) Suresh, R. R.; Lakshmanakumar, M.; Arockia Jayalatha, J. B. B.; Rajan, K. S.; Sethuraman, S.; Krishnan, U. M.; Rayappan, J. B. B. Fabrication of Screen-Printed Electrodes: Opportunities and Challenges. *J Mater Sci* **2021**, *56* (15), 8951–9006. https://doi.org/10.1007/s10853-020-05499-1.

(160) Perednis, D.; Gauckler, L. J. Thin Film Deposition Using Spray Pyrolysis. *J Electroceram* **2005**, *14* (2), 103–111. https://doi.org/10.1007/s10832-005-0870-x.

(161) Patil, P. S. Versatility of Chemical Spray Pyrolysis Technique. *Materials Chemistry and Physics* **1999**, *59* (3), 185–198. https://doi.org/10.1016/S0254-0584(99)00049-8.

(162) Mattox, D. M. *Handbook of Physical Vapor Deposition (PVD) Processing*, 2nd ed.; William Andrew: Oxford, UK, **2010**.

(163) Greene, J. E. Review Article: Tracing the Recorded History of Thin-Film Sputter Deposition: From the 1800s to 2017. *Journal of Vacuum Science & Technology A: Vacuum, Surfaces, and Films* **2017**, *35* (5), 05C204. https://doi.org/10.1116/1.4998940.

(164) Sivula, K.; Van De Krol, R. Semiconducting Materials for Photoelectrochemical Energy Conversion. *Nat Rev Mater* **2016**, *1* (2), 15010. https://doi.org/10.1038/natrevmats.2015.10.

(165) Tan, M. X.; Laibinis, P. E.; Nguyen, S. T.; Kesselman, J. M.; Stanton, C. E.; Lewis, N. S. Principles and Applications of

Semiconductor Photoelectrochemistry. In *Progress in Inorganic Chemistry*; Karlin, K. D., Ed.; Wiley, **1994**; Vol. 41, pp 21–144. https://doi.org/10.1002/9780470166420.ch2.

(166) Niu, F.; Wang, D.; Li, F.; Liu, Y.; Shen, S.; Meyer, T. J. Hybrid Photoelectrochemical Water Splitting Systems: From Interface Design to System Assembly. *Advanced Energy Materials* **2020**, *10* (11), 1900399. https://doi.org/10.1002/aenm.201900399.

(167) Dai, Y.; Yu, J.; Cheng, C.; Tan, P.; Ni, M. Engineering the Interfaces in Water-Splitting Photoelectrodes – an Overview of the Technique Development. *J. Mater. Chem. A* **2020**, *8* (15), 6984–7002. https://doi.org/10.1039/D0TA01670E.

(168) Furukawa, H.; Cordova, K. E.; O'Keeffe, M.; Yaghi, O. M. The Chemistry and Applications of Metal-Organic Frameworks. *Science* **2013**, *341* (6149), 1230444. https://doi.org/10.1126/science.1230444.

(169) Navalón, S.; Dhakshinamoorthy, A.; Álvaro, M.; Ferrer, B.; García, H. Metal–Organic Frameworks as Photocatalysts for Solar-Driven Overall Water Splitting. *Chem. Rev.* **2023**, *123* (1), 445–490. https://doi.org/10.1021/acs.chemrev.2c00460.

(170) Dan-Hardi, M.; Serre, C.; Frot, T.; Rozes, L.; Maurin, G.; Sanchez, C.; Férey, G. A New Photoactive Crystalline Highly Porous Titanium(IV) Dicarboxylate. *J. Am. Chem. Soc.* **2009**, *131* (31), 10857–10859. https://doi.org/10.1021/ja903726m.

(171) Shah, W. A.; Waseem, A.; Nadeem, M. A.; Kögerler, P. Leaching-Free Encapsulation of Cobalt-Polyoxotungstates in MIL-100 (Fe) for Highly Reproducible Photocatalytic Water Oxidation. *Applied Catalysis A: General* **2018**, *567*, 132–138. https://doi.org/10.1016/j.apcata.2018.08.002.

(172) Gomes Silva, C.; Luz, I.; Llabrés i Xamena, F. X.; Corma, A.; García, H. Water Stable Zr–Benzenedicarboxylate Metal–Organic Frameworks as Photocatalysts for Hydrogen Generation. *Chemistry A European J* **2010**, *16* (36), 11133–11138. https://doi.org/10.1002/chem.200903526.

(173) Alvaro, M.; Carbonell, E.; Ferrer, B.; Llabrés i Xamena, F. X.; Garcia, H. Semiconductor Behavior of a Metal-Organic Framework (MOF). *Chemistry A European J* **2007**, *13* (18), 5106–5112. https://doi.org/10.1002/chem.200601003.

(174) Ding, G.; Li, C.; Chen, L.; Liao, G. Porphyrin-Based Metal–Organic Frameworks for Photo(Electro)Catalytic CO_2 Reduction. *Energy Environ. Sci.* **2024**, *17* (15), 5311–5335. https://doi.org/10.1039/D4EE01748J.

(175) Feng, D.; Gu, Z.; Li, J.; Jiang, H.; Wei, Z.; Zhou, H. Zirconium-Metalloporphyrin PCN-222: Mesoporous Metal–Organic Frameworks with Ultrahigh Stability as Biomimetic Catalysts. *Angew Chem Int Ed* **2012**, *51* (41), 10307–10310. https://doi.org/10.1002/anie.201204475.

(176) Liu, F.; Rincón, I.; Baldoví, H. G.; Dhakshinamoorthy, A.; Horcajada, P.; Rojas, S.; Navalón, S.; Fateeva, A. Porphyrin-Based MOFs for Photocatalysis in Water: Advancements in Solar Fuels Generation and Pollutants Degradation. *Inorg. Chem. Front.* **2024**, *11* (8), 2212–2245. https://doi.org/10.1039/D3QI01996A.

(177) Guan, G.-W.; Zheng, S.-T.; Xia, M.; Li, K.-X.; Ouyang, Y.-S.; Yang, G.; Yang, Q.-Y. Incorporating CdS and Anchoring Pt Single Atoms into Porphyrinic Metal–Organic Frameworks for Superior Visible-Light and Sunlight-Driven H_2 Evolution. *Chemical Engineering Journal* **2023**, *464*, 142530. https://doi.org/10.1016/j.cej.2023.142530.

(178) Stanley, P. M.; Hemmer, K.; Hegelmann, M.; Schulz, A.; Park, M.; Elsner, M.; Cokoja, M.; Warnan, J. Topology- and Wavelength-Governed CO_2 Reduction Photocatalysis in Molecular Catalyst-Metal–Organic Framework Assemblies. *Chem. Sci.* **2022**, *13* (41), 12164–12174. https://doi.org/10.1039/D2SC03097G.

(179) Jin, J. Porphyrin-Based Metal–Organic Framework Catalysts for Photoreduction of CO_2: Understanding the Effect of Node Connectivity and Linker Metalation on Activity. *New J. Chem.* **2020**, *44* (36), 15362–15368. https://doi.org/10.1039/D0NJ03507F.

(180) Wei, Z.; Song, S.; Gu, H.; Li, Y.; Sun, Q.; Ding, N.; Tang, H.; Zheng, L.; Liu, S.; Li, Z.; Chen, W.; Li, S.; Pang, S. Enhancing the Photocatalytic Activity of Zirconium-Based Metal–Organic Frameworks Through the Formation of Mixed-Valence Centers. *Advanced Science* **2023**, *10* (29), 2303206. https://doi.org/10.1002/advs.202303206.

(181) Liu, L.; Xu, Q.; Zhu, Q. Electrically Conductive Metal–Organic Frameworks for Electrocatalytic Applications. *Adv Energy and*

Sustain Res **2021**, *2* (11), 2100100. https://doi.org/10.1002/aesr.202100100.

(182) Syzgantseva, M. A.; Ireland, C. P.; Ebrahim, F. M.; Smit, B.; Syzgantseva, O. A. Metal Substitution as the Method of Modifying Electronic Structure of Metal–Organic Frameworks. *J. Am. Chem. Soc.* **2019**, *141* (15), 6271–6278. https://doi.org/10.1021/jacs.8b13667.

(183) Daliran, S.; Oveisi, A. R.; Kung, C.-W.; Sen, U.; Dhakshinamoorthy, A.; Chuang, C.-H.; Khajeh, M.; Erkartal, M.; Hupp, J. T. Defect-Enabling Zirconium-Based Metal–Organic Frameworks for Energy and Environmental Remediation Applications. *Chem. Soc. Rev.* **2024**, *53* (12), 6244–6294. https://doi.org/10.1039/D3CS01057K.

(184) Assaad, N.; Sabeh, G.; Hmadeh, M. Defect Control in Zr-Based Metal–Organic Framework Nanoparticles for Arsenic Removal from Water. *ACS Appl. Nano Mater.* **2020**, *3* (9), 8997–9008. https://doi.org/10.1021/acsanm.0c01696.

(185) Portillo-Vélez, N. S.; Obeso, J. L.; De Los Reyes, J. A.; Peralta, R. A.; Ibarra, I. A.; Huxley, M. T. Benefits and Complexity of Defects in Metal-Organic Frameworks. *Commun Mater* **2024**, *5* (1), 247. https://doi.org/10.1038/s43246-024-00691-1.

(186) Gikonyo, B.; Montero-Lanzuela, E.; Baldovi, H. G.; De, S.; Journet, C.; Devic, T.; Guillou, N.; Tiana, D.; Navalon, S.; Fateeva, A. Mixed-Metal Zr/Ti MIL-173 Porphyrinic Metal–Organic Frameworks as Efficient Photocatalysts towards Solar-Driven Overall Water Splitting. *J. Mater. Chem. A* **2022**, *10* (46), 24938–24950. https://doi.org/10.1039/D2TA06652A.

(187) Akaishi, Y.; Yoshimura, G.; Mokuge, Y.; Sumi, K.; Vas-Umnuay, P.; Inomata, Y.; Kida, T. A Photoelectrochemical Capacitor Using Polyoxometalates Coupled with Semiconductor Nanocrystals as the Photosensitizer. *Chem. Commun.* **2024**, *60* (68), 9042–9045. https://doi.org/10.1039/D4CC01550A.

(188) Paille, G.; Gomez-Mingot, M.; Roch-Marchal, C.; Lassalle-Kaiser, B.; Mialane, P.; Fontecave, M.; Mellot-Draznieks, C.; Dolbecq, A. A Fully Noble Metal-Free Photosystem Based on Cobalt-Polyoxometalates Immobilized in a Porphyrinic Metal–

Organic Framework for Water Oxidation. *J. Am. Chem. Soc.* **2018**, *140* (10), 3613–3618. https://doi.org/10.1021/jacs.7b11788.

(189) Xiao, D.; Cheng, G.; She, H.; Chen, X.; Huang, J.; Wang, L.; Wang, Q. Enhanced Photoelectrochemical Water Splitting Performance of $BiVO_4$ Photoanode by Integrating Electron-Rich Polyoxometalate into Metal–Organic Framework. *J. Phys. Chem. C* **2024**, *128* (37), 15266–15276. https://doi.org/10.1021/acs.jpcc.4c03542.

(190) Rau, U.; Kirchartz, T. Charge Carrier Collection and Contact Selectivity in Solar Cells. *Adv Materials Inter* **2019**, *6* (20), 1900252. https://doi.org/10.1002/admi.201900252.

(191) Valadez-Villalobos, K.; Idígoras, J.; Delgado, L. P.; Meneses-Rodríguez, D.; Anta, J. A.; Oskam, G. Correlation between the Effectiveness of the Electron-Selective Contact and Photovoltaic Performance of Perovskite Solar Cells. *J. Phys. Chem. Lett.* **2019**, *10* (4), 877–882. https://doi.org/10.1021/acs.jpclett.8b03834.

(192) Kirchartz, T.; Bisquert, J.; Mora-Sero, I.; Garcia-Belmonte, G. Classification of Solar Cells According to Mechanisms of Charge Separation and Charge Collection. *Phys. Chem. Chem. Phys.* **2015**, *17* (6), 4007–4014. https://doi.org/10.1039/C4CP05174B.

(193) Schleuning, M.; Ahmet, I. Y.; Van De Krol, R.; May, M. M. The Role of Selective Contacts and Built-in Field for Charge Separation and Transport in Photoelectrochemical Devices. *Sustainable Energy Fuels* **2022**, *6* (16), 3701–3716. https://doi.org/10.1039/D2SE00562J.

(194) Grigioni, I.; Abdellah, M.; Corti, A.; Dozzi, M. V.; Hammarström, L.; Selli, E. Photoinduced Charge-Transfer Dynamics in WO_3/$BiVO_4$ Photoanodes Probed through Midinfrared Transient Absorption Spectroscopy. *J. Am. Chem. Soc.* **2018**, *140* (43), 14042–14045. https://doi.org/10.1021/jacs.8b08309.

(195) Rodríguez-Gutiérrez, I.; Djatoubai, E.; Su, J.; Vega-Poot, A.; Rodríguez-Gattorno, G.; Souza, F. L.; Oskam, G. An Intensity-Modulated Photocurrent Spectroscopy Study of the Charge Carrier Dynamics of WO_3/$BiVO_4$ Heterojunction Systems. *Solar Energy Materials and Solar Cells* **2020**, *208*, 110378. https://doi.org/10.1016/j.solmat.2019.110378.

(196) Moscoso, F. G.; Romero-Guerrero, J. J.; Rodriguez-Lucena, D.; Pedrosa, J. M.; Carrillo-Carrión, C. Nanosized Porphyrinic Metal–Organic Frameworks for the Construction of Transparent Membranes as a Multiresponsive Optical Gas Sensor. *Small Science* **2024**, 2400210. https://doi.org/10.1002/smsc.202400210.

(197) Noh, H.; Kung, C.-W.; Islamoglu, T.; Peters, A. W.; Liao, Y.; Li, P.; Garibay, S. J.; Zhang, X.; DeStefano, M. R.; Hupp, J. T.; Farha, O. K. Room Temperature Synthesis of an 8-Connected Zr-Based Metal–Organic Framework for Top-Down Nanoparticle Encapsulation. *Chem. Mater.* **2018**, *30* (7), 2193–2197. https://doi.org/10.1021/acs.chemmater.8b00449.

(198) Chen, M.; Long, Z.; Dong, R.; Wang, L.; Zhang, J.; Li, S.; Zhao, X.; Hou, X.; Shao, H.; Jiang, X. Titanium Incorporation into Zr-Porphyrinic Metal–Organic Frameworks with Enhanced Antibacterial Activity against Multidrug-Resistant Pathogens. *Small* **2020**, *16* (7), 1906240. https://doi.org/10.1002/smll.201906240.

(199) Buru, C. T.; Li, P.; Mehdi, B. L.; Dohnalkova, A.; Platero-Prats, A. E.; Browning, N. D.; Chapman, K. W.; Hupp, J. T.; Farha, O. K. Adsorption of a Catalytically Accessible Polyoxometalate in a Mesoporous Channel-Type Metal–Organic Framework. *Chem. Mater.* **2017**, *29* (12), 5174–5181. https://doi.org/10.1021/acs.chemmater.7b00750.

(200) An, Q.; Xu, Z.; Shang, W.; Wang, Y.; Liu, X.; Guo, D.; Zeng, M.; Jia, Z. Polyoxometalate-Based Metal–Organic Frameworks as the Solid Support to Immobilize MP-11 Enzyme for Enhancing Thermal and Recyclable Stability. *ACS Appl. Bio Mater.* **2022**, *5* (3), 1222–1229. https://doi.org/10.1021/acsabm.1c01252.

(201) Singla, R.; Singh, N.; Pandey, R.; Supriya, S. The Photochromism of UiO-66 Encapsulated Polyoxometalate Composites. *ACS Appl. Eng. Mater.* **2025**, *3* (8), 2275–2287. https://doi.org/10.1021/acsaenm.5c00146.

(202) Buru, C. T.; Platero-Prats, Ana. E.; Chica, D. G.; Kanatzidis, M. G.; Chapman, K. W.; Farha, O. K. Thermally Induced Migration of a Polyoxometalate within a Metal–Organic Framework and Its Catalytic Effects. *J. Mater. Chem. A* **2018**, *6* (17), 7389–7394. https://doi.org/10.1039/C8TA02562B.

(203) Knapp, J. E.; Ortín-Rubio, B.; Heck, F.; Gjorgjevikj, K.; Sleptsova, A.; Krause, S.; Bette, S.; Lotsch, B. V. Dynamic Breathing Behaviour of the Titanium-Based Metal–Organic Framework NTU-9 upon Adsorption of Water and Organic Solvents. *Chem. Sci.* **2025**, *16* (30), 13646–13654. https://doi.org/10.1039/D5SC02585K.

(204) Moscoso, F. G.; Rodriguez-Albelo, L. M.; Ruiz-Salvador, A. R.; Lopes-Costa, T.; Pedrosa, J. M. Enhancement of the Intrinsic Fluorescence of ZIF-8 via Post-Synthetic Cation Exchange with Cd^{2+} and Its Incorporation into PDMS Films for Selective Sulfide Optical Sensing. *Materials Today Chemistry* **2023**, *28*, 101366. https://doi.org/10.1016/j.mtchem.2022.101366.

(205) Wang, A.; Zhou, Y.; Wang, Z.; Chen, M.; Sun, L.; Liu, X. Titanium Incorporated with UiO-66(Zr)-Type Metal–Organic Framework (MOF) for Photocatalytic Application. *RSC Adv.* **2016**, *6* (5), 3671–3679. https://doi.org/10.1039/C5RA24135A.

(206) Chen, X.; Zhuang, Y.; Rampal, N.; Hewitt, R.; Divitini, G.; O'Keefe, C. A.; Liu, X.; Whitaker, D. J.; Wills, J. W.; Jugdaohsingh, R.; Powell, J. J.; Yu, H.; Grey, C. P.; Scherman, O. A.; Fairen-Jimenez, D. Formulation of Metal–Organic Framework-Based Drug Carriers by Controlled Coordination of Methoxy PEG Phosphate: Boosting Colloidal Stability and Redispersibility. *J. Am. Chem. Soc.* **2021**, *143* (34), 13557–13572. https://doi.org/10.1021/jacs.1c03943.

(207) Paz, R.; Viltres, H.; Gupta, N. K.; Rajput, K.; Roy, D. R.; Romero-Galarza, A.; Biesinger, M. C.; Leyva, C. Zirconium-Organic Framework as a Novel Adsorbent for Arsenate Remediation from Aqueous Solutions. *Journal of Molecular Liquids* **2022**, *356*, 118957. https://doi.org/10.1016/j.molliq.2022.118957.

(208) Chen, X.; Wei, Z.; Li, Y.; Sun, Q.; Ding, N.; Zheng, L.; Liu, S.; Chen, W.; Li, S.; Pang, S. Modulating the Conduction Band of MOFs by Introducing Tiny TiO_2 Nanoparticles for Enhanced Photocatalytic Performance: Importance of the Loading Position. *Inorg. Chem.* **2023**, *62* (27), 10572–10581. https://doi.org/10.1021/acs.inorgchem.3c00658.

(209) Lin, Z.-J.; Zheng, H.-Q.; Zeng, Y.-N.; Wang, Y.-L.; Chen, J.; Cao, G.-J.; Gu, J.-F.; Chen, B. Effective and Selective Adsorption of Organoarsenic Acids from Water over a Zr-Based Metal-Organic

Framework. *Chemical Engineering Journal* **2019**, *378*, 122196. https://doi.org/10.1016/j.cej.2019.122196.

(210) Lu, N.; Wang, Y.; Ning, S.; Zhao, W.; Qian, M.; Ma, Y.; Wang, J.; Fan, L.; Guan, J.; Yuan, X. Design of Plasmonic Ag-TiO_2/$H_3PW_{12}O_{40}$ Composite Film with Enhanced Sunlight Photocatalytic Activity towards o-Chlorophenol Degradation. *Sci Rep* **2017**, *7* (1), 17298. https://doi.org/10.1038/s41598-017-17221-4.

(211) Carrasco, S.; Sanz-Marco, A.; Martín-Matute, B. Fast and Robust Synthesis of Metalated PCN-222 and Their Catalytic Performance in Cycloaddition Reactions with CO_2. *Organometallics* **2019**, *38* (18), 3429–3435. https://doi.org/10.1021/acs.organomet.9b00273.

(212) Nunn, E. J.; Tsioumanis, D.; Whitehead, G. F. S.; Fisher, T. B.; Roberts, D. A.; Quinn, M. K.; Natrajan, L. S. Tuning the Performance of Metalloporphyrin-Based Pressure-Sensitive Paints through the Nature of the Central Metal Ion. *ACS Omega* **2024**, *9* (52), 51580–51590. https://doi.org/10.1021/acsomega.4c09045.

(213) Shang, Z.; Yang, X.; Meng, Q.; Tian, S.; Zhang, Z. A Ratiometric Near-infrared Fluorescent Probe for the Detection and Monitoring of Hypochlorous Acid in Rheumatoid Arthritis Model and Real Water Samples. *Smart Molecules* **2023**, *1* (2), e20220007. https://doi.org/10.1002/smo.20220007.

(214) Welter, E. S.; Garg, S.; Gläser, R.; Goepel, M. Methodological Investigation of the Band Gap Determination of Solid Semiconductors via UV/Vis Spectroscopy. *ChemPhotoChem* **2023**, *7* (6), e202300001. https://doi.org/10.1002/cptc.202300001.

(215) Makuła, P.; Pacia, M.; Macyk, W. How To Correctly Determine the Band Gap Energy of Modified Semiconductor Photocatalysts Based on UV–Vis Spectra. *J. Phys. Chem. Lett.* **2018**, *9* (23), 6814–6817. https://doi.org/10.1021/acs.jpclett.8b02892.

(216) Márquez, A.; Rodríguez-Pérez, M. J.; Anta, J. A.; Rodríguez-Gattorno, G.; Bourret, G. R.; Oskam, G.; Berger, T. Defects in Porous Networks of WO_3 Particle Aggregates. *ChemElectroChem* **2016**, *3* (4), 658–667. https://doi.org/10.1002/celc.201500435.

(217) Wu, Y.; Qu, Y.; Su, C.; Yang, X.; Yang, Y.; Zhang, Y.; Huang, W. Enhanced Photoinduced Carrier Separation in Fe-MOF-525/CdS for Photocatalytic Hydrogen Evolution: Improved Catalytic Dynamics

with Specific Active Sites. *Inorg. Chem.* **2023**, *62* (51), 21290–21298. https://doi.org/10.1021/acs.inorgchem.3c03378.

(218) Li, L.; Yu, X.; Xu, L.; Zhao, Y. Fabrication of a Novel Type Visible-Light-Driven Heterojunction Photocatalyst: Metal-Porphyrinic Metal Organic Framework Coupled with PW_{12}/TiO_2. *Chemical Engineering Journal* **2020**, *386*, 123955. https://doi.org/10.1016/j.cej.2019.123955.

(219) Li, S.; Mei, H.-M.; Yao, S.-L.; Chen, Z.-Y.; Lu, Y.-L.; Zhang, L.; Su, C.-Y. Well-Distributed Pt-Nanoparticles within Confined Coordination Interspaces of Self-Sensitized Porphyrin Metal–Organic Frameworks: Synergistic Effect Boosting Highly Efficient Photocatalytic Hydrogen Evolution Reaction. *Chem. Sci.* **2019**, *10* (45), 10577–10585. https://doi.org/10.1039/C9SC01866B.

(220) Liang, Y.; Yang, X.; Wang, X.; Guan, Z.-J.; Xing, H.; Fang, Y. A Cage-on-MOF Strategy to Coordinatively Functionalize Mesoporous MOFs for Manipulating Selectivity in Adsorption and Catalysis. *Nat Commun* **2023**, *14* (1), 5223. https://doi.org/10.1038/s41467-023-40973-9.

(221) Huang, Z.; Song, J.; Pan, L.; Zhang, X.; Wang, L.; Zou, J. Tungsten Oxides for Photocatalysis, Electrochemistry, and Phototherapy. *Advanced Materials* **2015**, *27* (36), 5309–5327. https://doi.org/10.1002/adma.201501217.

(222) Di Valentin, C.; Pacchioni, G. Spectroscopic Properties of Doped and Defective Semiconducting Oxides from Hybrid Density Functional Calculations. *Acc. Chem. Res.* **2014**, *47* (11), 3233–3241. https://doi.org/10.1021/ar4002944.

(223) Mi, Q.; Zhanaidarova, A.; Brunschwig, B. S.; Gray, H. B.; Lewis, N. S. A Quantitative Assessment of the Competition between Water and Anion Oxidation at WO_3 Photoanodes in Acidic Aqueous Electrolytes. *Energy Environ. Sci.* **2012**, *5* (2), 5694. https://doi.org/10.1039/c2ee02929d.

(224) Li, W.; Da, P.; Zhang, Y.; Wang, Y.; Lin, X.; Gong, X.; Zheng, G. WO_3 Nanoflakes for Enhanced Photoelectrochemical Conversion. *ACS Nano* **2014**, *8* (11), 11770–11777. https://doi.org/10.1021/nn5053684.

(225) Soltani, T.; Tayyebi, A.; Hong, H.; Mirfasih, M. H.; Lee, B.-K. A Novel Growth Control of Nanoplates WO_3 Photoanodes with Dual

Oxygen and Tungsten Vacancies for Efficient Photoelectrochemical Water Splitting Performance. *Solar Energy Materials and Solar Cells* **2019**, *191*, 39–49. https://doi.org/10.1016/j.solmat.2018.10.019.

(226) Costa, M. B.; De Araújo, M. A.; Tinoco, M. V. D. L.; Brito, J. F. D.; Mascaro, L. H. Current Trending and beyond for Solar-Driven Water Splitting Reaction on WO_3 Photoanodes. *Journal of Energy Chemistry* **2022**, *73*, 88–113. https://doi.org/10.1016/j.jechem.2022.06.003.

(227) Huang, J.; Yue, P.; Wang, L.; She, H.; Wang, Q. A Review on Tungsten-Trioxide-Based Photoanodes for Water Oxidation. *Chinese Journal of Catalysis* **2019**, *40* (10), 1408–1420. https://doi.org/10.1016/S1872-2067(19)63399-1.

(228) Kalanur, S. S.; Yoo, I.-H.; Cho, I.-S.; Seo, H. Effect of Oxygen Vacancies on the Band Edge Properties of WO_3 Producing Enhanced Photocurrents. *Electrochimica Acta* **2019**, *296*, 517–527. https://doi.org/10.1016/j.electacta.2018.11.061.

(229) Liu, Y.; Li, J.; Li, W.; He, H.; Yang, Y.; Li, Y.; Chen, Q. Electrochemical Doping Induced In Situ Homo-Species for Enhanced Photoelectrochemical Performance on WO_3 Nanoparticles Film Photoelectrodes. *Electrochimica Acta* **2016**, *210*, 251–260. https://doi.org/10.1016/j.electacta.2016.05.165.

(230) Liu, Y.; Li, J.; Li, W.; Yang, Y.; Li, Y.; Chen, Q. Enhancement of the Photoelectrochemical Performance of WO_3 Vertical Arrays Film for Solar Water Splitting by Gadolinium Doping. *J. Phys. Chem. C* **2015**, *119* (27), 14834–14842. https://doi.org/10.1021/acs.jpcc.5b00966.

(231) Su, J.; Guo, L.; Bao, N.; Grimes, C. A. Nanostructured $WO_3/BiVO_4$ Heterojunction Films for Efficient Photoelectrochemical Water Splitting. *Nano Lett.* **2011**, *11* (5), 1928–1933. https://doi.org/10.1021/nl2000743.

(232) Li, Y.; Zhang, L.; Liu, R.; Cao, Z.; Sun, X.; Liu, X.; Luo, J. WO_3@α-Fe_2O_3 Heterojunction Arrays with Improved Photoelectrochemical Behavior for Neutral pH Water Splitting. *ChemCatChem* **2016**, *8* (17), 2765–2770. https://doi.org/10.1002/cctc.201600475.

(233) Wang, J.; Zhou, T.; Zhang, Y.; Chen, S.; Bai, J.; Li, J.; Zhu, H.; Zhou, B. The Design of High Performance Photoanode of CQDs/TiO_2/WO_3 Based on DFT Alignment of Lattice Parameter and Energy Band, and Charge Distribution. *Journal of Colloid and Interface Science* **2021**, *600*, 828–837. https://doi.org/10.1016/j.jcis.2021.05.086.

(234) Bai, S.; Yang, X.; Liu, C.; Xiang, X.; Luo, R.; He, J.; Chen, A. An Integrating Photoanode of WO_3/Fe_2O_3 Heterojunction Decorated with NiFe-LDH to Improve PEC Water Splitting Efficiency. *ACS Sustainable Chem. Eng.* **2018**, *6* (10), 12906–12913. https://doi.org/10.1021/acssuschemeng.8b02267.

(235) Bai, S.; Zhang, K.; Sun, J.; Luo, R.; Li, D.; Chen, A. Surface Decoration of WO_3 Architectures with Fe_2O_3 Nanoparticles for Visible-Light-Driven Photocatalysis. *CrystEngComm* **2014**, *16* (16), 3289. https://doi.org/10.1039/c3ce42410c.

(236) Li, Y.; Liu, Z.; Zhang, J.; Guo, Z.; Xin, Y.; Zhao, L. 1D/0D WO_3/CdS Heterojunction Photoanodes Modified with Dual Co-Catalysts for Efficient Photoelectrochemical Water Splitting. *Journal of Alloys and Compounds* **2019**, *790*, 493–501. https://doi.org/10.1016/j.jallcom.2019.03.178.

(237) Singh, A.; Karmakar, S.; Basu, S. Role of Sputtered WO_3 Underlayer and NiFeCr-LDH Co-Catalyst in WO_3–$BiVO_4$ Heterojunction for Enhanced Photoelectrochemical Water Oxidation. *International Journal of Hydrogen Energy* **2021**, *46* (80), 39868–39881. https://doi.org/10.1016/j.ijhydene.2021.09.248.

(238) Vecchi, P.; Piccioni, A.; Mazzaro, R.; Mazzanti, M.; Cristino, V.; Caramori, S.; Pasquini, L. Charge Separation Efficiency in WO_3/$BiVO_4$ Photoanodes with CoFe Prussian Blue Catalyst Studied by Wavelength-Dependent Intensity-Modulated Photocurrent Spectroscopy. *Solar RRL* **2022**, *6* (7), 2200108. https://doi.org/10.1002/solr.202200108.

(239) He, G.; Li, W.; Qiu, W.; Xu, C.; Wang, K.; Chen, L.; Wang, Y.; Liu, Y.; Li, J. Constructing a Two-Dimensional $SnWO_4$ Nanosheet Array Film for Enhanced Photoelectrochemical Performance. *ACS Appl. Energy Mater.* **2022**, *5* (9), 11883–11891. https://doi.org/10.1021/acsaem.2c02547.

(240) Rodríguez-Gutiérrez, I.; Djatoubai, E.; Rodríguez-Pérez, M.; Su, J.; Rodríguez-Gattorno, G.; Vayssieres, L.; Oskam, G. Photoelectrochemical Water Oxidation at FTO|WO_3@$CuWO_4$ and FTO|WO_3@$CuWO_4$|$BiVO_4$ Heterojunction Systems: An IMPS Analysis. *Electrochimica Acta* **2019**, *308*, 317–327. https://doi.org/10.1016/j.electacta.2019.04.030.

(241) Wang, K.; He, H.; Li, D.; Li, Y.; Li, J.; Li, W. Photoelectrochemical Reduction of Cr (VI) on Plate-like WO_3/$BiVO_4$ Composite Electrodes under Visible-Light Irradiation: Characteristics and Kinetic Study. *Journal of Photochemistry and Photobiology A: Chemistry* **2018**, *367*, 438–445. https://doi.org/10.1016/j.jphotochem.2018.09.005.

(242) Gottesman, R.; Peracchi, I.; Gerke, J. L.; Irani, R.; Abdi, F. F.; Van De Krol, R. Shining a Hot Light on Emerging Photoabsorber Materials: The Power of Rapid Radiative Heating in Developing Oxide Thin-Film Photoelectrodes. *ACS Energy Lett.* **2022**, *7* (1), 514–522. https://doi.org/10.1021/acsenergylett.1c02220.

(243) Das, P. K.; Arunachalam, M.; Seo, Y. J.; Ahn, K.-S.; Ha, J.-S.; Kang, S. H. Functional Blocking Layer of Twisted Tungsten Oxide Nanorod Grown by Electrochemical Anodization for Photoelectrochemical Water Splitting. *J. Electrochem. Soc.* **2020**, *167* (6), 066501. https://doi.org/10.1149/1945-7111/ab7cc1.

(244) Jun, J.; Ju, S.; Moon, S.; Son, S.; Huh, D.; Liu, Y.; Kim, K.; Lee, H. The Optimization of Surface Morphology of Au Nanoparticles on WO_3 Nanoflakes for Plasmonic Photoanode. *Nanotechnology* **2020**, *31* (20), 204003. https://doi.org/10.1088/1361-6528/ab70cf.

(245) Xu, Z.; Zhuang, Q.; Zhou, Y.; Lu, S.; Wang, X.; Cai, W.; Zang, Z. Functional Layers of Inverted Flexible Perovskite Solar Cells and Effective Technologies for Device Commercialization. *Small Structures* **2023**, *4* (5), 2200338. https://doi.org/10.1002/sstr.202200338.

(246) Saxena, V.; Bhagat, N.; Choudhury, S.; Mahajan, A.; Singh, A. Phase Variation of Ultrathin WO_3 Electron-Transport Layer Prepared by Scalable Langmuir–Blodgett Technique to Boost Efficiency of Dye Sensitized Solar Cells. *Solar RRL* **2022**, *6* (8), 2200222. https://doi.org/10.1002/solr.202200222.

(247) Yadav, S.; Lohia, P.; Sahu, A. Enhanced Performance of Double Perovskite Solar Cell Using WO_3 as an Electron Transport Material. *J Opt* **2023**, *52* (2), 776–782. https://doi.org/10.1007/s12596-022-01035-3.

(248) Li, X.; Peng, K.; Chen, H.; Wang, Z. TiO_2 Nanoparticles Assembled on Kaolinites with Different Morphologies for Efficient Photocatalytic Performance. *Sci Rep* **2018**, *8* (1), 11663. https://doi.org/10.1038/s41598-018-29563-8.

(249) Zhang, L.; Xu, T.; Zhao, X.; Zhu, Y. Controllable Synthesis of Bi_2MoO_6 and Effect of Morphology and Variation in Local Structure on Photocatalytic Activities. *Applied Catalysis B: Environmental* **2010**, *98* (3–4), 138–146. https://doi.org/10.1016/j.apcatb.2010.05.022.

(250) Hromádko, L.; Motola, M.; Čičmancová, V.; Bulánek, R.; Macak, J. M. Facile Synthesis of WO_3 Fibers via Centrifugal Spinning as an Efficient UV- and VIS-Light-Driven Photocatalyst. *Ceramics International* **2021**, *47* (24), 35361–35365. https://doi.org/10.1016/j.ceramint.2021.09.079.

(251) Lin, H.; Huang, C. P.; Li, W.; Ni, C.; Shah, S. I.; Tseng, Y.-H. Size Dependency of Nanocrystalline TiO_2 on Its Optical Property and Photocatalytic Reactivity Exemplified by 2-Chlorophenol. *Applied Catalysis B: Environmental* **2006**, *68* (1–2), 1–11. https://doi.org/10.1016/j.apcatb.2006.07.018.

(252) Novak, T. G.; Kim, J.; DeSario, P. A.; Jeon, S. Synthesis and Applications of WO_3 Nanosheets: The Importance of Phase, Stoichiometry, and Aspect Ratio. *Nanoscale Adv.* **2021**, *3* (18), 5166–5182. https://doi.org/10.1039/D1NA00384D.

(253) Wang, F.; Di Valentin, C.; Pacchioni, G. DFT Study of Hydrogen Adsorption On the Monoclinic WO_3 (001) Surface. *J. Phys. Chem. C* **2012**, *116* (19), 10672–10679. https://doi.org/10.1021/jp302210y.

(254) Vanmaekelbergh, D.; De Jongh, P. E. Electron Transport in Disordered Semiconductors Studied by a Small Harmonic Modulation of the Steady State. *Phys. Rev. B* **2000**, *61* (7), 4699–4704. https://doi.org/10.1103/PhysRevB.61.4699.

(255) Bou, A.; Āboliņš, H.; Ashoka, A.; Cruanyes, H.; Guerrero, A.; Deschler, F.; Bisquert, J. Extracting *in Situ* Charge Carrier Diffusion Parameters in Perovskite Solar Cells with Light Modulated

Techniques. *ACS Energy Lett.* **2021**, *6* (6), 2248–2255. https://doi.org/10.1021/acsenergylett.1c00871.

(256) De Jongh, P. E.; Vanmaekelbergh, D. Investigation of the Electronic Transport Properties of Nanocrystalline Particulate TiO_2 Electrodes by Intensity-Modulated Photocurrent Spectroscopy. *J. Phys. Chem. B* **1997**, *101* (14), 2716–2722. https://doi.org/10.1021/jp962226n.

(257) Cao, F.; Oskam, G.; Meyer, G. J.; Searson, P. C. Electron Transport in Porous Nanocrystalline TiO_2 Photoelectrochemical Cells. *J. Phys. Chem.* **1996**, *100* (42), 17021–17027. https://doi.org/10.1021/jp9616573.

(258) Bisquert, J.; Vikhrenko, V. S. Interpretation of the Time Constants Measured by Kinetic Techniques in Nanostructured Semiconductor Electrodes and Dye-Sensitized Solar Cells. *J. Phys. Chem. B* **2004**, *108* (7), 2313–2322. https://doi.org/10.1021/jp035395y.

(259) Anta, J. A.; Casanueva, F.; Oskam, G. A Numerical Model for Charge Transport and Recombination in Dye-Sensitized Solar Cells. *J. Phys. Chem. B* **2006**, *110* (11), 5372–5378. https://doi.org/10.1021/jp056493h.

(260) Alvarez, A. O.; García-Tecedor, M.; Montañés, L.; Mas-Marzá, E.; Giménez, S.; Fabregat-Santiago, F. New Views on Carrier Diffusion and Recombination by Combining Small Perturbation Techniques: Application to $BiVO_4$ Photoelectrodes. *Solar RRL* **2022**, *6* (12), 2200826. https://doi.org/10.1002/solr.202200826.

(261) O'Donnell, S.; Chung, C.-C.; Carbone, A.; Broughton, R.; Jones, J. L.; Maggard, P. A. Pushing the Limits of Metastability in Semiconducting Perovskite Oxides for Visible-Light-Driven Water Oxidation. *Chem. Mater.* **2020**, *32* (7), 3054–3064. https://doi.org/10.1021/acs.chemmater.0c00044.

(262) Ninova, S.; Strach, M.; Buonsanti, R.; Aschauer, U. Suitability of Cu-Substituted β-$Mn_2V_2O_7$ and Mn-Substituted β-Cu2V2O7 for Photocatalytic Water-Splitting. *The Journal of Chemical Physics* **2020**, *153* (8), 084704. https://doi.org/10.1063/5.0019306.

(263) Widenmeyer, M.; Kohler, T.; Samolis, M.; Denko, A. T. D.; Xiao, X.; Xie, W.; Osterloh, F. E.; Weidenkaff, A. Band Gap Adjustment in Perovskite-Type $Eu_{1-x}Ca_xTiO_3$ via Ammonolysis. *Zeitschrift für*

Physikalische Chemie **2020**, *234* (5), 887–909. https://doi.org/10.1515/zpch-2019-1429.

(264) Suzuki, I.; Mizuno, Y.; Omata, T. Tunable Direct Band Gap of β-$CuGaO_2$ and β-$LiGaO_2$ Solid Solutions in the Full Visible Range. *Inorg. Chem.* **2019**, *58* (7), 4262–4267. https://doi.org/10.1021/acs.inorgchem.8b03370.

(265) Zhang, M.; Pham, H. K.; Fang, Y.; Tay, Y. F.; Abdi, F. F.; Wong, L. H. The Synergistic Effect of Cation Mixing in Mesoporous $Bi_xFe_{1-x}VO_4$ Heterojunction Photoanodes for Solar Water Splitting. *J. Mater. Chem. A* **2019**, *7* (24), 14816–14824. https://doi.org/10.1039/C9TA01791G.

(266) Sahoo, P. P.; Maggard, P. A. ChemInform Abstract: Crystal Chemistry, Band Engineering, and Photocatalytic Activity of the $LiNb_3O_8$—$CuNb_3O_8$ Solid Solution. *ChemInform* **2013**, *44* (25), chin.201325011. https://doi.org/10.1002/chin.201325011.

(267) Samu, G. F.; Veres, Á.; Endrődi, B.; Varga, E.; Rajeshwar, K.; Janáky, C. Bandgap-Engineered Quaternary $MBi_2{-}Ti_2O_7$ (M: Fe, Mn) Semiconductor Nanoparticles: Solution Combustion Synthesis, Characterization, and Photocatalysis. *Applied Catalysis B: Environmental* **2017**, *208*, 148–160. https://doi.org/10.1016/j.apcatb.2017.02.036.

(268) Eliziario Nunes, S.; Wang, C.-H.; So, K.; Evans, J. S. O.; Evans, I. R. Bismuth Zinc Vanadate, $BiZn_2VO_6$: New Crystal Structure Type and Electronic Structure. *Journal of Solid State Chemistry* **2015**, *222*, 12–17. https://doi.org/10.1016/j.jssc.2014.10.036.

(269) Liu, H.; Nakamura, R.; Nakato, Y. Bismuth–Copper Vanadate $BiCu_2VO_6$ as a Novel Photocatalyst for Efficient Visible-Light-Driven Oxygen Evolution. *ChemPhysChem* **2005**, *6* (12), 2499–2502. https://doi.org/10.1002/cphc.200500278.

(270) Zoellner, B.; O'Donnell, S.; Wu, Z.; Itanze, D.; Carbone, A.; Osterloh, F. E.; Geyer, S.; Maggard, P. A. Impact of Nb(V) Substitution on the Structure and Optical and Photoelectrochemical Properties of the $Cu_5(Ta_{1-x}Nb_x)_{11}O_{30}$ Solid Solution. *Inorg. Chem.* **2019**, *58* (10), 6845–6857. https://doi.org/10.1021/acs.inorgchem.9b00304.

(271) Zhou, L.; Shinde, A.; Newhouse, P. F.; Guevarra, D.; Wang, Y.; Lai, Y.; Kan, K.; Suram, S. K.; Haber, J. A.; Gregoire, J. M.

Quaternary Oxide Photoanode Discovery Improves the Spectral Response and Photovoltage of Copper Vanadates. *Matter* **2020**, *3* (5), 1614–1630. https://doi.org/10.1016/j.matt.2020.08.031.

(272) Newhouse, P. F.; Guevarra, D.; Zhou, L.; Wang, Y.; Umehara, M.; Boyd, D. A.; Gregoire, J. M.; Haber, J. A. Enhanced Bulk Transport in Copper Vanadate Photoanodes Identified by Combinatorial Alloying. *Matter* **2020**, *3* (5), 1601–1613. https://doi.org/10.1016/j.matt.2020.08.032.

(273) Wickramaratne, K. M. K.; Karki, S. B.; Ramezanipour, F. Electrocatalytic Properties of Oxygen-Deficient Perovskites $Ca_3Fe_{3-x}Mn_xO_8$(x = 1–2) for the Hydrogen Evolution Reaction. *Inorg. Chem.* **2023**, *62* (51), 20961–20969. https://doi.org/10.1021/acs.inorgchem.3c02243.

(274) Danladi, F. I.; Rawat, A.; Adak, A. K.; Zhang, C.; Sangwan, V. K.; Ananth, R.; Hersam, M. C.; Meletis, E. I.; Rajeshwar, K. Synthesis and Tuning of Electronic, Optical, and Photoelectrochemical Properties of Copper Metavanadate Alloys via Alkaline Earth Metal Substitution. *ECS J. Solid State Sci. Technol.* **2024**, *13* (7), 073010. https://doi.org/10.1149/2162-8777/ad5b88.

(275) Rawat, A.; Clark, L.; Zhang, C.; Cavin, J.; Sangwan, V. K.; Toth, P. S.; Janáky, C.; Ananth, R.; Goldfine, E.; Bedzyk, M. J.; Weiss, E. A.; Rondinelli, J. M.; Hersam, M. C.; Meletis, E. I.; Rajeshwar, K. Solution Combustion Synthesis and Characterization of Magnesium Copper Vanadates. *Inorg. Chem.* **2023**, *62* (23), 8903–8913. https://doi.org/10.1021/acs.inorgchem.3c00452.

(276) Vanmaekelbergh, D.; De Wit, A. R.; Cardon, F. Recombination in Semiconductor Electrodes: Investigation by the Electrical and Optoelectrical Impedance Method. *Journal of Applied Physics* **1993**, *73* (10), 5049–5057. https://doi.org/10.1063/1.353776.

(277) Rodríguez-Gutiérrez, I.; García-Rodríguez, R.; Rodríguez-Pérez, M.; Vega-Poot, A.; Rodríguez Gattorno, G.; Parkinson, B. A.; Oskam, G. Charge Transfer and Recombination Dynamics at Inkjet-Printed $CuBi_2O_4$ Electrodes for Photoelectrochemical Water Splitting. *J. Phys. Chem. C* **2018**, *122* (48), 27169–27179. https://doi.org/10.1021/acs.jpcc.8b07936.

(278) Vali, A.; Sarker, H. P.; Heredia Cervera, B.; Rodríguez-Gutiérrez, I.; Hossain, M. K.; Huda, M. N.; Oskam, G.; Rajeshwar, K. Optical,

Electrochemical, and Photoelectrochemical Behavior of Copper Pyrovanadate: A Unified Theoretical and Experimental Study. *J. Phys. Chem. C* **2021**, *125* (36), 19609–19620. https://doi.org/10.1021/acs.jpcc.1c04717.

(279) Grave, D. A.; Segev, G. Non-Unity Photogeneration Yield of Mobile Charge Carriers in Transition Metal-Oxides. *J. Phys. D: Appl. Phys.* **2022**, *55* (2), 023001. https://doi.org/10.1088/1361-6463/ac2640.

(280) Hossain, M. K.; Sarker, H. P.; Sotelo, P.; Dang, U.; Rodríguez-Gutiérrez, I.; Blawat, J.; Vali, A.; Xie, W.; Oskam, G.; Huda, M. N.; Macaluso, R. T.; Rajeshwar, K. Phase-Pure Copper Vanadate (α-CuV_2O_6): Solution Combustion Synthesis and Characterization. *Chem. Mater.* **2020**, *32* (14), 6247–6255. https://doi.org/10.1021/acs.chemmater.0c02227.

(281) Rodríguez-Pérez, M.; Rodríguez-Gutiérrez, I.; Vega-Poot, A.; García-Rodríguez, R.; Rodríguez-Gattorno, G.; Oskam, G. Charge Transfer and Recombination Kinetics at WO_3 for Photoelectrochemical Water Oxidation. *Electrochimica Acta* **2017**, *258*, 900–908. https://doi.org/10.1016/j.electacta.2017.11.140.

(282) Peón-Díaz, F. J.; Expósito-Gálvez, J. C.; Del Río, R. S.; Henríquez, R.; Anta, J. A.; Oskam, G. Exploring the Charge Carrier Dynamics in Carbon Nanotubes-TiO_2 Composites for Water Photooxidation. *Catalysis Today* **2024**, *438*, 114789. https://doi.org/10.1016/j.cattod.2024.114789.

(283) Peón-Díaz, F. J.; Expósito-Gálvez, J. C.; Segura-del-Río, R.; Henríquez, R.; Villalobos, S. F.; Rodríguez, D. J.; Oskam, G. Charge Carrier Dynamics of Chemical Vapor Deposited Carbon-Doped Titanium Dioxide Photoanodes. *Ceramics International* **2024**, *50* (24), 55134–55142. https://doi.org/10.1016/j.ceramint.2024.10.359.

(284) Ravishankar, S.; Riquelme, A.; Sarkar, S. K.; Garcia-Batlle, M.; Garcia-Belmonte, G.; Bisquert, J. Intensity-Modulated Photocurrent Spectroscopy and Its Application to Perovskite Solar Cells. *J. Phys. Chem. C* **2019**, *123* (41), 24995–25014. https://doi.org/10.1021/acs.jpcc.9b07434.

(285) Piccioni, A.; Vecchi, P.; Vecchi, L.; Grandi, S.; Caramori, S.; Mazzaro, R.; Pasquini, L. Distribution of Relaxation Times Based on Lasso Regression: A Tool for High-Resolution Analysis of IMPS

Data in Photoelectrochemical Systems. *J. Phys. Chem. C* **2023**, *127* (17), 7957–7964. https://doi.org/10.1021/acs.jpcc.3c00770.

(286) Viezbicke, B. D.; Patel, S.; Davis, B. E.; Birnie, D. P. Evaluation of the Tauc Method for Optical Absorption Edge Determination: ZnO Thin Films as a Model System: Tauc Method for Optical Absorption Edge Determination. *Phys. Status Solidi B* **2015**, *252* (8), 1700–1710. https://doi.org/10.1002/pssb.201552007.

(287) Tauc, J.; Grigorovici, R.; Vancu, A. Optical Properties and Electronic Structure of Amorphous Germanium. *Physica Status Solidi (b)* **1966**, *15* (2), 627–637. https://doi.org/10.1002/pssb.19660150224.

(288) Klahr, B.; Gimenez, S.; Fabregat-Santiago, F.; Bisquert, J.; Hamann, T. W. Photoelectrochemical and Impedance Spectroscopic Investigation of Water Oxidation with "Co–Pi"-Coated Hematite Electrodes. *J. Am. Chem. Soc.* **2012**, *134* (40), 16693–16700. https://doi.org/10.1021/ja306427f.

(289) Ennaceri, H.; Fischer, K.; Hanus, K.; Chemseddine, A.; Prager, A.; Griebel, J.; Kühnert, M.; Schulze, A.; Abel, B. Effect of Morphology on the Photoelectrochemical Activity of TiO_2 Self-Organized Nanotube Arrays. *Catalysts* **2020**, *10* (3), 279. https://doi.org/10.3390/catal10030279.

(290) Seiß, V.; Helbig, U.; Lösel, R.; Eichelbaum, M. Investigating and Correlating Photoelectrochemical, Photocatalytic, and Antimicrobial Properties of TiO_2 Nanolayers. *Sci Rep* **2021**, *11* (1), 22200. https://doi.org/10.1038/s41598-021-01165-x.

(291) Bertoluzzi, L.; Bisquert, J. Equivalent Circuit of Electrons and Holes in Thin Semiconductor Films for Photoelectrochemical Water Splitting Applications. *J. Phys. Chem. Lett.* **2012**, *3* (17), 2517–2522. https://doi.org/10.1021/jz3010909.

(292) Qiu, J.; Hajibabaei, H.; Nellist, M. R.; Laskowski, F. A. L.; Hamann, T. W.; Boettcher, S. W. Direct in Situ Measurement of Charge Transfer Processes During Photoelectrochemical Water Oxidation on Catalyzed Hematite. *ACS Cent. Sci.* **2017**, *3* (9), 1015–1025. https://doi.org/10.1021/acscentsci.7b00310.

(293) Srivastava, G. P. Surface Passivation by Dissociative Molecular Adsorption. *Vacuum* **2002**, *67* (1), 11–20. https://doi.org/10.1016/S0042-207X(02)00203-8.

(294) Wang, A.; Wang, J.; Sheti, S.; Dahlin, S.; Han, J.; Woo, J.; Xie, K.; Pettersson, L. J.; Olsson, L. A Deactivation Mechanism Study of Phosphorus-Poisoned Diesel Oxidation Catalysts: Model and Supplier Catalysts. *Catal. Sci. Technol.* **2020**, *10* (16), 5602–5617. https://doi.org/10.1039/D0CY00589D.

(295) Ta, K. M.; Cooke, D. J.; Gillie, L. J.; Parker, S. C.; Seal, S.; Wilson, P. B.; Phillips, R. M.; Skelton, J. M.; Molinari, M. Infrared and Raman Diagnostic Modeling of Phosphate Adsorption on Ceria Nanoparticles. *J. Phys. Chem. C* **2023**, *127* (40), 20183–20193. https://doi.org/10.1021/acs.jpcc.3c05409.

(296) Guerra-López, J.; González, R.; Gómez, A.; Pomés, R.; Punte, G.; Della Védova, C. O. Effects of Nickel on Calcium Phosphate Formation. *Journal of Solid State Chemistry* **2000**, *151* (2), 163–169. https://doi.org/10.1006/jssc.1999.8615.

(297) Dupont, M. F.; Donne, S. W. Charge Storage Mechanisms in Electrochemical Capacitors: Effects of Electrode Properties on Performance. *Journal of Power Sources* **2016**, *326*, 613–623. https://doi.org/10.1016/j.jpowsour.2016.03.073.

(298) Mohandas, N.; Bawari, S.; Shibuya, J. J. T.; Ghosh, S.; Mondal, J.; Narayanan, T. N.; Cuesta, A. Understanding Electrochemical Interfaces through Comparing Experimental and Computational Charge Density–Potential Curves. *Chem. Sci.* **2024**, *15* (18), 6643–6660. https://doi.org/10.1039/D4SC00746H.

(299) Lewis, N. S. Chemical Control of Charge Transfer and Recombination at Semiconductor Photoelectrode Surfaces. *Inorg. Chem.* **2005**, *44* (20), 6900–6911. https://doi.org/10.1021/ic051118p.

(300) Sherkar, T. S.; Momblona, C.; Gil-Escrig, L.; Ávila, J.; Sessolo, M.; Bolink, H. J.; Koster, L. J. A. Recombination in Perovskite Solar Cells: Significance of Grain Boundaries, Interface Traps, and Defect Ions. *ACS Energy Lett.* **2017**, *2* (5), 1214–1222. https://doi.org/10.1021/acsenergylett.7b00236.

(301) Kyaw, A. K. K.; Wang, D. H.; Gupta, V.; Leong, W. L.; Ke, L.; Bazan, G. C.; Heeger, A. J. Intensity Dependence of Current–Voltage Characteristics and Recombination in High-Efficiency Solution-Processed Small-Molecule Solar Cells. *ACS Nano* **2013**, *7* (5), 4569–4577. https://doi.org/10.1021/nn401267s.

(302) Castro-Chong, A.; Riquelme, A. J.; Aernouts, T.; Bennett, L. J.; Richardson, G.; Oskam, G.; Anta, J. A. Illumination Intensity Dependence of the Recombination Mechanism in Mixed Perovskite Solar Cells. *ChemPlusChem* **2021**, *86* (9), 1347–1356. https://doi.org/10.1002/cplu.202100233.

(303) Barr, T. J.; Meyer, G. J. Evidence for First-Order Charge Recombination in Dye-Sensitized Solar Cells. *ACS Energy Lett.* **2017**, *2* (10), 2335–2340. https://doi.org/10.1021/acsenergylett.7b00569.

(304) Xiao, S.; Chen, H.; Yang, Z.; Long, X.; Wang, Z.; Zhu, Z.; Qu, Y.; Yang, S. Origin of the Different Photoelectrochemical Performance of Mesoporous $BiVO_4$ Photoanodes between the $BiVO_4$ and the FTO Side Illumination. *J. Phys. Chem. C* **2015**, *119* (41), 23350–23357. https://doi.org/10.1021/acs.jpcc.5b07505.

(305) Wu, H.; Zhang, L.; Du, A.; Irani, R.; Van De Krol, R.; Abdi, F. F.; Ng, Y. H. Low-Bias Photoelectrochemical Water Splitting via Mediating Trap States and Small Polaron Hopping. *Nat Commun* **2022**, *13* (1), 6231. https://doi.org/10.1038/s41467-022-33905-6.

(306) Saeed, K. H.; Garcia Osorio, D.-A.; Li, C.; Banerji, L.; Gardner, A. M.; Cowan, A. J. Monitoring Interfacial Electric Fields at a Hematite Electrode during Water Oxidation. *Chem. Sci.* **2023**, *14* (12), 3182–3189. https://doi.org/10.1039/D2SC05628C.

(307) Hong, S.; Doughty, R. M.; Osterloh, F. E.; Zaikina, J. V. Deep Eutectic Solvent Route Synthesis of Zinc and Copper Vanadate N-Type Semiconductors – Mapping Oxygen Vacancies and Their Effect on Photovoltage. *J. Mater. Chem. A* **2019**, *7* (19), 12303–12316. https://doi.org/10.1039/C9TA00957D.

(308) Rawat, A.; Danladi, F. I.; Sarker, H. P.; Zhang, C.; Fulton, J.; Ananth, R.; Pereyra, A.; Hadke, S. S.; Kewalramani, S.; Sangwan, V. K.; Toth, P. S.; Janáky, C.; Bedzyk, M. J.; Hersam, M. C.; Meletis, E. I.; Rajeshwar, K. Structural, Optoelectronic, Magnetic, and Photoelectrochemical Consequences of Copper Insertion into Alkaline Earth Metal (Mg, Ca, or Sr) Pyrovanadate Compound Frameworks. *Inorg. Chem.* **2025**, *64* (14), 6994–7008. https://doi.org/10.1021/acs.inorgchem.5c00280.

Energy Conversion Nanomaterials & Devices group

Center for Nanoscience and Sustainable Technologies (CNATS)

Department of Physical, Chemical and Natural Systems

Universidad Pablo de Olavide

UNIVERSIDAD PABLO DE OLAVIDE SEVILLA

CNATS